Fall 12-2016

Extending the Reach of Directional Dark Matter Experiments Through Novel Detector Technologies

Nguyen S. Phan
University of New Mexico

Recommended Citation

Phan, Nguyen S.. "Extending the Reach of Directional Dark Matter Experiments Through Novel Detector Technologies." (2016).
https://digitalrepository.unm.edu/phyc_etds/108

Nguyen S. Phan
_____

Candidate

Physics and Astronomy
_____

Department

This dissertation is approved, and it is acceptable in quality and form for publication:

Approved by the Dissertation Committee:

Dinesh Loomba, Chairperson
_____

John Matthews
_____

Michael Gold
_____

James Battat
_____

Extending the Reach of Directional Dark Matter Experiments Through Novel Detector Technologies

by

Nguyen S. Phan

B.S., Astrophysics, University of New Mexico, 2009

DISSERTATION

Submitted in Partial Fulfillment of the

Requirements for the Degree of

Doctor of Philosophy

Physics

The University of New Mexico

Albuquerque, New Mexico

December, 2016

Dedication

For Mom & Dad

Acknowledgments

I would first like to thank Dinesh Loomba, my research advisor, for his guidance, patience, and continued encouragement. He has taught me how to be a scientist, and his integrity, I greatly admire.

I am also thankful to John Matthews, who gave me my first graduate research project and taught me a great deal. Robert Lauer, Eric Miller, and John Matthews provided many helpful suggestions and critique during our weekly group meetings.

Appreciation is owed to Eric Lee for his tremendous help on the hardware, for without his creative engineering skills, some of the projects in this thesis would not have come to fruition.

I would like to acknowledge Dmitry Vorobiev and Pete Zimmer for their assistance with the CCD camera.

Much gratitude is extended to committee member, James Battat, for his valuable recommendations in the revision of this thesis and tremendous help during the manuscript editing process for journal papers.

And finally, I am grateful to my mother, father, sisters, and brother for their unwavering support, continued patience, and immeasurable love. I owe all of my accomplishments to them.

Extending the Reach of Directional Dark Matter Experiments Through Novel Detector Technologies

by

Nguyen S. Phan

B.S., Astrophysics, University of New Mexico, 2009

Ph.D., Physics, University of New Mexico, 2016

Abstract

Dark matter is believed to comprise over 80% of the matter in the Universe. Its composition could be in the form of weakly interacting massive particles (WIMPs), which are predicted by extensions of the Standard Model, namely supersymmetric theories. Even though hints of its existence were detected in astronomical observations over eighty years ago, its detection through means other than the gravitational influence on observable luminous matter still eludes us.

Currently, there are many ongoing direct detection experiments, that aim to measure the signals left by the elastic scattering of WIMPs with nuclei in the detector target material. The detection and identification of dark matter is made difficult, however, by the small interaction cross-section with ordinary matter and the large parameter space that it could inhabit. As such large detectors are needed to probe this parameter space, but potential detections can appear ambiguous in origin due to the presence of backgrounds and a lack of a strong fingerprint in the energy spectrum of detected events. Fortunately, there are two signatures that could point to the Galactic origin of the signal. These are the annual modulation and directional signatures, but of the two, the latter can provide the strongest evidence.

This thesis discusses the many challenges of directional detection utilizing the low pressure time projection chamber (TPC) technology and describes the experimental

efforts to overcome them. A study of low-energy recoils to explore the achievable discrimination threshold and directional sensitivity in a real detector is described. Next, I discuss progress towards a path for detector scale-up while retaining sensitivity by employing a newly identified electronegative TPC gas. The development of a novel readout technology for large detectors is discussed. Finally, the last chapter is devoted to a new idea on a method to detect directionality in a high pressure detector.

Contents

Contents

Contents

Contents

Contents

Contents

List of Figures

List of Figures

List of Tables

Chapter 1

Introduction to Dark Matter

The nature of dark matter remains one of the most important longstanding and unresolved questions in physics. Since its discovery over eighty years ago by Fritz Zwicky through observations of the motions of galaxies in the Coma cluster [1], a considerable amount of evidence for its existence has accumulated through a variety of independent sources. Today, this body of evidence indicates that the matter content of the Universe is dominated by a non-luminous form of matter that is of an exotic and non-baryonic nature and accounts for over 80% of the matter density of the Universe. This chapter gives a brief outline of the framework for which the matter-energy density of the Universe is expressed. Next, we discuss the observational evidence for the existence of dark matter which range in scale from the cosmological to the galactic. Finally, a brief description of some of the possible candidates follows, with particular focus on a class of particles known as weakly interacting massive particles (WIMPs) - one of the leading dark matter candidates.

1.1 Modern cosmology

The discussion in this section will follow the formalism provided by Weinberg in his comprehensive treatment of modern cosmology [2]. In the modern cosmological

paradigm, the Universe is assumed to be isotropic and homogeneous. Under this assumption, the space-time line element can be written as

$$d\tau^2 \equiv g_{\mu\nu}(x)dx^\mu dx^\nu = dt^2 - a^2(t)\left[d\boldsymbol{x}^2 + K\frac{(\boldsymbol{x} \cdot d\boldsymbol{x})^2}{1 - K\boldsymbol{x}^2}\right], \qquad (1.1.1)$$

where $g_{\mu\nu}$ is the spacetime metric, K is the curvature parameter which can take on one of three values:

$$K = \begin{cases} +1 & \text{spherical} \\ -1 & \text{hyperspherical} \\ 0 & \text{Euclidean} \end{cases} \qquad (1.1.2)$$

and $a(t)$ is a function of time and known as the Robertson-Walker scale factor. The meaning of the curvature parameter will be more apparent in the discussion of the expansion of the Universe. Often, the line element is expressed in spherical polar coordinates, for which

$$d\boldsymbol{x}^2 = dr^2 + r^2 d\Omega, \qquad d\Omega \equiv d\theta^2 + \sin^2\theta d\phi^2. \qquad (1.1.3)$$

Substituting the expressions from Equation 1.1.3 into Equation 1.1.1 gives

$$d\tau^2 = dt^2 - a^2(t)\left[\frac{dr^2}{1 - Kr^2} + r^2 d\Omega\right], \qquad (1.1.4)$$

where one should note the the speed of light has been set to one.

In the Robertson-Walker spacetime, the scale factor $a(t)$ is related to the proper distance at time t between a comoving observer at radial distance r and the origin by

$$d(r,t) = a(t)\int_0^r \frac{dr}{\sqrt{1 - Kr^2}} = a(t) \times \begin{cases} \sin^{-1}r & K = +1 \\ \sinh^{-1}r & K = -1 \\ r & K = 0 \end{cases} \qquad (1.1.5)$$

Thus for a Euclidean geometry $(K = 0)$, the distance between the comoving observer and the origin simply grows as the scale factor. This is the basis of the famous Hubble Law, which relates the distance to a galaxy and its recessional velocity.

To relate the kinematics of the Universe to its dynamics and evolution, we must consider its matter and energy density. The conservation of energy and the requirements of homogeneity and isotropy on the components of the energy-momentum tensor describing the spacetime imply a continuity relation between the proper energy density ρ, pressure p, and scale factor a:

$$\frac{d\rho}{dt} + \frac{3\dot{a}}{a}(\rho + p) = 0. \tag{1.1.6}$$

The general solution to Equation 1.1.6 has an equation of state of the form:

$$\rho \propto a^{-3-3w} \tag{1.1.7}$$

where w is a time-independent parameter. In cosmology, there are usually three important components that contribute to the matter-energy density of the Universe:

- Hot Matter (e.g. radiation): $p = \rho/3$

$$\rho \propto a^{-4} \tag{1.1.8}$$

- Cold Matter (e.g. dust): $p = 0$

$$\rho \propto a^{-3} \tag{1.1.9}$$

- Vacuum energy: $p = -\rho$

$$\rho = \text{const.} \tag{1.1.10}$$

The contribution of the these various components determines the dynamics of the expansion of the Universe. The equation governing this evolution is the fundamental Friedmann equation which is given by:

$$\dot{a}^2 + K = \frac{8\pi G \rho a^2}{3}. \tag{1.1.11}$$

The meaning of the curvature constant K in both the line element and the Friedmann equation is made apparent by considering a co-moving ball of matter embedded in

the expanding Universe. The kinetic energy of a co-moving particle of mass m inside the ball at position $\boldsymbol{X}$ from its center is

$$KE = \frac{1}{2}m\dot{\boldsymbol{X}}^2 = \frac{m\dot{a}^2\boldsymbol{X}^2}{2a^2}. \tag{1.1.12}$$

The potential energy of the particle is given by

$$PE = -\frac{GmM}{|\boldsymbol{X}|} = -\frac{4\pi Gm\rho|\boldsymbol{X}|^2}{3}, \tag{1.1.13}$$

where $M = 4\rho|\boldsymbol{X}|^3/3$ is the mass interior to the particle. The total energy E is the sum of these two energies and can be written as

$$E = KE + PE = \frac{m|\boldsymbol{X}|^2}{a^2}\left[\frac{\dot{a}^2}{2} - \frac{4\pi G\rho a^2}{3}\right] = -K\frac{m|\boldsymbol{X}|^2}{2a^2}. \tag{1.1.14}$$

The last equality from Equation 1.1.14 follows from the Friedmann equation (Equation 1.1.11). If $E \geq 0$, the particle is able to escape to infinity, a similar condition to the one found in classical orbital mechanics. This condition is met when $K = 0$ or $K = -1$ which is the case of a Euclidean and hyperspherical geometry, respectively. In a homogeneous and isotropic Universe, each particle can be described in this manner. Thus each particle will move away from each other, implying a universal expansion. However, if $K = +1$, as in the case of a spherical geometry, the total energy is negative and the expansion will eventually stop and particles will fall back toward each other. This case is also often referred to as a closed Universe.

To determine which Universe we inhabit, we have to consider the matter-energy density of the Universe, ρ. From the Friedmann equation, we can define a critical density

$$\rho_{\text{crit}} = \frac{3H^2}{8\pi G}, \tag{1.1.15}$$

where $H \equiv \dot{a}(t)/a(t)$ is famous Hubble constant which characterizes the rate of expansion. At the present time t_0, the critical density is $\rho_{0,\text{crit}} = 1.878\times10^{-29}h^2 \text{ g cm}^{-3}$, where h is the Hubble constant in units of $100 \text{ km s}^{-1}\text{Mpc}^{-1}$ ($H = 100h \text{ km s}^{-1}\text{Mpc}^{-1}$

). This parametrization of the Hubble constant is a way to account for the uncertainty in its value. The value of the curvature constant K is determined by whether the density ρ is less than, equal to, or greater than the value of the critical density ρ_{crit}. The comparison can be made for any time t but is usually done for the present time t_0. In addition, a new dimensionless density parameter can be defined

$$\Omega = \frac{\rho}{\rho_{\text{crit}}} = \Omega_\Lambda + \Omega_M + \Omega_{\text{rel}}, \tag{1.1.16}$$

where $\Omega = 1$ corresponds to $K = 0$, a flat cosmology in which the expansion continues indefinitely.

The total density of the Universe, which is a mixture of vacuum energy, non-relativistic, and relativistic matter, can be expressed in terms of the dimensionless density parameter for each of the components as

$$\rho = \frac{3H_0^2}{8\pi G} \left[\Omega_\Lambda + \Omega_M \left(\frac{a_0}{a} \right)^3 + \Omega_{\text{rel}} \left(\frac{a_0}{a} \right)^4 \right]. \tag{1.1.17}$$

Note that the factor multiplying Ω_M an Ω_{rel} is related to how the density of non-relativistic and relative matter depends on the scale factor (Equations 1.1.9 and 1.1.8).

Observations from the Planck satellite of the cosmic microwave background (CMB) radiation, a thermal relic of the Big Bang, give values for Ω_Λ, Ω_M, and Ω_{rel} at the present time of

$$\begin{aligned}
\Omega_{0,\Lambda} &= 0.692 \pm 0.012, \\
\Omega_{0,M} &= 0.308 \pm 0.012, \\
\Omega_{0,\text{rel}} &= 5.4\alpha \times 10^{-5},
\end{aligned} \tag{1.1.18}$$

where $1 < \alpha < 10$ is a parameter that accounts for non-CMB contributions (e.g. neutrinos, gravitons, etc.) to the density of relativistic matter [3]. Although relatively insignificant today, the radiation density played a dominant role in the past and its significance is manifested in the CMB.

Summing the values of the density parameters in Equation 1.1.18 gives the value of the total density parameter at the present time as

$$\Omega_0 = 1.000 \pm 0.012 \tag{1.1.19}$$

which is consistent with a flat geometry and an indefinite expansion. The dominant contributor to this total density is a mysterious vacuum energy often called dark energy. The character of this energy density and the role that it plays throughout the history of the Universe is somewhat antithetical to the role of the radiation density. Unlike radiation, which was significant in the early Universe and at the time of radiation-matter decoupling ($\sim$377,000 years after the Big Bang), dark energy was negligible during this period. At the present time, however, it along with dark matter are the dominant components driving the evolution of the Universe. The nature of dark energy is a topic of intense research but is beyond the scope of this thesis.

Besides measuring the energy density of matter, the Planck observations can be used to separate this density in terms of the baryonic $\Omega_{0,B}$ and non-baryonic (dark matter) $\Omega_{0,D}$ components as

$$\begin{aligned} \Omega_{0,B} &= 0.0484 \pm 0.0004, \\ \Omega_{0,D} &= 0.258 \pm 0.004, \end{aligned} \tag{1.1.20}$$

where $\Omega_{0,M} = \Omega_{0,B} + \Omega_{0,D}$. Remarkably, the current data imply that dark matter is five times more abundant than baryonic, or ordinary, matter. Figure 1.1 shows the energy-density disribution in the Universe at the present time. Alongside the discovery of dark energy, this is one of the most surprising findings in the last century. Evidence that the matter content of the Universe is dominated by some new, yet undiscovered, form of matter exists at all scales. In Section 1.2, we discuss several of the many pieces of evidence for the existence of this form of matter.
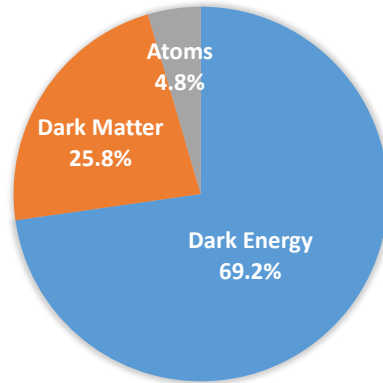
Figure 1.1: *Cosmological energy densities at the present time as derived from Planck observations [3]. Ordinary matter (atoms) make up only around 5% of the Universe while dark matter and dark energy are the dominant components. The small fraction due to photons and neutrinos are not shown.*

1.2   Observational evidence for dark matter

1.2.1   Cosmic microwave background

The CMB is the thermal remnant left over from the time when photons were in thermodynamic equilibrium with the hot plasma in the early Universe. Around that time, the Universe was composed of dark matter and a fluid of photons, baryons, and free electrons. Because of Thomson scattering between the photons and free ions, the Universe was opaque to radiation. But when the temperature dropped to ~3000 K, which occurred around 377,000 years after the Big Bang as a result of cosmic expansion, the photon energy dropped below the binding energy of hydrogen. This allowed electrons to combine with protons to form neutral atoms. Once this occurred, matter and radiation became decoupled, marking the time at which the Universe became transparent to radiation. The CMB observed today is composed of these relic photons that have been red-shifted into the microwave spectrum, and has a characteristic black-body temperature of $T(t_0) = 2.725 \pm 0.001$ K, and a corresponding number density of $n_R(t_0) = 410$ cm^{-3} [4].
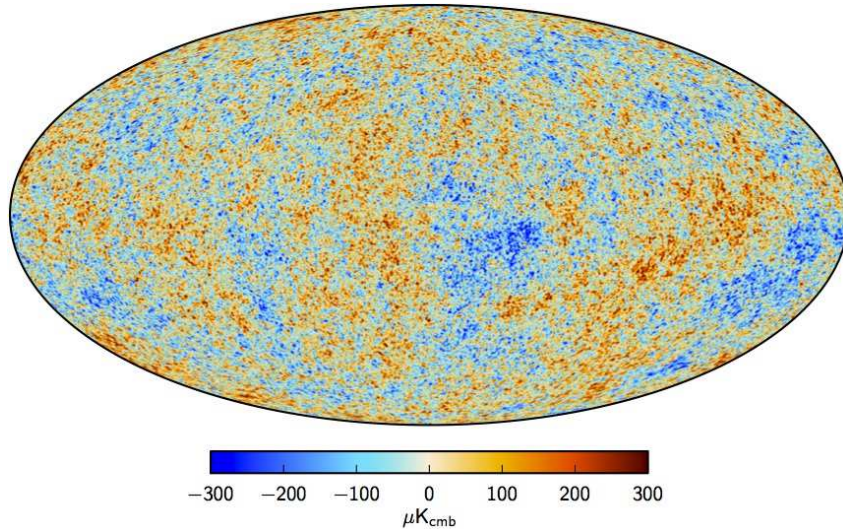
Figure 1.2: *CMB intensity skymap at 5 arcmin resolution derived from the joint baseline analysis of Planck, WMAP, and 408 Mhz. Credit: Ref. [5], reproduced with permission ©ESO.*

A skymap of the CMB radiation show minute anisotropies that arise from the primordial density fluctuations at the time of the photon-matter decoupling, also known as the era of recombination. In Figure 1.2, the temperature map of the CMB measured by Planck is shown [5]. Note how the temperature fluctuations are only on the scale of hundreds of microKelvins. Nevertheless, a detailed analysis of the power spectrum of the temperature anisotropy allows important cosmological parameters to be determined. For this analysis, the power spectrum may be expressed in terms of multipole moments as:

$$\left\langle \left(\frac{\delta T}{T}\right)^2 \right\rangle = \frac{1}{4\pi} \sum_{l=0}^{\infty} (2l+1)C_l, \tag{1.2.1}$$

where C_l is related to the coefficients from the decomposition of the temperature map in spherical harmonics [6]. Figure 1.3 shows the CMB power spectrum measured by Planck with the acoustic peaks being well-measured [3]. To understand the meaning behind these acoustic peaks, we can divide the power spectrum into three regions: $l < 10^2$, $10^2 < l < 10^3$, and $l > 10^3$ [6].
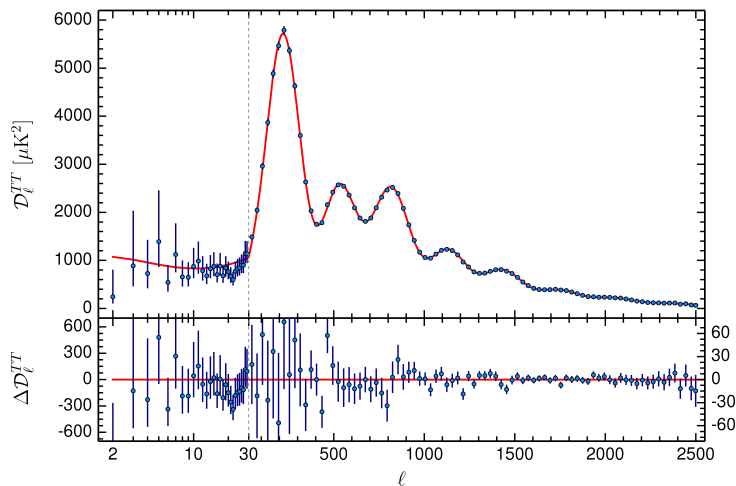
Figure 1.3: *Planck 2015 CMB temperature power spectrum. Shown in the upper panel in red is the best-fit base ΛCDM theoretical spectrum fitted to the Planck TT+lowP likelihood. In the lower panel, residuals with respect to this model are shown with $\pm 1\sigma$ error bars. Credit: Ref. [3], reproduced with permission ©ESO.*

In the region corresponding to large angular scales ($l < 10^2$), the power spectrum is relatively flat and consists of waves with oscillations that have periods longer than the age of the Universe. At angular scales between $10^2 < l < 10^3$, oscillations of the photon-baryon fluid are present because the scales are contained within the sound horizon. The peaks in this angular range correspond to regions with higher and lower densities than the average density while the troughs are regions with neutral compression. The importance of these peaks is that their relative ratio are related to the densities of baryons and dark matter. For instance, the amplitudes of the odd-numbered peaks relative to the even-numbered ones is indicative of the value of Ω_B. The abundance of dark matter, on the other hand, is tied to a suppression of all of the peaks, while the positions of the peaks is dependent on the curvature of the Universe.

Finally, at the smallest angular scales ($l > 10^3$), the power spectrum has a characteristic exponential damping. This feature is the result of photons diffusing out of over-dense regions which were smaller than the photon's mean free path during the

9

time of decoupling with matter. The transition from a radiation opaque Universe to a transparent one took place over a time-span of 50,000 years, during which time the mean free path of the photons was increasing along with the cosmic expansion, giving rise to this exponential damping.

Amazingly, the shape of the power spectrum and the location of the acoustic peaks can be fitted with just six parameters. The model that provides the best fit to the observed power spectrum and other independent cosmological observations is the ΛCDM model, where dark energy and cold dark matter are the dominant components in the Universe. The values of the cosmological parameters given in Eq. 1.1.18 are derived from a fit of the Planck data based upon this cosmological model in combination with lensing reconstruction. Analogous to the Standard Model of particle physics, ΛCDM is the reigning paradigm in modern cosmology.

Measurements of the CMB has help ushered in the era of precision cosmology and allowed for precise determination of the abundance of dark matter in the Universe. However, the evidence for dark matter existed much earlier than this recent development. In the next section, we discuss the first observational evidence for dark matter.

1.2.2   Galaxy clusters: Virial theorem

The earliest evidence for the existence of dark matter can be traced back to the work of Fritz Zwicky in 1933 [1], who realized that for a gravitationally bound system in steady state, the virial theorem relates its total gravitational mass to the kinematics of its constituents. This establishes a method to determine the mass of a system such as a galaxy cluster by observing the motion of its component galaxies. To derive this theorem, we start with the equation of motion for the ith component with mass, m_i, and position, $\vec{r_i}$, in a N-body system interacting gravitationally, which can be

expressed as:

$$m_i \ddot{\vec{r}_i} = -\sum_{j \neq i} G m_i m_j \frac{\vec{r}_i - \vec{r}_j}{|\vec{r}_i - \vec{r}_j|^3}. \tag{1.2.2}$$

Taking the dot product of both sides with $\vec{r}_i$ and summing over all i gives:

$$\sum_i m_i \vec{r}_i \cdot \ddot{\vec{r}_i} = -\sum_i \sum_{j \neq i} G m_i m_j \frac{\vec{r}_i \cdot (\vec{r}_i - \vec{r}_j)}{|\vec{r}_i - \vec{r}_j|^3}. \tag{1.2.3}$$

By rewriting $\vec{r}_i = 1/2(\vec{r}_i - \vec{r}_j) + 1/2(\vec{r}_i + \vec{r}_j)$ and noting the anti-symmetry of $(\vec{r}_i - \vec{r}_j)$ under pair exchange, Eq. 1.2.3 can be rewritten as:

$$\sum_i m_i \vec{r}_i \cdot \ddot{\vec{r}_i} = -\frac{1}{2} \sum_{j \neq i} \frac{G m_i m_j}{|\vec{r}_i - \vec{r}_j|} = U, \tag{1.2.4}$$

where U is the gravitational potential energy. Next, we note that the left hand side of Eq. 1.2.4 is related to the second time derivative of the moment of inertia of the system, which is given by:

$$\ddot{I} = 2 \sum_i m_i (\vec{v}_i^2 + \vec{r}_i \cdot \ddot{\vec{r}_i}) = 2 \left(2K + \sum_i m_i \vec{r}_i \cdot \ddot{\vec{r}_i} \right) \tag{1.2.5}$$

The combined results from Eq. 1.2.5 and Eq. 1.2.4 gives the virial theorem:

$$\frac{1}{2} \ddot{I} = 2K + U. \tag{1.2.6}$$

In the form given in Eq. 1.2.6, the virial theorem is difficult to apply in practice. However, there are two special cases where it becomes very useful [7]: The first case is when the system is in, or approximately in, steady state, so that $\ddot{I} = 0$, and there is a simple relation between the system's total kinetic and potential energies:

$$2K + U = 0. \tag{1.2.7}$$

The second special case occurs when the system is bound and the time average of its moment of inertia, $\langle I \rangle$, is at least quasi-periodic so that time derivative vanishes. Then, by taking the time average of Eq. 1.2.6 the theorem can be expressed as:

$$2 \langle K \rangle + \langle U \rangle = 0. \tag{1.2.8}$$

The condition of steady state and equilibrium is only valid when the age of the system is much longer than its dynamical timescale, which is the time required for components of the system to complete one orbit across the entire system [8].

Zwicky applied the virial theorem (Eq. 1.2.8) to the Coma cluster, a large cluster of galaxies containing over 1,000 members with a mean distance of 102 Mpc from the Earth. In practice, only the velocity along the line of sight, $v_\parallel$, and its dispersion along the same direction, $v_{\parallel,\text{rms}}$, can be determined observationally. However, on average, $v^2 = 3v_{\parallel,\text{rms}}^2$. If the cluster is assumed to be spherical and contains galaxies with the same mass, its total kinetic energy is given by $K = 3/2 M v_{\parallel,\text{rms}}^2$, where M is the total mass of the cluster. Additionally, the cluster's total gravitational potential energy can be expressed as

$$U = -\alpha \frac{GM^2}{R}, \tag{1.2.9}$$

where R is the radius of the cluster and $\alpha = 3/(5-n)$ is a constant with polytropic index n. Zwicky assumed the case of a uniform sphere, where $\alpha = 3/5$ ($n = 0$). Utilizing the virial theorem to relate the total kinetic and potential energies of the system, he arrived at a mass for the Coma cluster of

$$M = \frac{5 v_{\parallel,\text{rms}}^2 R}{G} \approx 1 \times 10^{15} h^{-1} M_\odot, \tag{1.2.10}$$

where, $\bar{v}_\parallel = 7300$ km s^{-1} and $v_{\parallel,\text{rms}} \approx 700$ km s^{-1} were used based on the known radial velocities for seven galaxies in the Coma cluster at the time. The dimensionless Hubble parameter, h, is 0.678 ± 0.009 based on Planck measurements [3]. Also, the total luminosity of the cluster in the visual band was known to be

$$L_V = 2 \times 10^{13} h^{-2} L_\odot, \tag{1.2.11}$$

thus giving the cluster a mass-to-light ratio $M/L \approx 50h$ in Solar units [8]. The results implied that over 95% of the mass in the Coma cluster is in some non-luminous form. As remarkable as Zwicky's results were, an improved analysis of the Coma

cluster that better handles the low statistics, effects of background contamination on the luminosity measurement, and identification of cluster size, gives $M/L \approx 400h$, suggesting the Zwicky actually underestimated the amount of non-luminous matter in the Coma cluster.

1.2.3 Galaxy clusters: Gas temperature

Another independent method to determine the mass of a galaxy cluster is through a measurement of the temperature of the gas trapped in its gravitational potential. Consider a spherical shell of gas in a spherically symmetric potential with radius, r, thickness, dr, and density, $\rho(r)$, the gravitational force on this shell is given by:

$$F_r = \frac{GM(r)}{r^2} 4\pi r^2 \rho(r) dr, \tag{1.2.12}$$

where $M(r)$ is the mass within radius r [4]. If we assume that the cluster is in hydrostatic equilibrium, the gravitational force on the shell is balanced by the pressure gradient, dP, across it. The condition for this equilibrium state is given by:

$$\frac{dP}{dr} = -\frac{GM(r)}{r^2} \rho. \tag{1.2.13}$$

As hydrogen makes up the dominant component of gas in a cluster, the pressure and temperature, T_e, are related through the ideal gas law by:

$$P = \rho \frac{k_B T}{m_H}, \tag{1.2.14}$$

where m_H is the mass of the hydrogen atom. Taking the derivative of Eq. 1.2.14 with respect to the radius, r, gives:

$$\frac{dP}{dr} = \frac{\rho k_B T}{m_H r} \left(\frac{d(\ln \rho)}{d(\ln r)} + \frac{d(\ln T)}{d(\ln r)} \right). \tag{1.2.15}$$

The relationship between the cluster mass and gas temperature is apparent by substituting Eq. 1.2.15 into Eq. 1.2.13, giving:

$$M(r) = -\frac{k_B T}{G m_H} r \left(\frac{d(\ln \rho)}{d(\ln r)} + \frac{d(\ln T)}{d(\ln r)} \right). \tag{1.2.16}$$

Typically, the density and temperature profiles can be measured by X-ray observations, but a good estimate can be obtained by assuming a model for the density profile. The beta model, proposed by Cavaliere and Fusco-Femiano [9, 10], parametrizes the density by:

$$\rho(r) = \rho(0) \left[1 + \left(\frac{r}{r_c} \right)^2 \right]^{-3\beta/2}, \tag{1.2.17}$$

where r_c, is the cluster core radius and $\beta = \mu m_H \sigma_r^2 / k_B T$. With the beta model, Eq. 1.2.16 can be written as:

$$M(r) = 1.6 \times 10^{15} \beta \left(\frac{T}{10 \text{ keV}} \right) \left(\frac{r}{\text{Mpc}} \right) \frac{(r/r_c)^2}{1 + (r/r_c)^2} M_\odot. \tag{1.2.18}$$

Using this method, Ref. [11] derived the X-ray masses for 14 clusters with $0.17 < z < 0.55$ and compared their results to dynamical masses obtained from galaxy velocities (virial theorem) and gravitational lensing studies. Within this cluster sample, the average values for the temperature, core radius, and β, are 6.5±2.1 keV, 103±58 kpc, and 0.72±0.08, respectively. The average dynamical to X-ray mass ratio, M_{dyn}/M_X, was found to be 1.04 ± 0.07 with discrepancies of up to a factor of 2 for individual clusters when compared against strong lensing surveys. This discrepancy could be due to a variety of systematic effects including mass clumps along the line of sight and unknown redshifts in the lensed objects. In addition, X-ray data lack the resolution to provide a detailed characterization of the X-ray emission in the cluster cores. Nevertheless, this issue does not change the startling conclusion that the mass of galaxy clusters is dominated by a non-luminous and non-baryonic form of matter. In fact, the average mass fraction of the X-ray emitting gas in the cluster sample is only $0.047 \pm 0.002 \ h^{-3/2}$, and is consistent with the results from the dynamical study of the Coma cluster which showed that over 95% of the cluster's mass is non-luminous.

1.2.4 Galactic rotation curves

We showed in the previous sections that there is an abundance of evidence for the existence of dark matter in the largest scale structures as characterized by the high mass-to-light ratios. However, the evidence is not only found on the largest scales but extends from the cosmological scale (Gpc) all the way down to the galactic scale (1-100 kpc). At the galactic level, one of the most robust pieces of evidence for dark matter is the observation of flat rotation curves for disk galaxies.

In disk galaxies, stars and gas move in approximately circular orbits around the galactic center with centripetal acceleration, v^2/r, where v is the rotational velocity and r is the orbital radius. This is due to the gravitational force exerted by all of the matter within the orbital radius, $M(r)$, on the orbiting object. By equating the centripetal force with the Newtonian gravitational force, the orbital velocity can be expressed as:

$$v(r) = \left(\frac{GM(r)}{r}\right)^{1/2}.$$ (1.2.19)

Thus measurements of the orbital velocity with orbital radius, which is often called the rotation curve, provides a way to probe the mass distribution of the galaxy.

Measurements of the orbital velocity were made for the Andromeda Galaxy (M31) in the optical by Rubin and Ford [12] and in the radio by Whitehurst and Roberts [13]. Combining both types of observations, Whitehurst and Roberts showed that the rotation curve for Andromeda is flat out to at least 30 kpc from the galactic center [14]. This implies that the mass of the galaxy increases linearly with radius and has a mass-to-luminosity ratio of > 200 [14]. Around the same time, flat rotation curves for over a half dozen other galaxies were reported by Einasto et al. [15]. They used data of the motions of dwarf galaxies orbiting around the main galaxy to determine the rotation curve out to about ten times the radius of the visible stellar disk. Similar to the rotation curve for Andromeda, the curves for the half dozen galaxies were flat between 10-100 kpc [15].

In the same year that Einasto et al. published their work, Ostriker et al. made a suggestion that the observed flat rotation curves can be explained if galaxies are embedded in a spherical isothermal halo [16]. The idea is that a typical galaxy is composed of a stellar disk and central bulge surrounded by an extended dark matter halo. This halo extends to over ten times the radius of the luminous stellar disk and accounts for most of the mass of the galaxy. From the flatness of the rotation curve, the density profile of the dark matter halo must fall off approximately as $\rho_d \propto r^{-2}$. One of the more popular parametrization for the halo density profile is due to Navarro, Frenk, and White:

$$\rho_{NFW}(r) = \frac{\rho_H}{(r/r_s)(1 + r/r_s)^2} \tag{1.2.20}$$

and is often referred to as the NFW profile [17]. For the Milky Way Galaxy, $\rho_H \sim 1.40 \times 10^7$ M$_\odot$/kpc^3 [18] and $r_s \sim 10 - 35$ kpc [19]. In the Solar neighborhood ($R_\odot = 8.0 \pm 0.5$ kpc), the local dark matter density is $\rho_\odot \sim 0.20 - 0.56$ GeV/cm^3 [19]. This quantity is related to the flux of dark matter on Earth and is very important in direct searches. But before discussing dark matter detection, we must first consider what it is we are searching for. In the next section, we discuss some of the candidates for dark matter and show that their properties are considerably diverse.

1.3 Dark matter candidates

1.3.1 Lower bound on the mass

One of the most important quantity for characterizing a particle is its mass. For dark matter particles, model-independent bounds, albeit extremely weak, on their masses do in fact exist. The lower bound is imposed by the requirement that dark matter particles must be confined in galaxies [20], a reasonable assumption given the observational evidence. For bosonic dark matter particles with mass M_D moving with speed v_D, their de Broglie wavelength, $\lambda = 2\pi/M_D v_D$, must be smaller than the

host galaxy. The most stringent bound is determined by considering dwarf galaxies, which have typical sizes of order 1 kpc and velocities usually of order 150 km/s. This implies a lower bound of,

$$M_D \gtrsim 3 \times 10^{-22} \, \text{eV}. \tag{1.3.1}$$

In the case of fermions, the lower bound is due to the Pauli exclusion principle which constrains the maximum phase space density of the dark matter particles to be less than the allowable value given by,

$$f_f = \frac{g_\chi}{(2\pi)^3}. \tag{1.3.2}$$

For dark matter in the halo of a galaxy, a reasonable distribution for the momentum is the Maxwell-Boltzmann distribution. The maximum of the phase space density occurs when the momentum, $\vec{p} = 0$, and is given by,

$$f^{\text{max}}(\vec{p}, \vec{x}) = \frac{\rho_D}{M_D^4} \frac{1}{(2\pi)^{3/2} v_D^3}. \tag{1.3.3}$$

With $g_\chi = 2$, $v_D \sim 150$ km/s, and $\rho_D \sim 15$ GeV/cm³ for the case of dwarf galaxies ($\rho_D \sim 0.5$ GeV/cm³ for galaxies like the Milky Way), the lower bound is given by,

$$M_D \gtrsim 750 \, \text{eV}. \tag{1.3.4}$$

1.3.2 Upper bound on the mass

At the upper bound of the mass range, the consideration is no longer centered on fundamental particles but instead on macroscopic compact objects. These objects are usually grouped into a category known as massive compact halo objects (MACHOs). Objects that fall under this classification are black holes, neutron stars, brown dwarfs, unassociated planets, and low luminosity stellar class bodies such as white and red dwarfs. Limits on the abundance of these objects can be placed through their dynamical effects on directly observable astronomical systems.

One of the most robust methods to survey the halo of our Galaxy for MACHOs is through gravitational microlensing, a method first proposed by Paczyński [22]. By continuously monitoring the brightness of millions of stars in the Magellanic Clouds over a timescale of hours to years, these dark halo objects can be detected when they pass over the observer's line of sight towards a star, causing a momentary brightening. The rate of the lensing events provides information about the number of these objects in the disk and halo of the Galaxy as well as their masses and kinematics.

The OGLE-II [23] and EROS-2 [24] surveys of the Magellanic Clouds have excluded baryonic MACHOs with masses in the range 10^{-7} to 30 $M_\odot$ as the dominant constituents of dark matter in the halo. In addition to the constraints from microlensing surveys, the parameter space for baryonic MACHOs is further reduced from the observed velocity dispersion in the disc [25] and evaporation of low mass gas clumps (snowballs) [26], thus effectively ruling MACHOs with masses greater than 10^6 $M_\odot$. Recently, a re-analysis of wide binary samples [27] by Quinn et al. [28] has further constrained the upper mass range of MACHOs to 500 $M_\odot$, leaving only a narrow window (30-500 $M_\odot$) in which baryonic MACHOs can be the primary constituents of the Galaxy's dark matter halo. This effectively excludes objects such as brown dwarfs and planets as possible dark matter candidates. The current bounds on MACHOs are shown in Figure 1.4.

The small window on allowable MACHO masses has been all but closed at the present time. A recent study of the orbits of wide binaries in the halo, which allows for estimates of the effects of the halo density on the passage of these objects through the galactic disk, has allowed new upper limits on the masses of MACHOs to be established. The limits range from 112 $M_\odot$ to less than 10 $M_\odot$ depending on the different subsamples of the binaries used in the analysis [29]. Thus, the upper bound on the mass of dark matter in the form of MACHOs is 10^{-7} $M_\odot$ ($\sim$2 lunar masses), and in effect, rules out objects composed of baryonic matter as being the dominant contributor to the observed dark matter density.
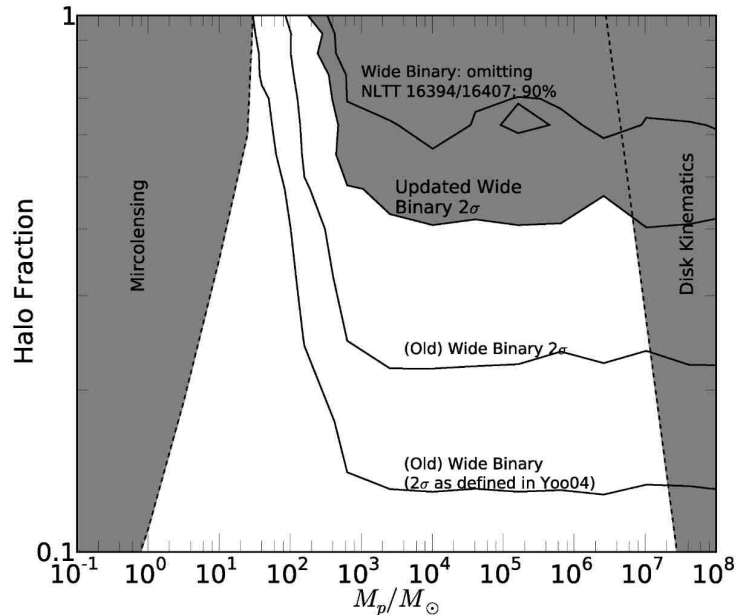
Figure 1.4: *The bounds on the masses of MACHOs in solar mass units and their contribution to the mass of the Milky Way's halo as determined from various astronomical surveys. Reproduced from Ref. [28].*

If dark matter is not composed of baryonic matter, then perhaps, they are made of new fundamental particles that have yet to be detected. The list of possible candidates is certainly long and a discussion that endeavors to cover all of them is well beyond the scope of this thesis. Rather, we discuss below in some detail three of the more promising particle dark matter candidates.

1.3.3 Axions

The axion, a light pseudoscalar boson, is one of many candidates for non-baryonic dark matter. The hypothetical particle was proposed in relation to the strong-CP problem, the apparent absence of charge-parity (CP) (combined charge conjugation (C) and parity inversion (P) symmetry) violation in quantum chromodynamics

(QCD). The possible CP violating term in the QCD Lagrangian can be written as,

$$\mathcal{L}_\theta = -\theta(\alpha_s/8\pi)\tilde{G}^a_{\mu\nu}G^a_{\mu\nu}, \tag{1.3.5}$$

where θ is a constant parameter, $\tilde{G}^a_{\mu\nu}$ is the gluon field strength, $G^a_{\mu\nu}$ is the dual tensor, and $\alpha_s \sim 1$ is the QCD gauge coupling constant, analogous to the fine structure constant, $\alpha = 1/137$, in electrodynamics [30].

Interestingly, $\mathcal{L}_\theta$ would also contribute to the hypothetical neutron EDM (electric dipole moment), d_n, via a coupling to the electromagnetic current. The connection between the neutron EDM and the θ parameter is given by

$$d_n = -3.3 \times 10^{-16}\theta \ (e \text{ cm}). \tag{1.3.6}$$

The recent experimentally determined bound on the neutron EDM of $d_n < 2.9 \times 10^{-26}$ (e cm) [31] leads to an upper bound on the θ parameter:

$$\theta < 9 \times 10^{-11} \tag{1.3.7}$$

[30]. The extreme smallness of this parameter has no apparent natural explanation, and the absence of a resolution is known as the strong-CP problem.

Peccei and Quinn [32, 33] proposed a possible solution to this problem through the introduction of a new global U(1) symmetry, often called PQ symmetry, that is spontaneously broken. In essence, the solution considers θ, not as a fixed parameter, but as a dynamical scalar field, $\theta(x)$. A consequence of this solution, realized by Weinberg and Wilczek, is the existence of a new light pseudoscalar particle called the axion [34, 35]. The precise mass of the axion is not known but is determined by the energy scale, f_a, which is the energy scale at which PQ symmetry is broken through the relation

$$m_a \approx 6 \, \text{eV} \left(\frac{10^6 \ \text{GeV}}{f_a} \right) \tag{1.3.8}$$

[36, 37, 38].

The impact of the axion in cosmology as a dark matter candidate is quantified by its density relative to the critical density of the Universe which is given by

$$\Omega_a \approx \left(\frac{6\ \mu eV}{m_a} \right)^{7/6} \tag{1.3.9}$$

[30]. If the axion accounts for all the dark matter in the Universe ($\Omega_m \approx 0.27$), this would correspond to $m_a \approx 18\ \mu$eV. This is within the open mass window for the axion (10^{-6} eV $< m_a < 10^{-2}$ eV). The upper limit in this mass range comes from the observed burst duration of supernova SN1987a, whereas the lower limit comes from the cosmological argument that an axion mass, $m_a < 1\ \mu$eV, would over-close the Universe and be inconsistent with observations.

To detect the axion, most searches rely on an axion-photon interaction known as the Primakoff effect [39]. These searches can be classified into three different types: helioscopic, haloscopic, and laser searches. The helioscopic search attempts to detect axions emitted from the center of the sun, which have a broad spectrum around 1-10 keV. These axions are produced in the solar interior by the Primakoff conversion of plasma photons in the Coulomb field of charged particles [40]. For solar axion detection, a helioscope requires a powerful magnet coupled to an X-ray detector. Often a buffer gas is also used to improve the sensitivity of the experiment to higher axion masses [41]. The CAST Collaboration [42, 43], employing a powerful magnet with a field of up to 9T over 9.3 m in length has placed stringent bounds on the strength of the axion-photon coupling. A future project, called IAXO [44], will attempt to provide a significant improvement in sensitivity over CAST and explore a broad range of QCD axion models.

In the haloscopic search, dark matter axions from the halo of the Galaxy are detected using a microwave cavity [45]. Instead of producing X-rays, as in solar axion searches, dark matter axions produce feeble radio waves that corresponds to the axion mass when in the presence of a strong magnetic field. To amplify this weak signal, a cavity that matches the Compton wavelength of the axion is used.
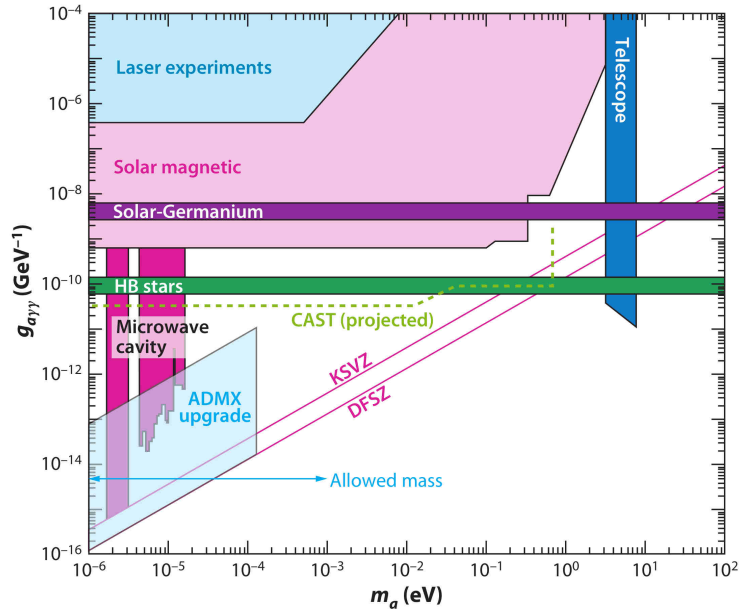
Figure 1.5: *Current constraints on the axion mass (m_a) and axion-photon coupling ($g_{a\gamma\gamma}$). The allowed mass range is shown by the horizontal blue line. Reproduced from Refs. [47] and [62] .*

The ADMX Collaboration [46] is a haloscopic search that has begun to probe the axion mass range consistent with dark matter.

The final type of axion search is unique in that it does not rely on cosmological or astrophysical sources. Often called light-shining-through-a-wall experiments, these searches employ a laser and a optical barrier under a magnetic field. The laser is a source of axions due to photon-axion mixing. When produced in this way, a axion can penetrate the barrier and then reconvert into a photon on the other side and be detected with a photon detector. The ALPS Collaboration [48] has used this method to place bounds on the axion mass. A proposed future experiment, called ALPS II [49], has the potential of setting bounds beyond those from astrophysics. Current constraints on the axion mass and axion-photon coupling are shown in Figure 1.5.

1.3.4 Sterile neutrinos

The observation of neutrino flavor oscillation in solar, atmospheric, accelerator, and reactor neutrinos strongly suggests the existence of right-handed neutrinos, often called sterile or singlet fermions [50]. Such particles would have zero electric, weak, and strong charges, and their interaction with ordinary matter would be extremely weak. In addition, the number of these right-handed fermions must be at least two in order to be consistent with experiment results [50].

Recall the bound on the phase-space density of fermionic dark matter given by the Pauli exclusion principle implies that if sterile neutrinos are a dark matter candidate, then their masses must be of order keV and above (1.3.4). Given their weak interaction with ordinary matter, the way in which sterile neutrinos can be detected is through their decay into other more easily detected particles. One such decay channel is to a photon and an active neutrino [51]. The energy of the photon produced in this decay process is given by

$$E_\gamma = \frac{M_1}{2}, \tag{1.3.10}$$

where M_1 is the mass of the decaying sterile neutrino. Given that the sterile neutrino mass must be in the keV range or above, the produced photon is in the X-ray or Gamma-ray spectrum, and hence, should contribute to the astronomical diffused X-ray/Gamma-ray background [52, 53]. Observations of this diffused background has placed limits on the mixing angle, φ, between the sterile neutrinos and matter which is related to the its mass by

$$\varphi^2 \lesssim 1.8 \times 10^{-5} \left(\frac{\text{keV}}{M_1} \right)^5. \tag{1.3.11}$$

This bound on the mixing angle implies that the lifetime of the sterile neutrino is much larger than the age of the Universe, a necessary requirement if it were to comprise a significant fraction of the dark matter content.

Searches for dark matter decay line in satellite data from XMM-Newton [57, 58], Chandra [54, 57, 55, 56], INTEGRAL [59, 60], and Suzaku[61] have not yielded any
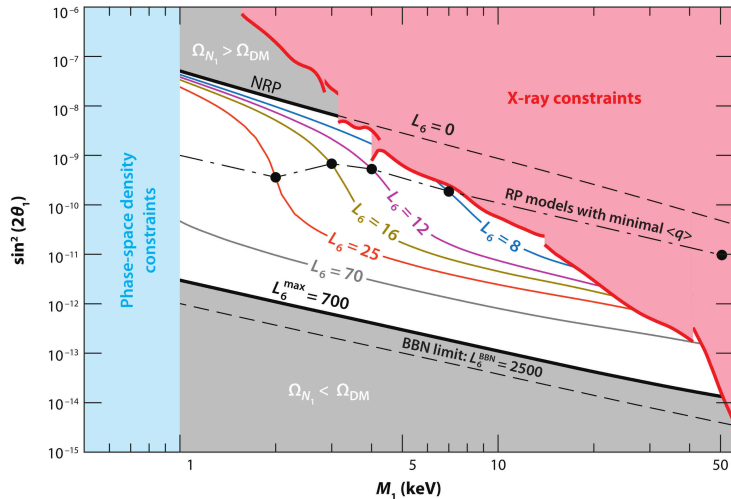
Figure 1.6: *The allowed region for sterile neutrino dark matter produced through mixing with active neutrinos is shown by the unshaded region. The allowed mass range is between 1-50 keV. Reproduced from Ref. [50].*

candidate lines in the energy range of ~ 0.5 keV-10 MeV. However, the combination of phase-space density constraints together with astrophysical and cosmological observations currently restrict the sterile neutrino mass to range of 1-50 keV [50]. The allowed region for sterile neutrino dark matter parameters is shown in Figure 1.6. Future improvements on these bounds will rely on next generation X-ray spectrometers that have much better energy resolution, effective area, and field-of-view than current instruments.

1.3.5 WIMPs

Perhaps the leading candidate for dark matter are a class of particles known as weakly interacting massive particles (WIMPs) which are predicted by many extensions of the Standard Model. These particles, with a mass in the range of $\sim$ few GeV - few TeV, have no electric charge and interact with ordinary matter through only the gravitational and weak forces. The extensions often take the form so called supersymmetric theories where a new multiplicatively conserved quantum number R

is introduced [2]. R takes the value +1 for all the particles of the Standard Model, and −1 for their supersymmetric partners. A consequence of this conservation law is that the lightest supersymmetric particle (LSP) with $R = -1$ is stable, but these particles can annihilate into Standard Model particles with $R = +1$ (the product of the Rs for the two supersymmetric particles is $(-1)(-1) = +1$). The neutralino, the spin−1/2 superpartner of some mixture of Standard Model neutral gauge and scalar bosons, is one of several LSP candidates.

Although particle physics can introduce many new particles as dark matter candidates, WIMPs being just one example, the reason WIMPs are a leading candidate is due to the so called "WIMP miracle". If dark matter is composed of WIMPs, it can be produced as a thermal relic of the Big Bang with a density consistent with that observed for dark matter. Consider in the hot and dense early Universe, all particles are in thermal equilibrium. As the Universe expands and cools to a temperature T below the the mass of dark matter particle M_D, the number of these particles becomes suppressed by the Boltzmann factor, $\exp(-M_D/T)$. This number does not drop to zero because the expansion decreases the density, n, of these particles, making it difficult for them to annihilate with each other. When this happens, the density of dark matter particles freezes out and approaches a constant value which is the thermal relic density.

The rate of annihilation per dark matter particle with its antiparticle is $n \langle \sigma v \rangle$, where n is the number density, $\sigma(v)$ is the annihilation cross section, and v is the relative velocity. The rate of decrease of the dark matter particles due to annihilation in a co-moving volume a^3 is $na^3 \times n \langle \sigma v \rangle$. In equilibrium, this annihilation rate is balanced by a creation rate $n_{\text{eq}}a^3 \times n_{\text{eq}} \langle \sigma v \rangle$. Thus the evolution with time of number of the dark matter particles in a comoving volume, shown in Figure 1.7, is given by the Boltzmann equation

$$\frac{d(na^3)}{dt} = - \left(n^2 - n_{\text{eq}}^2 \right) a^3 \langle \sigma v \rangle \tag{1.3.12}$$

[2]. When the Universe's temperature falls below M_D the creation term becomes
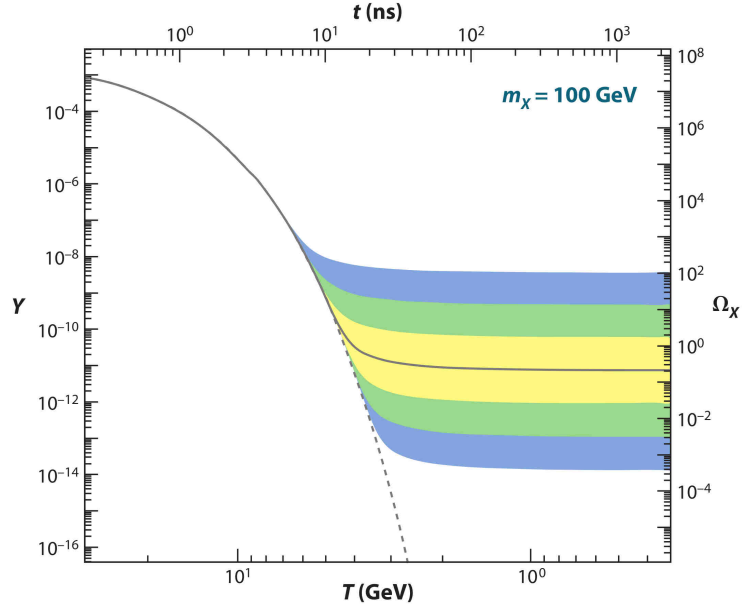
Figure 1.7: *The comoving number density (Y) and the thermal relic density (Ω_X) for the case of a 100 GeV WIMP as a function of the time (t) and corresponding temperature of the Universe (T). The solid gray contour shows the annihilation cross-section that gives the correct relic density while the dashed contour shows the number density for a particle that remains in thermal equilibrium. The shaded regions show the density corresponding to other values of the cross-section. Reproduced from Ref. [62].*

unimportant and Equation 1.3.12 becomes

$$\frac{d(na^3)}{dt} = -n^2 a^3 \langle \sigma v \rangle \,. \tag{1.3.13}$$

Both Equations 1.3.12 and 1.3.13 must be solved numerically, but an approximate answer can be obtained by considering the number density at freeze out, n_f. At this time, the annihilation rate is equal to the Hubble rate, that is $n \langle \sigma v \rangle = H$. The number density is then approximately given by

$$n_f \sim (M_D T_f)^{3/2} e^{-M_D/T_f} \sim \frac{T_f^2}{M_{\mathrm{Pl}} \langle \sigma v \rangle}, \tag{1.3.14}$$

where T_f is the freeze out temperature and M_{Pl} is the Planck mass [62]. The dark matter thermal relic density is then given by

$$\Omega_D = \frac{M_D n_0}{\rho_c} = \frac{M_D T_0^3}{\rho_c} \frac{n_0}{T_0^3} \sim \frac{M_D T_0^3}{\rho_c} \frac{n_f}{T_f^3} \sim \frac{x_f T_0^3}{\rho_c M_{\mathrm{Pl}}} \langle \sigma v \rangle^{-1} \,, \tag{1.3.15}$$
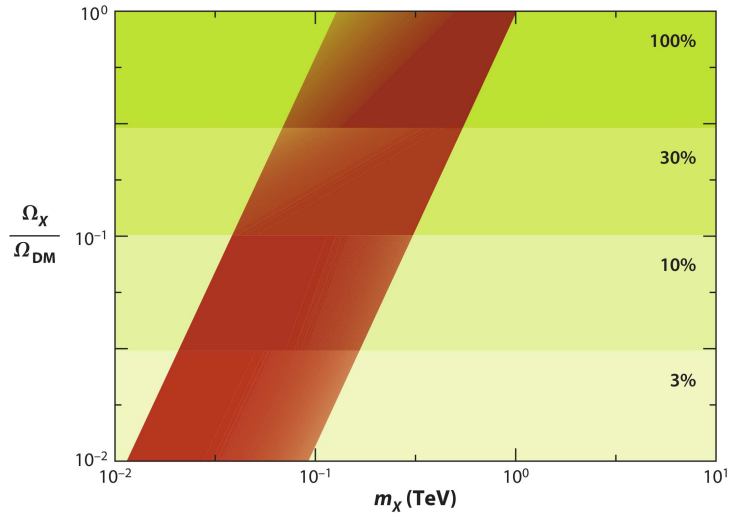
Figure 1.8: *Omega-WIMP mass plane with a band showing the natural values of these two parameters for a thermal relic. Reproduced from Ref. [62].*

where $x_f \equiv M_D/T_f$, ρ_c is the critical density, T_0 and n_0 are the present temperature and number density, respectively.

The product of the annihilation cross-section and relative velocity can be expressed as

$$\sigma v = k_w \frac{g_{\text{weak}}^4}{16\pi^2 M_D^2}, \tag{1.3.16}$$

where $g_{\text{weak}} \simeq 0.65$ is weak interaction gauge coupling and k_w is a dimensionless parameter of order one. Consequently, a particle that accounts for most of the dark matter in the Universe would have a mass in the range of 0.1-1 TeV [62] (Figure 1.8). This result has been called the WIMP miracle because a particle at the weak scale would be a natural and model-independent dark matter candidate.

If dark matter is composed of WIMPs, there are three strategies for detection: indirect detection, direct detection, and production in colliders. As dark matter (X) must have annihilated in the early Universe to give the observed relic density, one channel in which the annihilation can occur is to Standard Model particles (S) $(X + X \to S + S)$. The detection of Standard Model particles resulting from

27

annihilation is called indirect detection. It is important to note that even after freeze out, dark matter annihilation can continue to occur, particularly in regions with high densities of dark matter such as in the cores of galaxies. The annihilation rate is not exactly zero but only greatly suppressed after freeze out. In the production detection strategy, dark matter can be produced by colliding ordinary matter together through $(S + S \rightarrow X + X)$. Although the produced dark matter particles are not detected directly in this method due to their feeble interaction with ordinary matter, their existence can be inferred from the missing energy. Finally, in direct detection, dark matter particles from the Galaxy's halo can scatter off ordinary matter $(X + S \rightarrow X + S)$ through spin-independent and/or spin-dependent interactions. The recoiling target resulting from such an interaction can deposit enough energy to be detected in sensitive, low-background detectors. The focus of this thesis is on direct detection, with an emphasis on directional detection, and a more detailed discussion will be given in Chapter 2.

Chapter 2

WIMP Direct Detection

2.1 Introduction

In Chapter 1 we showed that evidence for dark matter exists at all scales, from the cosmological down to the galactic. One of the most promising candidates for this new and non-luminous form of matter are WIMPs, or Weakly Interacting Massive Particles. The theoretical motivation for these particles comes from extensions of the Standard Model, in particular, supersymmetric theories [63, 64, 65]. On the observational side, there are indications, perhaps circumstantial in nature, that a weak-scale particle would naturally produce the observed dark matter relic abundance. This so called WIMP miracle also implies that if WIMPs are the dominant constituent of dark matter, then they must have some small but finite coupling to ordinary matter. Without this coupling, the annihilation of dark matter in the early Universe would be prohibited, leading to an over-abundance today.

If WIMPs do, indeed, interact with ordinary matter and exists at all distance scales, a possible path towards their identification is through the direct detection method which searches for the interactions of WIMPs with target nuclei in low background terrestrial detectors. In this chapter, we discuss the mathematics of direct detection, with emphasis on the expected interaction rates in a given detector

and the signatures that can provide an unambiguous origin of the observed signal.

2.2   WIMP-nucleus scattering

The general expression for the differential scattering rate of dark matter particles with the detector target material is given by:

$$\frac{dR}{dE_R} \propto n_0 \sigma_0 |F|^2 S(E_R) \int_{v_{\min}}^{v_{\max}} \frac{1}{v} f(\vec{v}, \vec{v_E}) d^3 v. \tag{2.2.1}$$

In Eq. 2.2.1, $n_0 = \rho_D/M_D$ is the mean dark matter particle number density in the local Solar neighborhood for a WIMP of mass M_D and local density ρ_D. This parameter can be regarded as an astrophysical quantity because its value must be obtained from observations. Currently, estimates of the local dark matter density are in the range $0.2 \text{ GeVcm}^{-3} \leq \rho_D \leq 0.56 \text{ GeVcm}^{-3}$ [19]. The other terms in Eq. 2.2.1 are the WIMP-nucleus interaction cross-section σ_0, the form factor correction $|F|^2$, the detector efficiency $S(E_R)$, and the WIMP velocity distribution in the laboratory frame $f(\vec{v}, \vec{v_E})$. With the exception of the detector efficiency which depends on the particular experiment, we discuss each of the those terms in detail below.

2.2.1   WIMP velocity distribution

The standard model for the dark matter distribution surrounded our Galaxy is that of a spherical isothermal halo. The velocity distribution of WIMPs within is halo is often assumed to be Maxwellian and of the form:

$$f(\vec{v}, \vec{v_E}) \propto \exp\left[-(\vec{v} + \vec{v_E})^2/v_0^2\right], \tag{2.2.2}$$

where $\vec{v_E} \simeq 244 \text{ km s}^{-1}$ is the velocity of the Earth relative to the dark matter halo, $\vec{v}$ is the velocity of the dark matter particle onto the Earth-bound target, and $v_0 \simeq 230$ km s^{-1} is the most probable speed [66]. The normalization constant, k, is determined

by:

$$k = \int_0^{2\pi} d\phi \int_{-1}^{1} d\cos\theta \int_0^{v_{esc}} v^2 f(\vec{v}, \vec{v_E}) dv. \tag{2.2.3}$$

For the special case where the velocity distribution has no cutoff, that is $v_{esc} = \infty$,

$$k = k_0 = 4\pi \int_0^{\infty} \exp\left(-v^2/v_0^2\right) v^2 dv = (\pi v_0^2)^{3/2}. \tag{2.2.4}$$

However, in a realistic scenario, the velocity distribution must be truncated at some value. For the direct detection case, that value is the local galactic escape velocity, $|\vec{v} + \vec{v_E}| = v_{esc}$. This, of course, is necessary as any dark matter particle with a velocity exceeding the escape velocity would no longer be gravitational bound to the Galaxy and could never interact in an Earth-bound detector. For the Milky Way Galaxy, $v_{esc} \sim 600 \text{ km s}^{-1}$. Thus, k, is given by

$$k = 4\pi \int_0^{v_{esc}} \exp\left(-v^2/v_0^2\right) v^2 dv = 4\pi \left[\frac{v_0^2}{2} \int_0^{v_{esc}} \exp\left(-v^2/v_0^2\right) dv \right.$$
$$\left. -v_{esc} \exp\left(-v_{esc}^2/v_0^2\right) \right] = k_0 \left[\text{erf}\left(\frac{v_{esc}}{v_0}\right) - \frac{2}{\pi^{1/2}} \frac{v_{esc}}{v_0} \exp\left(-v_{esc}^2/v_0^2\right) \right] \tag{2.2.5}$$

In summary, the velocity distribution for the two cases is given by:

- **Maxwell distribution**: $v_{esc} = \infty$

$$f(\vec{v}, \vec{v_E}) = \frac{1}{(\pi v_0^2)^{3/2}} \exp\left[-(\vec{v} + \vec{v_E})^2/v_0^2\right] \tag{2.2.6}$$

- **Truncated Maxwell distribution**: $|\vec{v} + \vec{v_E}| = v_{esc}$

$$f(\vec{v}, \vec{v_E}) = \begin{cases} \left[J(\pi v_0^2)^{3/2}\right]^{-1} \exp[-(\vec{v} + \vec{v_E})^2/v_0^2] & v < v_{esc} \\ 0 & v \geq v_{esc} \end{cases} \tag{2.2.7}$$

with

$$J = \text{erf}\left(\frac{v_{esc}}{v_0}\right) - \frac{2}{\pi^{1/2}} \frac{v_{esc}}{v_0} \exp\left(-v_{esc}^2/v_0^2\right). \tag{2.2.8}$$

It is worth mentioning that the Maxwellian velocity distribution for WIMPs is merely an assumption. Many other forms for the velocity distribution have been explored [67]. Among these are the stream model, Sikivie's late infall (SLI) halo model, and anisotropic logarithmic-ellipsoidal models. Characterizing the WIMP velocity and mass distributions in our Galaxy would require a detector capable of measuring the directions of WIMP-induced recoils. The challenges to designing a directional detector is discussed in more detail in the subsequent chapters of this thesis.

2.2.2 Form factors

The effective scattering cross-section for WIMP on nucleus begins to fall off when the WIMP momentum is such that its wavelength h/q is no longer much larger than the nucleus size. This momentum dependence is encompassed in a term called the form factor, F^2, and the general behavior of the cross-section is then given by

$$\sigma(qr_n) = \sigma_0 F^2(qr_n), \tag{2.2.9}$$

where σ_0 is the zero momentum transfer cross-section. Functionally, the form factor depends on the dimensionless quantity $qr_n/\hbar$. Typically, $\hbar$ is taken to be one, and the correction term is ≤ 1. Here, r_n is the effective nuclear radius and $q = (2M_T E_R)^{1/2}$ is the momentum transferred to a target mass M_T and recoil energy E_R [66].

In general, the form factor is different for spin-independent and spin-dependent interactions, as well as the target nucleus of interest. However, in both cases, the form factor can be approximated in the first Born approximation as the Fourier transform of the density distribution of scattering centers, $\rho_s(r)$. Below, we give both the approximations as well as the more exact results for the two interaction cases.

- **Spin-independent**

  The approximation of the form factor for the spin-independent case is given by

the Fourier transform of the density distribution for a solid sphere as

$$F(qr_n) = 3j_1(qr_n)/qr_n = 3\left[\sin(qr_n) - qr_n\cos(qr_n)\right]/(qr_n)^3, \qquad (2.2.10)$$

where j_1 is the spherical Bessel function of the first kind. A more commonly used form factor for the spin-independent case is the one proposed by Helm [68]

$$F(qr_n) = 3\frac{j_1(qr_n)}{qr_n} \times e^{-(qs)^2/2}, \qquad (2.2.11)$$

where s is the nuclear skin thickness. Typically, $s \simeq 0.9$ fm and, for most A, $r_n \simeq 1.14A^{1/3}$ is used.

- **Spin-dependent**

  The form factor for the spin-dependent case can be obtained approximately by the Fourier transform of a thin shell

  $$F(qr_n) = j_0(qr_n) = \sin(qr_n)/qr_n. \qquad (2.2.12)$$

A more exact result is provided by Engel et al. [74]. For momentum transfers in the experimentally pertinent range $0 \leq qr_n \leq 6$, the form factor is approximated by

$$F^2(qr_n) = \begin{cases} j_0^2(qr_n) & qr_n < 2.55, \ qr_n > 4.5 \\ \text{constant} \simeq 0.047 & 2.55 \leq qr_n \leq 4.5 \end{cases} \qquad (2.2.13)$$

with $r_n \simeq 1.0A^{1/3}$ fm.

2.2.3   Cross-sections

The cross-section and form factor in Eq. 2.2.1 can be combined into an effective cross-section, $\sigma(E)$, which accounts for the energy dependence of the interaction. In general, this effective scattering cross-section is composed of two parts, a spin-independent part (σ^{SI}) and a spin-dependent part (σ^{SD}) and can be written as:

$$\sigma(E) = \sigma^{SI} + \sigma^{SD}. \qquad (2.2.14)$$

In this section, we discuss the expressions for the cross-sections for these two interaction types.

1. **Spin-independent cross-section**

   The spin-independent cross-section can be written as

$$\sigma^{SI} = \sigma_0 \left| F^2 \right|, \tag{2.2.15}$$

where $\left| F^2 \right|$ is the nuclear form factor discussed in the previous section and σ_0 is the zero-momentum transfer cross-section. For the spin-independent case, this cross-section can be expressed in the form

$$\sigma_0 = \frac{\mu_N}{\pi} |ZG^p + (A - Z)G^n|^2, \tag{2.2.16}$$

where Z is the number of protons, A is the mass number, and G^p and G^n are the WIMP-proton and WIMP-neutron coupling, respectively [67]. Note that $\mu_N = M_D M_T/(M_D + M_T)$ is the reduced mass between the WIMP and nucleus of interest. Equation 2.2.16 can be greatly simplified under the typically made assumption that $G^p = G^n$, allowing the cross-section to be expressed as

$$\sigma_0 = \frac{\mu_N^2}{\mu_p^2} A^2 \sigma_p, \tag{2.2.17}$$

where σ_p is the WIMP-proton cross-section. Equation 2.2.17 provides a very useful expression for comparing the results from experiments with different targets. Those results are expressed in the form of a limit curve on an exclusion plot where the vertical axis is the WIMP-proton cross-section and the horizontal axis is the WIMP mass. All combinations of WIMP masses and cross-sections above the curve are ruled out by the experiment under standard assumptions for the local dark matter density, velocity distribution and escape velocity, and nuclear form factors.

Because the cross-section in Eq. 2.2.17 scales as A^2, it is advantageous to choose a target with a high nucleon number. For example, ^{132}Xe, with $A = 132$, has a scattering cross-section that is 1089 times larger than ^{4}He, with $A = 4$. However, it is important to note that the total rate does not scale in this manner because for a given mass of target material, there are fewer nuclei in given mass of a high nucleon number target.

Another factor that must be considered is the energy threshold. Because this quantity is never truly zero in a real detector, matching the target mass to the WIMP mass can provide some advantages. For example, consider the case of a 1 GeV WIMP, a xenon detector might not necessarily be more sensitive than a helium detector because the recoil energies will typically be higher in the latter case due kinematics. In such a situation, the maximum recoil energy is 0.1 keV for Xe while it is much higher for He at 2.6 keV. Thus, the rate above detection threshold can be much higher for the He detector than the Xe detector even though Xe benefits from the nucleon enhancement factor. Nevertheless, in practice the choice of target is not easily made because the WIMP mass is an unknown quantity that can range from a few GeVs to a few TeVs.

2. **Spin-dependent cross-section**

   The spin-dependent cross-section for a nucleus, N, can be written as

   $$\sigma_N^{SD} = \frac{32\mu_N^2 G_F^2}{(2J_N + 1)\hbar^4} \left[a_p^2 S_{pp}(E) + a_n^2 S_{nn}(E) + a_p a_n S_{pn}(E) \right], \qquad (2.2.18)$$

   where G_F is the Fermi coupling constant, J_N is the nucleus total angular momentum, $a_p(a_n)$ is the effective WIMP-proton(neutron) coupling, and S_{pp}, S_{nn}, S_{np} are dimensionless parameters characterizing the nuclear form factor [67]. These parameters are given by

$$S_{pp} = S_{00} + S_{11} + S_{01}, \tag{2.2.19}$$

$$S_{nn} = S_{00} + S_{11} - S_{01}, \tag{2.2.20}$$

$$S_{pn} = 2(S_{00} - S_{11}), \tag{2.2.21}$$

where S_{00}, S_{11}, and S_{01} are the nuclear spin structure functions. For a proton-odd nucleus,

$$S_{pp} = \frac{\lambda_N^2 J_N (J_N + 1)(2J_N + 1)}{\pi}, \tag{2.2.22}$$

$$S_{nn} = 0, \tag{2.2.23}$$

$$S_{pn} = 0, \tag{2.2.24}$$

and for a neutron-odd nucleus,

$$S_{pp} = 0, \tag{2.2.25}$$

$$S_{nn} = \frac{\lambda_N^2 J_N (J_N + 1)(2J_N + 1)}{\pi}, \tag{2.2.26}$$

$$S_{pn} = 0. \tag{2.2.27}$$

Thus, the spin-dependent cross-section for WIMP-proton is given by

$$\sigma_p^{SD} = \frac{24\mu_p^2 G_F^2}{\pi \hbar^4} a_p^2 \tag{2.2.28}$$

and similarly for the WIMP-neutron spin-dependent cross-section. The expression in Eq. 2.2.28 is useful for comparing experiments with different targets by normalizing to a standard cross-section. This, of course, is similar to what is done in the spin-independent case. So by combining Eqs. 2.2.18 and 2.2.28, the

Table 2.1: *The natural abundance (NA) and nuclear spin for select targets [70, 71, 72, 73, 74, 75].*

Target	NA (%)	J_N	S_p	S_n	$\lambda_{N,p}^2 J_N(J_N+1)$	$\lambda_{N,n}^2 J_N(J_N+1)$
^{1}H	99.9885	1/2	0.5	0	0.75	0
^{3}He	0.000137	1/2	-0.081	0.552	0.020	0.914
^{7}Li	92.41	3/2	0.38	0	0.24	0
^{19}F	100.0	1/2	0.4751	-0.0087	0.677	2.3×10^{-4}
^{23}Na	100.0	3/2	0.2477	0.0199	0.102	6.60×10^{-4}
^{35}Cl	75.78	3/2	-0.051	-0.0088	0.004	1.3×10^{-4}
^{73}Ge	7.73	9/2	0.009	0.372	9.9×10^{-5}	0.168
^{93}Nb	100.0	9/2	0.48	0.04	0.28	2.0×10^{-3}
^{127}I	100.0	5/2	0.354	0.064	0.175	5.7×10^{-3}
^{129}Xe	26.44	1/2	0.0128	0.300	4.92×10^{-4}	0.27
^{131}Xe	21.18	3/2	-0.012	-0.217	2.4×10^{-4}	7.85×10^{-2}

spin-dependent cross-section for a proton-odd nucleus, N, can be expressed in terms of the WIMP-proton cross-section as

$$\sigma_N^{SD} = \frac{4}{3} \frac{\mu_N^2}{\mu_p^2} \lambda_N^2 J_N(J_N + 1)\sigma_p^{SD}. \tag{2.2.29}$$

A similar expression can be written in terms of the WIMP-neutron cross-section for a neutron-odd target nucleus. It is evident that for spin-dependent dark matter searches, it is important to choose a target containing nuclei with a high spin factor rather than one with a high nucleon number as is the case for spin-independent WIMP searches. One of the nuclei typically used in spin-dependent searches is ^{19}F, which is a proton-odd nucleus, where $\lambda_N^2 J_N(J_N + 1) = 0.677$. This target also has the advantage of having a high natural abundance, so there is no need for isotopic enrichment. But fluorine is only one of the many targets used for spin-dependent searches, among these are xenon(^{129}Xe), iodine (^{127}I), and sodium (^{23}Na). The nuclear spin parameters for targets typically used in direct dark matter searches are tabulated in Table 2.1.

2.2.4 Total event rate

To compute the total interaction rate, we first consider the differential event rate per unit mass on a target with atomic number, A, which is given by

$$dR = \frac{N_0}{A}\sigma_0 v \, dn, \tag{2.2.30}$$

where N_0 is Avogadro's number, σ_0 is the zero-momentum transfer cross-section, and dn is the differential particle number density [66]. In general, σ_0 must be replaced by $\sigma(E_R)$ with the form factor included for either the spin-independent or spin-dependent case. Because the form factor is of order one, using the zero-momentum cross-section provides a reasonably accurate result that can be computed analytically.

First, consider the simple special case, $v_E = 0$ and $v_{\rm esc} = \infty$, the event rate is

$$R = \frac{N_0}{A}\sigma_0 \int_0^\infty v \, dn = \frac{N_0}{A}\frac{\rho_D}{M_D}\sigma_0 \langle v \rangle \tag{2.2.31}$$

where the last equality follows by substituting the differential number density, $dn = (n_0/k)f(\vec{v}, \vec{v_E})d^3v$, into the integrand and the definition $\langle v \rangle = (1/k)\int v f(v)d^3v$. Recall that $n_0 = \rho_D/M_D$ is the mean dark matter particle number density and $k = k_0 = (\pi v_0^2)^{3/2}$. It is often useful to define an event rate, R_0 as

$$R_0 \equiv \frac{2}{\sqrt{\pi}}\frac{N_0}{A}\frac{\rho_D}{M_D}\sigma_0 v_0 \tag{2.2.32}$$

so that R can be written as

$$R = R_0 \frac{2}{\sqrt{\pi}}\frac{\langle v \rangle}{v_0} = R_0 \frac{1}{2\pi v_0^4}\int v f(\vec{v}, \vec{v_E})d^3v. \tag{2.2.33}$$

For $v_E \neq 0$ and a finite $v_{\rm esc}$, the most general form for the event rate, $R(v_E, v_{\rm esc})$, is found by integrating over the truncated Maxwell velocity distribution. This gives

$$R(v_E, v_{\rm esc}) = R_0 \frac{k_0}{k}\left\{\frac{1}{2}\left[\pi^{1/2}\left(\frac{v_E}{v_0} + \frac{1}{2}\frac{v_0}{v_E}\right)\operatorname{erf}\left(\frac{v_E}{v_0}\right) + \exp\{(-v_E^2/v_0^2)\}\right]\right.$$
$$\left. - \exp\{(-v_{\rm esc}^2/v_0^2)\}\left(\frac{v_{\rm esc}^2}{v_0^2} + \frac{1}{3}\frac{v_E^2}{v_0^2} + 1\right)\right\} \tag{2.2.34}$$

Note that k_0 and k are given by Eqs. 2.2.4 and 2.2.5, respectively, and typically the velocities are taken to be $v_0 = 230 \text{ km s}^{-1}$, $v_E = 244 \text{ km s}^{-1}$, and $v_{\text{esc}} = 600 \text{ km s}^{-1}$. The event rate, R_0, is determined by considering a WIMP mass, M_D, WIMP density $\rho_D \simeq 0.3 \text{ GeVcm}^{-3}$, and target nucleus with atomic number A. The units for the event rates are often expressed as the number of events per kg of target material per year of exposure.

2.2.5 Differential event rate

To include the form factor, detector efficiency, and other experimental effects such as energy threshold, the differential rate is needed. Using the differential form of Eq. 2.2.33, we obtain

$$\frac{dE}{dE_R} = \frac{R_0}{E_0 r} \frac{k_0}{k} \frac{1}{2\pi v_0^2} \int_{v_{\text{min}}}^{v_{\text{max}}} \frac{1}{v} f(\vec{v}, \vec{v_E}) d^3 \vec{v} \tag{2.2.35}$$

Here, r is defined as

$$r = 4 M_D M_T / (M_D + M_T)^2 \tag{2.2.36}$$

and v_{min} as

$$v_{\text{min}} = (2 E_{\text{min}} / M_D)^{1/2} = (E_R / E_0 r)^{1/2} v_0 \tag{2.2.37}$$

with

$$E_{\text{min}} = E_R / r \tag{2.2.38}$$

and

$$E_0 = 1/2 (M_D v_0^2) = (v_0^2 / v^2) E, \tag{2.2.39}$$

[66]. Using these definitions, the differential event rate for non-zero v_E and $v_{\text{esc}} = \infty$ is given by

$$\frac{dR(v_E, \infty)}{dE_R} = \frac{R_0}{E_0 r} \frac{\pi^{1/2}}{4} \frac{v_0}{v_E} \left[\text{erf}\left(\frac{v_{\text{min}} + v_E}{v_0}\right) - \text{erf}\left(\frac{v_{\text{min}} - v_E}{v_0}\right) \right]. \tag{2.2.40}$$

(a) $M_D = 10$ GeV, $E_{th} = 0$ keV

(b) $M_D = 10$ GeV, $E_{th} = 5$ keV

(c) $M_D = 10$ GeV, $E_{th} = 10$ keV

(d) $M_D = 10$ GeV, $E_{th} = 20$ keV
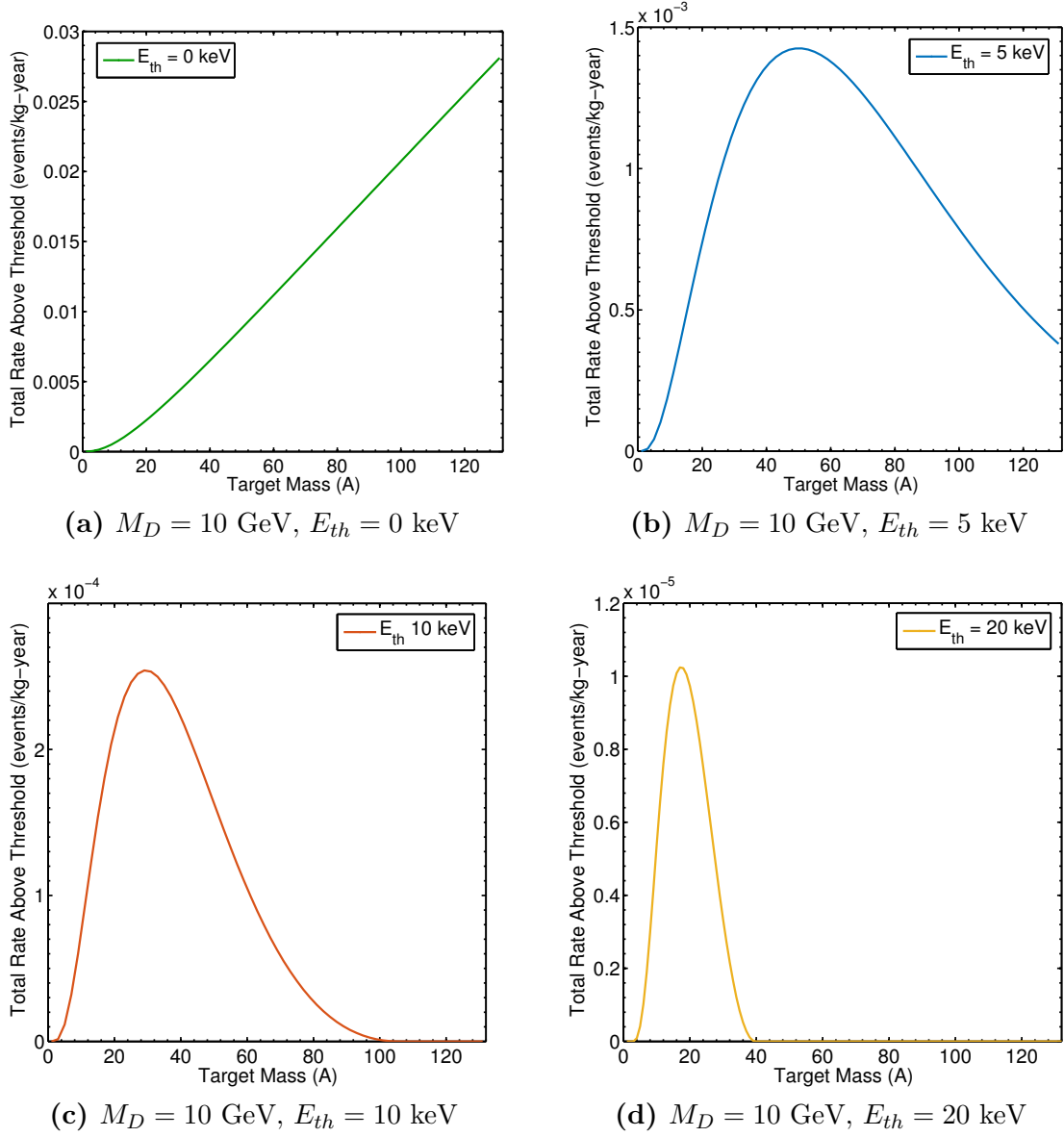
Figure 2.1: *The total rate above threshold as a function of the target nucleus atomic number A for $M_D = 10$ GeV. The rates are for spin-independent interaction at a cross-section $\sigma_{Wp} = 10^{-46}$ cm^2. (a)-(d) Shows the dependence of the maximal rate and the corresponding target mass number on the energy threshold. At zero threshold, the A^2 enhancement factor dominates, but at higher thresholds, the optimal target mass number is close to the WIMP mass. Also, note the precipitous decline of the total rate with energy threshold.*

(a) $M_D = 100$ GeV, $E_{th} = 0$ keV

(b) $M_D = 100$ GeV, $E_{th} = 10$ keV

(c) $M_D = 100$ GeV, $E_{th} = 20$ keV

(d) $M_D = 100$ GeV, $E_{th} = 50$ keV
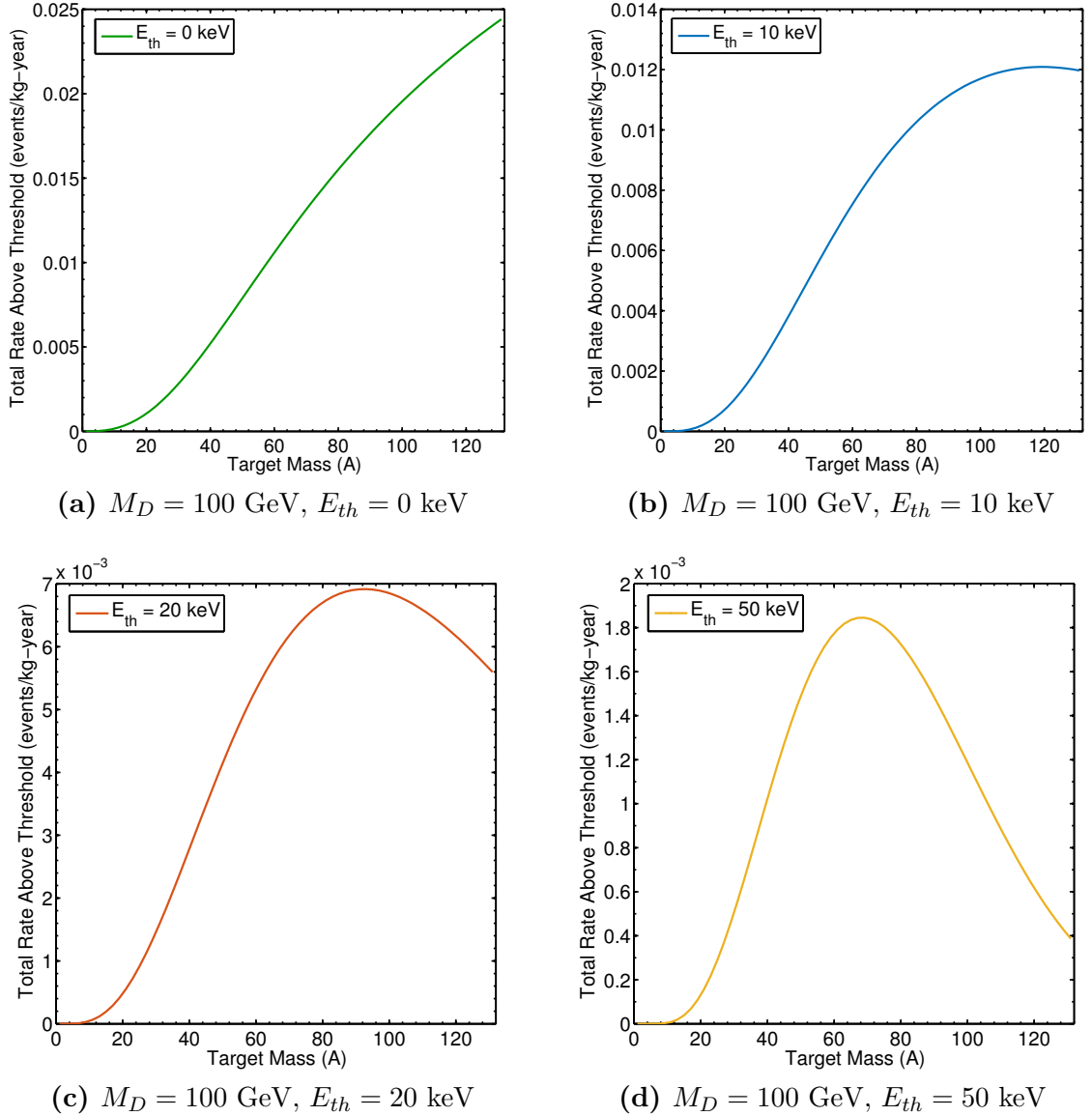
Figure 2.2: *The total rate above threshold as a function of the target nucleus atomic number A for $M_D = 100$ GeV. The rates are for spin-independent interaction at a cross-section $\sigma_{W-p} = 10^{-46}$ cm^2, which is approximately the world's current leading limit at 100 GeV [76]. (a)-(d) Shows the dependence of the maximal rate and the corresponding target mass number on the energy threshold. At zero threshold, the A^2 enhancement factor dominates, but at higher thresholds, the optimal target mass number is close to the WIMP mass. Compared to the 10 GeV case, the total rate falls much slower with energy threshold. Despite that, these rates show that a ton-scale or larger detector is necessary to push lower the detection limit.*

(a) Spin-independent, $M_D = 10$ GeV **(b)** Spin-independent, $M_D = 100$ GeV
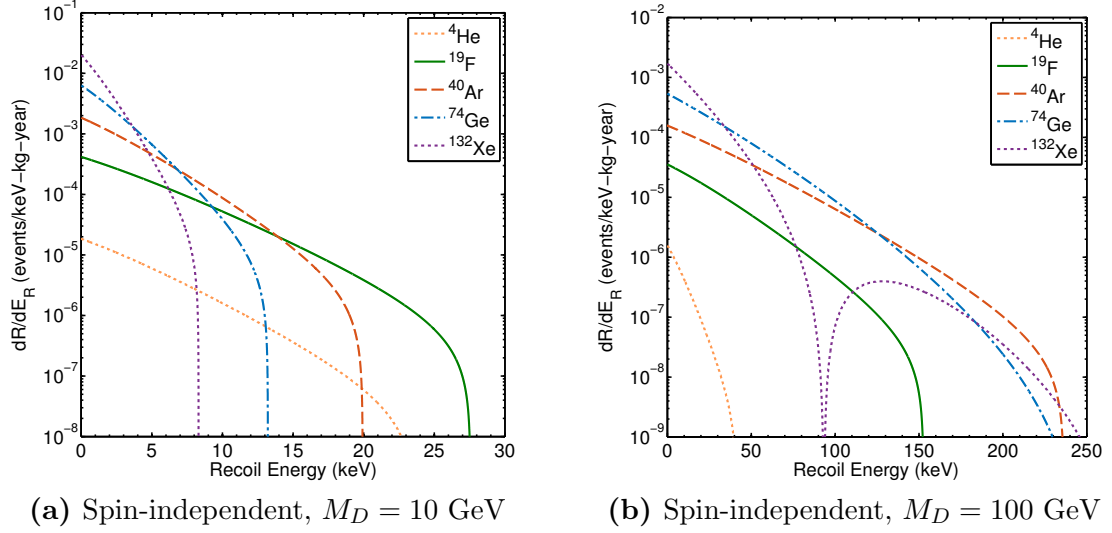
Figure 2.3: *The spin-independent differential rate for $M_D = 10$ and $M_D = 100$ GeV for several different target masses. The cross-section is taken as $\sigma_{Wp}^{SI} = 10^{-46}$ cm^2.*

For a finite escape velocity, the differential rate is given by

$$
\frac{dR(v_E, v_{esc})}{dE_R} = \frac{R_0}{E_0 r} \frac{k_0}{k} \left\{ \frac{\pi^{1/4}}{4} \frac{v_0}{v_E} \left[\mathrm{erf}\left(\frac{v_{min} + v_E}{v_0} \right) - \mathrm{erf}\left(\frac{v_{min} - v_E}{v_0} \right) \right] \right. \\
\left. - \exp\left(-v_{esc}^2 / v_0^2 \right) \right\}
\tag{2.2.41}
$$

The effects of the nuclear form factor and detection efficiency can be accounted for by taking the product of these functions with the differential event rate in Eq. 2.2.41. In Figures 2.1 and 2.2, we show the total rates for two WIMP masses and different target atomic number by integrating the differential rate with the form factor included. The rates are shown for different energy thresholds to illustrate its dependence on the effects of nucleon enhancement and kinematic mass matching. The energy dependence of the rate is easily seen in the differential spectrum, shown in Figures 2.3 and 2.4 for the spin-dependent and spin-independent cases, respectively.

(a) Spin-dependent, $M_D = 10$ GeV   **(b)** Spin-dependent, $M_D = 100$ GeV
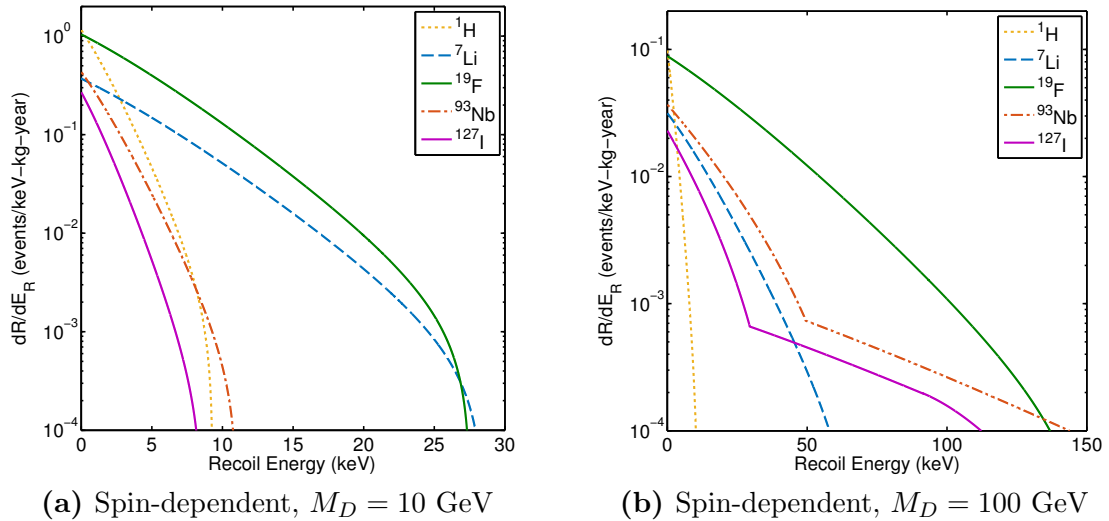
Figure 2.4: *The spin-dependent differential rate for $M_D = 10$ and $M_D = 100$ GeV for several different target masses. The cross-section is taken as $\sigma_{Wp}^{SD} = 10^{-40}$ cm^2, which is approximately the world's current leading limit at 100 GeV in the spin-dependent parameter space [77, 78].*

2.3   WIMP Galactic signatures

Direct detection is limited by several factors, one being the extremely low WIMP-nucleon interaction cross-sections predicted by extensions of the Standard Model [79], leading to a requirement of large detector masses. Another is the feature-less, exponentially-falling recoil energy spectrum expected from WIMP interactions, which encourages low detection thresholds. These issues are compounded by the presence of large backgrounds whose signals could mimic those expected from WIMPs. Although powerful techniques have been developed to discriminate and shield against a majority of these backgrounds, the misidentification of backgrounds for signal continues to plague the field [80, 81, 82, 83]. For these reasons the definitive proof of discovery in dark matter searches rests on the detection of specific signatures of the WIMP-nucleus interaction arising from the Galactic origin of the WIMPs.
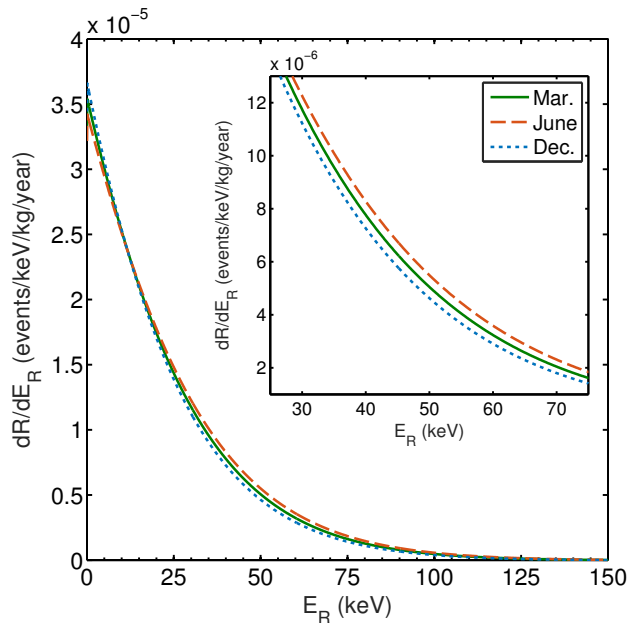
Figure 2.5: *The differential rate for a 100 GeV WIMP scattering off ˆ19F at three different times of the year (March, June, and December). The cross-section is taken to be $\sigma_{WP}^{SI} = 10^{-46}$ cm^2 which is the location of the world's current leading limit at this WIMP mass. The annual modulation effect is extremely small and would require a very high number of events to observe.*

2.3.1 Annual modulation

One such textbook signature is the annual modulation in the interaction rate caused by the seasonal variation in the relative velocity of the Earth-bound detector with the dark matter halo [84, 85]. Figure 2.5 shows the modulation in the differential rate at three different times of the year and for three different energy thresholds. The effect is relatively small at low threshold (a few percent), however, and many known backgrounds also modulate seasonally [87, 88, 89, 90, 91]. Although several experiments have observed an excess above expected backgrounds [92, 93, 94, 95, 96], the results are inconsistent with null results obtained by others [97, 98, 76].

This modulation in the interaction is due to the seasonal variation in the target velocity relative to the dark matter halo, $\vec{v_E}$. In general, this velocity is the vector
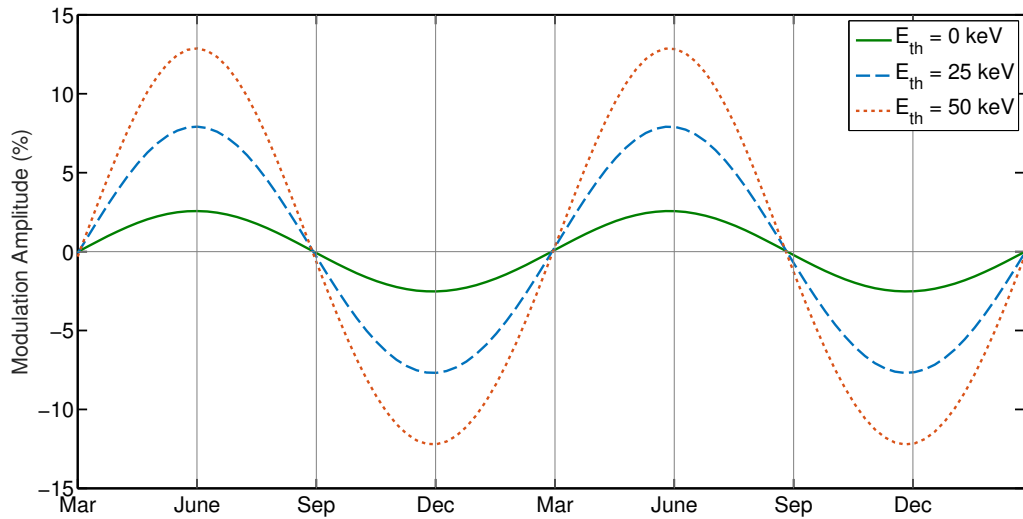
Figure 2.6: *Event rate modulation amplitudes as a function of the time of the year for three different energy thresholds. The modulation increases with energy threshold and has a maximum(minimum) in June(December).*

sum of the galactic rotation, the Sun's proper motion relative to the nearby stars, and the Earth's rotation around the Sun (the Earth's rotation around its own axis is negligible). Of these three components, only the Earth's velocity relative to the halo varies seasonally. Thus, the annual modulation signature is due to the orbital motion of the Earth, which has mean speed of $\langle u_{E,\text{rot}} \rangle = 29.79$ km s^{-1}. The effect is actually much smaller than value indicated by this mean speed because velocities must be added vectorially and the Earth's orbital plane is steeply inclined relative to the Galactic plane, so only a small component of the velocity plays a role.

The galactocentric velocity of the Earth-bound target can approximated by

$$v_E \simeq 244 + 15 \sin(2\pi\tau) \text{ km s}^{-1}, \tag{2.3.1}$$

where τ is the time elapsed from March 2nd, in years [66]. Note that the factor in front of the sine function is approximately $\langle u_{E,\text{rot}} \rangle \times \sin(\eta_{\text{eclip}} = 60°) \simeq 15$ km s^{-1}, where η_{eclip} is the inclination of ecliptic relative to the galactic plane. Expression 2.3.1 can be incorporated into the expression for the differential rate and numerically inte-

grated to determine the annual variation in the rate. In Figure 2.6, the modulation amplitude with season is shown for three different energy thresholds (0, 25, and 50 keV). Although the modulation amplitude increases with energy threshold, the event rate decreases so that a larger exposure would be needed to acquire enough events to detect the signature. In addition, there are known backgrounds that modulate seasonally with the same phase. A possible approach for alleviating this problem is to have detectors in both the Northern and Southern hemispheres and compare the phases of the detected signals. This approach, however, does not address the need for the extremely large exposures needed to detect the modulation at cross-sections beyond the world's current leading limits. A further complication is that at those large exposures, there is a contribution from coherent neutrino scattering to the detected rate. This contribution also modulates seasonally.

2.3.2 Directionality

As shown above, the annual modulation signature is relatively small and would require a tremendous number of events to identify. Moreover, it is also prone to backgrounds that the modulate seasonally with the same phase as the signature expected from dark matter. There is, however, a more robust and definitive Galactic signature–the sidereal modulation in the direction of the WIMP flux [85]. Due to the solar system's motion around the Galaxy, the flux appears to come from the direction of the constellation Cygnus, but as the Earth rotates through a sidereal day, the position of Cygnus, and hence, the direction of the incoming flux changes in the detector's frame of reference. This signature is detected as a modulation in the mean nuclear recoil track direction, which is peaked in the direction opposite to Cygnus.[1] Figure 2.7 shows the flux of 100 GeV WIMPs and the induced recoil directions for fluorine in Galactic coordinates. The directional signature provides a more definitive separation of a dark matter signal from backgrounds, and it is also much larger than

---

[1]At low recoil energies, the peak is in a ring about the direction opposite Cygnus [86].
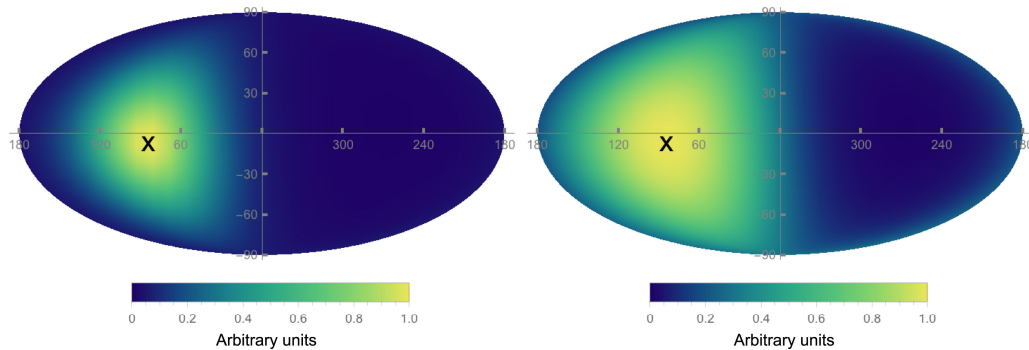
Figure 2.7: *(Left) The flux of 100 GeV WIMPs capable of producing 25 keV fluorine recoils in Galactic coordinates represented in a Mollweide equal-area projection skymap. (Right) The distribution of recoil directions for 25 keV fluorine recoils induced by 100 GeV WIMPs in Galactic coordinates. The direction of the laboratory is shown by the black cross. Reproduced with permission from Ref. [118].*

the annual modulation effect due to the strong angular dependence of the nuclear recoil direction [85]. There are currently several underground experiments that have varying degrees of sensitivity to this directional signature, including DRIFT [99, 100], NEWAGE [101], MIMAC [102], and DMTPC [103]. In addition, there are a number of efforts performing R&D on directionality [104, 119, 120, 121, 122, 123]. For a thorough review of directional dark matter detection see Refs. [124] and [118].

To calculate the directional signal, we first consider the double differential event rate per unit detector mass

$$\frac{dR}{dE_R d\Omega} = 2M_T \frac{1}{M_T} \int \frac{d\sigma}{dq^2 d\Omega} n_0 v f(\vec{v}) d^3 v, \qquad (2.3.2)$$

which follows from the product of the double differential cross-section, $d\sigma/dq^2 d\Omega$, with the WIMP flux $n_0 v f(\vec{v})$ [67]. Here, $dq^2 = 2M_T dE_R$ and $d\Omega = 2\pi d(\cos\theta)$, where θ is the angle between the recoil direction and the initial WIMP direction. The double differential cross-section can be expressed as

$$\frac{d\sigma}{dq^2 d\Omega} = \frac{d\sigma}{dq^2} \frac{1}{2\pi} \delta\left(\cos\theta - \frac{q}{2\mu v}\right) = \frac{\sigma_0 |F(q)|^2}{8\pi \mu^2 v} \delta\left(v\cos\theta - \frac{q}{2\mu}\right), \qquad (2.3.3)$$

where the Dirac δ-function imposes momentum conservation in Eq. 2.3.3. Inserting

the expression in Eq. 2.3.3 into the integrand of Eq. 2.3.2 yields

$$\frac{dR}{dE_R d\Omega} = \frac{n_0 \sigma_0 \, |F(qr_n)|^2}{4\pi\mu_T^2} \hat{f}(v_q, \hat{\mathbf{q}}) \tag{2.3.4}$$

where

$$\hat{f}(s, \hat{\mathbf{s}}) = \int \delta(\vec{v} \cdot \hat{\mathbf{s}} - s) f(\vec{v}) d^3 v \tag{2.3.5}$$

is the 3-dimensional Radon transform of the velocity distribution function $f(\vec{v})$ [105]. The geometrical interpretation of the transform is that it is the integral of the velocity distribution, $f(\vec{v})$, on a plane orthogonal to some reference direction $\hat{\mathbf{s}}$ at a distance s from the origin.

The advantage of expressing the recoil momentum distribution in terms of the Radon transform is the way it transforms under a change of reference frame. Consider that the WIMP velocity in the laboratory frame, $\vec{v}_{\mathrm{lab}}$, is related to its velocity in the Galactic rest frame, $\vec{v}_0$, and the velocity of the laboratory, $\vec{v}_E$, with respect to the Galactic rest frame is given by

$$\vec{v}_{\mathrm{lab}} = \vec{v}_0 - \vec{v}_E. \tag{2.3.6}$$

The unique feature of the Radon transform is that its form in the Galactic and laboratory frames are simply related by

$$\hat{f}_{\mathrm{lab}}(s, \hat{\mathbf{s}}) = \hat{f}_{\mathrm{gal}}(s + \vec{v}_E \cdot \hat{\mathbf{s}}, \hat{\mathbf{s}}). \tag{2.3.7}$$

Using this property of the Radon transform, the differential recoil momentum distribution in the laboratory frame is given by

$$\frac{dR}{dE_R d\Omega} = \frac{n_0 \sigma_0 \, |F(qr_n)|^2}{4\pi\mu_T^2} \hat{f}_{\mathrm{gal}}(v + \vec{v}_E \cdot \hat{\mathbf{r}}, \hat{\mathbf{r}}) \tag{2.3.8}$$

where $\hat{\mathbf{r}}$ is the nuclear recoil direction in the laboratory frame. The Radon transform of the Maxwell and truncated Maxwell distributions are given by
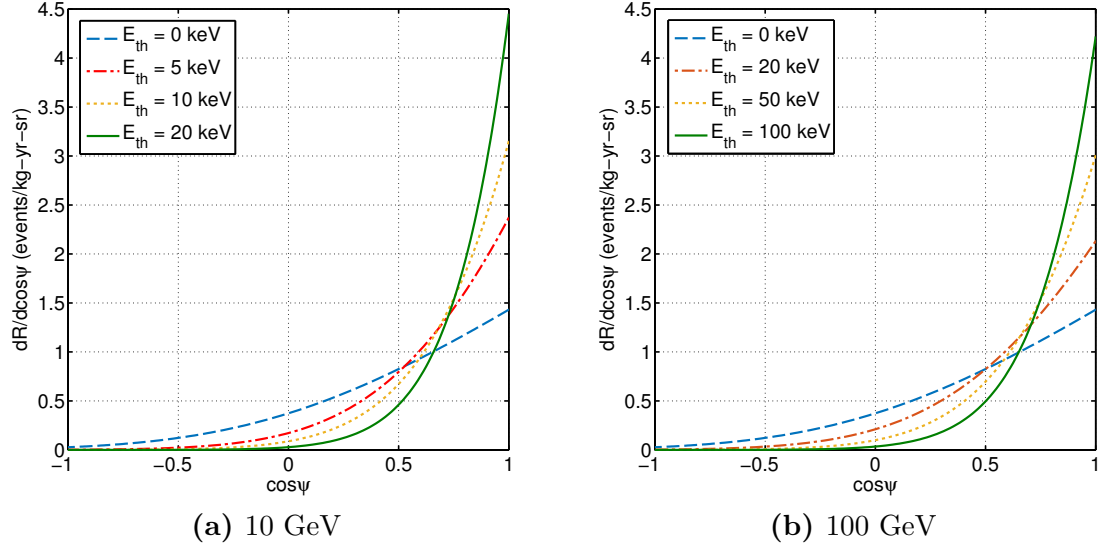
Figure 2.8: *Normalized angular spectra of ^{19}F recoils as measured in the laboratory frame for WIMP masses of 10 and 100 GeV. The angle ψ is measured relative to the axis defined by the anti-direction of Solar motion. At zero energy threshold, the angular spectrum is the same regardless of the WIMP mass. This is due to the assumption of isotropic scattering in the center-of-mass frame. Note also that the spectra become more forward peaked at higher energies because these recoils are more likely caused by WIMPs traveling in the opposite direction of Solar motion and whose speeds are boosted in the laboratory frame.*

- **Maxwell distribution**: $v_{\text{esc}} = \infty$

$$\hat{f}_{\text{lab}}(v, \hat{\mathbf{r}}) = \frac{1}{(\pi v_0^2)^{1/2}} \exp\left[-\frac{[v + \vec{v}_E \cdot \hat{\mathbf{r}}]^2}{v_0^2} \right]. \tag{2.3.9}$$

- **Truncated Maxwell distribution:** $|\vec{v} + \vec{v_E}| = v_{\text{esc}}$

$$\hat{f}_{\text{lab}}(v, \hat{\mathbf{r}}) = \frac{1}{N_{\text{esc}}(\pi v_0^2)^{1/2}} \left\{ \exp\left[-\frac{(v + \vec{v}_E \cdot \hat{\mathbf{r}})^2}{v_0^2} \right] - \exp\left[-\frac{v_{\text{esc}}^2}{v_0^2} \right] \right\} \tag{2.3.10}$$

with

$$N_{\text{esc}} = \text{erf}\left(\frac{v_{\text{esc}}}{v_0} \right) - \frac{2}{\sqrt{\pi}} \frac{v_{\text{esc}}}{v_0} \exp\left[-\frac{v_{\text{esc}}^2}{v_0^2} \right] \tag{2.3.11}$$

[67]. Often $\vec{v}_E$ is taken to be $\vec{v}_\odot$, the velocity of the Sun relative to the Galactic rest frame given that the orbital motion of the Earth is a very small contribution. Thus $\vec{v}_E \cdot \hat{\mathbf{r}} = \vec{v}_\odot \cdot \hat{\mathbf{r}} = -v_\odot \cos\psi$, where the last equality follows by taking the reference direction to be aligned with the average direction of the WIMP wind (anti-parallel to the direction of the Solar motion). In Figure 2.8, the normalized angular spectra for two WIMP masses are shown. As could be anticipated, the anisotropy in the recoil direction becomes more pronounced at higher energies. But even at zero threshold, the anisotropy is very apparent.

2.4 Limits from direct detection experiments

Direct detection experiments employ a wide variety of technologies and target materials. Below, we show the current status of dark matter searches. In Figure 2.9, the limits set by several experiments are shown for the spin-dependent parameter space. All combinations of WIMP masses and cross-sections above a contour are ruled out by the that particular experiment. In this space, the world's leading limit is set by the PICO-2L and PICO-60 experiments, which utilize the bubble chamber technology [77, 78]. The leading directional experiment is DRIFT [111], which utilizes the low-pressure time projection chamber technology (TPC). To bridge the vast gap (nearly a factor of 2000) between the directional experiments and the leading experiments will require a tremendous effort in improving the sensitivity of low-pressure TPCs, or possibly the development of new directional detector technologies. The challenges and path toward achieving this goal will be discussed in Chapter 3.

In the spin-independent space (Figure 2.10), the situation is even more daunting for directional experiments. The world's most sensitive experiment [76] which utilizes a liquid xenon target is many orders of more sensitive than the leading directional experiment. Given the A^2 enhancement of heavier targets and the density advantage of liquid and solid-state experiments in this parameter space, it is difficult to see
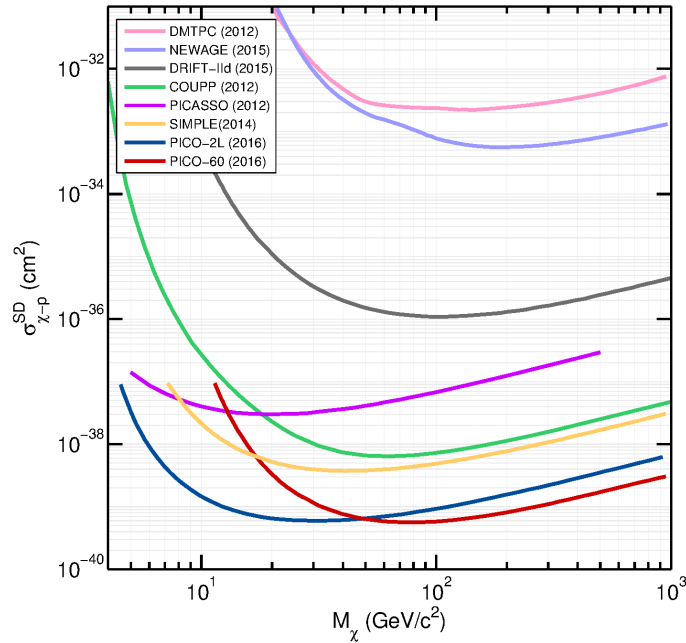
Figure 2.9: *The 90% C.L. limit set by direct detection experiments in the spin-dependent parameter space. The current world's leading limits are set by the PICO-2L (navy blue) [77] and PICO-60 experiment (red) [78], along with limits from COUPP (green) [106], PICASSO (purple) [107], and SIMPLE (yellow) [108]. In directional searches, limits from DMTPC (pink) [109] and NEWAGE (light blue) [110] are shown along the leading limit is set by the DRIFT-IId experiment (gray) [111].*

a path where directional experiments, which utilizes lighter target masses and low-density detection media to improve directional sensitivity, can bridge the sensitivity gap. However, in the low WIMP mass range (< 10 GeV), there still exists room for directional experiments utilizing low-pressure technology to make an impact. To do so would require achieving much better discrimination and directional thresholds than what has currently been shown experimentally. Lastly, although somewhat speculative at this point, directional experiments could play a critical role in direct dark matter searches beyond the neutrino floor [115, 116, 117, 118]. But at present, it remains unclear how present directional experiments can be scaled-up for this role.
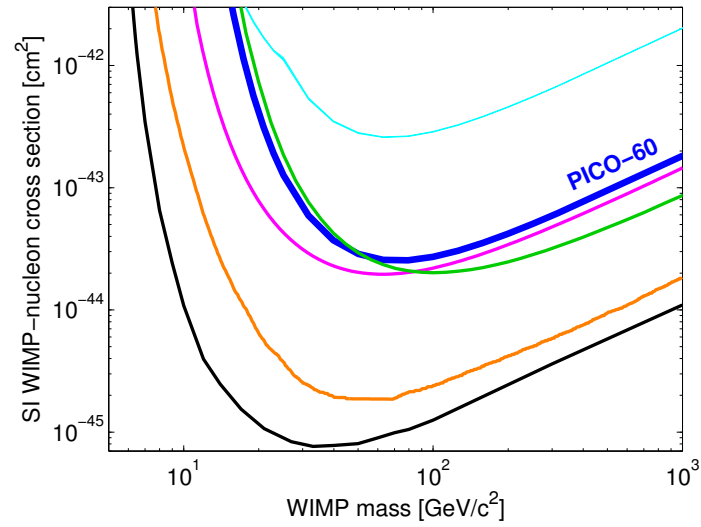
Figure 2.10: *The 90% C.L. limit set by several direct detection experiments in the spin-independent parameter space. The current world's leading limit is set by the LUX experiment (black) [112], along with limits from COUPP (light blue) [106], PICO-60 (blue) [78], XENON100 (orange) [97], DarkSide-50 (green) [113], and CDMS-II (magenta) [114]. Reproduced with permission from Ref. [78].*

Chapter 3

Overcoming the Challenges for Directional Detection

3.1 Challenges for directional detectors

3.1.1 Range of low-energy nuclear recoil

The main challenge for directional detection is that the low energy, tens of keV (henceforth, keVr), WIMP-induced nuclear recoil tracks are extremely short in liquids and solids (10's - 100's nm) (Figure 3.1 shows the range as a function of recoil energy for gas only). Thus, although R&D is underway to develop technologies for solid [119, 120, 123] and high pressure gas targets, [121, 122], most experiments use low-pressure gas targets where directionality has been demonstrated [125, 103]. In this low-energy regime, the recoiling nucleus will produce only a few hundred to a few thousand ionization pairs in the detection medium, with track lengths on the order of a millimeter even at pressures below 100 Torr (0.13 atm). Consequently, a natural choice for technology, which is currently employed by all gas-based directional experiments, has been the Time Projection Chamber (TPC) invented by D. Nygren [126]. This allows for full 3-dimensional (3D) reconstruction of the recoil track,

together with the flexibility to choose gas targets and operating pressures over a broad range. With cubic-meter-scale TPCs, the DRIFT experiment has pioneered the use of this technology for directional searches. With detectors that have a demonstrated directionality signature down to recoil energies of ~40 keVr [125, 127], DRIFT has set competitive limits on spin-dependent interactions for dark matter [111].
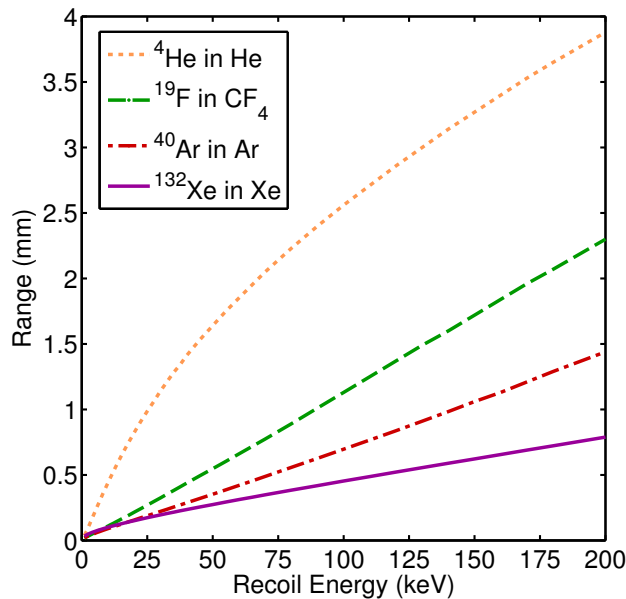
Figure 3.1: *SRIM simulations of the projected track range as a function of energy for several different ions recoiling in their parent gas [128]. The gas density is 4.87×10^{-4} g cm^{-3}, which for CF$_4$ is equivalent to 100 Torr at NTP (normal temperature and pressure: 20°C, 760 Torr).*

Nevertheless, many challenges remain, not least of which is the scalability of the current generation of directional experiments to reach the sensitivity required to test future claims of detection by non-directional experiments. To accomplish this, an emphasis on maximizing sensitivity will need balancing with the scalability, cost, and robustness of the technology. In the next chapter, we discuss an experiment aimed at measuring the intrinsic properties of low-energy electron and nuclear recoil tracks and how they place fundamental limitations on the sensitivity of directional dark matter searches. The nature of these tracks determine energy thresholds for

both discrimination and directionality, with the latter defined as the energy at which the directional signature becomes detectable. As we show in the chapters to follow, these two energy thresholds are not the same, with the onset of directionality having a higher energy threshold than discrimination. It is important to keep this in mind because, all else being equal, the true determinant of sensitivity for directional dark matter searches is the directionality threshold. For the gas-based TPC detectors of interest here, the physical processes that affect the overall sensitivity - for both discrimination and directionality - involve energy loss, straggling, diffusion, signal generation (gas gain), and readout resolution. These are briefly discussed here.

3.1.2   Track topology of low-energy nuclear recoils

The direction of a recoiling atom in a gas-based TPC is reconstructed from the ionization track produced along its path. For both electrons and nuclear recoils, this track is never straight due to multiple scattering (or straggling) with the constituents of the gas. This results in a loss of resolution which varies with gas pressure, the energies and the masses of the recoiling particle and gas atoms. For example, a 50 keVr fluorine recoil in 100 Torr CF_4 has an average range of 548 µm (Figure 3.1) but suffers significant range straggling, defined as the standard deviation of the particle's final position relative to its initial direction, of about 183 µm and 139 µm in the longitudinal and lateral directions, respectively [128]. In Figure 3.2, the straggling exhibited by 50 keVr fluorine recoils in CF_4 is shown. The half angle of the cone formed by these straggled recoils can exceed 45° and becomes even worse at lower recoil energies and for heavier targets. This effectively places a bound on the best attainable angular resolution of a detector even before diffusion and readout resolution are taken into account.

(a) XY projection

(b) XZ projection
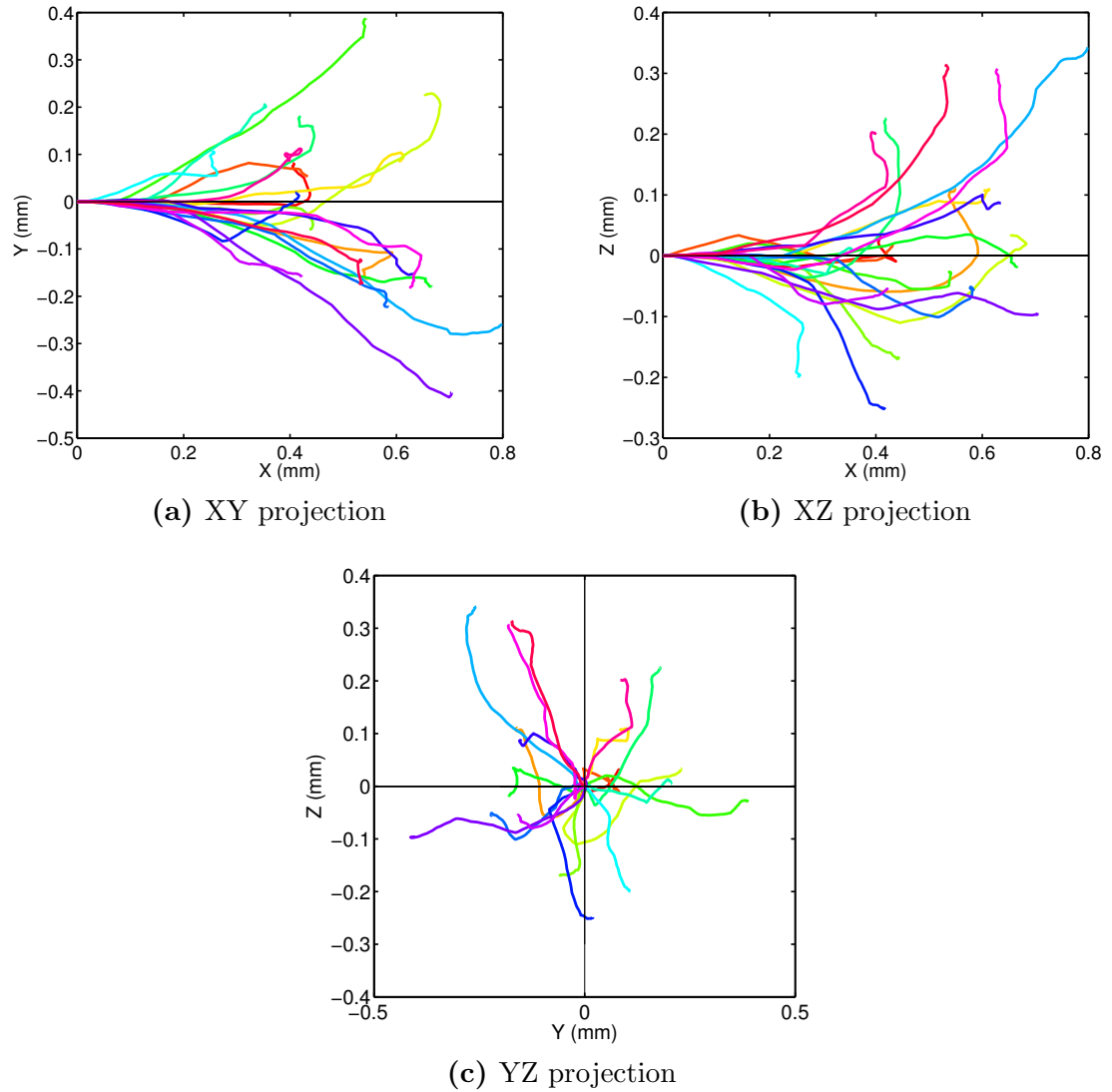
(c) YZ projection

Figure 3.2: *SRIM simulations of 20 fluorine recoils in 100 Torr CF$_4$ with energies of 50 keVr. All recoils are initially traveling in the X direction but begin to deviate from this direction due to straggling. (a)-(c) show the projections of the the recoil for the three planes. The straggling occurs both in the longitudinal and lateral directions and is a significant fraction of the mean track length. The ratio of straggle range to the mean recoil range depends on the energy of the recoil as well as its type and the energy loss medium.*

3.1.3 Diffusion

Following the generation of the ionization track, the negative charge drifts in a uniform electric field down to the TPC readout plane, where it undergoes amplification before being read out by the data acquisition. During the drift, the ionization that defines the track undergoes additional loss of resolution due to diffusion, which depends on the drift distance, the strength of the drift field, and the nature of the drifting charge carrier and gas. With electron drift, a select few gases such as carbon tetrafluoride (CF_4) have relatively low diffusion, which, for a drift distance of 20 cm, an electric field of 400 V/cm, and a pressure of 100 Torr, is approximately $\sigma_T = 790$ µm (recommended by Ref. [129] based on a fit to the measurements of Refs. [130, 131, 132]) and $\sigma_L = 580$ µm (values in Ref. [133] derived from measurements in Ref. [134]) for the transverse and longitudinal dimensions, respectively.

Even lower diffusion is possible for negative ion drifting gases such as carbon disulfide (CS_2), whose molecules have a high electron affinity. These molecules capture the primary electrons to form negative ions that drift with a very low velocity and low diffusion due to thermal coupling with the bulk gas. The use of an electronegative gas to suppress diffusion without a magnetic field was first proposed by Martoff et al. [135], and measurements of mobility and diffusion in CS_2 mixtures [135, 136, 137, 138, 139, 140] indeed indicate thermal behavior for drift fields up to where measurements exist. Using the diffusion temperatures reported in Ref. [140] for CS_2, the transverse and longitudinal diffusion widths are 320 µm and 330 µm, respectively, for a drift length of 20 cm at a field of 1000 V/cm. In Figure 3.3, the normalized longitudinal and transverse diffusion for CF_4 and CS_2 are shown. Note that for CF_4, the data points are for a pressure of 100 Torr, and in general, the diffusion for an electron drift gas is pressure dependent. Conversely, the diffusion for an electronegative gas should be independent of pressure in the low reduced field (E/p) regime. This is discussed in more detail in Chapter 7. Besides the clear advantage of an electronegative gas from a resolution standpoint, detector operation in

the presence of high voltages and fields is quite stable in low pressure CS_2 (electrical discharges are suppressed). However, one of the downsides of CS_2 is its lack of spin-sensitive targets (if a spin-dependent search is the goal), which necessitates mixing it with a gas such as CF_4 that contains ^{19}F, a target with high nuclear spin content.
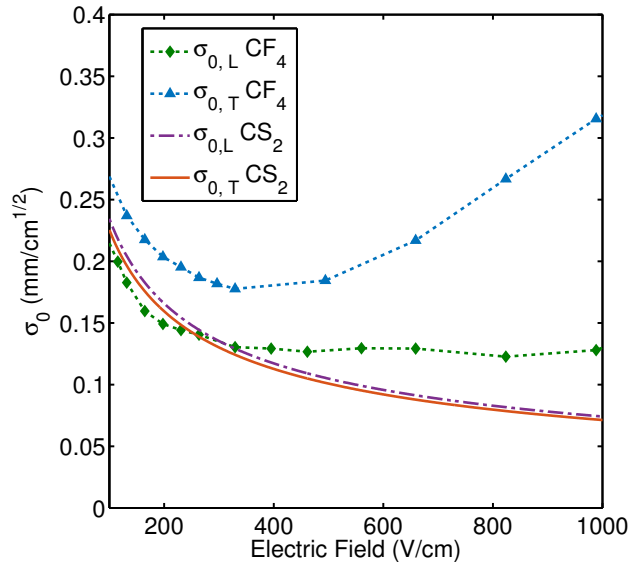
Figure 3.3: *The normalized transverse, $\sigma_{0,T}$, and longitudinal, $\sigma_{0,L}$, diffusion for CF_4 and CS_2. The data points for CF_4 are for a pressure of 100 Torr and are derived from Ref. [129] which came from a fit to the measurements of Refs. [130, 131, 132] while the curves for CS_2 are obtained from the diffusion temperatures reported in Ref. [140] with $T_L = 312$ K and $T_T = 296$ K.*

3.1.4   Gas gain

Finally, after the charge arrives at the readout plane it must undergo avalanche amplification before being read out. Here the large gas gain, needed for high signal-to-noise, is not easily achieved due to electrical instability at the low gas pressures required for directionality. For example, in Multi-Wire Proportional Chambers (MWPCs) used in the DRIFT detectors, typical gas gains are $\lesssim 1000$ [141]. But much higher gas gains have been achieved in other avalanche devices at low pressures [142, 143].

Thus, the dependence of the gas gain on the avalanche device is an important factor to consider when designing a high signal-to-noise detector, particularly in the low pressure regime.

3.1.5 Axial vs. vector sensitivity

Most physical processes, like those described above, degrade the directional sensitivity. There is one, however, that has the potential to greatly enhance sensitivity if an intrinsic asymmetry in the energy loss of the recoil exists and is detectable. Such an asymmetry would provide a means for assigning a head-tail (HT) sense to the track. The implication for directional sensitivity, based on simulations, is that with accurate head-tail, or vector, tracking only $\sim$10 dark matter events are needed for discovery, versus of order $\sim(10^2 - 10^3)$ for experiments with no-HT, or axial, tracking [146, 145, 147, 148, 149]. Table 3.1 shows the number of events needed to reject isotropy for 90% and 95% confidence levels with different readout configurations. Possessing vector track reconstruction ability provides about one order of magnitude improvement in sensitivity over the comparable axial reconstruction.

Studies of the ionization energy loss (dE/dx) of low energy recoils indeed predict a decrease with decreasing energy along the direction of the traveling recoil [144]. Although a HT asymmetry of this nature has been measured down to about 40 keVr [125], it appears to be small and after straggling and diffusion its detection is diminished to the point where the statistical advantage over the axial case is reduced. Future experimental measurements are needed to determine the lowest energy at which this effect exists as well as its dependence on the recoiling atom and detection medium.

Table 3.1: *The number of events above a 20 keVr threshold required to reject isotropy for 90%, N_{90}, and 95%, N_{95} confidence levels [148]. The results assume zero-backgrounds and optimal alignment of the readout for the case of 2D. In general, vector(head-tail) reconstruction reduces the number of events needed to reject isotropy by one order of magnitude over a similar axial readout.*

Readout configuration	N_{90}	N_{95}
3D vector readout	7	11
3D axial readout	81	130
2D vector readout	12	18
2D axial readout	190	270

3.2 Steps for extending directional sensitivity

The nature of low pressure TPCs places many limitations on the sensitivity of directional detectors employing this technology. This section gives a brief outline of the steps that can be taken to maximize the performance of a low pressure detector while retaining discrimination and directional sensitivity.

1. **Achieve the lowest discrimination threshold and directional sensitivity:** It is clear that for a given volume of target material, the way to increase the sensitivity is to have the lowest possible detection threshold, or in other words, detection efficiency. For example, in the case of a 100 GeV WIMP scattering off fluorine, a detector with an energy threshold of 10 keVr would be sensitive to ∼67% of the nuclear recoil energy spectrum whereas a detector with a threshold of 100 keVr would be sensitive to less than 1% of the energy spectrum. Given that the WIMP-induced recoil energy spectrum is a steeply falling exponential, it is important to push the threshold down as low as possible. This, however, is not a simple task as the of presence of backgrounds grows at lower energies and discrimination becomes more difficult.

   For a directional detector, there is the added complication that, in addition to the discrimination threshold, there is also a directional threshold. The former is determined by the relative difference in the energy loss processes of electron

versus nuclear recoils, but the latter is determined by the energy loss process of the nuclear recoils alone. Different recoiling targets will behave differently, but even the same target will have distinctly different behavior with gas densities and energies. Furthermore, the directional threshold does not tell entire story. That is to say that what truly matters is the directional *sensitivity*, which is often characterized by the number of events or exposure needed to detect a directional signature at some confidence level (see Table 3.1). As such, it is entirely conceivable that a detector with a lower directional threshold can have a worse directional sensitivity than one with a higher threshold. Such a situation may arise when comparing the directional performance of a 1D detector vs. a 3D detector or between a detector with axial reconstruction vs. one with vector reconstruction. Thus, determining what is possible in terms of the discrimination and directional sensitivity as well as what is needed to achieve best performance is an important step in the development of directional detectors.

2. **Maximize the target in a given volume:** For a given volume, the interaction rate increases with increasing target density. In practice, this would seem to be quite straightforward to achieve, but for low-pressure directional detectors this is not the case. First, as the directional signature hinges on being able to measure the track of a low-energy nuclear, increasing the pressure/density shortens the track range and makes it all the more difficult to determine the direction. However, lowering the target density in order the lengthen the track would enhance the directional signature of a given event but at the expense of a reduction in target mass. Thus, there is a balance between maximizing the event rate and improving the ability to reconstruct the direction of a low-energy recoil.

   For low-pressure TPCs, there is also the added complication of electrical stability at low pressures. This means that for directional detectors, choosing the

target density/pressure is not necessarily a simple task. In addition, not all of the material inside the detection volume is the desired target. Specifically, for spin-dependent dark matter searches, only the spin-dependent targets are important. The spin-independent targets actually have a deleterious effect on the sensitivity of the detector. They do not contribute to the detection rate but at the same time contribute to the overall density of the detector which affects track lengths and directional sensitivity as well as discrimination power.

3. **Increase detector volume by scaling in the Z(drift) dimension:** Once the sensitivity of a given volume has been maximized to the greatest extent possible by lowering detection threshold, maximizing directional sensitivity, and increasing target density, the next step is detector scale-up. The dimension that can be most easily scaled-up in a cost-effective manner is the drift, or Z, dimension because additional readout electronics are not needed when scaling this dimension. However, there is a great impediment in pursuing this path – diffusion. The diffusion experienced by a charge cloud scales as $\sqrt{L}$, where L is the drift length. It is apparent then that the Z-extent of the detector cannot be increased to any arbitrary length. When the maximum diffusion at a given detector length exceeds the track lengths of interest for directional dark matter searches, directional information in those tracks has been lost and increasing the detector length beyond that point no longer yields any improvements in the directional detection rate.

4. **Increase detector volume by scaling in the X-Y(lateral) dimension:** When detector scaling in the Z-dimension has reached its maximum point, the next step is the scale in the lateral, or X-Y, dimension. These dimensions define the plane containing the charge amplification and the track imaging devices and the associated readout electronics. For this reason, scaling in this dimension is the least cost-effective path and is the last resort. Regardless

of the track imaging technology employed, whether it be pixels, strips, wires, or optical devices such as CCDs, the number of readout channels and their cost and complexity increase with the area being imaged. Consequently, an imaging technology that possesses high-resolution but at the same time has low-cost and low-complexity is greatly desired.

5. **Detecting directionality using a new method:** The discussion thus far has focused on how to increase the sensitivity of low-pressure TPCs for directional dark matter searches. The difficulties in achieving this are centered on the fact the both background discrimination and directional sensitivity depend on the ability to measure the track topology of low-energy recoils. This necessitates operating at low pressures to lengthen recoil tracks, limiting detector drift lengths to keep diffusion at bey, and employing high resolution readouts to image the short tracks. These requirements constrain the sensitivity of directional detectors while making their costs and complexity high. A method that can determine the direction of low-energy recoils without needing to image the tracks would break free of those constraints.

3.3   Outline of the experimental work to extend directional detector sensitivity

3.3.1   Chapter 4: CCD Detector Discrimination

In Chapter 4, we describe the detector performance of a small, high resolution, high signal-to-noise GEM-based TPC with a 2D CCD readout. Using data from alpha, X-ray, gamma-ray, and neutron sources, we show how the salient features seen in the electron and nuclear recoil tracks can be used for background discrimination in dark matter searches. Critical for this are the precision measurements of the fundamental properties of both electron and nuclear recoil tracks down to the lowest detectable

energies. Such measurements are necessary to provide a benchmark for background discrimination and directional sensitivity that could be used for future optimization studies for directional dark matter experiments.

3.3.2 Chapter 5: Directional Sensitivity of Prototype CCD Detector

In Chapter 5, we use the data from the detector described in Chapter 4 to characterize the directionality of nuclear recoil tracks. We show that the discrimination threshold, discussed in Chapter 4, is much lower than the directional threshold. Besides determining the threshold for directionality, we also use the data to determine the number of nuclear recoil events needed to identify a directional signature with the CCD detector for both a ^{252}Cf neutron induced recoil spectrum as well as a WIMP-induced recoil spectrum. For this, we determined the detector angular resolution and its head-tail, or vector, sensitivity as a function of energy.

Furthermore, because maximizing the directional sensitivity per unit volume of a low pressure TPC is critical to allowing the exploration of the currently relevant WIMP parameter space, we proceed to use the directional results obtained with the CCD detector to optimize a directional detector. This is done by maximizing the directional recoil rate as a function of operating pressure, target, and WIMP mass.

3.3.3 Chapter 6: Electron Recoil Imaging with the CCD Detector

The detection optimization results from Chapter 5 indicates that for low mass WIMP ($\sim 1-10$ GeV) detection, very low pressures will be needed to optimize the directional rate. The first step towards this goal is to achieve the best possible discrimination threshold. As will be discussed in Chapter 4, necessary for this is the ability to image electron recoil tracks with high signal-to-noise and high-resolution down to the lowest

energies. We will show in Chapter 6 that with the CCD readout technology, this is at least achievable over a pressure range of 35-100 Torr. Energy spectra and images of individual tracks of 5.9 keV ^{55}Fe recoils obtained with the CCD camera will be presented.

3.3.4   Chapter 7: SF$_6$–A New Negative Ion TPC Gas

As discussed in Section 3.1, an electronegative gas such as CS$_2$ provides many advantages over an electron drift gas. Much lower diffusion can be achieved in an electronegative gas as compared to an electron gas. This allows scaling of the detector in the drift dimension, often termed the Z dimension, without the added costs of increasing the readout area in the lateral, or X-Y, dimension. Given the low target mass of gas-based TPCs, scaling a detector in such a way as to preserve performance (i.e. resolution, electrical stability, detection efficiency) while keeping costs in check is an important objective to pursue.

CS$_2$ would appear to provide all of those desired traits. However, there are many issues with using CS$_2$ in a directional dark matter detector, among which are its lack of a spin-dependent target, toxicity, and detector maintenance and operation issues. We present a study of a new TPC gas that could possess the advantages of an electronegative gas but without the downsides of CS$_2$. This gas is SF$_6$, or sulfur hexafluoride. In Chapter 7, we present measurements made with SF$_6$ as the primary gas in a low pressure TPC. We show that SF$_6$ is an attractive gas for directional dark matter detection. In particular, the high fluorine content is desirable for spin-dependent sensitivity, negative ion drift ensures low diffusion over large drift distances and allows scaling in the Z-dimension without increasing readout costs, and the multiple species of charge carriers allow for full detector fiducialization.

3.3.5   Chapter 8: Novel High-Resolution Tracking Readout

In the discussion of the ways to improve the sensitivity of directional detectors in Section 3.2, we stated that scaling the detector in the X-Y dimension is the most costly and should be done only after all other avenues have been explored. It is possible, however, to reduce, and perhaps eliminate, some of the obstacles for X-Y scaling by utilizing a new track imaging technology. Chapter 8 will discuss the development of a novel track imaging readout at the University of New Mexico that requires a minimal number of readout channels, reconstructs tracks with high-resolution, and enables efficient detector scale-up.

3.3.6   Chapter 9: Beyond Low-pressure Directional Detectors

In the last Chapter, we present an idea on a possible method for determining the 1D direction of recoils in a TPC that does not require imaging the track. This is born out of the work on SF_6 but possibly could be applied in other gases as well. The idea is of the same flavor as the columnar recombination idea proposed by David Nygren for high pressure xenon detectors, but does have an important distinguishing feature of possibly being able to reconstruct the 1D *vector* direction rather than just an *axial* direction of a recoil.

Chapter 4

CCD Detector Discrimination

4.1 Introduction

Based on the discussion in Section 3.1, it is clear that there is a large parameter space available for optimizing directional experiments to have the highest sensitivity, but with economical, robust and scalable designs. In this chapter, we defer the optimization discussion and focus instead on measuring the intrinsic properties of low-energy electron and nuclear recoils to determine what is truly achievable in a real detector. For this goal, we made measurements with a small prototype TPC, which has the lowest diffusion that a realistic experiment could achieve, and chose a readout technology with an emphasis on high-resolution and high signal-to-noise. The detector is based on Micro-patterned Gas Detector (MPGD) technology. For a review of the development of MPGD technology, see Ref. [153]. Additionally, refer to Ref. [154] for the webpage of the RD51 Collaboration whose goal is the advancement of MPGD technologies.

(a) CCD detector   **(b)** Detection region
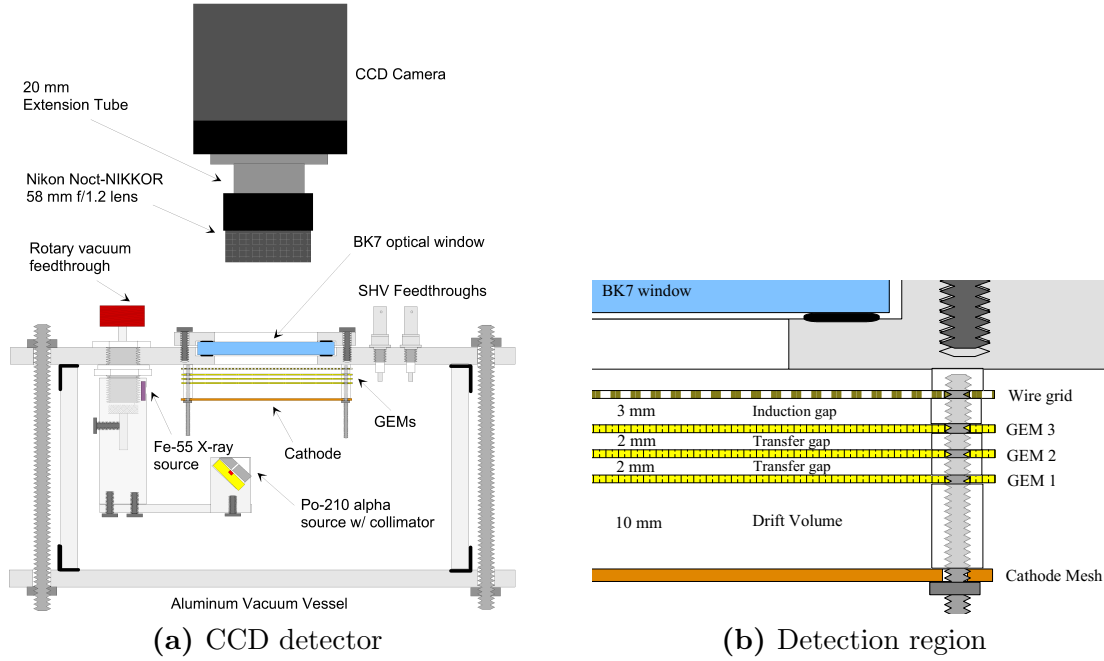
Figure 4.1: *(a) A schematic of the CCD detector showing the relative positions of detector components. The optical system, which consists of the CCD and lens, sits outside the vacuum vessel and images only the central 2.8 cm × 2.8 cm region of the topmost GEM surface. The internally mounted ^{55}Fe and ^{210}Po sources are used for calibrations. (b) A close up view of the detection volume and GEM stack showing the dimensions of the important regions.*

4.2 Detector setup

The detector consisted of three standard copper GEMs (Gaseous Electron Multipliers [155]; see Ref. [156] for a review) arranged in a cascade with 2 mm separation between them (Figure 6.1). The GEMs were manufactured at CERN from 7×7 cm^2 sheets of kapton (50 µm thick) clad on both sides by copper and mounted on G10 frames. The surface of each sheet was chemically etched with bi-conical holes of diameter of 50/70 µm (inner/outer) configured in a hexagonal pattern with 140 µm pitch. A cathode, placed 1 cm below the GEMs, was fabricated from a 7×7 cm^2 copper mesh made from 140 µm wires with ~320 µm pitch. A 1 mm pitch anode wire grid plane made from 20 µm thick gold plated tungsten wires was located 3 mm above the top

most GEM (GEM 3), forming the induction gap. The detector was housed inside an aluminum vacuum vessel and calibrated using ^{55}Fe (5.9 keV X-rays) and ^{210}Po (5.3 MeV alphas) sources, both mounted inside the vacuum vessel. A rotary feed-through was used to individually turn both calibration sources on or off, as needed. Before operating the detector the vacuum vessel was pumped down to < 0.1 Torr and back-filled with 100 Torr of pure (99.999%) CF_4 gas. A BK-7 glass window was positioned above the readout grid to allow scintillation light from the final amplification stage (GEM 3) to be viewed by the CCD. The BK-7 glass material was chosen due to its high transmittance of CF_4 scintillation, whose optical component is peaked around 620 nm [157, 158], and its lower cost relative to quartz.

A back-illuminated Finger Lakes Instrumentation (FLI) charge-coupled device (CCD) camera (MicroLine ML4710-1-MB) with a 1024×1024 pixel sensor array (CCD47-10-1-353) made by E2V was mounted on top of the vacuum vessel. The 13×13 µm^2 square pixels occupy the 18.8 mm diagonal sensor, which has a peak quantum efficiency of 96% at 560 nm. The camera could be read out at two speeds, 700 kHz and 2 MHz, with 16-bit digitization, and during data taking the sensor was cooled to the lowest stable operating temperature of $-38\,°C$ by a built-in Peltier cooler. At this temperature, the read-out noise was measured at $\sim$10 e$^-$ rms and the dark current was < 0.1 e$^-$/pix/sec. A fast 58 mm f/1.2 Nikon Noct-NIKKOR lens was mated to the CCD camera through a 20 mm extension tube for close-focusing imaging. The CCD-lens system imaged a 2.8×2.8 cm^2 region of the top most GEM surface. The known pitch of the holes on this surface were used to calibrate the length-scale of the field of view.

4.3 GEM gain

A 5.9 keV ^{55}Fe X-ray source was used to measure the effective gas gain, which includes the loss of electrons in the charge flow from the detection volume to the collection

and readout surface. With a W-value (the average energy per ionization) of 34.2 eV in CF_4 [159], the primary ionization from the 5.9 keV X-ray creates, on average, 172 electron-ion pairs per conversion event. To measure the gas gain we used the standard procedure of using a pulser and capacitor to determine the preamplifier pulse height to charge calibration. In our case, we used an ORTEC 448 research pulse generator and an ORTEC 142IH charge sensitive preamplifier, which comes with a built-in 1 pF capacitor for this purpose. With the calibration results from this procedure the ^{55}Fe energy spectrum obtained using a multi-channel analyzer (MCA) was used to determine the gas gain. All gain measurements were made by reading out the signals from the last GEM electrode (GEM3 in Figure 6.1) with the preamplifier.

We also attempted using the anode wire grid to read out the signal, as often found in the literature, but found that corona limited the maximum achievable gain. The presence of the anode grid was not superfluous, however, as we found that the sparking probability tended to increase without it. Reference [160] has a discussion on the operation of multiple GEMs without the use of an anode board or wire plane for readout.

To optimize the GEM voltages, the detector was left for about 1 hour with alpha irradiation at each setting to test for stability. If no sparks occurred during this time, then the detector was deem to be stable. The voltages are then changed and procedure was repeated until the setting corresponding to the highest stable gain was found. At a pressure of 100 Torr, with the biases of GEMs 1 and 2 = 290 V and GEM 3 = 460 V, we obtained an effective gain $> 3 \times 10^5$. These settings corresponded to a drift field of 400 V/cm, transfer field of 1.45 kV/cm, and induction field of 315 V/cm. The unbalanced powering scheme with different biases on the GEMs was used to circumvent the corona problem we experienced while operating in balanced power mode at low pressures (75 Torr and 100 Torr). The disadvantage of such a power scheme with a large fraction of the gain coming from the last GEM is an increase
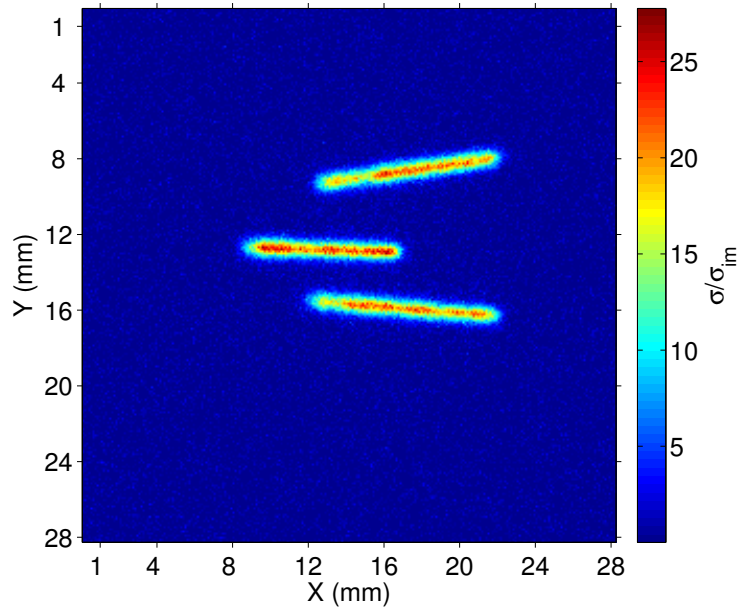
Figure 4.2: *Image of alpha track segments in 100 Torr CF_4 with an effective gas gain of 1×10^5 and 6×6 CCD binning. The image is contrast adjusted to show the signal to noise in units of σ_{im}, the rms of the image background. The track segments (∼1 cm) correspond to the parts of the tracks well before the Bragg peak and demonstrate the extremely high signal-to-noise level achieved with the brightest part of the tracks being $> 20\sigma_{im}$ above the noise.*

in the sparking probability. Indeed, sparking was observed with the ^{210}Po alpha source (5.3 MeV) turned on when operating at a gain of 2.5×10^4 at 75 Torr and 3×10^5 at 100 Torr. Although the sparks did not damage the GEMs or other detector components during the test runs (1 hour per voltage setting), they did saturate the CCD, producing an artifact known as residual images or ghost images [161].

Ghost images are often associated with front-illuminated CCDs, rather than back-illuminated CCDs, but were nevertheless observed in the CCD used in this work. They appeared in frames taken after the initial saturation event and did not fade until many hours afterwards; in general, the relaxation time depends on the temperature of the CCD. Even though they can be identified as spatially non-varying objects across successive frames, or can be dealt with by flooding the sensor with IR light,

a technique known as RBI flushing, their presence is indicative of instability with the potential of damaging the detector. Thus, we adjusted the GEM voltages to find the maximum gain attainable without sparking or corona at 100 Torr, to ensure stable long-term detector operation. Stability was found with GEM 1 = 279 V, GEM 2 = 334 V, and GEM 3 = 380 V, drift field of 400 V/cm, transfer fields of 1.40 kV/cm and 1.67 kV/cm between GEMs 1 and 2 and GEMs 2 and 3, respectively, and induction field of 260 V/cm between GEM 3 and the grid. With these settings an effective gain of $\sim 1 \times 10^5$ was achieved. The excellent signal to noise achieved at this gain is illustrated by the alpha tracks in Figure 4.2, which show a peak signal of $> 20\sigma_{\mathrm{im}}$ above the noise level. Besides its use for gain measurements, the charge signal from the preamplifier was not used in the subsequent analysis of the data. As the CCD camera was operated in non-trigger mode, it would be difficult to correlate the charge signal with a particular event in the CCD image. Additionally, events with energies above three times the ^{55}Fe energy would saturate the preamplifier. However, using both the charge and light signals should further aid discrimination.

4.4 Detector calibrations

4.4.1 CCD calibration

The standard approach to CCD calibration was adopted where each CCD image (or frame) was calibrated using a set of co-averaged flat-field and dark frames. The flat-field frames were used to correct for vignetting and pixel to pixel variation in sensitivity, and the dark frames corrected for the variable accumulation rate of dark current across pixels. The calibration was done by subtracting the co-averaged dark frame from each image frame and then dividing the resulting frame by the normalized, co-averaged flat-field. Bias frames, which correct for the electronic bias that is seen as structure in the data frames, were not used since this information is also present in the dark frames. The pedestal due to amplifier bias was removed using the overscan
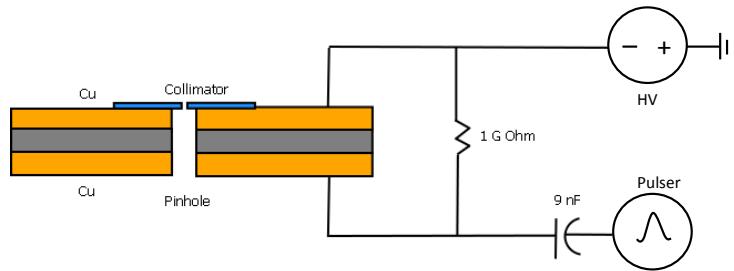
Figure 4.3: *A schematic of the pinhole cathode and high voltage pulser setup used to measure transverse diffusion. Both surfaces of the cathode are held at a fixed voltage with a high voltage power supply. The capacitor isolates the pulser from the high voltage but allows a spark to be initiated in the pinhole generating ionization in all directions. The 10 µm collimator reduces the transverse extent (perpendicular to electric field) of the ionization entering the drift volume (region on top of the collimator) to point-like dimensions.*

region present in each frame.

With the CCD being read-noise limited, pixels were binned 6 × 6 prior to digitization and read out at the slowest allowable speed of the CCD electronics, 700 kHz, to improve signal to noise. This binning factor combined with the imaging area translated to each binned pixel imaging a ∼165 × 165 µm² area of the GEM, which is well-matched to the 140 µm GEM pitch. The measured read noise was 10 e^- rms/pix, and at the −38°C operating temperature of the CCD, the dark current was ∼0.03 e^-/pix/sec for 1 × 1 binning. As the latter scales with pixel area, the 6 × 6 binning and 5 second exposures used in all of our data runs contributed a dark current of ∼6 e^- to the total system noise.

The calibration frames were averaged using an algorithm that rejects pixels hit by cosmic rays and radioactivity by comparing the value of the same pixel across each frame, and rejecting those above three sigma of the initial average of these pixels. The average value of the pixels was then recalculated excluding the rejected pixels and the same procedure repeated until convergence in the average was reached. This procedure was applied to all pixels to create master flat and dark calibration frames.

4.4.2 Transverse diffusion

The detector track reconstruction and angular resolution is intrinsically tied to the diffusive properties of electrons in the target gas. With our CCD readout, only the transverse, or lateral, diffusion could be measured as the longitudinal component required timing resolution from the GEM charge readout that is well beyond the capability of the ORTEC preamplifier used here. To measure the lateral diffusion, a point source was generated at a specially constructed cathode made from an insulating sheet sandwiched between two strips of copper tape. The cathode had a small hole punctured at its center with a 10 µm collimator placed over the hole on the side facing the drift volume. The electrodes of the cathode were connected to a power supply and a 12 kV high voltage pulse generator; Figure 4.3 shows a schematic of the cathode and electrical connections. The HV pulser was used to generate a spark inside the hole, which produced ionization that appeared as a point source 'track' in the drift volume after passing through the collimator.[1]

We imaged a collection of tracks and measured the spread in their light profiles. Each of the light profiles was fitted using a Gaussian curve, and an average $\sigma_{\text{tot}} = 345 \pm 5$ µm (stat) was obtained for the sample of tracks. The main contribution to the spread is expected from diffusion of the electron cloud as it travels the full distance from the cathode to the final GEM stage. This was confirmed using data from Refs. [129, 133] and results from the MAGBOLTZ program [162], which predict $\sigma_{\text{diff}} = 326$ µm for the diffusion in our detector. The MAGBOLTZ result indicates that contributions to σ_{diff} are divided about equally, when added in quadrature, between the drift gap and the two transfer gaps between the GEM stages. A secondary source to σ_{tot} is expected from the GEM pitch and the 3-GEM cascade. Attributing this wholly to the difference between σ_{tot} and σ_{diff} yields 65 ± 9 µm per GEM when

---

[1]As a check on this technique for generating point tracks, we also used alpha track segments (e.g., Figure 4.2) and found that measurements of their widths gave results in good agreement.
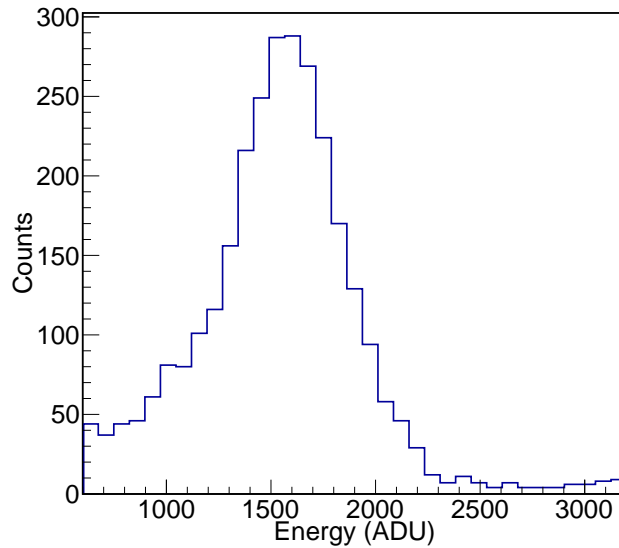
Figure 4.4: *An ^{55}Fe energy spectrum obtained with the CCD camera and used to calibrate the energy of recoils for one of the sub-runs. The energy is shown in ADUs (analog-to-digital-units). The conversion factor is found by taking the ratio of the fitted peak of the spectrum to the average energy of an ^{55}Fe recoil (5.9 keV).*

added in quadrature. This value is consistent with our expectation that the track spread due to the GEM pitch is roughly half of its 140 μm pitch. We expect other contributions, such as smearing due to imperfect optics, to be minor compared to these. Although quite low in our prototype detector, diffusion could be further reduced if the transfer gap contribution could be eliminated, or if a negative ion drift gas such as the CS_2 could be employed. With diffusion scaling as $\sqrt{L}$ with drift distance, these considerations become critical for scale up to large detectors; this is discussed further in Section 4.7.2.

4.4.3 Energy calibration

Energy calibrations were done using ^{55}Fe X-ray and ^{210}Po alpha sources. The alpha track calibration was made by first using SRIM [128] to calculate the Bragg curve of a 5.3 MeV alpha in 100 Torr CF_4. We measured the location of the alpha source relative

Table 4.1: *Detector Parameters*

Detector Parameters	
CCD and Imaging Parameters	
Peak QE	96% (560 nm)
Pixel Size (1 × 1 binning)	13×13 µm^2
Pixel Binning	6×6
Binned Pixel Imaging Scale	165 µm/pix
Imaging Area	2.8×2.8 cm^2
Read Noise @ 700 kHz	10 e$^-$ rms
Operating Temperature	$-38°$ C
Dark Current	0.03 e$^-$/s/pix
Exposure Time	5 sec
Vessel Parameters	
Detection Volume	$2.8 \times 2.8 \times 1.0$ cm^3
CF$_4$ Pressure	100 Torr
Effective Gas Gain	10^5
Effective Transverse Diffusion	345 ± 5 µm

to the drift volume and determined the part of the track that would be imaged by the CCD camera. Figure 4.2 shows segments of alpha tracks imaged by the CCD camera at the maximum stable gain. By comparing the total integrated light output in the image of the alpha track with the energy calculated from the SRIM generated Bragg curve, we obtained the light to energy conversion factor, ADU/keV$_\alpha$. Since $> 99\%$ of the energy lost by an alpha particle before its Bragg peak is through ionization, we can treat this as keV electron-equivalent energy (keVee).

For an independent calibration method we imaged the electronic recoils from ^{55}Fe X-ray interactions and obtained an energy spectrum of the scintillation signal; see Figure 4.4. At our maximum stable effective gain, ^{55}Fe tracks were visible at 6×6 pixel binning with a FWHM energy resolution of 38%. To our knowledge, this represents the first optically obtained spectrum of ^{55}Fe in a TPC detector (details provided elsewhere). The two calibration methods give results that are within 20%

of each other. The small difference could be due to a systematic in determining the alpha segment imaged by the CCD camera. In the analysis of the data to follow, we will use the energy conversion factor derived from the ^{55}Fe energy calibration. Lastly, a summary of important detector parameters discussed thus far is included in Table 4.1.

4.5 ^{60}Co and ^{252}Cf data runs

To study our detector's response to nuclear recoils, and its ability to distinguish these from gamma backgrounds, we used a ^{252}Cf neutron source and a ^{60}Co gamma source. For the ^{60}Co run, the source was placed outside the vacuum vessel but inside a lead housing to protect the CCD sensor from direct gamma-ray interactions; there was no lead between the source and the outer vessel wall. The neutron run was conducted in a similar manner but with the addition of lead bricks between the source and detector to attenuate the large number of gammas from ^{252}Cf. In total, about 96 and 36 hours of neutron data and gamma data were collected, respectively. To evaluate the detector's directional sensitivity half of the neutron data was collected with the neutrons directed in the $-x$ direction, an axis lying in the imaging plane, and the other half with the neutrons directed in the $+x$ direction.

For each data taking sequence, or sub-run, the vessel was pumped out and back-filled with fresh CF_4 gas to a pressure of 100 ± 0.05 Torr and sealed. This was followed by powering up the GEMs to the voltage settings corresponding to maximum stable gain (see Section 4.3). The CCD pixels were binned 6×6 on-chip and the chip cooled to the lowest stable operating temperature of $-38\,^{\circ}\mathrm{C}$, which was monitored by an internal sensor in the camera. An energy calibration was done with an ^{55}Fe source at the start and end of each sub-run sequence. The high drift speed of electrons in CF_4 made it impossible to trigger the CCD (open and shut the shutter) using the charge signal from the first GEM stage. Therefore, we operated in non-trigger mode

with the CCD camera successively taking 5 second exposures over a duration of about 12 hours for each sub-run. This corresponded to approximately 9 hours of live time after accounting for the CCD readout time. The detector was refilled after each sub-run to avoid substantial gain degradation due to changes in gas purity from out-gassing during the data taking sequence. As this and other effects including temperature and composition changes from charge avalanching caused the gain to drift over time, we used the average of the values measured at the end and start of each data sequence for the energy calibration constant. In total, eight sub-runs were conducted for the neutron data and three for the gamma data.

We analyzed the data using an image analysis algorithm developed with MAT-LAB and its image processing toolbox. First, images were calibrated and binned 4×4 in software, and pixels above a set threshold of $3.2\sigma_{\text{im}}$ were identified as objects. All objects found crossing the image boundaries were rejected. The binned image was then up-sampled back to its original size, resulting in an index image for the pixel locations of all identified objects. In the remainder of the analysis, all object properties were determined from the original, non-software binned image. To exclude hot pixels and CCD events (objects resulting from direct interactions of cosmic rays, radioactivity, neutrons, or gamma rays with the CCD sensor), we required objects to contain at least four contiguous pixels. Separated pixels belonging to a local grouping of pixels above threshold were connected back to the primary grouping by morphologically closing the object using a disk-shaped structuring element with a radius of two pixels. In essence, the closing operation, which is a dilation follow by an erosion, connected all pixels above threshold that lay within the radius of the structure element. Each identified object was fitted with a position and an intensity weighted ellipse, which, along with the pixel grouping in the unfitted object, were used to determine some of its important properties such energy, track length, width, skewness, and energy loss profile.

4.6 Results

4.6.1 Background discrimination

The background rate in a detector can vary widely depending on its size and the materials used in its construction, with even the most stringent requirements on radio-purity not eliminating all sources of backgrounds. Consequently, fiducialization and discrimination are of critical importance to dark matter and other rare event searches that require large detection volumes. One important source of backgrounds are gamma-rays and X-rays that can interact inside the detector to produce electronic recoils. For tracking detectors, the stopping power, dE/dx, provides a powerful tool for discriminating between electronic and nuclear recoils. Electronic recoils have a much lower average dE/dx and, hence, much longer ranges as compared to nuclear recoils of the same energy, a fact that is evident in the range versus energy plots shown in Figures 4.5 and 4.6. Given the inability of our detector to measure the Z-component of the track, the range in these figures is 2D. Of course, to maximize separation between the nuclear and electronic recoil bands, a detector with full 3D tracking capability is desirable (see Section 4.7.3).

4.6.2 Gamma and neutron data

Using the reconstructed tracks passing the track identification algorithm from the ^{60}Co gamma run, the 2D range as a function of energy is shown in Figures 4.5a and 4.5b. The hard vertical edge at 2 keVee is the result of a software threshold set on the energy of detected objects to reduce the number of false event detections during the initial track finding stage of the analysis. The sub-mm events in the lower left region of Figure 4.5a are the CCD events described in Section 4.5, which are due to direct interactions of ionizing radiation with the CCD sensor. As these CCD events suffer no diffusion, they tend to have extremely high standard deviations of their pixel values as well as very high average intensities (total intensity/number of pixels).

(a) ^{60}Co data pre-cuts   **(b)** ^{60}Co data post CCD cuts
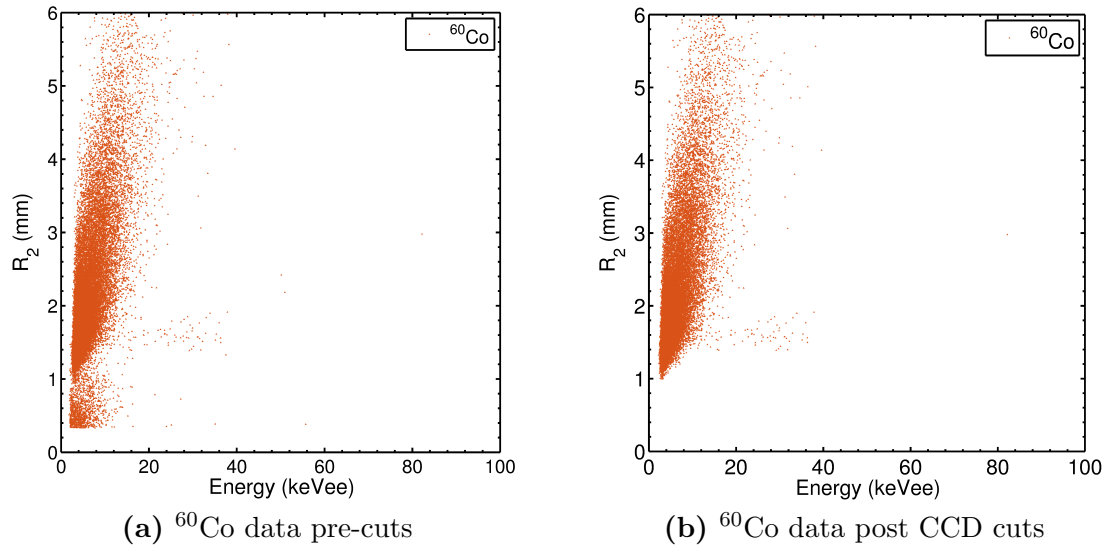
Figure 4.5: *(a) The projected range (R_2) vs. energy plot of data from the ^{60}Co gamma run. The events with short range and low energy in the lower left corner of the plot are called CCD events, which result from the direct interaction with the imaging sensor. (b) The same data after analysis cuts are made to remove the CCD events. The events in the short horizontal band extending to 40 keVee lie in the nuclear recoil band (see Figure 4.6 and text). These events are likely due to radon progeny recoils occurring at the cathode or GEM surfaces.*

Therefore, cuts made on these two parameters, in addition to track size, were used to efficiently remove this class of events. The events in the small branch protruding from the primary vertical band at around 1.5 mm are mostly due to detector intrinsic backgrounds from decays of radon daughters. These are sometimes referred to as radon progeny recoils, or RPRs, and occur at the detector surfaces [164, 163]. Events in the primary vertical band have low average dE/dx and correspond to electron recoil events. These are primarily due to Compton scatterings of the 1.17 and 1.33 MeV gamma rays emitted in the beta decay of ^{60}Co, with a small fraction from ambient and intrinsic electromagnetic backgrounds in the detector. Altogether, there were 27, 644(25, 761) events from the gamma run before(after) applying the selection cuts to remove CCD events.

(a) ^{252}Cf data post CCD cuts   **(b)** ^{252}Cf data post selection cuts
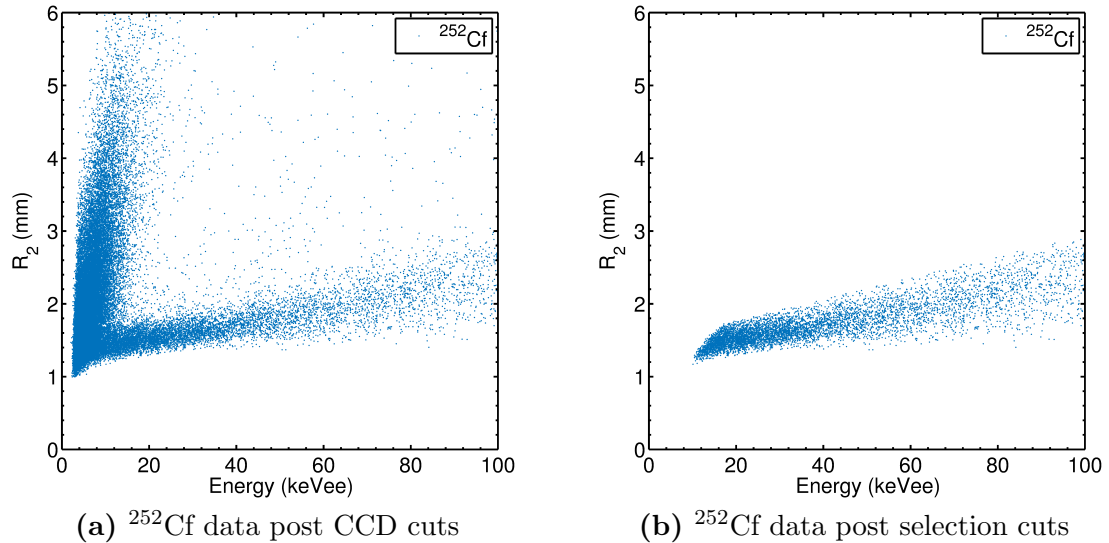
Figure 4.6: *(a) The projected range (R_2) vs. energy plot of data from the ^{252}Cf run after applying the CCD event cuts. The events not part of the two bands are most likely segments of proton recoils created by neutron interactions with hydrogen-rich materials in the detector. (b) The same data with nuclear recoil selections cut applied. The lowest energy recoils post-cuts extend to ~10 keVee (23 keVr).*

The same plots for reconstructed tracks from the ^{252}Cf neutron run are shown in Figures 4.6a and 4.6b. Two distinct bands are present. The vertical band is the same electronic recoil band observed in the gamma run, while the second, near-horizontal band contains the high dE/dx nuclear recoils (both carbon and fluorine with a ratio implied by a GEANT simulation of 1:6). The events forming the "haze" between these two primary bands have dE/dx values inconsistent with being due to Compton scatters, and they were absent in the ^{60}Co data. Their dE/dx is also inconsistent with those of carbon or fluorine recoils as their lengths far exceed the maximum of these recoiling ions at a given energy. Since these events were only seen in the neutron runs, we believe that they are segments of proton recoils from neutron interactions with hydrogen rich material in the detector such as the GEM kapton substrate.

From Figure 4.6a, it is evident that even before any selection criteria are applied, there is good separation of nuclear recoils from electronic recoils down to low energies.

Nevertheless, we used the ^{60}Co data to develop an algorithm that maximizes the rejection of electronic recoils while retaining a high detection efficiency for nuclear recoils. One parameter that gave good separation between the two recoil classes is the ratio of the projected Bragg curve peak (peak of the light distribution in keVee) to the track length (major axis of the fitted ellipse in mm). A histogram of the natural logarithm of this parameter, defined as η, is shown in Figure 4.7 for both the ^{60}Co and ^{252}Cf data. The distribution of the former has mainly one population whereas the latter, which contains both electronic and nuclear recoils, has two. The one with the larger $\log \eta$ corresponds to nuclear recoils, as also confirmed by noting that they lie in the nuclear recoil band in the R_2 versus energy plots (Figures 4.6). Based on these distributions, we defined the gamma cut of $\log \eta < 0.50$ to reject electronic recoils.

Applying this cut to the gamma run eliminated all but 65 events, of which 56 have energies below 38 keVee and 9 have energies between 110 and 440 keVee. We show below that these events are nuclear recoils and, in particular, the 56 lower energy events are consistent with RPRs from alpha decays occurring at detector surfaces [164, 163], such as the cathode or GEM, while the remaining 9 of higher energies are probably segments of alpha tracks associated with those decays. The ratio is not 1:1 because the alphas have much higher energies, and hence, greater probability to cross the image frame edge and be rejected by the analysis.

There are several pieces of evidence that support the RPR interpretation. First, a zoom-in of the $\log \eta$ histogram of the ^{60}Co data, shown in Figure 4.7b, clearly shows the 65 events in question forming a distinct population, which overlaps that of the nuclear recoil events from the ^{252}Cf data in Figure 4.7a. That these events are nuclear recoils is further corroborated by the fact that they lie in the nuclear recoil band in the R_2 versus energy plane, as shown in Figure 4.8a. Finally, the evidence that these events are mostly, if not all, due to RPRs comes from their energy distribution. For the 56 lower energy events this distribution has a mean of 26 keVee with a cut-off

(a) Discrimination parameter histogram

(b) ^{60}Co data RPR separation
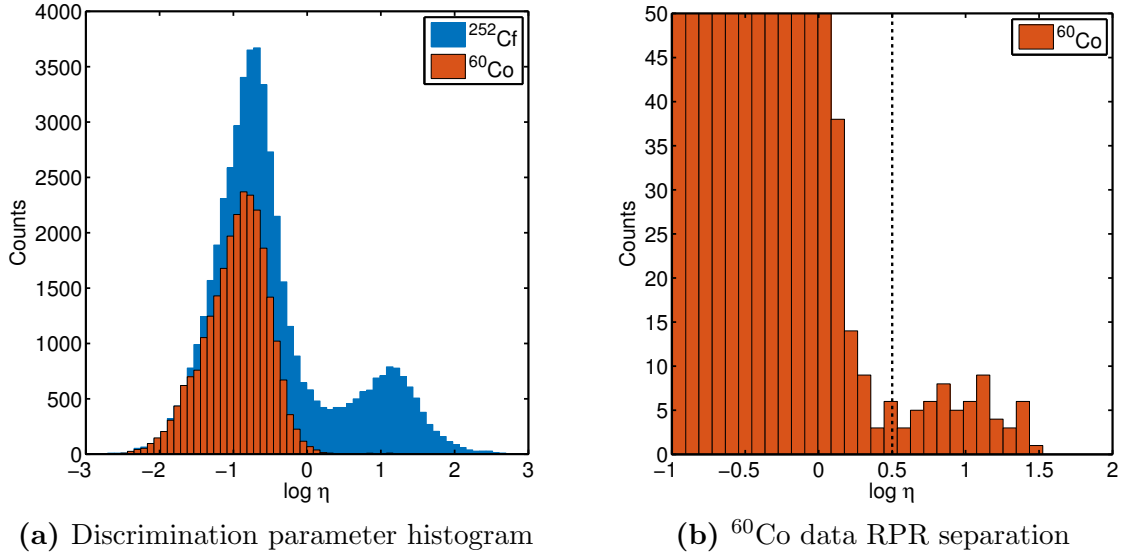
Figure 4.7: *(a) A histogram of the discrimination parameter, log η, defined as the ratio of the Bragg curve peak to track length, for the ^{60}Co (red) and ^{252}Cf (blue) runs. There are two distributions in the ^{252}Cf data representing the nuclear and electronic recoils while only one prominent one in the ^{60}Co data which contains the electronic recoils. (b) A histogram of the log η parameter for the ^{60}Co data zoomed in to see the small distribution of RPR events which overlaps the nuclear recoil peak in the ^{252}Cf data. The vertical dotted line at 0.50 is the value of the cut set on this parameter used for discrimination.*

at 38 keVee, consistent with the ionization energy distribution from the short-lived lead isotopes in the radon chain [165].

After excluding the 65 RPR and associated alpha events, the ^{60}Co dataset contains 25, 696 events, which we identify as electronic recoils. Applying the gamma cut described above removes all of these, resulting in the detector's gamma rejection at $\leq 3.9 \times 10^{-5}$. This rejection level is achieved at a pressure of 100 Torr with two dimensional (2D) track reconstruction, and may be improved further with full 3D reconstruction (Section 4.7.3) and/or by operating at lower pressure, where tracks are longer and better resolved. Additionally, more sophisticated analysis algorithms should give better results.

The resulting energy spectrum from the ^{252}Cf run after applying the analysis cuts

(a) ^{60}Co and ^{252}Cf data post selection cuts

(b) Recoil Energy Spectrum
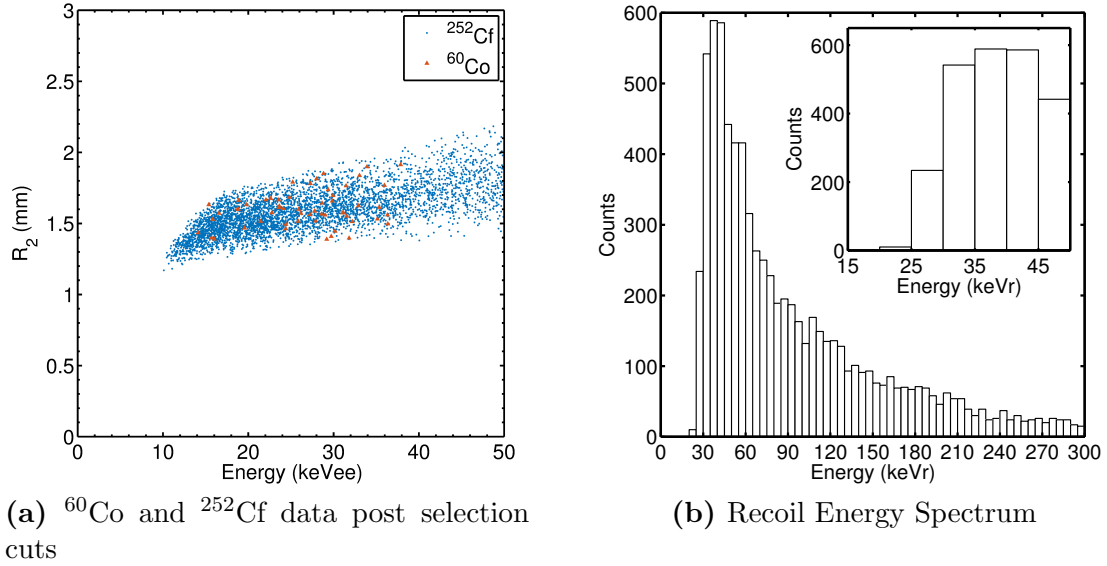
Figure 4.8: *(a) The R_2 vs energy plot for events passing the analysis cuts for nuclear recoils from both the ^{60}Co and ^{252}Cf datasets. The events remaining from the ^{60}Co data lie in the nuclear recoil band and have an energy distribution consistent with RPRs, as discussed in the text. (b) The measured energy spectrum of carbon and fluorine recoils from ^{252}Cf neutrons after analysis cuts were applied to remove the electronic recoils. The spectrum, which is peaked around 35 keVr, was derived assuming the quenching factors from [166] and that all recoils were fluorine.*

to remove CCD events and electron recoils is shown in Figure 4.8. Conversion from the measured energy in keVee to nuclear recoil energy in keVr is based on the fluorine quenching factors from Ref. [166]. The spectrum rises from 20 keVr to 35 keVr, where it peaks, indicating that maximum nuclear recoil efficiency has been reached. Thus, the effective discrimination threshold of this detector is approximately at 10 keVee ($\sim$23 keVr), see Figure 4.8a and inset in Figure 4.8b. At 100 Torr, this is the lowest discrimination threshold of any directional detector to date. Nevertheless, our $\sim$10 keVee discrimination threshold is significantly above the detection threshold, which we estimate to be 2 keVee for a diffused, point-like event based on our ^{55}Fe calibration data (see Figure 4.4). Our directional threshold is higher yet, $\sim$2$\times$ the discrimination threshold, with the reason being that nuclear recoil tracks are shorter due to their

higher dE/dx, and therefore become unresolved at higher energies; further details are discussed in a separate paper on directionality. The importance of a low energy threshold, for both discrimination and directionality, is that it provides one path towards increasing the sensitivity of directional dark matter detectors. In fact, it is critical for a low mass WIMP search as the recoil energy spectrum is shifted towards lower energies. Finally, sample recoil images from the ^{60}Co and ^{252}Cf runs are shown in Figures 4.9, 4.10, and 4.11.

4.7 Discussion

The break down of discrimination in our detector below $\sim$10 keVee ($\sim$23 keVr) is due to a number of effects that lead to the convergence of electron and nuclear recoil tracks in the range versus energy parameter space. These are due to physical effects, such as diffusion and energy-loss processes, as well as detector limitations. We discuss these below in Sections 4.7.1 and 4.7.2, and describe possible ways to circumvent them to improve discrimination.

4.7.1 The discrimination threshold

The discrimination at low energies is affected first and foremost by diffusion; as tracks fall below the resolution limit, range versus energy no longer works as a discriminant. Even if diffusion were suppressed, however, energy-loss processes affecting both electrons and nuclear recoils could pose fundamental limits to discrimination.

For electrons the dominant effects are the well known energy-loss fluctuations and straggling (e.g., Figures 4.9b, 4.9c, and 4.10), which give rise to a large spread in their range. These effects becoming stronger at lower energies, pushing the short-track tail of the electron distribution below the diffusion limit. There, these electron recoils merge with the nuclear recoil population (Figures 4.5 and 4.6) which, with their much larger dE/dx, are already unresolved at $\sim$20 keVee ($\sim$40 keVr). In addition, the
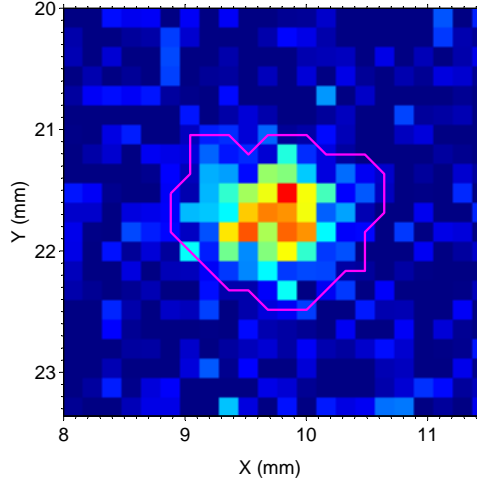
(a) 9 keVee electron recoil
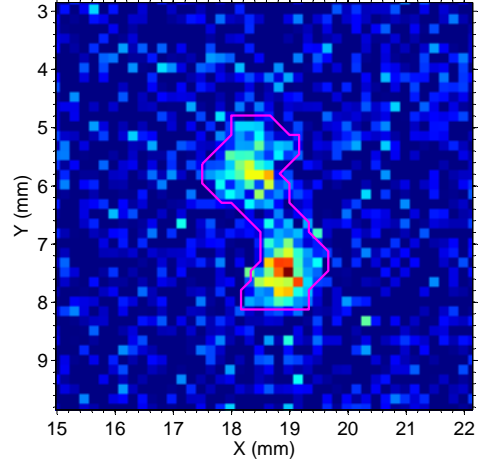
(b) 13 keVee electron recoil
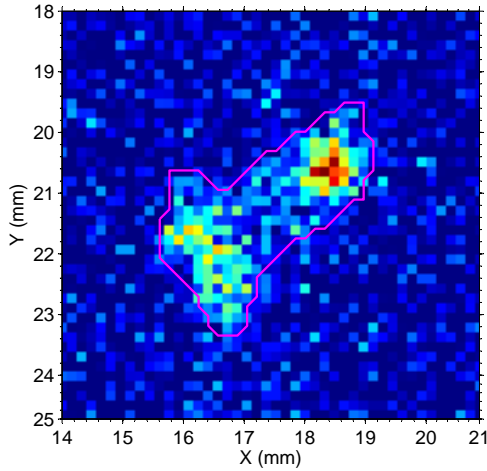
(c) 21 keVee electron recoil
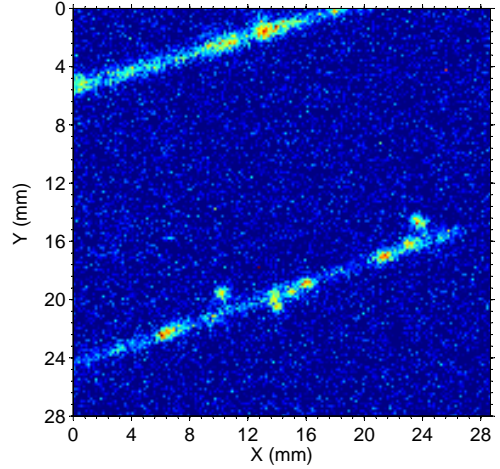
(d) > 30 keVee electron recoils

Figure 4.9: *(a-d) Electron recoils of different energies from the ^{252}Cf and ^{60}Co runs. The images have been contrast adjusted to enhance visualization. The magenta contours trace out the track boundaries and are included as a visualization aid and to help illustrate the straggling of low energy recoils and the clumpy ionization deposition. (d) Two high energy electronic recoils containing smaller delta ray tracks emerging perpendicular to the primary electronic recoil track. These image boundary crossing tracks were rejected from the analysis and were found only by visually scanning events by eye.*

(a) Electron Recoil

(b) Projected Bragg Curve
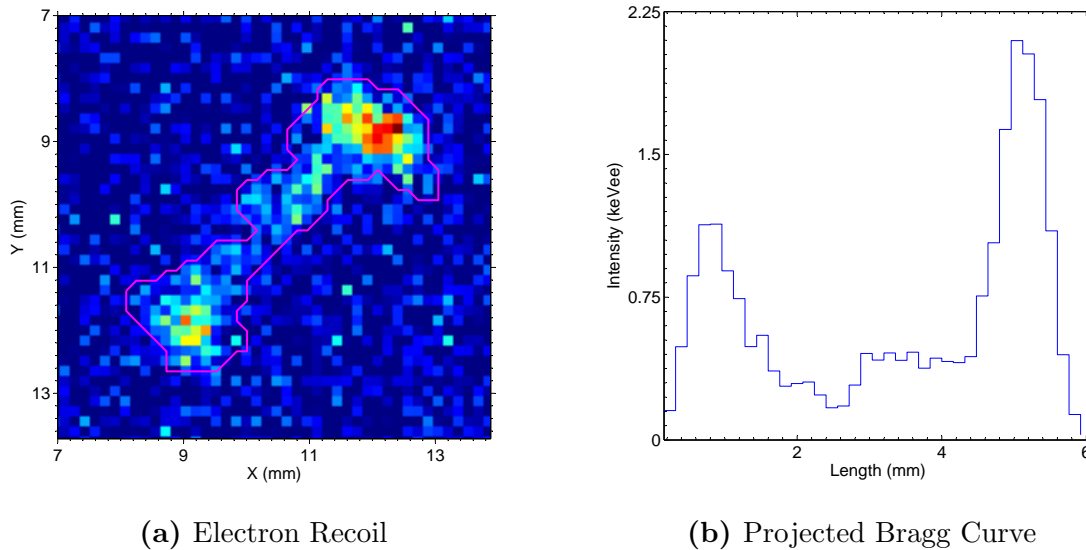
Figure 4.10: *(a) An image of a 24 keVee electronic recoil in 100 Torr CF_4. The magenta curve traces out the perimeter of the track and helps in visualizing the straggling of the recoil. (b) The Bragg curve of the recoil, obtained from the projection of the track along the major axis of the fitted ellipse, shows the large energy fluctuations that are also clearly apparent in the CCD image. A detector with a lower signal to noise ratio would only see the brightest region(s) of the track and possibly misidentifying them as a nuclear recoil(s).*

probability for large angle scattering at low energies increases for electrons, producing a trajectory that is almost diffusive in nature. As a result the energy is deposited into smaller unresolved regions of space, which, together with projection of the track to 2D, systematically biases the dE/dx upward towards that of nuclear recoils. In Figure 4.6 events of a given energy affected in this manner have their R_2 underestimated and drop down into the nuclear recoil band.

For nuclear recoils the opposite trend occurs, whereby energy-loss in the ionization channel (the detectable dE/dx) decreases as the ions slow down, with other energy-loss channels making up the difference. Both theoretical (Ref. [166]) and experimental (Ref. [167]) studies of the ratio of ionization to total energy-loss (the quenching factor) indicate values less than 0.25 for E < 10 keVr in a variety of gases
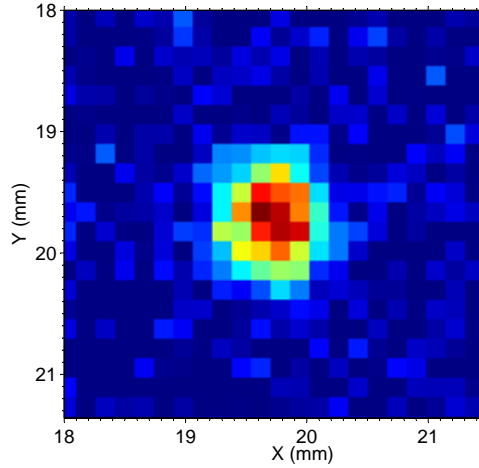
(a) 28 keVr ($\sim$ 13 keVee) nuclear recoil
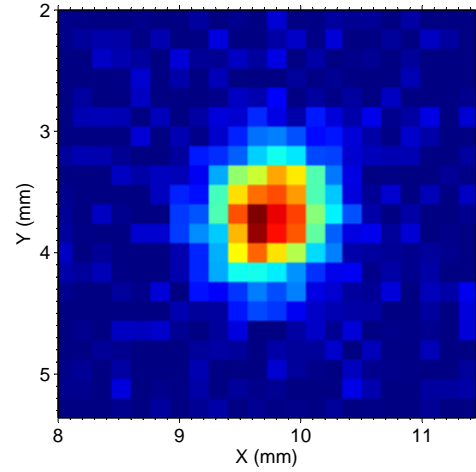
(b) 53 keVr ($\sim$ 28 keVee) nuclear recoil
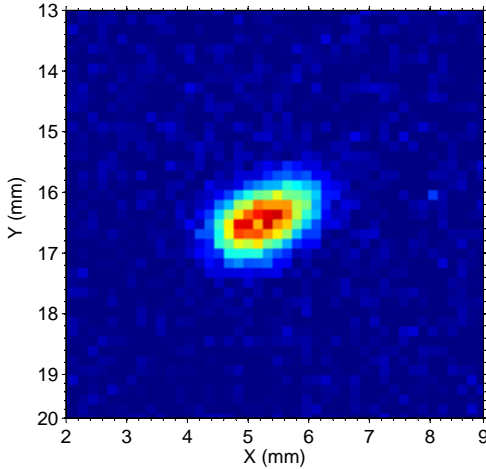
(c) 104 keVr ($\sim$ 66 keVee) nuclear recoil
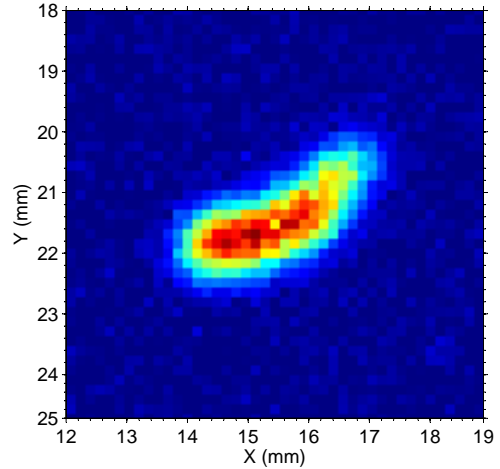
(d) 214 keVr ($\sim$ 160 keVee) nuclear recoil

Figure 4.11: *(a-d) Nuclear recoils from the ^{252}Cf runs at various kinetic energies in 100 Torr CF_4 using the Hitachi quenching factors and assuming all the nuclear recoils are fluorine atoms. The images have been contrast adjusted to enhance visualization and have different X/Y scales. The directionality and asymmetry in the energy deposition often referred to as the head-tail signature become apparent for the highest three energy recoils. In all images, the average neutron direction is from left to right. Also note how the track in (a) deposits roughly the same amount of energy as the electronic recoils in Figures 4.9a and 4.9b but appear in a much tighter area with a higher intensity peak pixel value. A lower signal-to-noise and lower resolution detector could fail to differentiate the track in (a) from that in Figure 4.9a.*

and their mixtures. This effect underestimates the energy of events of a given track length in Figure 4.6, pushing them leftward into the electronic recoil band.

Thus, the detected dE/dx for both classes of recoils converges at low energies, potentially posing a fundamental limit on discrimination using the range versus energy technique. The energy where this occurs cannot be determined from our data where, as mentioned above, the limitations on discrimination are due to diffusion. Progress toward this goal will require resolving tracks below our E < 10 keVee threshold, for example by lowering the gas pressure to lengthen tracks. From a practical perspective, directional gas TPCs have been shown to operate down to 20 Torr ([168, 169]), and with Thick GEMs (THGEMs) good gas gain has been demonstrated down to 0.5 Torr in certain gases [142, 143]. So, measurements in the 10 - 40 Torr pressure range could feasibly map out the possible parameter space for discrimination below 10 keVee, and will likely lower the threshold as well. Exploring gas mixtures with lower straggling and energy loss fluctuations should also be attempted. All such efforts will be most critical for low mass WIMP searches where energy thresholds < 10 keVr (note this is recoil energy, not ionization energy) are desired. Depending on the degree of quenching, the detected energy in this regime could be as low as a few keVee, where achieving both discrimination and directionality could be extremely challenging.

4.7.2 Detector improvements

Besides lowering the pressure and optimizing gas mixtures, improvements in the detector itself could also lead to better discrimination and directionality. The three detector parameters that we believe play a critical role for this are signal-to-noise, resolution, and tracking dimensionality (discussed in Section 4.7.3). We restrict our discussion to an optical detector of the type used here, but many of the ideas apply to charge readout detectors as well.

A benefit of signal-to-noise, especially where discrimination is concerned, is that

(a) Noise Added

(b) Original

(c) Filtered Original
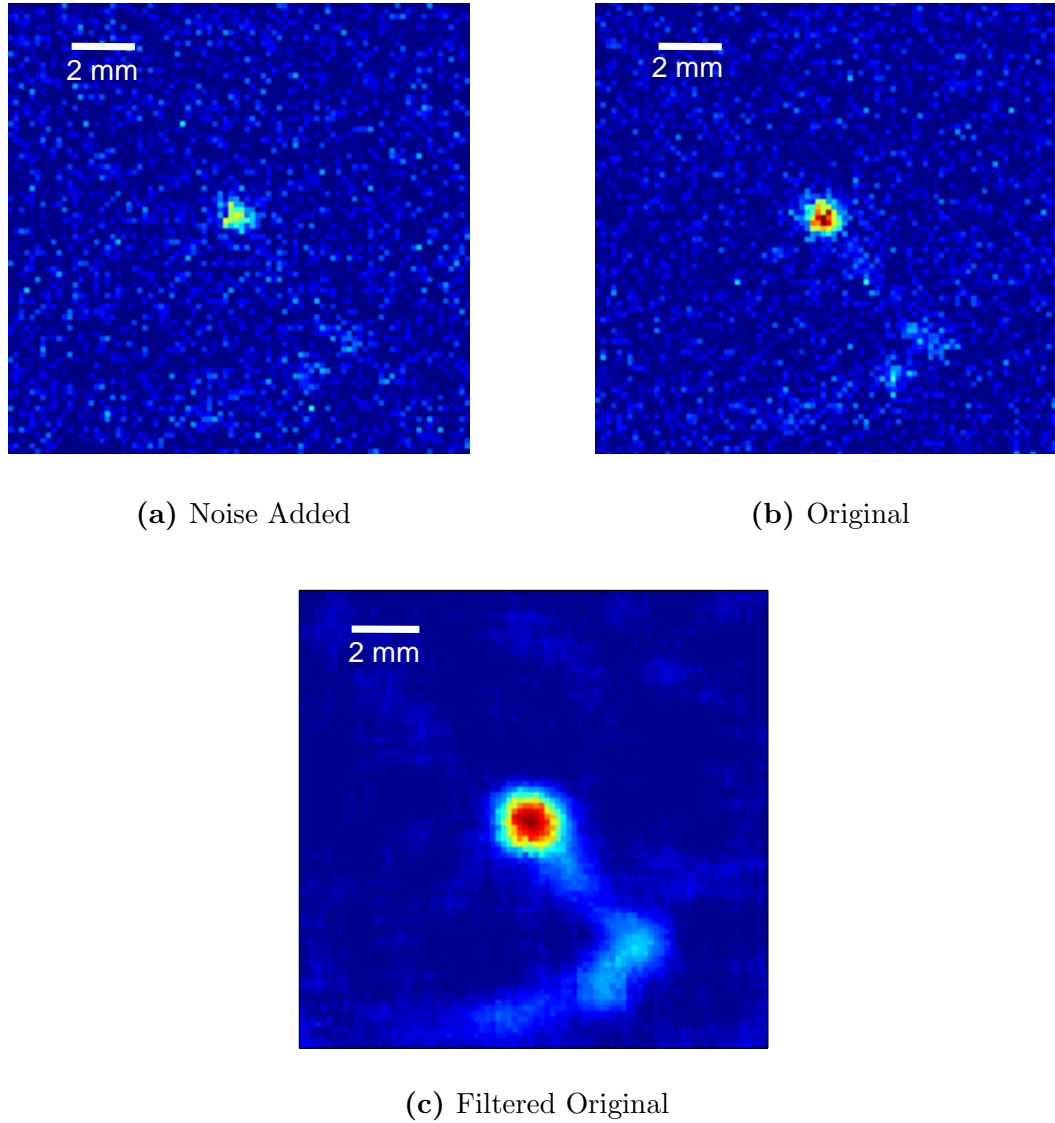
Figure 4.12: *An ~16 keVee event from the ^{252}Cf run shown with different signal-to-noise levels. The middle panel (b) shows the original calibrated CCD image, and the left panel (a) shows the same but with 50% higher noise added in software. The right panel (c) is the original image with a Gaussian noise reduction filter applied. See text for details.*

it enables full mapping of electron tracks that have large energy-loss fluctuations of the type seen in Figures 4.9b, 4.9c, and 4.10. These tracks show regions with high energy-loss interspersed with barely discernible regions of low energy-loss. A detector with low signal-to-noise would detect only the peak regions, which, due to their systematically higher dE/dx, would look like nuclear recoil tracks. This is illustrated in Figure 4.12, where we show three images of an event from the ^{252}Cf run, each with a different signal-to-noise level. Figure 4.12b is the original calibrated CCD image obtained by our detector, showing a track with a high density segment and a suggestion of a very faint tail. In Figure 4.12a, we artificially added about 50% more noise to the image in software. In this image the long faint tail of the recoil is lost in the noise, leaving just the bright high density region that could easily be misidentified as a low energy nuclear recoil track. Finally, in Figure 4.12c the original image has been processed using a Gaussian noise reduction filter. The long faint tail is now clearly visible as is its connection to the brighter segment, leaving little doubt that this is an electron track.

The two obvious paths to achieving high signal-to-noise are to lower the noise and/or increase the signal. The former approach would require a reduction in the CCD camera system noise, which is usually dominated by the read noise for short exposures, but the tradeoff is slower readout speed or more costly multi-node read-outs. In the direction of increasing signal, there are many approaches that could be taken. The first is boosting the CCD sensor quantum efficiency, which, for the back-illuminated CCD used here, is already highly optimized. Secondly, one can increase signal through better light collection with a more efficient optical system (faster lens), and/or a setup that allows for more light collection by decreasing the distance between the GEM and lens. However, the latter approach requires a sacrifice of imaging area whereas the former requires a potentially uneconomical and sophisticated custom lens design. Although both are potential drawbacks for scale-up to large detector volumes, these approaches should be considered if cheaper CCDs

or other technologies become available in the future.

Another approach is to increase the light output by selecting gas mixtures with higher avalanche photon yield, defined as the number of photons per secondary electron released during amplification, or by increasing the absolute gas gain. Although we have achieved very high gas gain in our detector with the triple-GEM stack, the light yield of CF_4, albeit one of the better scintillating gases, could be improved further. For example, the addition of Ar at high concentrations has been shown to increase the photon yield of pure CF_4 [158, 170] from ~0.3 to ~0.7 [171]. Although a number of excellent gas scintillators exist, consideration of the spectrum (e.g., optical vs. UV) and whether the target is optimal for the specific WIMP search (e.g., spin-dependent vs. spin independent) must be taken into account. The gas gain could also be increased, but saturation effects have been noted at high gains [172], where both the gain and photon yield are charge density dependent. This could have a deleterious effect on both energy and directional sense determination.

Detector resolution, also critical for both directionality and discrimination, is governed by various design and operation choices such as the readout pitch, gas mixture, pressure and diffusion. How pressure can be used to vary track lengths and how the choice of gas can effect fluctuations and straggling were briefly discussed above, so we focus on the other two factors here. Diffusion can be reduced by limiting the maximum drift distance and by making a judicious choice of gas mixture. Although CF_4 exhibits relatively good diffusive characteristics for an electron drift gas, negative ion gases such as CS_2, which drift in the thermal regime, provide the lowest diffusion possible without employing magnetic fields (see Section 3.1). The low diffusion in our small detector, $\sigma \sim 0.35$ mm, is not far from the average value of $\sigma \sim 0.5$ mm achieved with CS_2 over a 50 cm drift in the DRIFT detector. Thus, the diffusion achieved in our detector is a reasonable goal for a large scale directional experiment, and any meaningful reduction would likely require other techniques.

In principle, the readout pitch of the detector should be fine enough to extract

the maximum information possible with the given diffusion. The effective pitch in our detector, which is due to a combination of the GEM pitch, 140 µm, and the CCD binned pixels, 165 µm, was a little less than half the sigma due to diffusion, $\sigma \sim 0.35$ mm. This allowed tracks to be measured with a sufficient number of independent samples to extract features, such as energy-loss fluctuations and asymmetry in ionization, important for discrimination and directionality.

A good example demonstrating this for discrimination is found by comparing the images of the electronic recoil and nuclear recoil shown in Figures 4.9a and 4.11a, respectively. Both have similar detected energy but the electronic recoil looks more disperse with larger fluctuations, and the nuclear recoil more concentrated and smoothly distributed. These differences are consistent with the energy-loss processes discussed above, and could be used in more sophisticated algorithms to improve discrimination and directionality. The finer pitch also opens the door to deconvolution techniques, such as those used in astronomy (for example, see [173]), which could be applied to achieve better resolution.

4.7.3   Background discrimination: 1D, 2D, and 3D

The detector parameter that is arguably most critical for good discrimination and directionality is the number of independently measured track components. Although full 3D track reconstruction is preferred, any benefit it brings to discrimination or the directional sensitivity must be justified relative to the cost increase or added design and operational complexity. Here we study the improvement in discrimination from 1D to 2D to 3D and, except for brief remarks below, postpone the discussion on directionality for a separate paper.

We begin by studying the difference in discrimination power between 1D and 2D. For this we took our 2D data from the ^{60}Co and ^{252}Cf runs and reduced them to 1D. We have defined the X(Y) component of the track length as $R_2 \cos\theta(R_2 \sin\theta)$, where θ is the reconstructed angle of the track in the X-Y plane. Of course, this

(a) X Component

(b) Y Component

(c) R_2 Length
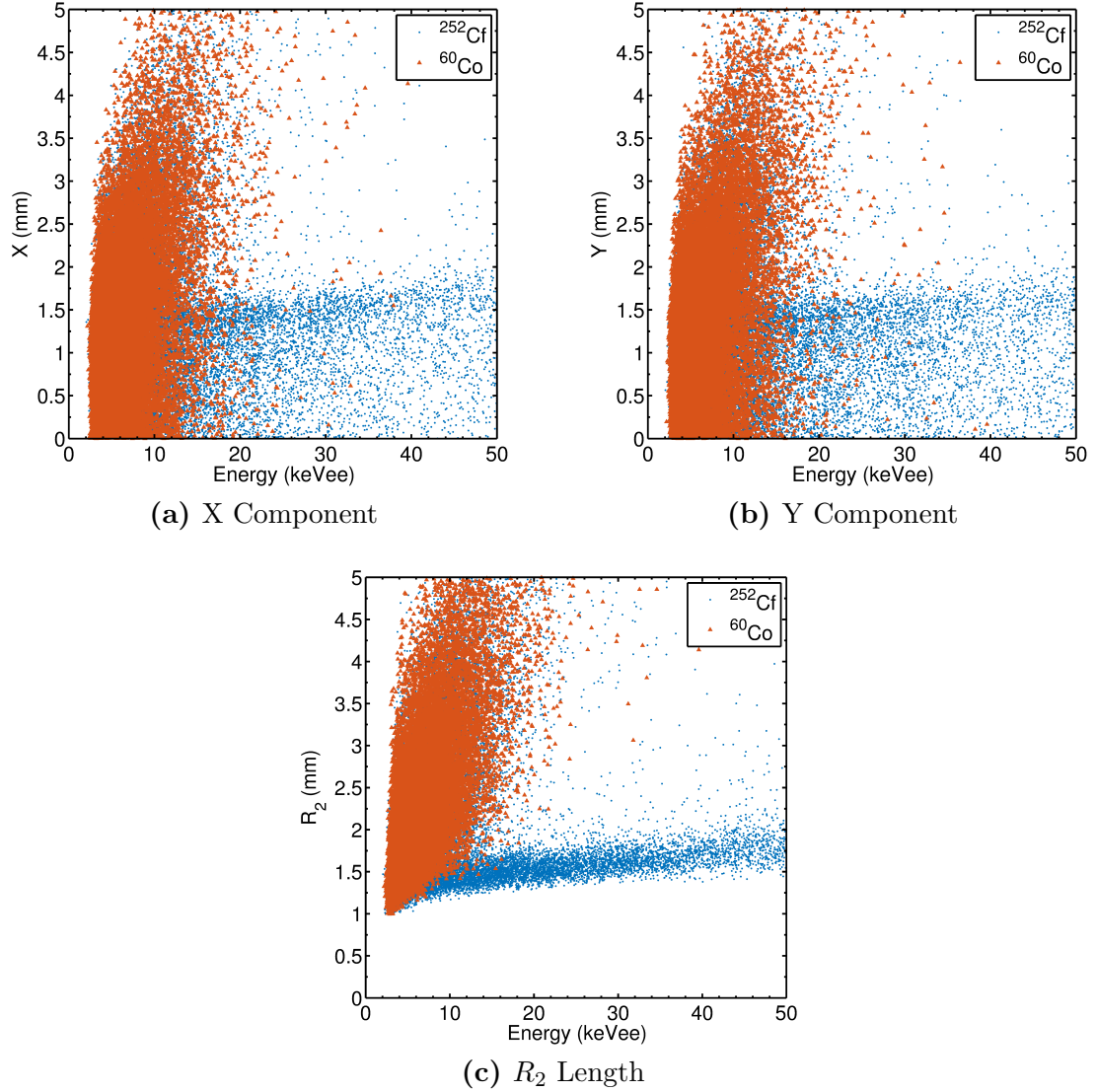
Figure 4.13: *(a) and (b) Plots of the X and Y, 1D components of the track length vs. energy for the ^{60}Co run overlaid on top of the ^{252}Cf run. These show the approximate level of discrimination that a 1D detector would achieve. (c) The 2D projected track length vs. energy data from the same two data runs reproduced for comparison (from Figures 4.5 and 4.6). For all 3 panels the RPRs from the ^{60}Co have been removed to show the true separation between the electronic recoil and the nuclear recoil bands. In the 2D data there is separation of the bands down to about 10 keVee (23 keVr), but in the 1D data (a-b), events from the electronic recoil bands are leaking into the nuclear recoil region up to energies > 35 keVee (62 keVr).*

artificially extends the 1D track length down to zero, whereas the diffusion in a real 1D detector would impose a minimum. Nevertheless, this effect, which is apparent in Figures 4.13a and 4.13b, does not change the relative comparison we wish to make here. In addition, to better gauge the separation between the electronic and nuclear recoil bands, the 65 events associated with RPRs in the ^{60}Co were removed from this dataset.

In Figures 4.13a and 4.13b the X and Y, 1D components of the tracks are plotted as a function of energy, respectively. As one would expect, the electronic recoil bands in these two figures are very similar because their recoil directions are distributed more or less isotropically in the imaging plane. The nuclear recoil band, although smeared out greatly in both figures, is marginally denser in Figure 4.13a because the neutrons were directed along the X-axis. For comparison, an overlay of the 2D, R_2 versus E data from both runs is also shown in Figure 4.13c.

The results show significantly better discrimination with 2D tracks versus 1D. In 2D, discrimination is achieved down to ∼10 keVee (23 keVr), whereas in 1D, electron events from the ^{60}Co run have strayed into the nuclear recoil band out to energies of ∼35-40 keVee (∼65 keVr). This effectively puts the discrimination energy threshold of the 2D data at a factor ∼3 lower than the 1D data, which would correspond to a factor of ∼7(70) times higher detection sensitivity for a WIMP of mass 100(30) GeV·c^{-2} scattering off fluorine through spin-independent interaction. Perhaps cuts made on other track parameters could be used to reduce this gap, but it is unlikely that 1D discrimination would improve to extend the threshold much below 30 keVee (55 keVr).

Next, with the aid of simulations we explored the potential difference in discrimination capability between a 2D vs. 3D detector. The simulation program SRIM(CASINO) [128]([174]) was used to simulate nuclear(electronic) recoil tracks with an isotropic distribution in 3D and with the same energy distribution as our

(a) 2D Reconstruction   **(b)** 3D Reconstruction
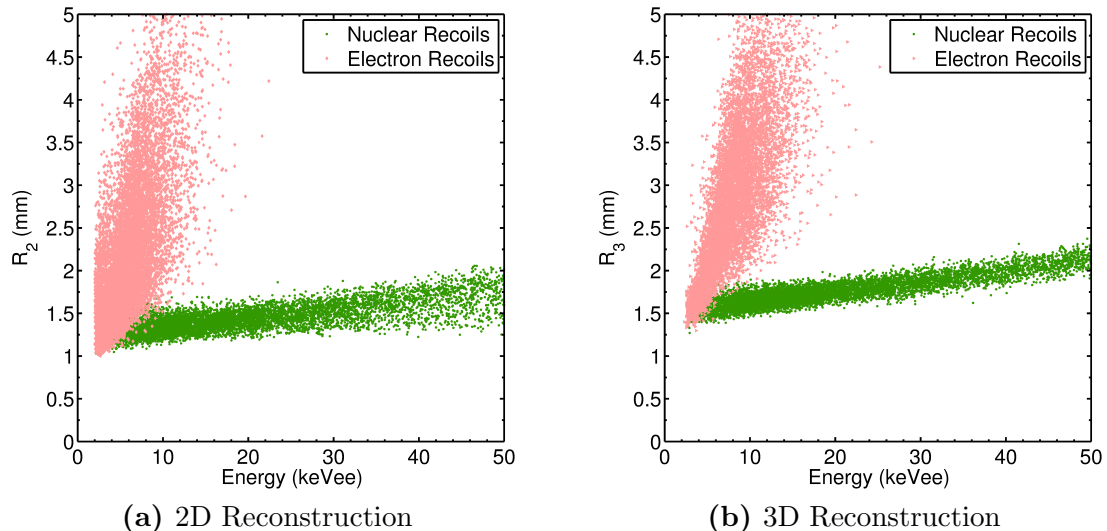
Figure 4.14: *Simulation of range vs. energy for fluorine and electron recoils in 100 Torr CF_4 for 2D (a) and 3D (b) track reconstructions. In the 2D reconstruction (a), events from the electron band leak into the nuclear band up to energies of ~9 keVee. But in the 3D reconstruction (b) events from the two bands are separable down to energies of ~6 keVee.*

calibration data.[2] Each simulated track was then projected onto the image plane with the pixellization, noise, and signal adjusted to match those of our CCD detector. The diffused and signal-to-noise adjusted projected track from each image plane (XY, XZ, YZ) was analyzed using the same image analysis algorithm as the one used for our neutron and gamma data (Section 4.5). We note that the simulations do not take into account secondary recoils but merely serve as a qualitative demonstration of the improvement in background discrimination with 3D tracking. A quantitative statement about the improvement level requires a more detailed simulation of the detector with a more rigorous treatment of energy loss, gas diffusion, amplification stage effects, and detection efficiency, which is beyond the scope of the paper. A more comprehensive simulation-based study of discrimination between electron and nuclear recoils in a directional dark matter experiment can be found in Ref. [175].

---

[2]We note that the nuclear recoil simulations do not take into account secondary recoils.

The results of these simulations are shown in Figures 4.14a and 4.14b. As expected, the nuclear recoil band for the case of 3D reconstruction (Figure 4.14b) is much tighter than the 2D case (Figure 4.14a). The 3D distribution of the electron band is still dominated by the effects of straggling and energy loss fluctuations (discussed in Section 4.7.1), resulting in large scatter in both range and energy. However, in the region where the two bands intersect, the 3D electron events are more tightly distributed than in 2D, yielding better separation from the nuclear recoils. This results in about a ~35% lower discrimination threshold, which, not surprisingly, is not as large as the difference seen between the 1D and 2D data. Nevertheless, when combined with lower, ~10-20 Torr, operating pressures and better track reconstruction algorithms, 3D could push the discrimination threshold into the few keVee region of interest for low mass WIMP searches.

With regards to the WIMP directional signature, the advantage of 3D track reconstruction in directional searches has been a subject of numerous studies and discussions. Using the criteria of number of events needed to reject isotropy, these studies show only a factor few difference between 2D and 3D when perfect HT sense recognition is assumed [146, 145, 147]. If other variables are included then even 1D appears competitive [149]. This would seem to suggest that multi-dimensional tracking is something desired but not absolutely necessary. There are two caveats to this, however. The first is that the assumption of perfect HT sense recognition is unrealistic, and we argue that higher dimensionality is needed even to approach this goal. The second is that, in the case of low pressure TPCs, discrimination power and directional sensitivity are coupled to the tracking dimensionality of the detector. As the primary discriminant is the stopping power, dE/dx, robust discrimination requires high quality measurements of both energy and track range. The latter, as we have shown here, is best accomplished with a 3D detector. A more extensive discussion on the relationship between tracking dimensionality and directional sensitivity is reserved for 3.3.2.

The realization of full 3D tracking capability with high resolution nevertheless comes with added costs and technological challenges. For example, the relatively fast drift speed of electrons in gases such as CF_4 makes it difficult to get sufficient spatial resolution in the third dimension (the drift, or Z, direction). Although these depend on the detector technology, in the case of a TPC the relatively fast drift speed of electrons in gases such as CF_4 makes it difficult to get sufficient spatial resolution in the third dimension (the drift, or Z, direction). Even though several groups have succeeded in resolving the Z-component of the track with specialized fast electronics [176, 165, 177], the ~1000× slower drift speeds of negative ion drift gases have an advantage in this regard. Nevertheless, several directional experiments have demonstrated the capability to resolve the Z-component of the track using specialized fast electronics [176, 165, 177]. In this regard, negative ion drift gases such as CS_2 have an advantage because their drift speeds are ~1000× slower. For example, the DRIFT experiment, which uses CS_2 gas mixtures, achieves superb resolution (< 100 µm) for the Z-component of the track with very cheap, commercially available electronics.

Other advantages of negative ion drift include low, thermal diffusion, and with the recent discovery of multiple negative ion charge carriers in CS_2+O_2 mixtures, the ability to fully fiducialize the detector [179]. The latter is a necessary ingredient for zero background operation, as also demonstrated by the DRIFT experiment [111]. All of these advantages offset the few disadvantages of CS_2 mixtures, one being its toxicity, and the other its lack of spin-dependent sensitivity, which requires mixtures such as the 30:10:1 Torr $CS_2+CF_4+O_2$ used in DRIFT. Recent work indicates that another negative ion gas, pure SF_6, has all of the advantages of CS_2+O_2, but is also fluorine rich for spin-dependent sensitivity, and benign [180]. In regard to optical TPCs of the type used in this work, the qualities that make for an ideal negative ion gas are not expected to result in good or any scintillation. However, preliminary results in CS_2+CF_4 mixtures have shown good scintillation yield with negative ion

behavior in certain mix proportions. These and many other considerations represent a large parameter space of quantities such as gas mixture, pressure, and amplification scheme that remain to be explored to optimize for the detection and study of low energy recoils.

4.8 Conclusion and prospects

In this work we have described a small high resolution, high signal-to-noise GEM-based TPC with a 2D CCD readout. The detector was designed to make detailed studies of low energy electron and nuclear recoil tracks for the purpose of directional dark matter searches. Detector performance was characterized using alpha particles from ^{210}Po, X-rays from ^{55}Fe, gamma-rays from ^{60}Co, and $\sim$MeV neutrons from ^{252}Cf. Stable gas gains upward of 10^5 were achieved in 100 Torr of pure CF_4 with a triple-GEM cascade, resulting in a very high signal-to-noise. This, together with an effective 165 µm track sampling and low diffusion, $\sigma \sim 0.35$ mm, provided the means for detecting events with energies down to a few keVee.

With our ^{60}Co and ^{252}Cf data we also studied discrimination between electronic and nuclear recoils. Using the standard range versus energy technique, relatively simple selection criteria were used to demonstrate excellent discrimination down to $\sim$10 keVee, or $\sim$23 keVr recoil energy. This result, the best to date at 100 Torr, was especially aided by the high spatial resolution and signal-to-noise of the detector. Without the latter, the large energy-loss fluctuations suffered by low energy electrons would cause only the peak intensity regions of the tracks to be detected. Such tracks would be reconstructed with their dE/dx and track lengths systematically too high and too low, respectively, resulting in these events being misidentified as nuclear recoils. That both high spatial resolution and high signal-to-noise are necessary for good discrimination is an important result of this work.

Pushing the discrimination threshold to even lower energies is an important fu-

ture goal, especially critical for directional low mass WIMP searches. Our ∼10 keVee threshold is due to a combination of diffusion and electron straggling, which results in the merger of the electron and nuclear recoil populations in the R_2 versus E parameter space. Two paths around this are to lower the gas pressure to lengthen tracks, and full 3D track reconstruction. The former would allow mapping the parameter space for discrimination below our 10 keVee threshold and find any fundamental limit if it exists. The influence of track dimensionality on discrimination was also investigated and, using our data, we found that the 1D threshold is a factor ∼3 higher than 2D. Using simulations we also found better separation between the electron and nuclear recoil populations in 3D versus 2D, resulting in about ∼35% lower discrimination threshold in 3D. In addition to these two strategies, better analysis techniques that take full advantage of the difference seen between electron and nuclear recoil tracks (e.g., compare Figures 4.9a and 4.11a) should be investigated in the future.

Finally, the data obtained in this work can also be used to characterize the directionality of the nuclear recoil tracks. With their higher dE/dx, we find that these tracks become unresolved at energies around ∼20 keVee (∼40 keVr), resulting in a directionality threshold that is a factor ∼2 higher than the discrimination threshold. That these two thresholds are not the same is another important result from this work, which, given the differences in the energy-loss processes of electrons and nuclear recoils, is perhaps not surprising. A detailed analysis of the directional signature, and its implications for WIMP detection, will be described in Chapter 5.

Chapter 5

Directional Sensitivity of Prototype CCD Detector

5.1 ^{252}Cf directionality

5.1.1 Angular resolution

The directional sensitivity of the detector is characterized by two parameters, the angular resolution, or how well the track orientation (axial direction) is determined, and the charge asymmetry (skewness/head-tail) along that axial direction. These two properties are highly correlated as both depend on the amount of diffusion, track length, recoil energy, and detector resolution. Nevertheless, the ability to measure the track axial orientation does not guarantied that a sense can be well measured.

To determine how well the detector can reconstruct the track orientation, the angular resolution as a function of energy is calculated. First, nuclear recoil directions from a ^{252}Cf neutron spectrum scattering off fluorine are simulated. An energy and recoil direction are specified for each simulated nuclear recoil event. The recoil directions within an energy range are then projected down onto the 2D imaging plane and smeared with a *resolution function* taken to be the von Mises distribution,

which is the circular analogy of the Gaussian distribution on a line. The maximum likelihood method is then used to find the smearing width that gives the best agreement between the simulated recoil direction distribution and the measurement-based distribution within the given energy bin. The result is an *effective* 2D angular resolution and is shown in Fig. 5.1, but note that the results are not needed, or used, in the analysis in the subsequent sections of this chapter.

The other approach is to take the recoil directions within an energy range and then smear them in three dimensional space with a *resolution function* taken to be the Fisher distribution [181, 182, 183, 184] of varying concentration parameter or width before projecting down to 2D. The Fisher distribution, also known as the von Mises-Arnold-Fisher distribution, is the generalization of the von Mises distribution on the circle to the sphere, and both belong to a family of distributions called Langevin distributions [182]. Once smeared, the directions are then projected down onto the two dimensional detection plane, and the same method described above is used to find the best fit smearing width.

In this case, the 2D angular resolution is defined as the width that contains 68% coverage of the projected smearing function about the mean direction. It is very important to note that both Figs. 5.1 and 5.2 do not truly represent a 2D angular resolution because it is difficult to define such a quantity in 3D. The reason being that the angular resolution of a given event depends not only on its energy and track length but also on the inclination of the track relative to the imaging plane. However, with the above definition, the angular resolution of a flat(uniform) angular distribution in 3D projected down onto 2D is $\sim 61°$ as shown in Fig. 5.2 by the dot-dashed horizontal line. The fit is done for energy bins of 20 keVr in width and the results are shown in Fig. 5.2 for the case in which the initial recoil directions are parallel to the detection plane. The reason for this approach is that it also gives us the 3D angular resolution of a detector that possesses the same resolution in each of its dimensions. This will be important in the WIMP anisotropy study detailed
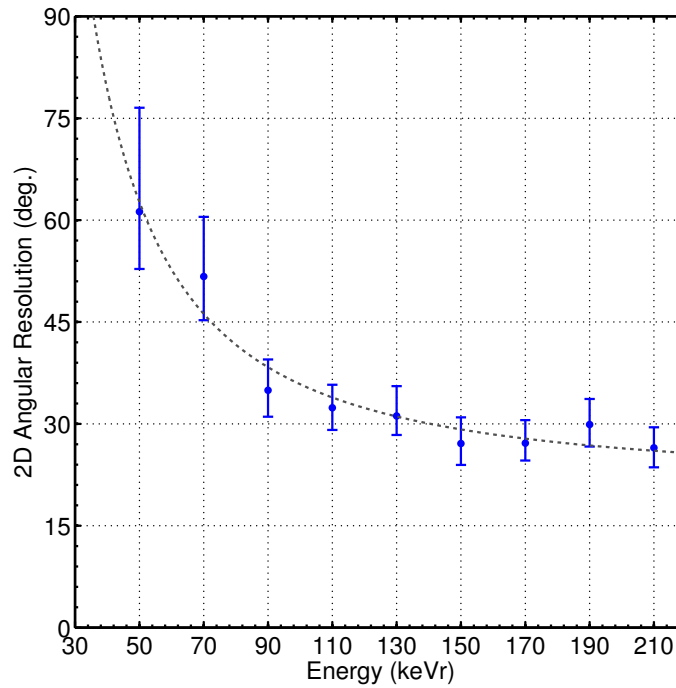
Figure 5.1: *2D detector angular resolution as a function of energy derived by projecting the simulated data onto the 2D imaging plane. Data in 20 keVr energy bin are then smeared with the von Mises distribution and compared to measurements in the same energy bin to extract the best fit angular resolution.*

in Sec. 5.3. Similar to the results shown in Fig. 5.1, the projected 2D results from Fig. 5.2 are not used in any of the forthcoming analysis of the data.

It should also be mentioned that multiple scattering events have not been included into the simulation used to derived these results, so the angular resolution as determined by this method should represent a conservative estimate as the secondaries will tend to broaden the angular distribution. This effect could be the reason for the poor fitting results found for data below 40 keVr. Nevertheless, the trend, given by the fitted curve in Figs. 5.1 and 5.2 suggests that axial directionality extends down to this energy. Also, note here that the energy scale is in nuclear recoil energy and not electron equivalent because to compare the simulated results with measurement we must convert the detected energy into recoil energy using the fluo-
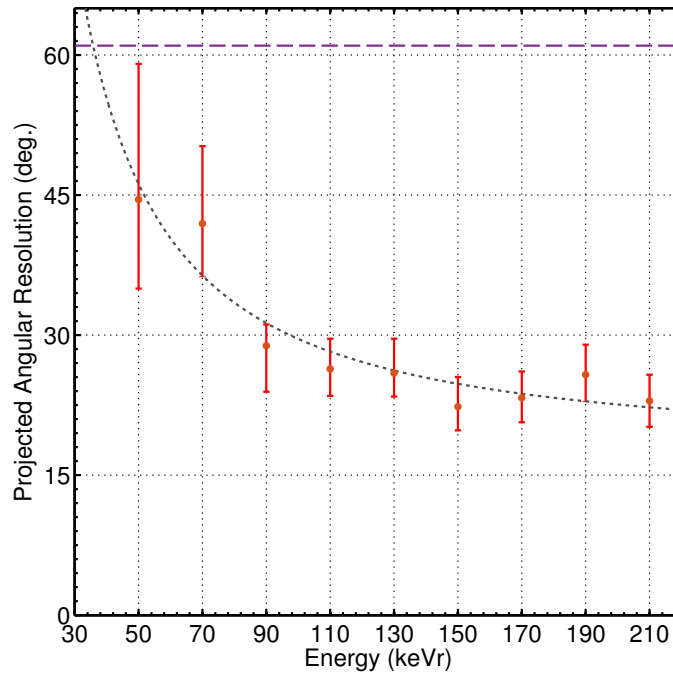
Figure 5.2: *The 2D detector angular resolution as function of energy derived by smearing in 3D and projecting onto 2D to compare with measurements. The horizontal bars represent the widths of the energy bins while the vertical errors bars show the 68% confidence intervals.*

rine quenching factors from Ref. [166]. The assumption of the quenching factors will affect these results. In addition, because the angular resolution depends not only on the pixellization of the detector readout and diffusion but also on the amount of straggling exhibited by the recoiling target, these numbers could improve for a target that exhibits less straggling such as helium.

5.1.2 Head-tail signature

For the sense(head-tail) determination, we define the skewness parameter s on the projected Bragg curve light distribution to quantify the level of charge asymmetry. This distribution is obtained by projecting the track onto its reconstructed major

axis, and s is defined by:

$$s = \frac{\frac{1}{n}\sum\limits_{i=1}^{n}(x_i - \bar{x})^3}{\left[\frac{1}{n-1}\sum\limits_{i=1}^{n}(x_i - \bar{x})^2\right]^{3/2}} \tag{5.1.1}$$

where n is the number of samples in the distribution, x is the location of a sample along the distribution, and $\bar{x}$ is the distribution mean. By considering the image coordinate system and location of the neutron source in the data run discussed in Chapter 4, nuclear recoils from the first half of run are expected to be predominantly negative skewed while those from the second half should be mostly positive skewed as the energy loss rate through ionization of a low energy nuclear recoil has been shown to decrease along its recoiling path [125].

We find that using a threshold of $3.2\sigma_{\mathrm{im}}$, where σ_{im} is the rms of the image background, to optimize detection of tracks is not the optimal value to calculate the skewness because the boundary pixels are rather noisy and can cause large fluctuations in the skewness measurements. By taking track pixels inside an isophote with a higher threshold value of $3.8\sigma_{\mathrm{im}}$ and using them to obtain the projected Bragg curve, we obtain a better result for the skewness. This procedure is applied to all nuclear recoil events to obtain a skewness distribution. Figure 5.3 shows the difference in skewness between the average skewness $S_{\pm x}$ in the $+x$ and $-x$ directed data as a function of energy, and indicates that the head-tail signature is measurable in our CCD detector down to $\sim$30 keVee ($\sim$ 60 keVr) at 100 Torr CF_4. All error bars are statistical and represent the standard errors of the means.

Because nuclear recoils resulting from scattered neutrons off of the lead shielding, detector, and surrounding material have not been taken into account, directional energy threshold could be better than what is suggested by Fig. 5.3. A full GEANT simulation is needed for a complete characterization of the backgrounds, but a simulation for the DRIFT detector suggested that about 30% of the nuclear recoils are due to scattered neutrons from a ^{252}Cf source [127]. Another effect that could affect the
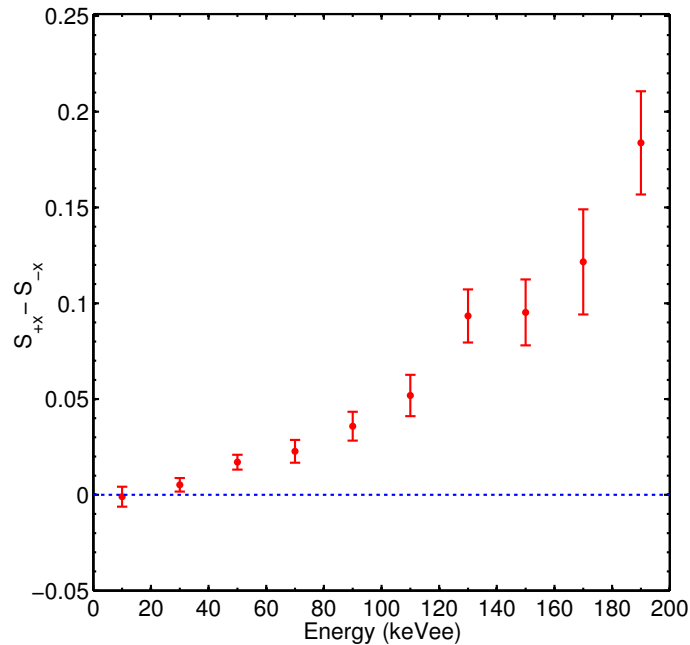
Figure 5.3: *Skewness difference between $+x$ and $-x$ directed runs in energy bins with a 20 keVee width for nuclear recoil events. $S_{\pm x}$ is the mean of the skewness distribution in a given energy bin for the $+x$ and $-x$ directions. The results indicate that even at 100 Torr, the head-tail signature exists down to a nuclear recoil energy of ~ 0 keVee (~ 60 keVr). The error bars represent the standard errors.*

head-tail measurement is gas gain and light quenching at high ionization densities. Chapter 6 contains a longer discussion of this issue, but given the smallness of the asymmetry even a few percent effect can drastically alter the results. Calibration, gain fluctuations, and readout noise will also play an important role in any skewness measurement.

In addition, there is much work to be done on the image analysis side. A more robust method for identifying tracks and determining their properties is needed, as the current approach is very sensitive to outlying pixels, which have the lowest signal-to-noise ratio of pixels within a given track. Moreover, the present method relies on the correct determination of the track orientation prior to calculating the skewness, a difficult task in the case of effectively round tracks that have ill-defined major axes.

5.1.3 Directional vs. discrimination thresholds

The results thus far show that our ability to separate electronic from nuclear recoils as discussed in Chapter 4 is much better than our directionality sensitivity. This is not a surprising finding since those two features are independent. The directional signature is solely dependent on the physics of nuclear recoil energy loss inside the target medium whereas discrimination depends on the difference in stopping powers between electronic and nuclear recoils. Given sufficient signal to noise, the energy at which we can discriminate between the two classes of events is dictated by the ability to resolve the track of the electronic recoil since they have lower dE/dx, but this energy will be lower than the energy at which we can resolve nuclear recoil track. As such it is not necessary that the discrimination energy threshold should coincide with the directional energy threshold even though there could be cases where they do match. Unless there is some detector limitation that causes the thresholds to overlap, directional dark matter detectors should be able to set two different limits, a directional limit and non-directional limit.

Consequently, it would be prudent for an experiment to push the discrimination threshold down to as low a level as possible regardless of where directionality disappears in that detector. Within the same detector, any potential dark matter signal would first appear as non-directional, and this would allow the experiment to anticipate when the directional signature will be seen and allow for the comparison of a non-directional result with a directional one from the same experiment without issues of systematics when comparing results between different experiments.

(a) AR ≤ 1.0 **(b)** AR ≤ 0.9

(c) AR ≤ 0.8 **(d)** AR ≤ 0.7
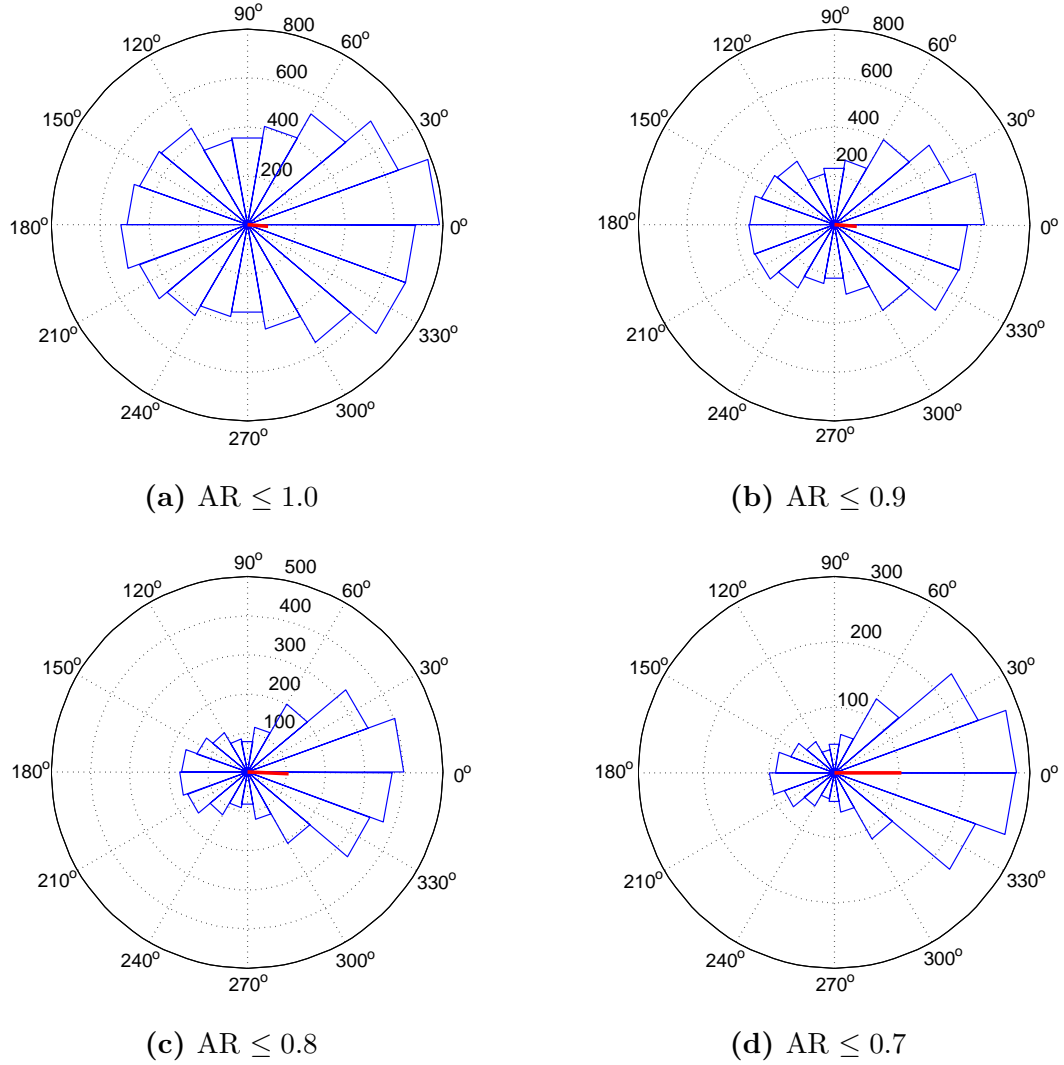
Figure 5.4: *(a)-(d) Circular histograms of reconstructed directions from events passing the nuclear recoil selection cuts and have axis ratio less than or equal to the specified value. The red line segment shows the mean resultant direction which agrees with the expected direction based upon the position of the neutron source.*

5.2 Rejecting isotropy for ^{252}Cf neutrons

5.2.1 No Quality Cuts

The number of events needed to detect a directional signal and reject isotropy in the ^{252}Cf data set is determined from combining the reconstructed orientation with the skewness measurement to define a vector direction for each event. The $-x$ directed neutron data are combined with the $+x$ directed data by a sign change in the skewness parameter of the $-x$ data set. This allows for the representation of a recoil direction as a point on the unit circle. A circular histogram of all the recoil directions generated using the CircStat toolbox [185] is shown in Fig. 5.4a. The red line segment represents the mean direction and resultant length of the recoil directions and shows agreement with the known average direction of the neutrons. We see in Fig. 5.4a that in addition to the primary, forward directed peak, there is a antipodal peak that is predominantly comprised of tracks with incorrectly assigned skewnesses and suggests that even when the reconstructed track orientation is close to the true orientation the probability of correctly determining the (sense)direction is low as is shown in Fig. 5.6a.

The minimum number of events, N, needed to reject isotropy is determined by using a bootstrap method that draws N samples from the data set, with replacement, 10^4 times. In each trial or experiment we perform the $V-$test for isotropy. This test is a modified Rayleigh test with the alternative hypothesis being that the data is not uniformly distributed around the circle, but has a mean direction, $\bar{\phi}_0$ which is given by the neutron average direction. We define the length of the mean vector of a sample of size, N, with angles, a_i, as

$$r = \sqrt{X^2 + Y^2} \tag{5.2.1}$$

with

$$X = \sum_{i=1}^{N} \frac{\cos a_i}{N}, \qquad Y = \sum_{i=1}^{N} \frac{\sin a_i}{N}. \tag{5.2.2}$$

The test statistic, V, is defined as

$$V = R\cos(\bar{\phi}_N - \bar{\phi}_0), \tag{5.2.3}$$

where $R = Nr$ and $\bar{\phi}_N$ is mean direction of the sample [186]. The significance of the test statistic is determined by comparing it with the critical value,

$$u = V\sqrt{\frac{2}{N}}. \tag{5.2.4}$$

Adopting the same method as found in [146], for each experiment we calculate the rejection factor, R_J, which is the probability of measuring a smaller value of the test statistic under the assumption that the null hypothesis is true. The acceptance factor, A_C, is defined as the fraction of the experiments in which the alternative hypothesis is true and reject the null hypothesis at confidence level, R_J. The number of events needed to reject isotropy at a given confidence level, $C.L.$, requires that $R_J = A_C = C.L.$

5.2.2 Axis Ratio Cut

To select out the more elongated and, hence, better reconstructed track orientations, a cut is made on the axis ratio (AR), defined as the ratio of minor axis to major axis of the track fitted ellipse. The distribution of events with different axis ratios are shown in Fig. 5.4b, Fig. 5.4c, and Fig. 5.4d. The backward directed peak remains but the ratio of the amplitudes of the two peaks is increasing with more events being correctly reconstructed in the forward direction as more elongated tracks are selected, implying that tracking, the axial reconstruction of the track orientation, is better than head-tail sensitivity.

This brings up the question of whether it is more important to push down the energy where head-tail is seen or improve upon the level of head-tail at a comparatively higher energy. One could argue that the two approaches are not independent as aiming for the former requires improving resolution (detector readout, gas diffusion) and

Table 5.1: *Top: $N_{90,no}$ and $N_{90,w}$ are the number of events needed to reject isotropy at 90% confidence level for different cuts on the axis ratio (AR) without and with weighting, respectively. The column labeled f_{60} is the fraction of events above 60 keVr with an axis ratio less than or equal to the axis ratio cut in the corresponding row. N_{90} is the number of events above 60 keVr needed to reject isotropy before applying the axis ratio cut and is obtained by dividing the numbers in the weighted column, $N_{90,w}$, by those in the f_{60}. Thus, it can be regarded as the exposure, in number of events, needed to reject isotropy above the 60 keVr threshold. Bottom: Same as top table but for 95% confidence level.*

Axis Ratio	$N_{90,no}$	$N_{90,w}$	f_{60}	N_{90}
1.0	100	57	1.00	57
0.9	79	44	0.87	51
0.8	47	29	0.63	46
0.7	26	17	0.42	41
0.6	16	12	0.27	44
0.5	10	8	0.16	50

Axis Ratio	$N_{95,no}$	$N_{95,w}$	f_{60}	N_{95}
1.0	131	73	1.00	73
0.9	104	61	0.87	70
0.8	60	38	0.63	60
0.7	35	24	0.42	57
0.6	21	15	0.27	56
0.5	13	10	0.16	63

operating at lower pressures to increase track length. But those same steps should also improve the head-tail measurement at higher energies. However, it is possible that at some energy, the intrinsic charge asymmetry is so small that it cannot be measured well and very little improvement in identifying a directional signature can be gained. Conversely, it is also possible that the asymmetry can be well measured at low energies but the recoil direction cannot because straggling lowers the probability of correctly identifying the axial direction of the track.

To enhance the directional signature it is prudent to remove diffusion limited tracks from the directional test because these tracks provide little to no directional information and act as a uniform background on top of the directional signature. As such, a cut is made on the axis ratio (AR) to select out more elongated tracks.

For each axis ratio cut value, the procedure outlined above to test for isotropy is performed on the subset of the data that passed the axis ratio cut. From the determined minimum number of events needed to reject isotropy in this subset, the number of events above 60 keVr, $N_{90(95)}$, that are needed before a cut is made on the axis ratio value to obtain that subset is calculated by dividing the number of events by the fraction of events with an AR less than equal to the cut value. In effect, we are determining the exposure above the 60 keVr threshold needed to reject isotropy in terms of the the number of events. The values of $N_{90(95)}$ that are needed to reject the null hypothesis of isotropy at confidence levels of 90% and 95% are given in Table 5.1.

5.2.3 Weighting events

The axis ratio cut is essentially a binary weighting scheme that does not fully utilize all of the available information, and a further improvement can be made by extending the weighting to a continuous scale. This is done through a redefinition of the modified Rayleigh test statistic to contain a weight for each input direction [187]. For N vectors, the mean X and Y are redefined as

$$X = \sum_{w=1}^{N} w \cos a_w, \qquad Y = \sum_{w=1}^{N} w \sin a_w, \tag{5.2.5}$$

where $w = 1, \ldots, N$ is the rank of the vector. The vector with the lowest weight has rank 1 while the next lowest has rank 2 and so on. The weighting parameter, $\rho \equiv (1 - AR) \times |s|$, is found to give better results than parameters such as the energy, track length, magnitude of the skewness, or a combination of those. The choice of the weighting parameter is not too restrictive, so other parameters could potential provide better results than the one used here.

The weighted resultant vector length and resultant direction are defined as

$$R^2 = X^2 + Y^2, \qquad \bar{\phi}_N = \arctan\left(\frac{Y}{X}\right) \tag{5.2.6}$$

while the test statistic is defined as

$$Z_w = \sqrt{\frac{2}{N}} R \cos{(\bar{\phi}_N - \bar{\phi}_0)} \qquad (5.2.7)$$

and is calculated via Monte Carlo simulations under the null hypothesis of isotropy. An axis ratio cut of 0.67 with vector weighting is found to minimize the number of events above 60 keVr needed to reject isotropy. The exposure, in terms of the number of events, needed at 90(95)% C.L. are 41(54). The number is derived by taking the 18(20) events remaining after apply the axis ratio cut at 0.67 and dividing it by the fraction of events above 60 keVr passing this cut. Using the weighted mean angle of the 18(20) events passing the cut and above 60 keVr, we calculate that the half-angle of the confidence cone for pointing back to the source direction is 34(35)°. Using the 41(54) events give poorer pointing directions.

There could be a question as to why we choose to quote the minimum numbers in the column labeled $N_{90(95)}$ [41(54)] rather than those in $N_{90(95),w}$ [18(20)]. The reason being that in order to get the 18 quality events at 90% C.L. with an AR cut of 0.67 for input into the directional test, 41 events are needed before applying this particular cut. To put it another way, the detector exposure needed to reject isotropy at a threshold of 60 keVr is the exposure needed to obtain 41 events and not the 18 events. Moreover, if the events were due to WIMP interactions, than it is clear that even those events that did not pass the AR cut will still provide important information about the nature of the WIMP from their energy distribution and therefore should not be disregarded entirely.

5.2.4 Slice cut

The axis ratio, however, is be the best parameter to use because it is highly correlated with the recoil energy. For a ^{252}Cf recoil spectrum, Fig. 5.5 shows that when a cut is made to remove events with AR ≥ 0.7 to test for directionality, essentially all of the events below 100 keVr are removed. This is problematic when applied to a WIMP
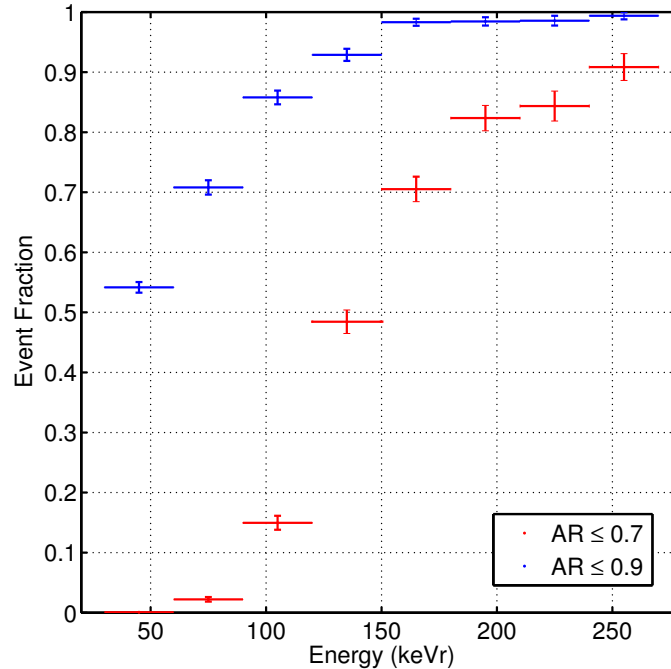
Figure 5.5: *The fraction of events with an axis ratio of less than or equal to 0.7 and 0.9.*

induced recoil spectrum, which for certain WIMP and target mass combinations, may have few, if any, events at energies above 100 keVr. Consequently, cuts made with the axis ratio parameter is not optimal.

A non-energy correlated track quality cut parameter can be constructed by dividing the nuclear recoil band in the range and energy parameter plane into slices of equal range widths (not number of events) and only select recoils in the top slices which have longer ranges and better measured skewnesses. The improved directionality for events in the top of the recoil band can be seen when comparing Figs. 5.6b, 5.6c, and 5.6d which shows how the head-tail signature as quantified by the fraction of events in the forward/backward directions change for the different slices.

By replacing the axis ratio cut with the range slice cut, we find that the exposure, in terms of the number of events, needed to reject isotropy at 90(95)% C.L. is 45(73) (compared with 41(54) using the axis ratio cut with weighting scheme) using the

(a) All events

(b) Top third

(c) Middle third

(d) Bottom third
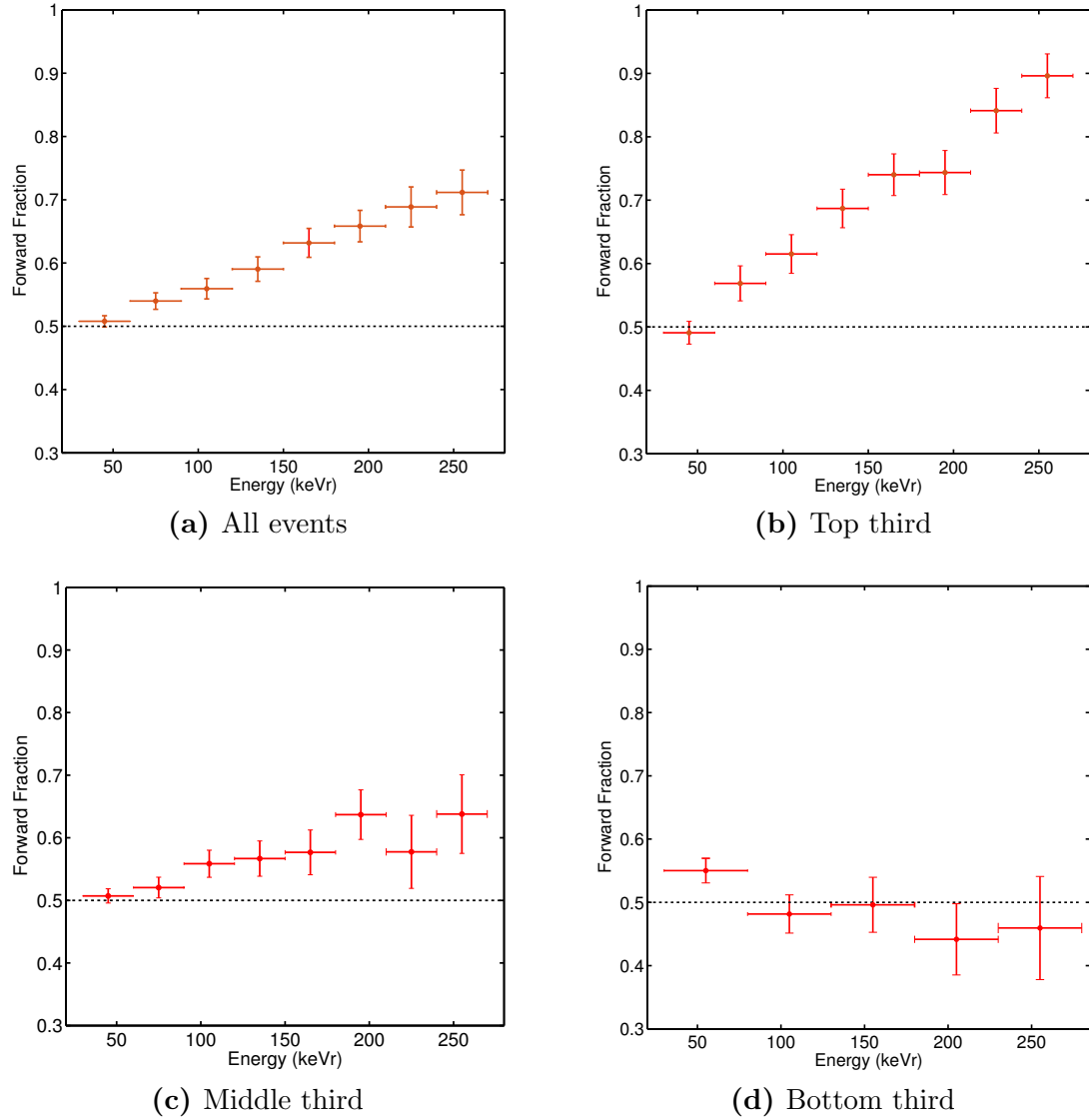
Figure 5.6: *The fraction of events with the correct sense, defined as the ratio of the number of events in the forward half circle to the total number of events for different slices in the range vs. energy plot.*

same weighted modified Rayleigh test. The optimal slice cut corresponds to selecting events in the top half of the band which contains about 45% of the events. It is important to note that there is a bias with this cut since it favors carbon recoils which have longer ranges than fluorine recoils of the same energy, but since the ratio of carbon to fluorine recoils is about 1:6, even assuming that all of the carbon recoils are in the top half, the band will still be dominated by fluorine recoils. In fact, there is a slight bias even when no cuts are applied because we are not able to separate carbons from fluorines and so have to treat all recoils as fluorines.

The purpose of this cut is to demonstrate that selecting tracks that are less straggled and/or have larger projections onto the detection plane will improve the directional signature as showed in Figs. 5.6b, 5.6c, and 5.6d. In addition, our aim is to find a parameter that is not highly correlated with the energy and is more suitable when applied to a WIMP recoil spectrum.

Of course, other cuts and weighing schemes can also be considered. Nevertheless, even our relatively straight forward and simple cut and weighing parameters provide a significant improvement. If no track quality selection cuts and weighing are used, then 100(131) events are needed to reject isotropy at 90(95)% C.L. above a 60 keVr threshold using the modified Rayleigh test. Therefore, the combination of track quality cuts and event weighting provide over a factor of two reduction in the number of events.

It is important to emphasize that the numbers in Table 5.1 are for a recoil spectrum from a fixed position ^{252}Cf neutron source aligned in the optimal plane of a 2D detector. In general, the number needed to reject isotropy for a WIMP spectrum will depend on the WIMP and target masses, Galactic halo model, and 2D or 3D readout. Also, we have not taken into account the nuclear recoil detection efficiency of the detector after nuclear recoil selection cuts are made to discriminate against electron recoils. That, however, should not significantly change the results given that the discrimination threshold is ∼25 keVr while the directional threshold is ∼60

keVr. But in general, the number of nuclear recoil detections that are needed before applying analysis cuts in order to claim the existence of a directional signature is higher in a realistic detection scenario and highlights the need for a robust method to discriminate against backgrounds and retain maximum detector sensitivity.

Finally, we remark that while the number of events needed to reject isotropy are often stated in literature on directional dark matter detection, it can be easily misinterpreted. What should be minimized in a directional dark matter search is not the number of events needed to detect an anisotropic signal but rather the detector exposure, a product of the detector fiducial mass and live-time. That is because the number of events needed to reject isotropy can be lowered by increasing the energy threshold because the higher energy events are more anisotropic and also better reconstructed from the experimental point of view (e.g. an AR cut of 0.5). However, since the WIMP recoil spectrum is exponentially falling, high energy events are rarely detected and do not exist above a certain energy cut-off which depends on the Galactic escape velocity or halo model and the WIMP and target masses.

5.3   Rejecting isotropy from a WIMP spectrum

To determine the number of events from a WIMP recoil spectrum needed to reject isotropy, we use the CCD detector angular resolution and the probability of correctly identifying head-tail. Only the 3D detection scenario will be considered so that the detector orientation and time-dependent coordinate transformation from lab to Galactic coordinates can be ignored. In essence, we imagine a 3D detector with the same diffusion and resolution in each of the dimensions as well as the same signal-to-noise as our CCD detector. This is a reasonable extrapolation because the resolution and head-tail measurements should only be better in the 3D case. For a discussion on the differences between 2D and 3D readout in regards to WIMP detection, see Refs. [145, 146].
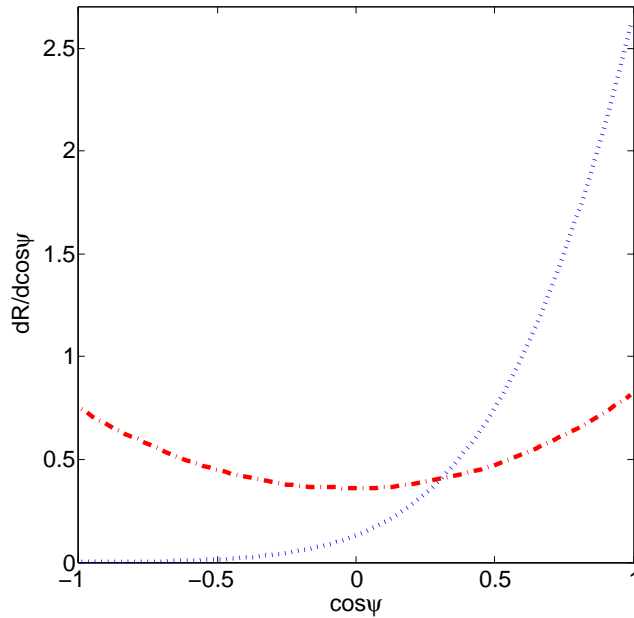
Figure 5.7: *The normalized angular spectra for a 100 GeV WIMP scattering off fluorine with a 40 keVr energy threshold. The dotted(blue) curve represents the intrinsic angular spectrum for the standard halo model WIMP induced nuclear recoils without detector reconstruction properties included. The dot-dash(red) curve is the angular spectrum after the detector resolution and probability for head-tail determination are included.*

WIMP induced fluorine recoils are generated with an energy and recoil direction using the derivation of the WIMP induced nuclear recoil spectrum from [66] and the angular spectrum from [66, 85]. The standard spherical halo model with a Maxwellian velocity distribution is assumed, with the corresponding dark matter density, $\rho_D = 0.3$ GeVc^{-2}cm^{-3}, local Galactic escape velocity, $v_{esc} = 600$ kms^{-1}, and solar velocity around the center of the Galaxy, $v_0 = 230$ kms^{-1} [66]. The WIMP events are binned in energy and then smeared with the Fisher distribution in 3D using the concentration parameter/smearing width that was determined to give the best match of the smeared simulated angular distribution to the measured angular distribution in that energy bin (Sec. 5.1.1). A sense is assigned to each event using the probability for correctly determining head-tail from the data of all events. We

find that the improved head-tail probability using the top slice (Fig. 5.6b) does not significantly change the results. The WIMP angular spectrum before and after applying detector reconstruction properties for a 100 GeV WIMP scattering off a fluorine target is shown in Fig. 5.7.

The same procedure as outlined in Appendix C of [146] is used. N samples from the WIMP recoil spectrum are drawn, and for each N, 10^4 experiments are conducted. In each experiment, a test statistic for the directional test is calculated for the N samples. The set of experiments at each N gives the probability distribution, $p_A(T; N)$, of the test statistic. The probability distribution for the null hypothesis of isotropy, $p_0(T; N)$, is calculated with Monte Carlo simulations. A comparison of the two distributions allows us to determine the number of events needed to reject isotropy at 90(95)% C.L.

There are two classes of directional tests that can be considered, axial and vector. The axial tests do not make use of the head-tail information and are only sensitive to the detector angular resolution and intrinsic angular spectrum of the recoils whereas the vector tests will also include the head-tail information. The axial tests considered are the modified Bingham test($\mathcal{B}$) [188, 181], the Giné test ($\mathcal{G}$) [189], and the axial cosine test [190]. In addition, a likelihood ratio test ($\mathcal{L}$) is also conducted with the null hypothesis, H_0, for isotropy, and H_A being the alternative hypothesis which has as its spectrum the WIMP angular spectrum for the standard halo model convolved with detector angular resolution and probability for correct head-tail determination and is shown as the dot-dash (red) curve in Fig. 5.7. From this figure, it is apparent that the forward/backward asymmetry is very small and a subsequent application of the directional tests will show that the fraction of the time in which the sense of the recoil can be correctly determined is not sufficient to provide an improvement over the axial case.

The number of events needed to reject isotropy for a 40 keVr threshold and fluorine target at 90 and 95% C.L. for the tests considered are shown in Table 5.2 for
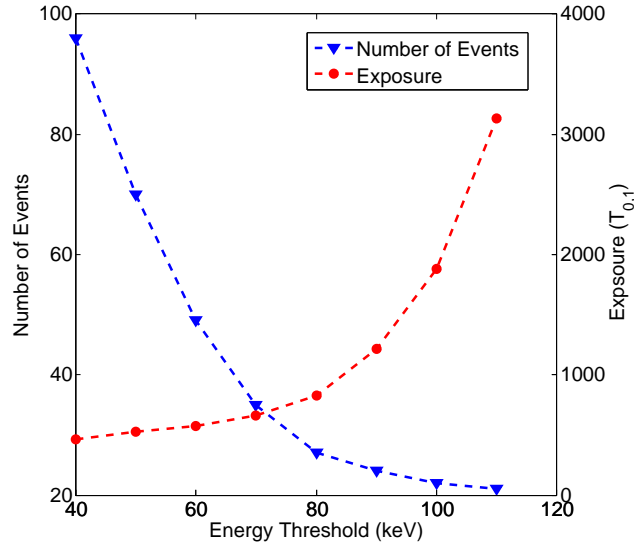
Figure 5.8: *Number of events and exposure needed to reject isotropy at 90% C.L. as a function of the energy threshold. This shows that even though the number of events decreases with increasing energy threshold, the exposure needed to rule out isotropy increases. As such, the number of events is not the important quantity to look at.*

several different WIMP masses. However, the more meaningful quantity to consider is the detector exposure needed for isotropy rejection and is shown in the last column of Table 5.2. To demonstrate why exposure is the more pertinent quantity to look at, the behavior of the number of events and exposure with energy threshold is plotted in Fig.5.8. One of the interesting feature in Fig.5.8 is that the change in exposure is relatively flat between 40 keVr and 70 keVr such that reducing the energy threshold from 70 keVr to 40 keVr only lowers the exposure by about 30%. Going from 40 keVr to 70 keVr, the improvement in detector angular resolution offsets the reduction in the total rate with increasing energy threshold. But above 70 keVr, the resolution improvement can no longer counterbalance the exponentially falling energy spectrum, causing the exposure to rise rapidly.

To calculate the exposure numbers, the minimum number of events in each row of Table 5.2 is divided by the fraction, $f(E)$, of the total rate above the energy

Table 5.2: *Number of events, $N_{90(95)}$, and exposure, $T_{90(95)}$, needed to reject isotropy at 90(95)% C.L. for the directional tests considered at different WIMP masses, M_χ [GeV] for a 40 keVr threshold. The exposure has units $[T_{0,1}]$, defined as the exposure needed at zero energy threshold to detect one event.*

			N_{90}		
M_χ/GeV	$\langle|\cos\theta|\rangle_w$	$\mathcal{B}$	$\mathcal{G}$	$\mathcal{L}$	$T_{90}/T_{0,1}$
30	87	173	177	85	2092.1
100	96	221	224	102	461.8
1000	95	242	244	113	305.9
			N_{95}		
M_χ/GeV	$\langle|\cos\theta|\rangle_w$	$\mathcal{B}$	$\mathcal{G}$	$\mathcal{L}$	$T_{95}/T_{0,1}$
30	140	249	253	139	3379.6
100	159	316	318	174	764.8
1000	156	344	351	183	502.3

threshold, E, to give the relative exposure,

$$T_{\text{rel, }90(95)}(E) = \frac{N_{90(95)}(E)}{f(E)}, \tag{5.3.1}$$

where, $f(0) = 1$ and $f(E_{\max}) = 0$ with $E_{\max}$ being the maximum possible recoil energy. The absolute exposure needed to reject isotropy has units, $T_{0,1}$, where

$$T_{0,1} = \frac{1}{R_0}, \tag{5.3.2}$$

and R_0 is the total event rate at zero energy threshold with units of events per kg-year. Therefore, $T_{0,1}$ is defined as the exposure needed to observe one event at zero threshold, and in this way, no assumptions are needed to be made regarding the WIMP-nucleon cross-section as the fraction of total rate above a chosen threshold does not scale with cross-section for a particular WIMP and target mass.

For a better perspective on the detector size needed for a directional dark matter search, consider the case in which the WIMP mass is 100 GeV and the WIMP-proton spin-independent cross-section is $\sigma_{\chi p}^{\text{SI}} = 10^{-46}$ cm^2, slightly below the current best direct detection limits in this parameter space [76]. In this case, $T_{0,1}$ is approximately 1087 kg-year (rate of 9.2×10^{-4} events per kg-year at zero threshold) for scattering off

fluorine, so that the absolute exposure needed to reject isotropy at 90% C.L. and 40 keVr threshold is $T_{90} \times T_{0,1} \simeq 5.0 \times 10^5$ kg-year. This poses a considerable challenge for directional experiments using low pressure TPCs as the detector technology. With a CF_4 specific volume of 0.27 $m^3 kg^{-1}$ at NTP (normal temperature and pressure), a 5.0×10^5 kg detector operating at a pressure of 100 Torr would be on the order of 10^6 m^3.

Now consider the spin-dependent case with a cross-section of $\sigma_{\chi p}^{SD} = 10^{-40}$ cm^2, a value close to the current best spin-dependent limit [77, 78]. In this situation, $T_{0,1}$ is approximately 0.5 kg-year (rate of 2 events per kg-year at zero threshold). Here, the absolute exposure needed to reject isotropy at 90% C.L. and 40 keVr threshold is $T_{90} \times T_{0,1} \simeq 231$ kg-year. CF_4 has a fluorine mass fraction of 0.886, so a detector with 261 kg of CF_4 mass (231 kg of fluorine mass) operating at a pressure of 100 Torr would be on the order of 536 m^3.

Whether considering the spin-independent or spin-dependent case, the limitation on the drift length of tracking TPCs imposed by diffusion poses a considerable challenge to scaling detectors to sizes needed to detect a directional signature. To circumvent this limitation, a large readout area in the lateral dimensions is required, but such a readout is one of the primary drivers of detector cost and complexity. We address these issues in more detail in Chapters 7 and 8.

5.4 Directional detector optimization

The requirement for large detection volumes cannot be circumvented by simply increasing the target gas density for several reasons. One being that even though the event rate scales with the target density, the pressure cannot be chosen too high because the low energy tracks that are of interest in directional dark matter searches will not be resolvable and both discrimination and directionality suffer. On the other hand, the pressure cannot be set too low as the event rate would be degraded from
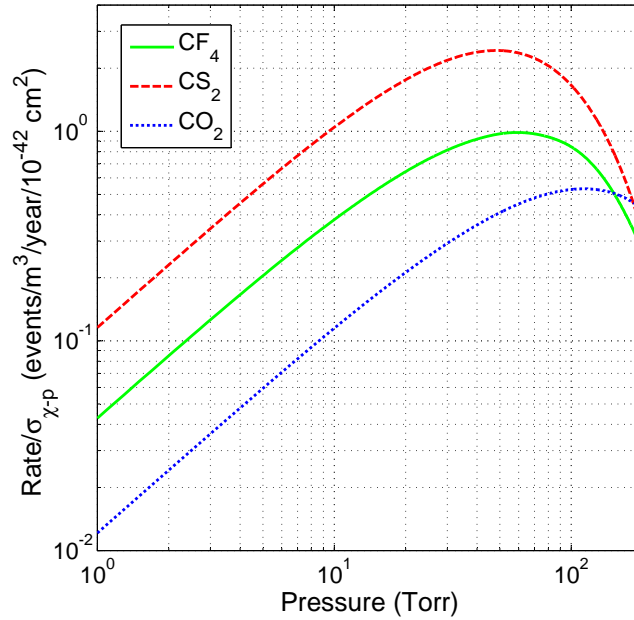
Figure 5.9: *The expected rate as a function of pressure in several different gases for a 100 GeV WIMP. The directional track range is taken to be 0.4 mm.*

a scarcity of target material and the large detection volume problem would be exacerbated. Consequently, the proper choice of operating pressure is a very important factor to consider.

For the CCD detector, results from the neutron data can be used to find its optimal pressure, with the two relevant quantities to consider being the energy thresholds for axial and vector(head-tail) directionality of 40 keVr and 60 keVr, respectively. For CF_4 at 100 Torr, fluorine recoils of those energies have average track lengths of 0.4 mm and 0.6 mm, respectively. But as shown with the WIMP simulations in the preceding sections, the head-tail effect is not sufficiently strong enough to provide a significant improvement over axial case in terms of reducing the number of events/exposure needed to reject isotropy. As such, we will use 0.4 mm as the directional range for the CCD detector.

Taking 0.4 mm as the directional range, we conduct SRIM simulations at differ-

ent pressures for each gas mixture to find the recoil energy that gives an average track length of 0.4 mm and define the directional energy threshold as the energy corresponding to the directional range at the given pressure. For a chosen directional range, the pressure sets the energy threshold, which determines the total directional rate. The simulations are done for the spin-independent case and uses the same halo parameters as those in Sec. 5.3. The total directional rate above threshold as a function of pressure for three different gases with the WIMP mass taken to be 100 GeV is shown in Fig. 5.9. For a similar but more detailed analysis using a different approach, see Ref. [191]. The pressure corresponding to the peak rate in Fig. 5.9 is defined as the optimal pressure, but note that spin-independent rate is expressed relative to a cross-section of 10^{-42} cm^2. This cross-section is arbitrarily chosen and does not affect the results because what truly matters is the shape of the curves in Fig. 5.9 and the locations corresponding to the maximal rate. These do not depend on the value of the cross-section.

Figure 5.10 shows how the optimal pressure varies with the WIMP mass, and as expected the pressure/energy threshold decreases with WIMP mass due to a softening energy spectrum. For a 100 GeV WIMP, the optimal pressure for a CF$_4$ target is approximately 60 Torr, assuming a directional threshold of 0.4 mm. Although that pressure is not too far away from the 100 Torr in which the neutron data were acquired, any reduction in pressure makes detector operation more challenging as the change in pressure is in the direction of increasing instability from gas breakdown, often characterized by the Pachen curve, which is a relationship between breakdown voltage as a function of the reduced electric field (E/p), for the particular gas.

The situation for a 10 GeV WIMP is even more challenging as the optimal operating pressure is approximately 10 Torr for CF$_4$. However, Refs. [142, 143] have demonstrated low pressure operation of thick GEMs in Ar/CO$_2$ and Isobutane gas mixtures down to about 1 Torr while achieving stable operation at high gas gains. Though it is not necessary to operate at the optimal pressure, any chosen pressure
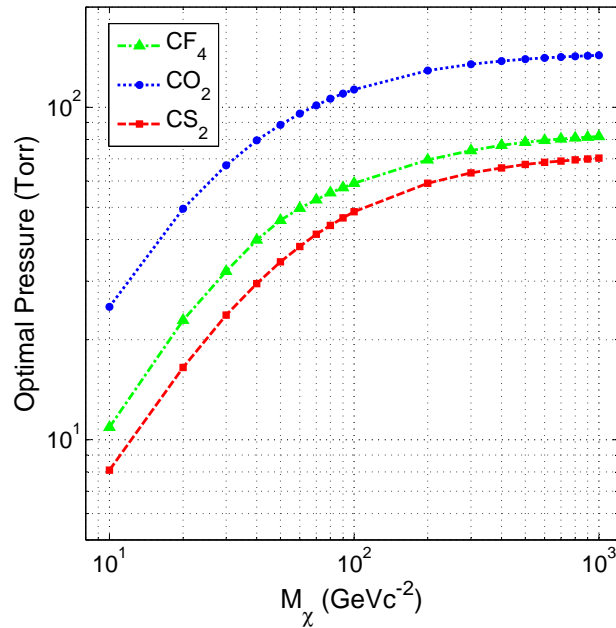
Figure 5.10: *The optimal pressure as a function of WIMP mass for three different gases.*

that is too far away from the optimal will result in a substantial reduction in the total directional rate.

In addition, the choice of target gas is more constraining than in the 10 GeV case because of the low optimal operating pressure. Electronegative gases such as CS_2 may be unsuitable for low mass WIMP detection because they cannot be operated at an arbitrarily low pressure as electron drift gases can be because the capturing of the primary electrons to form negative ions depends on the density of the gas. As the density is lowered, the mean capture length is increased, and at extremely low pressures will exceed the recoil track length and degrade resolution in the drift direction. Still, it remains to be seen how low CS_2 and other electronegative gases can be operated at while still maintaining good resolution in the drift direction. This is discussed further in Chapter 7.

But under the assumption that optimal pressure operation is possible, the ap-

proximate detector size needed to reject isotropy for different WIMP masses can be determined from Fig. 5.11. As shown earlier, 96 events are needed to reject isotropy at 90% C.L. for a 40 keVr (0.4 mm) threshold. For a 100 GeV WIMP, the optimal pressure for CF_4 is 60 Torr and the detector size needed to detect the required number of events in one year is $\sim$370 m^3 (10^{-42} cm^2)$/\sigma_{\chi-p}$, where $\sigma_{\chi-p}$ is the WIMP-proton spin-independent cross-section. If the directional threshold is 0.2 mm, the corresponding optimal pressure is 120 Torr. This means that the detector volume needed to reject isotropy is reduced by a factor of two to $\sim$165 m^3 (10^{-42} cm^2)$/\sigma_{\chi-p}$. Finally, for a 0.8 mm directional threshold, the detector volume is increased by a factor of two.

It is important to note that the picture presented here is rather simplistic. We are treating the rate above the 40 keVr threshold equally, which is to say that events are being given equal weights regardless of their energies. In addition, events are also treated equally regardless of where they originate in the detector. For a real detector, this of course cannot be true as events further from the readout will suffer higher diffusion and have worse resolution. Nevertheless, the optimization procedure presented in this Section can be easily extended to account for the aforementioned issues. The goal of this optimization is to provide a conceptual framework for how directional detectors should be optimized.

5.5   Conclusion

We have shown what is achievable with a high signal-to-noise and high resolution CCD detector operated at 100 Torr, which is a relatively pressure when compared to typical directional experiments. Excellent background discrimination down to $\sim$25 keVr, axial directionality down to $\sim$40 keVr, and vector directionality down to $\sim$60 keVr were demonstrated. For a *vector* directional energy threshold of 60 keVr, 41 events were needed to reject isotropy at 90% C.L. from a ^{252}Cf neutron source
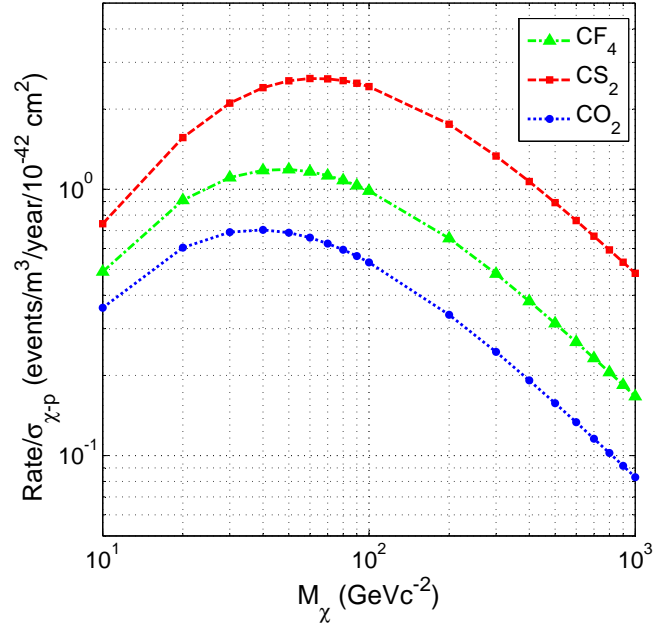
Figure 5.11: *The total directional rate at the optimal pressure for a directional range of 0.4 mm as a function of WIMP mass for several different gases.*

with using a combination of event weighting and quality cuts. When considering the case of a 100 GeV WIMP induced recoil spectrum, the probability for correctly determining head-tail was not sufficient to provide a significant improvement over the axial data. At the *axial* directional threshold of 40 keVr, 96 events were needed to reject isotropy at 90% C.L. With this directional threshold, we showed that the optimal pressure for a CF_4 detector is 60 Torr.
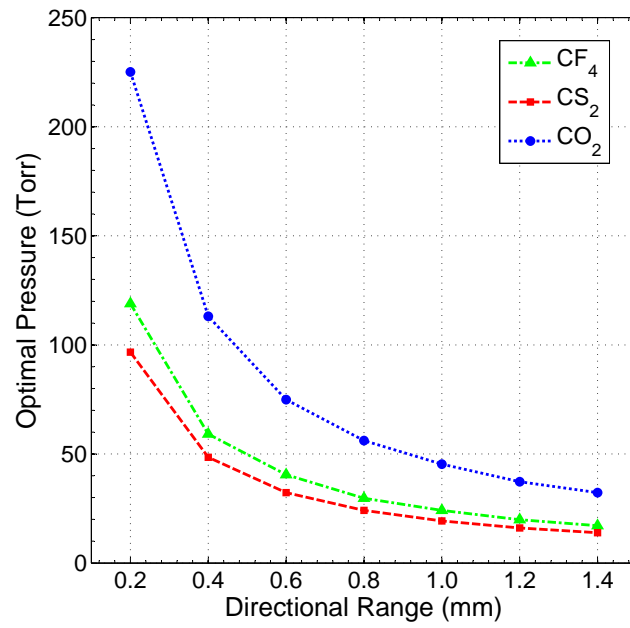
Figure 5.12: *The dependence of the optimal pressure on the directional range for a 100 GeV WIMP. A smaller directional range allows for operation at much higher pressures.*

Chapter 6

Electron Recoil Imaging with the CCD Detector

6.1 Introduction

In Chapter 4, we showed that signal-to-noise is a critical detector parameter for discrimination. For low-mass WIMP directional detection, the results of the optimization study in Chapter 5 suggest that very low-pressure operation is needed. In this chapter, we present the capability of a high-resolution and high signal-to-noise CCD detector capable of imaging low-energy recoils over broad range of pressures. We show that with sufficient gas gain and light collection efficiency, the tracks produced by 5.9 keV ^{55}Fe X-rays can be imaged optically by a low-noise, high quantum efficiency CCD camera. This is to our knowledge the first time that an ^{55}Fe spectrum has been acquired with an optical *imaging* device.

To accomplish this, we used a low-pressure TPC operated over a range of 35-100 Torr in CF_4 with GEM/thick GEM (THGEM) amplification and CCD camera readout. GEMs are a micro-pattern amplification device invented by F. Sauli at the European Organization for Nuclear Research (CERN) [155], and further information on the operation of GEMs with CCD readout can be found in Refs. [150, 151, 152].

THGEMs are very similar to GEMs but with dimensions (thickness, hole size, and pitch) that are typically about one order of magnitude larger, and exceptionally high gas gains have been achieved in both types of amplification devices over a wide range of pressures [142, 143].

The operating principle of our detector is as follows: A particle creates an ionization track in the detection volume. The ionization drift towards the GEM/THGEM amplification device due to an electric field between the cathode and opposing GEM/THGEM surface. Upon arriving at the amplification device, the ionization is channeled into the GEM/THGEM holes where a strong dipole electric field is established through a potential difference between the top and bottom surfaces of device. Once inside this strong field region, electrons are multiplied by collisional avalanche, a process that also creates scintillation light in some gases such as CF_4. In a multi-GEM/THGEM arrangement, the ionization then drifts onto the next GEM/THGEM stage and is amplified once more until it arrives at the last stage. Once there, the charges are amplified for the last time, and the scintillation light is imaged by a low-noise CCD camera and a fast lens setup looking down on the surface of the final amplification stage.

6.2   Detector setup

The detector setup and amplification device is shown in Figure 6.1 and is very similar to the setup used to make in the measurements described in Chapter 4. At each pressure, the choice of amplification device (single GEM/THGEM or multiple GEM/THGEM) is made to maximize stability, gas gain, and spatial resolution. For the 100 Torr measurement, the detector consists of three standard copper GEMs (Gaseous Electron Multipliers) arranged in a cascade with 2 mm separation between them (Figure 6.1). The GEMs are manufactured at CERN and consist of a 50 µm thick sheet of kapton with an area of 7×7 cm^2. The sheet is cladded with copper on
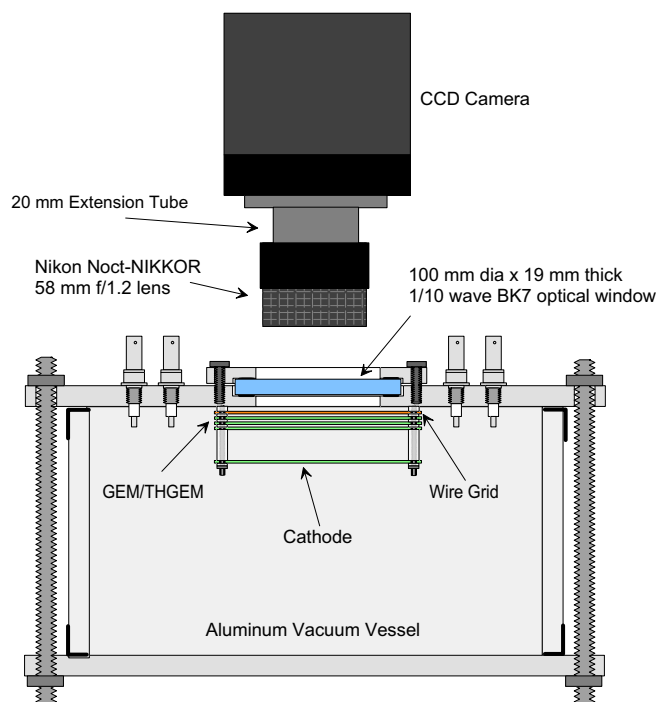
(a) Detector Vessel
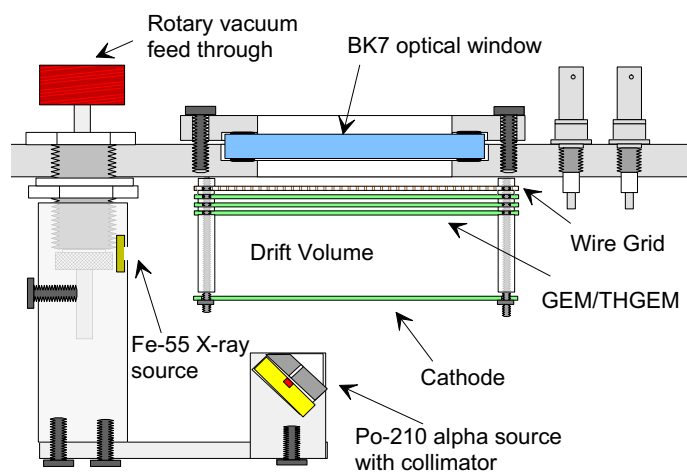
(b) Detection Volume

Figure 6.1: *(a) A simplified drawing of the CCD detector showing the aluminum vacuum vessel and CCD camera setup, excluding the rotary feed-through, camera mount, and calibration sources for clarity. The light shielding box is also excluded to show the lens and extension tube. (b) A close up view of the detection volume, showing the locations of the calibration sources, cathode, wire grid, and GEMs/THGEMs.*

both surfaces and mounted on G10 frames. The GEM surface is chemically etched with a hexagonal array of bi-conical holes of diameter of 50/70 µm (inner/outer) and at a pitch of 140 µm. For a thorough review of GEMs, see Ref. [156]. Below the GEMs sits a 7×7 cm^2, ~ 360 µm thick copper cathode mesh with ~ 500 µm pitch. Together the surface of the cathode and the nearest GEM surface form a 1 cm detection volume (drift volume). Finally, situated 3 mm above the top most GEM (GEM 3) is a 1 mm pitch anode wire grid plane made from 20 µm thick gold plated tungsten wires, forming the induction gap.

At 50 Torr, the standard CERN GEMs are replaced by a single copper coated thick GEM (THGEM). We observe that GEMs appear unsuited for high gain operation in lower pressure. For instance in 75 Torr, the maximum stable gas gain is insufficient for imaging ^{55}Fe tracks. The THGEM is made from a 0.4 mm thick PCB with ~ 0.3 mm holes mechanically drilled over a 3×3 cm^2 copper coated area. The holes have a pitch of 0.5 mm, and due to the lower pressure of operation and the longer ranges of tracks, the drift gap is increased from 1 cm to 2 cm. In addition, the separation from the amplification device and the wire grid is increased from 3 mm to ~ 7 mm.

In the 35 Torr measurements, two THGEMs with a 9.5×9.5 cm^2 active area (avalanche area) are used for the amplification stage. These THGEMs have the same hole size, thickness, and pitch as the one used in the 50 Torr measurements. The drift gap, transfer gap between the THGEMs, and induction gap between the THGEM and wire grid are 2 cm, 4 mm, and 9.5 mm, respectively. In addition, the wire grid size is increased to match the THGEM area by laying copper tape around the perimeter of the wire frame.

For all pressure measurements, the detector is housed inside a ~ 10 liter cylindrical aluminum vacuum vessel. Calibration is done using internally mounted ^{55}Fe (5.9 keV X-rays) and ^{210}Po (5.3 MeV alphas) sources, which could be individually turned on or off using a rotary feed-through (Figure 6.1b). Prior to powering up the

GEMs/THGEMs, the vacuum vessel is pumped out to < 0.1 Torr for at least one day before back-filling with pure (99.999%) carbon tetrafluoride (CF_4) gas. A 4-inch diameter BK-7 glass window positioned above the wire grid to allowed scintillation light from the final amplification stage to be captured by the lens and CCD camera.

The optical system consisted of a fast 58 mm f/1.2 Nikon Noct-NIKKOR lens mated to a back-illuminated Finger Lakes Instrumentation (FLI) CCD camera (MicroLine ML4710-1-MB) through a 20 mm extension tube for close-focusing imaging. The whole setup is mounted on top of the vacuum vessel (Figure 6.1a) in a light tight box. The camera contained an E2V made 18.8 mm diagonal sensor with a 1024×1024 pixel array (CCD47-10-1-353), each pixel with a size of 13×13 μm^2. The mid-band coated CCD sensor has a peak quantum efficiency of 96% at 560 nm and could be cooled down to a stable operating temperature of $-38°$C using the built-in Peltier cooler. Two readout speeds are available, 700 kHz and 2 MHz, with 16-bit digitization and maximum 16×16 on-chip pixel binning. At the lowest operating temperature and slowest readout mode, the read-out noise is ~ 10 e$^-$ rms and the dark current was ~ 0.03 e^-/pix/sec at 1×1 on-chip pixel binning. At our focusing distance, the CCD-lens system imaged $\sim 3 \times 3$ cm^2 region of the GEM/THGEM surface. The known pitch of the holes on this surface is used to calibrate the length-scale of the images.

6.3   Detector Calibrations

6.3.1   GEM/THGEM Gain

The gas gain was determined using an ORTEC 448 research pulse generator and an ORTEC 142IH charge sensitive preamplifier, which read out the charge signal from the last GEM/THGEM surface rather than the wire grid. The pulse generator output was connected to the test input of the preamplifier, which uses a built-in 1 pF capacitor for calibration purposes. This allowed the preamplifier gain (fC/V) to be

determined. The ^{55}Fe 5.9 keV X-ray calibration source was then used to determine the effective gas gain from the output voltage signal of the preamplifier. The X-ray source created on average 172 electron-ion pairs per conversion event, which was calculated from the W-value (the average energy per ionization) of 34.2 eV for CF_4 [159].

For each pressure the maximum stable gain was determined iteratively by raising the GEM/THGEM voltages and testing for stability. The latter was done by firing a highly ionizing source (^{210}Po alpha source) into the detection volume. If no sparks occur over several hours, then the voltage setting was deemed stable and the procedure repeated until the maximum stable gain was found.

At a pressure of 100 Torr, a maximum stable effective gain of $\sim 1 \times 10^5$ was achieved with GEM 1 = 279 V, GEM 2 = 334 V, and GEM 3 = 380 V, and a drift field of 400 V/cm. With these GEM voltages the transfer fields were 1.40 kV/cm and 1.67 kV/cm between GEMs 1 and 2, and 2 and 3, respectively, and an induction field of 260 V/cm between GEM 3 and the grid. A higher effective gas gain of $\sim 2 \times 10^5$ was achieved with GEMs 1 and 2 = 290 V and GEM 3 = 450 V, where the drift, transfer, and induction fields were 400 V/cm, 1.45 kV/cm, and 360 V/cm, respectively. This setting, however, was not entirely stable under alpha irradiation, which initiated a spark about once per hour. Nevertheless, we were able to acquire ^{55}Fe images and an energy spectrum without any sparks at this setting.

For the 50 Torr measurements, the THGEM was powered to a voltage of 830 V and the drift field was set to 200 V/cm in order to maintain the same reduced field as in the 100 Torr measurements. The induction field was 824 V/cm with the wire grid at a lower voltage than the top THGEM surface so that all electrons produced in the avalanche were collected by this electrode. The electrical stability at this voltage setting was similar to the highest gain setting at 100 Torr in that both were moderately but not completely stable. For this measurement, we estimate the gain to be $\sim 1.5 \times 10^5$.

Finally, in the 35 Torr measurements, the THGEM voltage biases were THGEM 1 = 573 V and THGEM 2 = 470 V, where THGEM 1 is the one facing the cathode and THGEM 2 is nearest to the wire grid. The drift, transfer, and induction fields were 200 V/cm, 718 V/cm, and 495 V/cm, respectively. Here, the gas gain is estimated at $\sim 1.6 \times 10^5$.

6.3.2 CCD Calibration

The CCD images (or frames) were calibrated using a set of co-averaged flat-field and dark frames. Dark frames, taken with the same exposure time as the image frame but with the camera shutter closed, were used to correct for the variable accumulation rate of dark current across the pixels in the CCD sensor. Flat-field frames are used to correct for vignetting and pixel to pixel variation in light sensitivity, and were acquired by taking exposures of a uniformly illuminated screen.

For each type of calibration frame, a set of such frames were co-averaged together to create a master calibration frame. The averaging was done with an algorithm that rejected cosmic rays and radioactivity hit pixels by comparing the value of the same pixel across the set of frames, and excluding those above three sigmas of the initial average of the pixels. The average was re-computed and the process repeated until there was a convergence in the average value of the pixels. Finally, the calibration of a data image was done by subtracting the master dark frame from each image frame and dividing the resulting frame by the normalized, master flat-field frame.

6.4 Results

6.4.1 100 Torr

A sample image containing ^{55}Fe tracks taken at the maximum stable gain setting in 100 Torr CF$_4$ is shown in Figure 6.2a. On chip binning of 6×6 was used for this
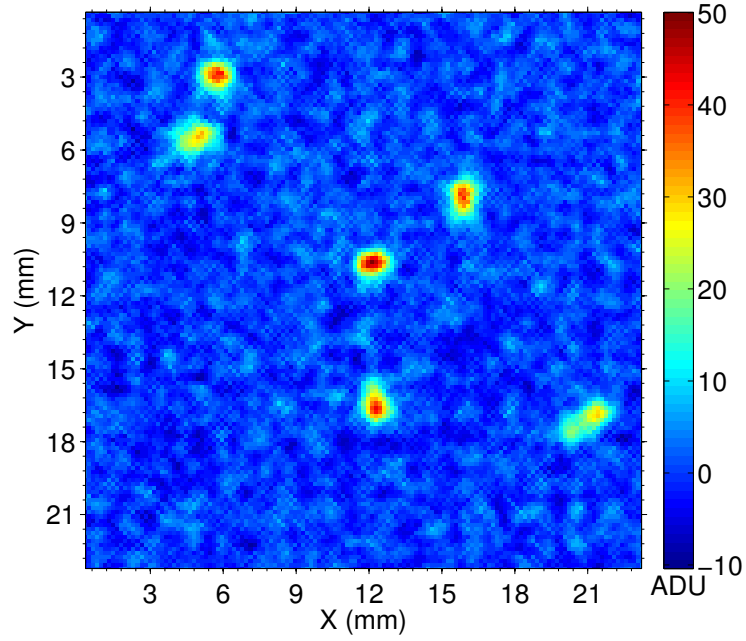
(a) ^{55}Fe tracks
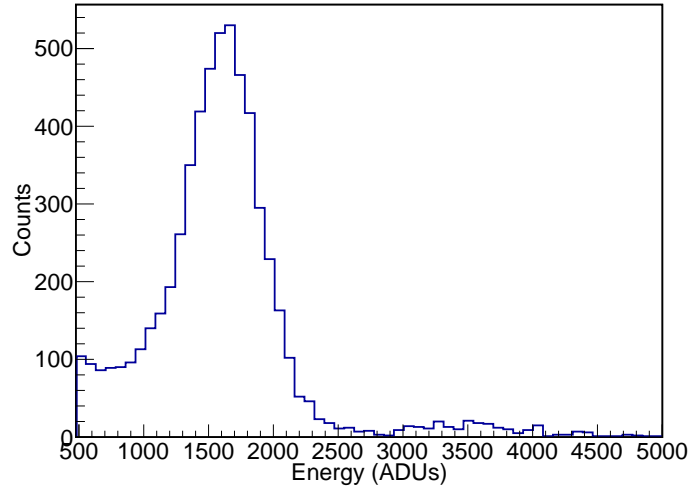
(b) ^{55}Fe energy spectrum

Figure 6.2: *(a) An image of ^{55}Fe tracks acquired at 6×6 on-chip binning in 100 Torr CF_4 with an averaging filter of block size 5×5 applied to the image to enhance signal-to-noise. The image is captured at the maximum stable gas gain of $\sim 10^5$ and has a pixel scale of 165 µm/pix. (b) An energy spectrum of ^{55}Fe obtained optically from CCD imaging of electronic recoil tracks at 6×6 on-chip binning and the maximum stable gain. The data is a combination of the start and end data sets in the day eight run (see Figure 6.6). The smaller secondary feature to the right of the primary peak is the result of event pile-up.*

image, resulting in each binned pixel imaging 165 µm × 165 µm in real space. The signal is well above the noise in the CCD image and individual tracks are resolved. With this level of signal-to-noise and resolution one could easily characterize the spatial uniformity of the gas gain across the GEMs.

The corresponding energy spectrum using images of these tracks is shown in Figure 6.2b in units of ADUs[1]. The peak value in the spectrum is obtained from a fit which comprises of a single Gaussian signal component and a constant plus exponential for the background components. The range of the fit is set so as to exclude the secondary peak seen at ~3500 ADU, which is due to pile-up events. The fit has a reduced χ^2 (χ^2/ndf) = 0.66, a peak value of $\mu_{100\text{Torr}} = 1621 \pm 5$ ADU, and $\sigma_{100\text{Torr}} = 264 \pm 5$ ADU. The FWHM energy resolution is 38% and we obtain an energy conversion factor of 275 ADUs/keV.

In Figures 6.3a and 6.3b, a sample image of ^{55}Fe tracks obtained at a gain of ~2 ×10^5 in 100 Torr CF_4 is shown along with the corresponding energy spectrum. The same procedure for fitting the spectrum as described above gives a peak value of 2610 ± 15 ADU, σ of 329 ± 16 ADU, and energy conversion factor of 443 ADUs/keV. Interestingly, the FWHM energy resolution is 30%, significantly better than that of the moderate gain 100 Torr data. A possible explanation for this is that with the higher ΔV of GEM 3 resulting in a higher electric field inside the GEM holes, the probability for electron attachment is suppressed in this region. The competition of attachment with the avalanche process will lower gas gain and result in larger fluctuations, which will worsen energy resolution.

6.4.2   35 & 50 Torr

In Figure 6.4, two sample images of ^{55}Fe tracks taken at a pressure of 50 Torr in CF_4 are shown. The tracks are longer and much better resolved than those in the 100 Torr data, and additionally, differences in ionization density are also clearly visible.

---

[1]Analog to Digital Units, with 1 ADU equal to ~1.3 e^- produced in our CCD sensor.
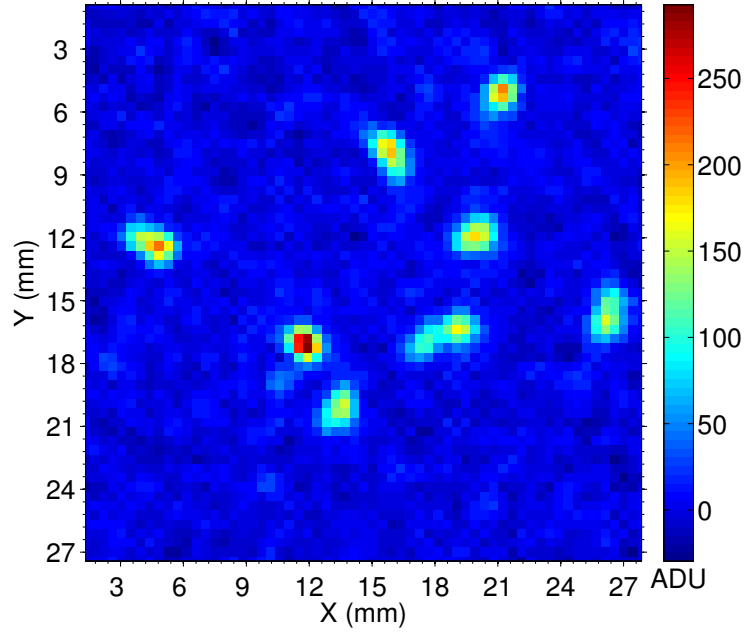
(a) ^{55}Fe tracks
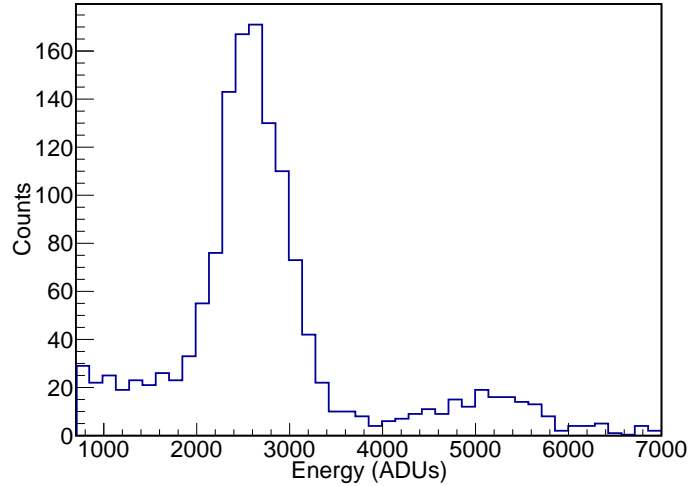
(b) ^{55}Fe energy spectrum

Figure 6.3: *(a) An image of ^{55}Fe tracks acquired at 16×16 on-chip binning (pixel scale of 440 µm/pix) in 100 Torr CF_4 with an averaging filter of block size 3×3 applied to the image to enhance signal-to-noise. The image is captured at the maximum gas gain of $\sim 2 \times 10^5$ and shows that even in 100 Torr, ^{55}Fe tracks are resolved. (b) An ^{55}Fe energy spectrum obtained optically from CCD imaging of electronic recoil tracks at 16×16 on-chip binning and maximum gain of $\sim 2 \times 10^5$. The smaller secondary feature to the right of the primary peak is due to event pile-up.*
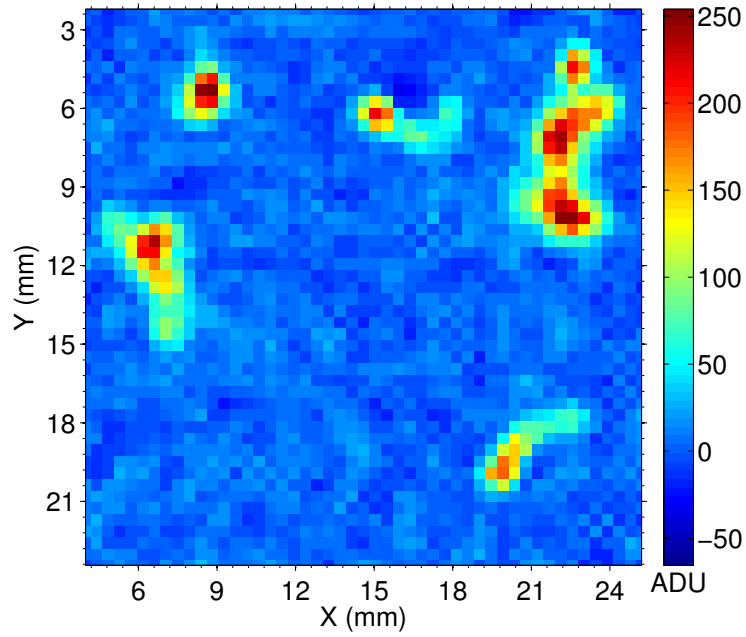
(a) ^{55}Fe tracks 50 Torr CF4
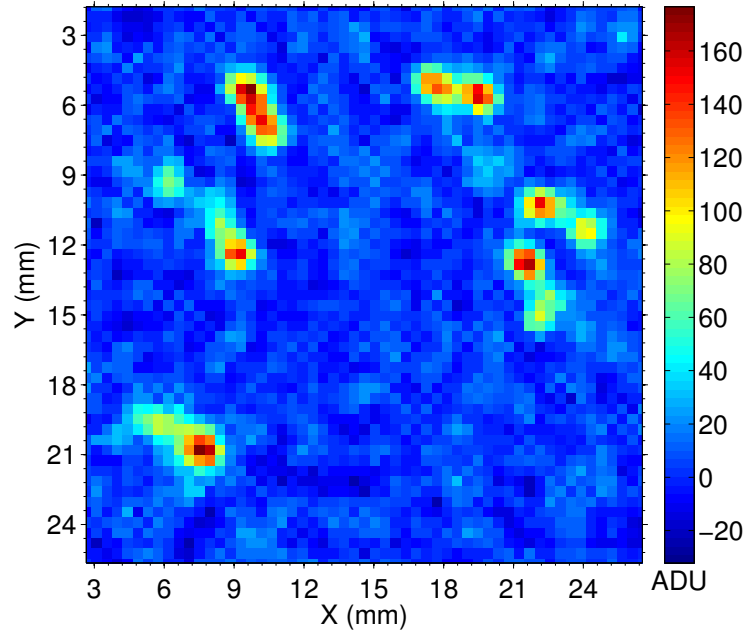
(b) ^{55}Fe tracks 50 Torr CF4

Figure 6.4: *(a)-(b) Images of 5.9 keV ^{55}Fe electronic recoil tracks in 50 Torr CF4 at 16×16 on-chip binning. An averaging filter with a 3×3 block size has been applied to the image to improve signal-to-noise without significantly degrading resolution. At this pressure, the tracks are well resolved and fluctuations in energy loss and range straggling are also clearly visible.*
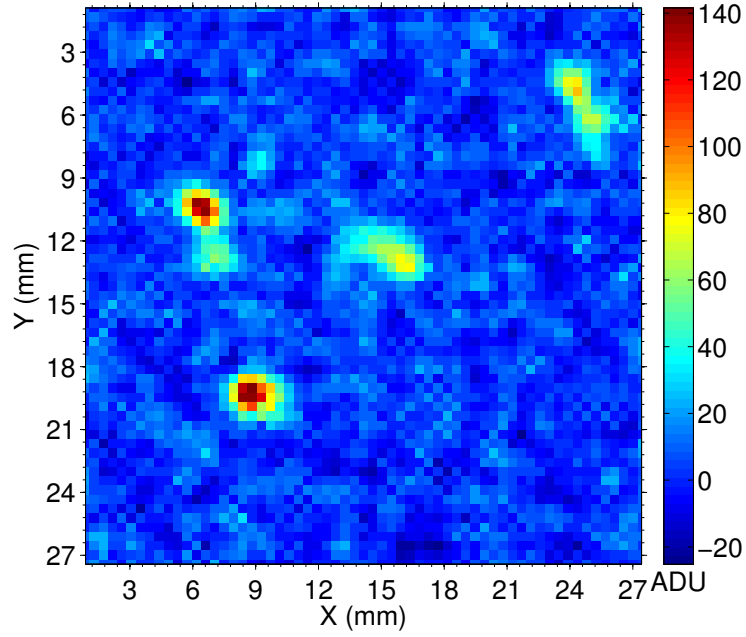
(a) ^{55}Fe tracks in 35 Torr CF$_4$
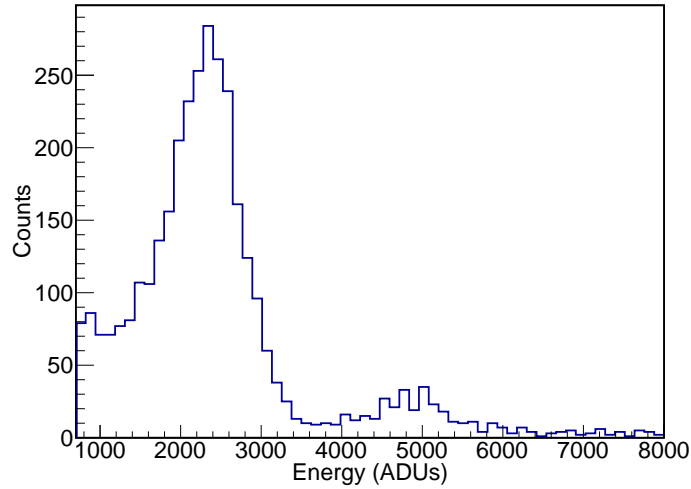
(b) ^{55}Fe energy spectrum 35 Torr CF$_4$

Figure 6.5: *(a) An image of ^{55}Fe tracks in 35 Torr CF$_4$ with an averaging filter applied to enhance signal to noise. The tracks are clearly resolvable as extended objects rather than diffused points at this pressure. (b) An energy spectrum obtained from CCD imaged ^{55}Fe electronic recoil tracks in 35 Torr at 16×16 on-chip binning and maximum stable gain. The smaller secondary feature on the right of the primary peak is due to event pile-up.*

The corresponding energy spectrum is not shown because not enough images were taken at this pressure due to an issue with electrical stability. Nevertheless, these images unambiguously show that electron recoils with energies as low as 5.9 keV are resolvable given sufficient detector signal-to-noise and imaging resolution. This is an important topic in rare event searches such as directional dark matter experiments where discrimination between electronic and nuclear recoils is of great interest.

For the 35 Torr data, a sample image containing ^{55}Fe tracks is shown in Figure 6.5a. The tracks are clearly resolvable but the resolution is not quite as good as the 50 Torr data due to the transfer region within the double THGEM amplification structure. Also, note that diffusion in electron gases scales with $\sqrt{1/p}$ at a fixed reduced field, where p is the pressure. The energy spectrum obtained from a series of these images is shown in Figure 6.5b. A fit of the spectrum to a single Gaussian signal component and a background component which consists of a uniform and exponential components gives a reduced χ^2 (χ^2/ndf) = 0.80. The fitted peak value is $\mu_{35\text{Torr}} = 2327 \pm 18$ ADU and $\sigma_{35\text{Torr}} = 400 \pm 28$ ADU. This gives a FWHM energy resolution of 40% which is similar to, within errors, the energy resolution obtained from the moderate gain 100 Torr data.

6.4.3 Contamination effects on light yield

An interesting feature observed in our 100 Torr data was the apparent difference in the ratio of the optical spectrum peak to the corresponding effective gas gain for the two gain settings, $\sim 1 \times 10^5$ and $\sim 2 \times 10^5$. In the moderate but stable gain data, the ratio is ~ 0.016, and in the high gain data, the ratio is ~ 0.013. This ratio could be thought of as an effective photon yield and implies that the high gain data has a photon yield that is approximately 19% lower than the moderate gain data. This observation could be due to different effects which, unfortunately, are difficult to disentangle in our data. We nevertheless describe the various possibilities as some of them could have a negative impact on applications such as directional dark matter
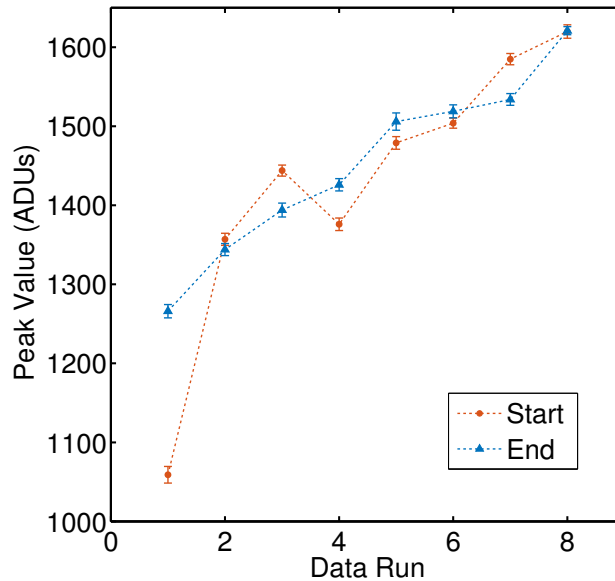
Figure 6.6: *The fitted peak value of the ^{55}Fe energy spectrum at the start and end of the day over eight days of data taking. With the exception of the first data run, the start and end peak values are within 4%. The large change ($\sim$ 20%) seen between the start and end in the first data set is likely due to insufficient time for the GEMs to charge up and stabilize. The raising peak value with run number is likely the result of a reduction in concentration of contaminants with the additional pump down in-between runs.*

searches.

The first possibility is that it could be a charge density effect, where the photon yield decreases (is quenched) with increasing charge density at high gas gains so that the total number of photons emitted for every secondary electron created in the avalanche region is reduced. Instead of an overall quenching of light it could also be that the emission spectrum from CF_4 changes with the gas gain, so that the number of photons produced in the wavelength range of sensitivity for our CCD camera and lens is reduced.

The simplest explanation, however, is the presence of trace light-suppressing contamination in the gas. We can explore this possibility by comparing data from many ^{55}Fe imaging sequences taken over several days at the moderate but stable gain voltage setting. Eight days of data were taken in total, with a set of images acquired

at the beginning and end of each day for a total of 16 data sets. For each imaging sequence, approximately two hours of ^{55}Fe imaging data was acquired, and all data sets were analyzed identically. In between the two ^{55}Fe imaging sequences for each day, a neutron data sequence was conducted for other purposes. At the end of each day of data taking, which lasts about 16 hours each, the vessel was pumped out for 2-3 hours and back-filled with fresh gas. Throughout the 8 days, the vessel was sealed and no changes were made to the experimental setup other the pump out and back-filling with fresh gas at the start of each day. Thus, if the detector had any impurities at the start of day 1, or was out-gassing, this should lead to the last day in the sequence (day 8) having the highest gas purity.

The results of the data runs are plotted in Figure 6.6 which shows the fitted peak value for the start and end of each day of data acquisition. The large difference in the start and end spectrum peak values for data run 1 is most likely the result of insufficient time given for the GEM to charge up and reach a stable operational state. With the exception of run 1, the start and end spectrum peak values are always within 4% of each other, which suggests that out-gassing from materials inside the detector vessel and compositional change of the gas from avalanche does not cause the light output to change significantly over a single day. Nevertheless, the spectrum peak value does rise fairly monotonically over the 8 days of data runs. This is likely due to out-gassing, which can have a long half-life in sealed vessels which have not been baked out.

Between run 1 and run 8 the light output increased by 28% in the end series, and by 53% in the start series. The end series is monotonically increasing whereas the start series has an inflection which indicates that the GEM charge up time is important. The differences in peak values between runs 1 and 8 in both series could completely explain the 19% photon yield difference between the high gain and moderate gain data sets. The ratio of peak value to gas gain for end-run 1 is 0.013 which is the same value as that for the high gain data set. Nevertheless, we cannot

entirely rule out other effects such as a charge density dependent photon yield or a charge up time effect. Finally, there is also a question of how long the pump down time must be because Figure 6.6 shows that the light output is still increasing even after day 8.

6.4.4   Charge density effects on light yield

Light output quenching resulting from gas contamination could be dealt with with a long pump down and/or continuous filtering of the gas in a circulation system. However, quenching due to high charge density arising from either high gas gains and/or high primary ionization densities raises several interesting and important questions. Is the charge quenched or saturated by a similar amount to the light, so the the charge to light ratio is the same in the quenched region as it is in the unquenched region? How does the onset of quenching change with the type of the gas and pressure/density? Finally, does the quenching behavior change when different amplification devices are used? In other words, if all operating parameters (i.e. gas, pressure, gain, etc.) are the same, does the effect differ when multi-wire proportional chambers (MWPCs) are used rather than GEMs or THGEMs?

It may be crucial to answer these questions particularly in regards to directional dark matter detection in which the sense (vector direction) of the ionization track is determined by measuring the asymmetry in the charge deposition along the track. If quenching plays a significant role in the low pressure regime that directional dark matter experiments operate in, this can place a constraint on how well the directional signature can be measured in gas based TPCs operated at high gas gains.

6.5   Conclusion

We have shown that a GEM and THGEM based detector can be operated in low pressure CF_4 (35-100 Torr) with gains exceeding 2×10^5. This allowed individual

^{55}Fe tracks to be imaged by a low noise CCD camera and for an optically measured spectrum to be obtained for the first time. We found that it is important to pump down the detector for an extended period of time to reduce contaminants in the gas that can suppress light output. However, it is not clear if light quenching at high charge densities is a significant effect for experiments that use the asymmetry in charge density to determine the recoil direction of a track. Finally, we showed that electronic recoils as low as 5.9 keV in energy can be resolved. This is important for rare event searches such as direct dark matter detection experiments that rely on differences in stopping power to discriminate between different types of recoils.

Chapter 7

SF$_6$–A New Negative Ion TPC Gas

7.1 Introduction

Based upon the discussion in Chapter 3, particularly on the diffusive behavior of electronegative gases, CS$_2$ would appear to provide a considerable advantage to track imaging detectors. But on closer inspection, CS$_2$ presents many issues for use in a directional dark matter detector. In pursuit of a solution to those problems, we have identified a gas that could possess the advantages of an electronegative gas but without the negative aspects of CS$_2$. This gas is SF$_6$, or sulfur hexafluoride. In this chapter, we present the first measurements with SF$_6$ as the primary gas in a low pressure Time Projection Chamber (TPC). Our measurements demonstrate that SF$_6$ is an attractive gas for directional dark matter detection. In particular, the high fluorine content is desirable for spin-dependent sensitivity, negative ion drift ensures low diffusion over large drift distances, and the multiple species of charge carriers allow for full detector fiducialization. This allows for a near optimal target mass fraction per volume ($\sim 80\%$), thus maximizing the sensitivity per unit volume. In addition, SF$_6$ also maximizes the sensitivity per volume per readout by enabling scaling in the Z-dimension without increasing readout costs.

7.2   SF$_6$ properties

Sulfur hexafluoride (SF$_6$) is an inert, odorless, and colorless gas commonly known as an electron scavenger because of its large electron attachment cross-section [192, 193, 194, 195, 196, 197, 198, 199, 200]. The high electron affinity coupled with its non-toxicity and non-flammability make it suitable for use in many practical applications, including as a gaseous dielectric insulator in high voltage power devices, plasma etching of silicon and Ga-As based semiconductors, thermal and sound insulation, magnesium casting, and aluminum recycling (Refs. [201, 202] provide an extensive review of the properties and applications of SF$_6$). In particle detectors, SF$_6$ has been used as a quencher in Resistive Plate Chambers (RPCs) operated in both avalanche and streamer modes, enabling more stable operation by suppressing streamer formation in the former, and reducing the energy of discharges and allowing lower voltage operation in the latter [203, 204]. As a result of its many diverse commercial and research applications, SF$_6$ is one of the most extensively studied gases [201].

Nevertheless, with the exception of RPCs, studies of SF$_6$ in conditions applicable to particle physics detectors are scarce. Although SF$_6$ was considered as a negative ion gas in rare searches [205], the high electron affinity was deemed a barrier for stripping the electron from the negative ion in the avalanche region, a necessary first step for initiating gas gain amplification. However, with the advent of Micro-patterned Gas Detectors (MPGDs), which have flexible geometries that can sustain high electric fields in the avalanche region even at low pressures, the potential for achieving gas gain in SF$_6$ may be realized. Demonstrating this for low energy event detection would open up the possibility for its use in a variety of experiments, such as directional dark matter searches. Our work provides the first experimental evidence that SF$_6$ is in fact an excellent choice as a negative ion gas for TPC-based directional dark matter experiments.

Directional searches in TPCs require low pressures, to lengthen recoil tracks, and

low diffusion so they can be resolved, both of which are ideally suited to negative ion gases. The idea of negative ion drift with carbon disulfide (CS$_2$) was first proposed by Martoff to circumvent the use of magnetic fields to achieve low diffusion in large TPCs [135]. Negative ion TPCs were first successfully demonstrated with CS$_2$-based gas mixtures by DRIFT, a directional dark matter experiment [206, 111]. At present DRIFT employs a mixture of 30:10:1 Torr CS$_2$:CF$_4$:O$_2$, which leverages the benefits of negative-ion CS$_2$ with the spin content of fluorine, an ideal target for spin-dependent (SD) interactions with WIMPs[1], and the capability to fiducialize the detector provided by O$_2$ [179]. This multi-component DRIFT gas mixture was tailored for directional DM searches where low diffusion, low backgrounds and the SD limit-setting capabilities are all essential.

As demonstrated in this work, SF$_6$ has all of benefits of the DRIFT gas mixture, along with additional advantages that make it more amenable to the underground environment. We begin by discussing the motivation behind, and benefits of each component of the CS$_2$/CF$_4$/O$_2$ gas mix for directional dark matter experiments, and how these are matched by SF$_6$.

In a detector with an electronegative gas, like CS$_2$, the free electrons produced by an ionization event are quickly captured, forming anions that drift in the thermal regime to the amplification and readout region. In this regime, diffusion scales as $\sqrt{L/E}$, where L is the drift distance and E is the strength of the drift field, making it desirable to have high fields to minimize diffusion. With this, good tracking resolution can be achieved over long drift distances, which are two necessary conditions for the high quality track reconstruction and large detection volumes required for directional dark matter and other rare event searches. Like CS$_2$, which has an electron affinity of 0.55 eV [207], SF$_6$ is highly electronegative with electron affinity of 1.06 eV [208].[2]

---

[1]For SD dark matter searches neither ^{12}C or ^{32}S atoms have the nuclear spin content to be suitable detection targets, whereas ^{19}F is excellent in this regard [70]

[2]The values quoted for SF$_6$ were recommended by Ref. [208] based on results from Ref. [209] and Ref. [210], and the value for CS$_2$ is the most precise to date. Note however

Thus, SF$_6$ should also behave like a negative ion gas, with similar drift properties to CS$_2$.

An additional advantage of electronegative gases is that they tend to display superior high voltage performance at low pressures over electron drift gases, such as CF$_4$ and N$_2$. SF$_6$ is especially well suited in this regard, having a breakdown field strength that is about three times higher than air [212] and N$_2$ [213, 214] at pressures below one atmosphere.

The CF$_4$ in the DRIFT gas mixture, as mentioned above, provides the fluorine target for SD WIMP interactions. In this regard, with its high fluorine content, SF$_6$ has a clear advantage over CS$_2$/CF$_4$ mixtures for SD searches. Thus, if the potential of SF$_6$ as a negative ion gas are borne out, there would be no need to sacrifice precious detection volume to the non spin-dependent CS$_2$, leading to a significant increase in the sensitivity to dark matter.

The motivation for O$_2$ in the DRIFT gas mixture came from the recent discovery that the combination CS$_2$/O$_2$ produces features in the signal waveform that allow event fiducialization [179]. This enabled the ability to reject backgrounds from detector surfaces, a critical advance for gas TPCs used in rare searches. With this, DRIFT demonstrated a ∼50 day, zero background limit that is currently the world's best for a directional experiment [111]. We show in Section 7.4 that the signal waveform in SF$_6$ also contains similar features that can be used for fiducialization (Section 7.8).

There are a number of other advantages of SF$_6$ over CS$_2$/CF$_4$O$_2$ mixtures. One is the ability to purify via recirculation, which has not been demonstrated to satisfaction with any CS$_2$ mixture but should be straightforward with SF$_6$. This would lower backgrounds and also lower costs and the manpower needed for transporting gas underground. With respect to safe underground operations another advantage of SF$_6$ is its non-toxicity and non-flammablilty, whereas CS$_2$ is highly toxic and,

---

that, similar to SF$_6$, the experimentally determined electron affinities of CS$_2$ have a large spread, ranging from ∼ $0.5 - 1.0$ eV [211].

with the addition of O$_2$, flammable and potentially explosive [215]. CS$_2$ also has a tendency to be absorbed into detector surfaces making operation and maintenance arduous. Finally, SF$_6$ has an extremely high vapor pressure of 15,751 Torr at room temperature, compared to about 300 Torr for CS$_2$.

In order to realize the very appealing prospects of SF$_6$, the key features we need to demonstrate in this work are:

1. Gas amplification and the efficient stripping of the electron from SF$_6^-$ in the gain stage.

2. Gas gain and its dependance on pressure. For example, if good gas gain can be achieved at high pressure, it would have implications for double-beta decay searches with SeF$_6$ (selenium hexafluoride), which has a similar molecular structure [216].

3. Low thermal diffusion in SF$_6$, as expected from a negative ion gas, and how it compares to CS$_2$.

4. Features in the signal waveforms that could be used to fiducialize events along the TPC's drift direction.

7.3   Experimental apparatus and method

7.3.1   Acrylic detector

The TPC detector used to make measurements for this work (Figure 7.1) consisted of a 60 cm long acrylic cylinder with an inner diameter of 30.5 cm. The two ends of the detector were made from aluminum plates, one serving as the cathode that could be powered up to a maximum voltage of -60 kV, and the other as the grounded anode. The acrylic TPC with its aluminum end-caps also served as the vacuum vessel. The field rings were made from a kapton PC flex board with 1.3 cm wide
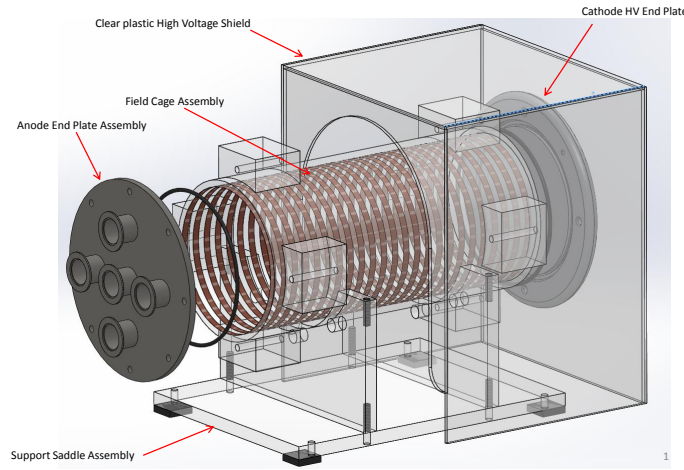
(a) Acrylic cylindrical detector
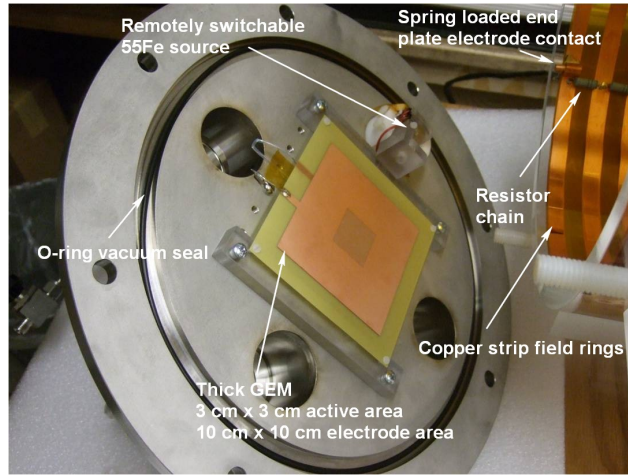
(b) Inner view of anode end plate

Figure 7.1: *(a) A schematic of the detector showing its primary cylindrical acrylic body, field cage, aluminum end plates, support saddle, and high voltage shield. The laser (not shown) sits near the anode plate and fires pulses through a quartz window onto the cathode to create photoelectrons at a known location. (b) A photograph of the inner side of the anode plate which shows the O-ring, switchable ^{55}Fe source, and THGEM.*

copper strips placed at a pitch of 2.54 cm and connected to 23 (56 MΩ) resistors. Gas amplification was provided by a single 0.4 mm thick GEM (THGEM) that was custom fabricated at CERN with an active area of 3×3 cm^2. The THGEM had a hole pitch of ∼0.5 mm and hole diameter of ∼0.3 mm, with an annular region of

thickness 0.05 mm etched around the holes to eliminate burring from the drilling process. The THGEM was mounted on two acrylic bars attached to the anode plate. The surface of the THGEM facing the cathode was grounded to the anode plate while the other surface was held at high voltage (610 − 1020 V). Signals were read out from the high voltage surface with an ORTEC 142 charge sensitive preamplifier, which had a 20 ns rise-time (at zero capacitance) and a 100 µs decay time constant.

7.3.2 Charge generation

Ionization was introduced into the gas volume either with an internally mounted and remotely switchable ^{55}Fe 5.89 keV X-ray source (Figure 7.1b), or by a system using a Stanford Research Systems (SRS) NL100 337.1 nm pulsed nitrogen laser, which was used to produce photoelectrons by illuminating the aluminum cathode. The NL100 laser had a FWHM pulse width of 3.5 ns, a pulse energy of 170 mJ, and a peak power of 45 kW. The spot size in the longitudinal, or drift, dimension was essentially a delta function, whereas the projected spot size in the X and Y (lateral) dimensions was a 1×3 mm^2 rectangle. Measurements of transverse diffusion require an instrumented XY readout, which is the subject of future work.

7.3.3 Operation and data acquisition

After the vacuum vessel was sealed, a long pump-down with an Edwards XDS10 dry scroll vacuum pump (base pressure < 0.1 Torr) was conducted to minimize outgassing from the acrylic cylinder and other components inside the detector. The vessel was then back-filled with approximately 200 Torr of SF$_6$ gas (99.999% purity), and flushed. This was done to dilute any residual out-gassed contaminants that the vacuum pump was not able to remove. The vessel was once again back-filled with gas to approximately 200 Torr and slowly pumped down to the final operating pressure, with a precision of 0.05 Torr. During this slow pump down, both the cathode and

GEM were ramped up to operating voltages. This procedure assured a minimum time between the introduction of fresh gas into the detector and the start of data acquisition.

As the various measurements of SF$_6$ properties were performed as a function of the operating pressure and drift field, these were changed between each setting. This was done by raising the pressure back up to 200 Torr and, as before, slowly pumping down to the new pressure setting while concurrently setting the new cathode voltage. This procedure was repeated between each set of measurements, and its importance will be explained in Section 7.4.3 where the presence and effects of water vapor are discussed.

Although the focus of this paper is on SF$_6$, for comparative purposes we also present measurements of CS$_2$ properties made using the same setup. For this gas, the operating procedure was different than the one used for the SF$_6$. After the long pump down, the detector was back-filled to the operating pressure and all sets of measurements were taken without a pressure raise and pump down between each setting. When the cathode was brought to full operating voltage, a spark-down period of $30 - 60$ minutes allowed micro-sparks due to the acrylic charging-up to subside before powering up the THGEM to full voltage.

All measurement waveforms were acquired with a Tektronix TDS 3054C digital oscilloscope and National Instruments data acquisition software, where every triggered event was read out and saved to file for analysis. The saved files contain the voltage signals from the ORTEC charge sensitive preamplifier, which integrated the charge collected by the THGEM readout surface with a rise time of ~100 ns, and an exponential decay time constant of $\tau = 100$ µs. The current, $I(t)$, entering the preamplifier is related to the detected voltage signal, $V(t)$, by

$$I(t) \propto \frac{dV}{dt} - \left(-\frac{V}{\tau}\right),\tag{7.3.1}$$

where the second term is for removing the decay tail. We used Equation 7.3.1 to compute $I(t)$ from our measurements of $V(t)$. After the conversion, pulses were

smoothed with a Gaussian filter to suppress high frequency noise and to improve signal to noise. We then extracted the drift speed, diffusion, and other quantities from these processed waveforms.

7.4 SF$_6$ waveforms

7.4.1 Capture and transport in SF$_6$

Measurements made under differing conditions have shown that electron capture by the electronegative SF$_6$ molecule occurs rapidly [192, 193, 194, 195, 196, 197, 198, 199, 200] with the immediate product being SF$_6^{-*}$, a metastable excited state of the anion, SF$_6^-$. The latter forms subsequently from the collisional or radiative stabilization of the excited state [202]. The electron capture cross-sections by SF$_6$ are very large [192, 193, 194, 195, 196, 197, 198, 199, 200] and estimates of the capture mean-free-path are about a micron at the pressures and drift fields of our experiments. This assumes that the electrons produced by the laser illumination of the cathode have near zero kinetic energies, where the capture cross-sections peak. The metastable SF$_6^{-*}$ leads to subsequent products besides SF$_6^-$, whose relative abundances depend on the lifetime of SF$_6^{-*}$, the electron energy, gas pressure, temperature, and drift field:

$$\text{SF}_6 + \text{e}^- \rightarrow \text{SF}_6^{-*} \qquad \text{(attachment, metastable)} \tag{7.4.1}$$

$$\text{SF}_6^{-*} \rightarrow \text{SF}_6 + \text{e}^- \qquad \text{(auto-detachment)} \tag{7.4.2}$$

$$\text{SF}_6^{-*} + \text{SF}_6 \rightarrow \text{SF}_6^- + \text{SF}_6 \qquad \text{(collisional stabilization)} \tag{7.4.3}$$

$$\text{SF}_6^{-*} \rightarrow \text{SF}_5^- + \text{F} \qquad \text{(auto-dissociation)} \tag{7.4.4}$$

Thus, after the quick electron capture leading to SF$_6^{-*}$, the auto-detachment re-action (7.4.2) will compete with collisional stabilization, reaction (7.4.3), and auto-dissociation, reaction (7.4.4). To determine whether auto-detachment plays a significant role in our experiment, which could lead to a significant distortion of the waveform, we consider bounds on the lifetimes of these reactions.

Measurements of lifetimes for auto-detachment have a broad range, from ~10 µs to one ms, depending on the experimental technique used. Under collision-free conditions, time-of-flight (TOF) mass spectrometric experiments indicate the lifetime is between $10 - 68$ µs [217, 218, 219, 220, 221, 222]. Measurements made with ion cyclotron resonance (ICR) experiments, however, give lifetimes in the ms range [223, 224, 225]. The difference in measured lifetimes between the two techniques reflect different electron energies, with those in ICR experiments typically much lower than in TOF experiments [202], and closer to the energies in our experiment.

The lifetime for collisional stabilization (7.4.3) depends on the cross-section and collision rate. The former is large, and the latter can be estimated by considering the collision mean-free path, λ, for SF$_6^{-*}$ in SF$_6$. Assuming that this is similar to that of SF$_6^-$ in SF$_6$, we can use:

$$\lambda = \frac{(3MkT)^{1/2} v_d}{eE} \tag{7.4.5}$$

[226], where $T = 296$ K, M is the mass of the SF$_6$ molecule, v_d is the drift speed, and E is the drift field. Using our measured drift speeds (see Section 7.5) we estimate $\lambda \sim 0.1 - 1$ µm, implying a collisional mean-free time of $\sim 1 - 10$ ns. This is many orders of magnitude less than the lifetimes for auto-detachment, indicating that the latter process should be inconsequential in our experiment. This is confirmed by our waveforms shown in Section 7.4.2.

Besides reactions (7.4.3) and (7.4.4), which lead to the production of SF$_6^-$ and SF$_5^-$, other processes occurring at either the site of initial ionization or during drift to the anode can lead to additional negative ion species. For example, the metastable

SF$_6^{-*}$ produced initially can also lead to F$^-$ and SF$_4^-$ (e.g., via auto-dissociation [202]), although at much lower probabilities; reactions producing these species have much lower production cross-sections and require much higher electron energies than those for SF$_6^-$ and SF$_5^-$ [227, 228, 229, 230]. Therefore, in our experiment we expect the initial charge carriers to be dominated by SF$_5^-$ and SF$_6^-$, with their relative contributions estimated from production cross-sections.

The cross-section for reaction (7.4.3) is peaked at zero electron energy [230, 231, 232, 233], falling by a factor of about 100 at 0.1 eV [229, 230, 234], whereas that for reaction (7.4.4) has a peak at zero eV [234] and a smaller one at ∼0.38 eV [229, 230, 234]. At zero eV, the SF$_6^-$ cross-section is larger by a factor 1000 than that for SF$_5^-$, but only a factor ∼30 at 0.1 eV because the SF$_6^-$ cross-section falls much more rapidly with energy than that of SF$_5^-$. For the low electron energies expected in our experiments, however, SF$_6^-$ should be the dominant charge carrier arriving at the anode. Because of the higher mobility of SF$_5^-$ ([235, 236, 237], and see Section 7.5 below) we should detect two peaks in the signal waveform, with the faster SF$_5^-$ arriving earlier in time. This is the basis for fiducialization, and is discussed in detail in Section 7.8.

A number of possible reactions involving the drifting SF$_5^-$ and SF$_6^-$ with the neutral gas could, however, complicate this simple picture. At low drift fields, neutral, electron-hungry SF$_6$ molecules will form clusters around the negative ions [235]. Clusters of SF$_6^-$(SF$_6$)$_n$ and SF$_5^-$(SF$_6$)$_n$ ($n = 1, 2, 3, ...$) have been observed but with mobilities less than those of SF$_5^-$ and SF$_6^-$ [235]. This phenomena could therefore partly explain the long tail observed on the slow side of the SF$_6^-$ peak in our low reduced field waveforms (Figure 7.4a).

In addition to clustering, the drifting SF$_5^-$ and SF$_6^-$ could also interact with the neutral molecules or contaminants in the gas leading to other species (see Section 7.4.3). These could appear as distinct features in our measured waveforms. More important for us is the collisional detachment of energetically stable SF$_5^-$ and

SF$_6^-$ via the following reactions:

$$SF_5^- + SF_6 \rightarrow SF_5 + SF_6 + e^- \qquad \text{(collisional detachment)} \qquad (7.4.6)$$

$$SF_6^- + SF_6 \rightarrow SF_6 + SF_6 + e^- \qquad \text{(collisional detachment).} \qquad (7.4.7)$$

Such processes would be followed by re-attachment via reaction (7.4.1), and the subsequent reactions (7.4.3) and (7.4.4) that lead back to SF$_5^-$ or SF$_6^-$. The attachment/detachment of the electron could result in a smeared waveform due to the different drift speeds of the charge carriers. However, the probability of detachment via reactions 7.4.6 and 7.4.7 is very small for center-of-mass energies < 60 eV [238]. In comparison to the electron affinity of SF$_5$ $(2.7 - 3.7$ eV) [239] and SF$_6$ $(1.06$ eV), the threshold energy for detachment is much larger and is attributed to competing charge-transfer and collision-induced dissociation processes [238, 240, 241]. Nevertheless, there is evidence that energetically unstable states of SF$_6^-$ (i.e. SF$_6^{-*}$) can contribute to collisional detachment [238, 240]. The relative contributions of these effects depend on the interaction energies at different reduced fields, but the detailed mechanisms is well beyond the scope of this work.

7.4.2 Waveform features

With an overview of the chemistry of electron drift and attachment in SF$_6$, we now turn to a detailed look at our data. Shown in Figures 7.2 and 7.3 are the averaged current waveforms acquired in 20 Torr SF$_6$ ($N = 6.522 \times 10^{17}$ cm^{-3} at $T = 296$ K) for six different drift field strengths. The averaging was done using one thousand individual waveforms, each acquired by illuminating the cathode with the nitrogen laser. The laser also provided the initial trigger for the DAQ system.

At low fields, the waveform consists of two peaks, one much smaller than the other, and a low amplitude broad component distributed outside the region of the two peaks. The large main peak is SF$_6^-$ and the smaller secondary peak arriving
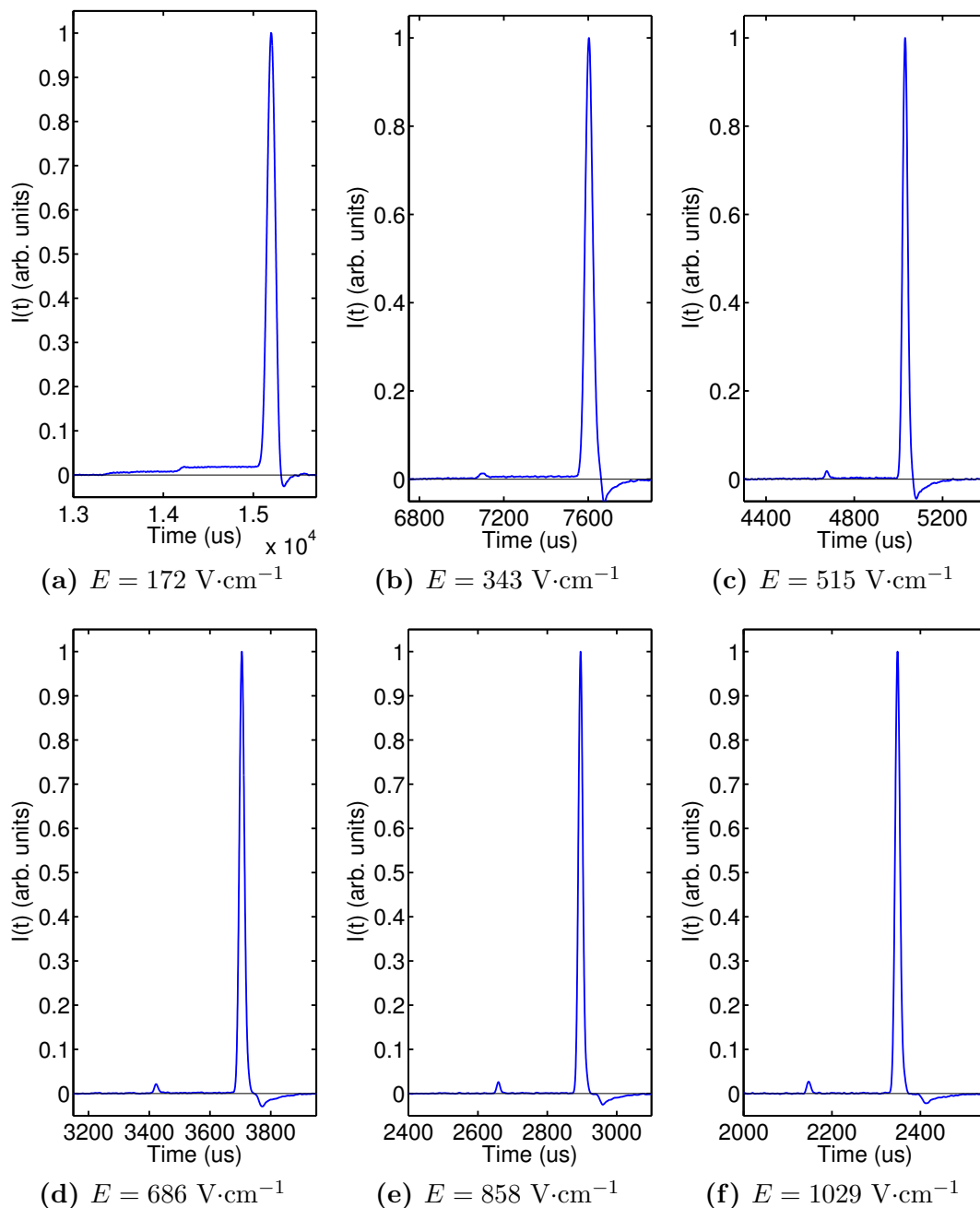
Figure 7.2: *(a) - (f) The average waveforms acquired in 20 Torr SF$_6$ at six different electric fields. At low fields (a), there is an additional broad structure in addition to the two peaks. This component appears to decrease in magnitude with increasing electric field and seemingly vanishes at the highest field (f).*
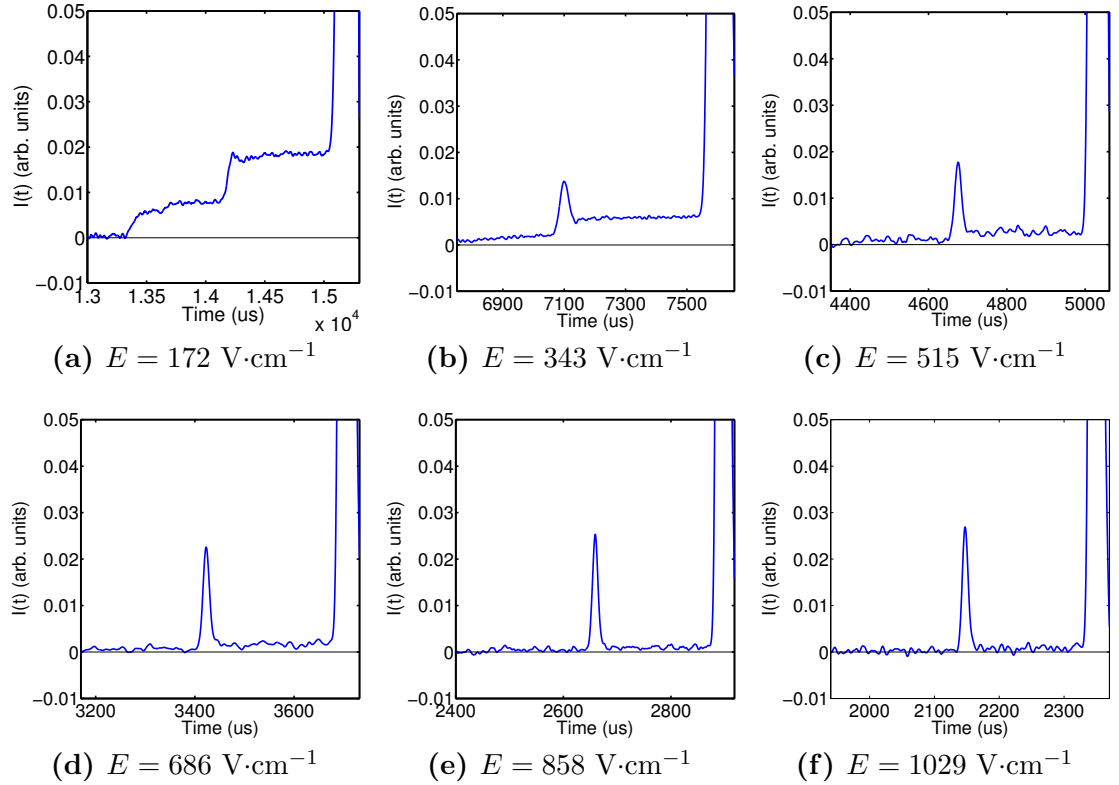
Figure 7.3: *(a)-(f) The zoomed in views of the waveforms from Figure 7.2. Charge outside of the peaks appears to decrease with increasing field strength while the SF$_5^-$ peak begins to emerge and grow in amplitude.*

earlier is SF$_5^-$. The non-peak component does not appear continuous but displays a step in amplitude at the location of the smaller peak, and a second step to the baseline at an earlier time. With increasing field strength, this non-peak component gradually subsides until it is barely discernible at $E = 1029$ V·cm^{-1} (Figure 7.3f) leaving just the two sharp peaks. The origin of this component is water vapor contamination from out-gassing in the acrylic vessel, and is subject of Section 7.4.3.

The waveforms show a similar behavior as a function of inverse pressure, $1/p$. Figure 7.4 shows portions of waveforms taken at three pressures with a fixed drift field, $E = 86$ V·cm^{-1}, the lowest used in our experiment. The broad component decreases relative to the main SF$_6^-$ peak as the pressure is reduced, similar to what is

observed with increasing drift field at fixed pressure. This anti-correlation between the pressure and drift field would imply a reduced field (E/p or E/N) dependence, but a detailed look at the data does not support this. Comparing the waveforms in Figure 7.3c and Figure 7.5b (blue curve), both at the same reduced field but different E and p, we see clear differences in the amount of charge in the non-peak region (both waveforms are normalized with the SF_6^- peak amplitude set to one).

Two other notable features seen on the right side of the SF_6^- peak are the small negative amplitude dip and the long tail at low E/p. As discussed in Section 7.4.2, the latter could be due to $SF_6^-(SF_6)_n$ and $SF_5^-(SF_6)_n$ clusters that drift at a slower speed than the SF_6^- anion. The production and drift of $SF_6^-(H_2O)_n$ clusters, which is discussed in Section 7.4.3, could also contribute to this tail. But at higher reduced fields, the formation of such weakly bound clusters should be suppressed, which is supported by our higher E/p data (Figures 7.4b and 7.4c). The second feature, the negative amplitude dip, is due to how the THGEM surfaces were electrically connected. The surface facing the cathode was grounded to the aluminum anode end-cap, while the other readout surface is at positive high voltage. As a result, the motion of the positive ions in the avalanche away from the readout induces a small positive signal, then the negative dip occurs as they approach the ground, which is capacitively coupled to the readout surface.

7.4.3   Water vapor contamination

The relative contribution of the broad component to the waveform discussed above (Figures 7.2, 7.3 and 7.4) was found to depend on the length of the pump-out period prior to operation, and the subsequent rate of out-gassing as monitored with the baratron. Given the propensity for plastics to absorb water vapor and O_2, the acrylic TPC vessel was an obvious source of contamination. After numerous tests, which included separately adding small quantities of O_2 and water vapor into SF_6, we confirmed that the broad component was due to H_2O.

(a) 40 Torr, $E = 86$ V·cm^{-1} **(b)** 30 Torr, $E = 86$ V·cm^{-1} **(c)** 20 Torr, $E = 86$ V·cm^{-1}
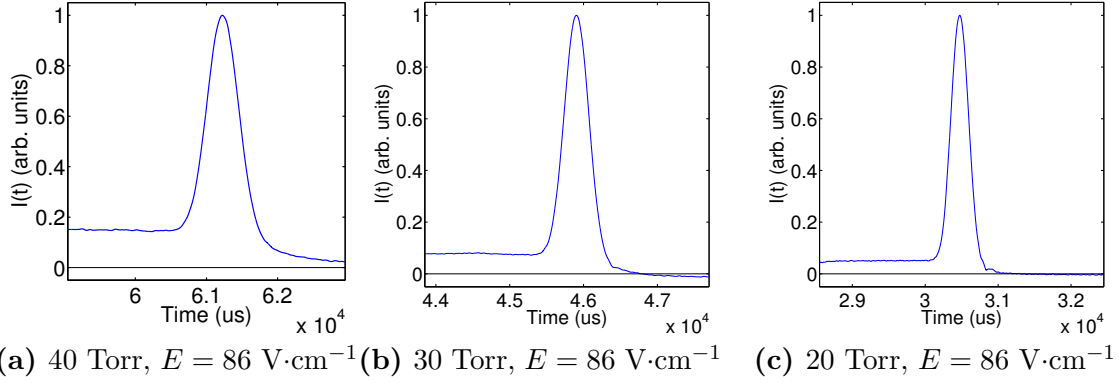
Figure 7.4: *(a)-(c) Average waveforms for 40, 30, and 20 Torr SF$_6$ at $E = 86$ V·cm^{-1}. Note the long tail on the right side of the peak in (a), which could be due to clustering at low reduced fields in SF$_6$.*

(a) 40 Torr, $E = 515$ V·cm^{-1} **(b)** 40 Torr, $E = 1029$ **(c)** 20 Torr, $E = 1029$
V·cm^{-1} V·cm^{-1}
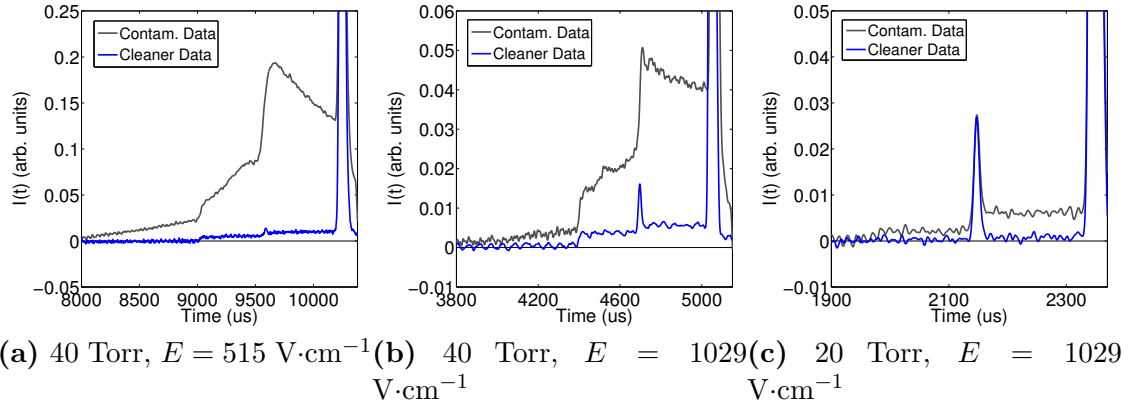
Figure 7.5: *(a)-(c) Comparison of waveform shapes for data with higher (gray) and lower (blue) levels of water vapor contamination at several different reduced fields. The primary SF$_6^-$ peak (outside the vertical range of the plots) has been normalized to 1 in every case. The effect can be considerable ($\sim 20\%$) at lower reduced fields (a) but appears to diminish at a higher reduced field (c).*

To reduce the out-gassing rate and dilute the concentration of contaminants, a long pump-down period (several days) followed by the flushing procedure outlined in Section 7.3.3 was performed. This greatly reduced the water vapor contamination whose relative effect on the waveforms is shown in Figure 7.5 for several different

reduced fields. These plots show that the effect of water vapor on the waveform is large at low reduced fields (Figure 7.5a), but subsides significantly at a higher reduced fields (Figure 7.5c) where it is only at the percent level in the high contamination data. We can place an upper bound on the amount of water vapor contamination in these data using observations of the long term out-gassing rate. By attributing the pressure rate-of-rise entirely to the out-gassing of water vapor, we estimate that the amount in the more contaminated data (gray waveforms in Figure 7.5) was $<1\times10^{-1}$ Torr. In the cleaner data (blue curves in Figure 7.5), where the detector had a much longer pump down period, we estimate that the amount of water vapor was <2 $\times10^{-3}$ Torr. The additional step of flushing the vessel twice with SF$_6$ gas was also undertaken prior to data taking for the cleaner data.

While the effect of water vapor is quite significant, the physical mechanisms responsible for the observed features and their dependence on the reduced field are not fully understood. Previous studies of electron attachment to water have shown that the single molecule does not have a negative ion state [242], so it is unlikely that reactions of H$_2$O molecules with the primary electrons produced at the cathode are involved. However, electron binding can occur in clusters of water molecules $(H_2O)_n^-$, where cluster sizes with $n \geq 2$ have been observed [243]. Given the high electron affinity of SF$_6$ and the extremely low H$_2$O concentration, even in the high contamination data, the probability of such clusters forming at the primary ionization site should be low.

Stable $SF_6^-(H_2O)_n$ clusters, with $n = 1-3$, are also known to form [244, 245, 246], thus a more likely scenario is one where water molecules interact directly with SF$_6^-$ anions that are drifting towards the anode[3]. Because these clusters drift slower than SF$_6^-$, they cannot account for the broad component in the waveform, but they can undergo further reactions with H$_2$O, producing the negative ions SOF$_4^-$ and F$^-$(HF)$_2$

---

[3]$SF_5^-(H_2O)_n$ clusters should also be produced, however, we ignore them and their reactions here, because SF$_5^-$ is only produced at a few percent in our experiment (Figure 7.3).

with a relative probability of 4:1 [246]. If these ions drift faster than SF$_6^-$, as argued below, they could be responsible for much of the broad component observed in our waveforms.

With this brief overview of the chemistry of SF$_6^-$ in water vapor we can describe how some of the key features arise in the waveforms observed in our experiments. The first is the evolution of the broad component of the waveform, which subsides with increasing E/p, essentially disappearing at the highest reduced fields in our measurements (e.g., Figures 7.3, 7.5). This indicates that the cluster mediated reactions converting SF$_6^-$ into SOF$_4^-$ and F$^-$(HF)$_2$ become suppressed at higher E/p. In our model these reactions require the stable formation and survival of the SF$_6^-$(H$_2$O)$_n$ clusters, which are weakly held together by hydrogen bonds that are unlikely to survive at high E/p. Without these clusters the pathway to subsequent reactions is closed, leaving only SF$_6^-$ and SF$_5^-$ as observed.

Focusing on the low E/p data where the effects of water vapor are most prominent, we expand our model to explain some of the key features in the waveforms. In our description of SF$_6^-$ and its interactions with water vapor as many as four species can be involved in transporting a negative ion from the cathode to the anode. The drift velocity of this ion will therefore be a weighted average of each species', with the weighting determined by where exactly the conversion from SF$_6^-$ to SF$_6^-$(H$_2$O)$_n$, and SF$_6^-$(H$_2$O)$_n$ to either SOF$_4^-$ or F$^-$(HF)$_2$ occurs. That the broad component of the waveform extends from the SF$_6^-$ peak down below the SF$_5^-$ means that the SOF$_4^-$ and F$^-$(HF)$_2$, and any other cluster mediated reaction products, travel faster than SF$_6^-$, with some even faster than SF$_5^-$. Although we have no data on their mobilities in SF$_6$, this is reasonable given that both SOF$_4^-$ and F$^-$(HF)$_2$ are lighter than SF$_6^-$. If we assume such a correlation between molecular mass and drift velocity (see Equation 7.5.4), then F$^-$(HF)$_2$ would have the highest drift velocity, followed by SF$_5^-$, SOF$_4^-$ and SF$_6^-$, in that order.

Adopting this assumption we can explain two prominent features in the high

contamination waveforms at low E/p, the steps in amplitude at ~4400 µs and ~4700 µs in Figure 7.5b. In our model, the former is essentially the shortest drift time in the waveform, which should correspond to $F^-(HF)_2$ being produced close to the cathode and traveling the full length of the detector. Similarly, the second step at ~4700 µs should correspond to the next shortest drift time, that of SOF_4^-. The fact that this step coincides with the SF_5^- peak (Figure 7.5b, blue curve) agrees with our assumption that two species having similar masses should have similar drift speeds.

Summarizing then, our model predicts that the charge in the region (region 1) between the SF_6^- peak and the step at ~4700 µs should consist of a mixture of SOF_4^- and $F^-(HF)_2$, while in the region (region 2) between ~4700 µs and ~4400 µs it should be solely due to $F^-(HF)_2$. That the charge in region 1 is much larger than in region 2 is expected because, as noted above, SOF_4^- and $F^-(HF)_2$ are produced in the ratio 4:1.

A more detailed analysis of the rich structure observed in the waveforms of the high contamination data is beyond the scope of this paper, nor is it relevant for the goals of directional dark matter detection. For our purposes, the key features of the waveform are the SF_5^- and SF_6^- peaks and their properties, and the remainder of this work will describe their application to directional dark matter searches. The data used in the following sections was taken with a minimum water contamination, similar to the the clean data acquired using the techniques described above (Figures 7.3 and 7.5).

In hindsight, our acrylic-based TPC detector, which was designed for high reduced field operation, was not an ideal choice for operating with SF_6 due to its permeability to water vapor and high out-gassing rate. Moreover, this concern extends well beyond acrylic and encompasses a broad collection of polymer-based materials that are hygroscopic. If plastics cannot be avoided, for example because of their desired low radioactivity, then care should be taken to minimize any water vapor contamination during detector construction and data acquisition. Besides the techniques used here

to achieve this, we have also considered the use of desiccant and gas recirculating and purification as commonly done in TPCs.

7.4.4   Relative peak charge and amplitude

With the preceding discussion of the global features of the SF$_6$ waveform, we now turn our focus to the SF$_5^-$ peak. The importance of detecting both SF$_5^-$ and SF$_6^-$ peaks is that they enable the ability to fiducialize events along the drift direction in the TPC. This provides a powerful tool for rejecting backgrounds in the type of rare searches of interest here, as discussed further in Section 7.8 where fiducialization is demonstrated using this tool.
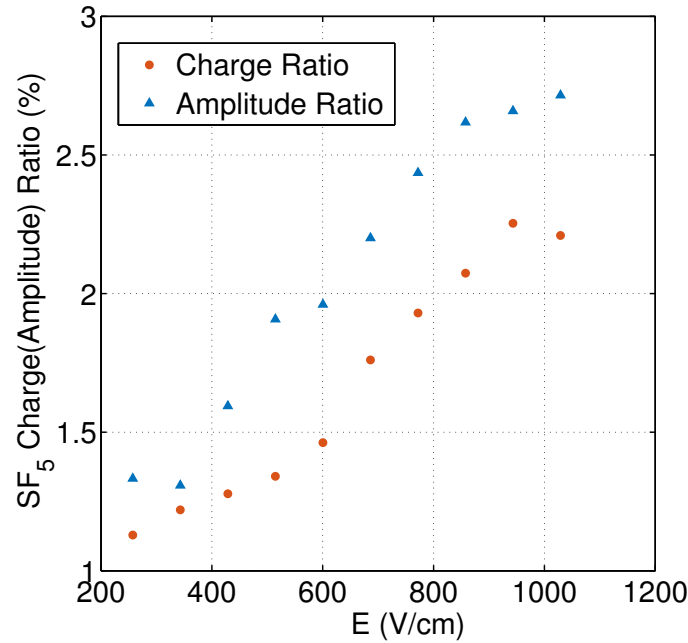
Figure 7.6: *The detected charge and amplitude of the SF$_5^-$ peak relative to SF$_6^-$ in 20 Torr as a function of the electric field. Both quantities increase with electric field but then appear to taper off at a field strength of $\sim$ 900 V·cm^{-1}. It is important to note, as discussed in the text, that these are detected quantities and not necessarily the relative amounts produced in the detection volume.*

To study the behavior of the secondary SF$_5^-$ peak with field strength, an average

of a thousand waveforms was made for each of ten different electric field strengths between 257-1029 V·cm^{-1}, all at fixed $p = 20$ Torr. From these averaged waveforms, the amplitudes of the SF$_5^-$ and SF$_6^-$ peaks and the amount of charge contained within the peaks was computed. The evolution of the fraction of charge in the SF$_5^-$ peak and its amplitude relative to the SF$_6^-$ peak as a function of the electric field are shown in Figure 7.6. Both the relative charge and amplitude rise with increasing field strength but then appear to taper off at a field strength of $\sim$900 V·cm^{-1} (E/p = 45 V cm^{-1} Torr^{-1}).

The amplitude(charge) of the SF$_5^-$ peak measured at the highest reduced field (20 Torr/1029 V cm^{-1}= 158 Td) is $\sim$2.8%(2.2%) that of SF$_6^-$, which is what their relative capture cross-sections at an electron energy of $\sim$ 0.1 eV would predict. It is important to note that this is the *detected* ratio of SF$_5^-$ to SF$_6^-$ and is likely to be lower than what was produced at the site of ionization. This is because of the higher electron affinity of SF$_5^-$ ($2.7 - 3.7$ eV), which could lead to a lower gas gain relative to SF$_6^-$ due to the greater difficulty in stripping the electron in the THGEM.

As the detectability of the small SF$_5^-$ peak is critical for fiducialization, it will require high signal-to-noise as well as investigation into possible methods to enhance it. For example, the ratio of SF$_5^-$ to SF$_6^-$ is known to rise at higher electron energies and gas temperatures, with reports indicating that it can exceed 39% at 593 K [195]. This is further discussed in Section 7.8.2.

7.5   Reduced mobility

The drift velocities of SF$_6^-$ and SF$_5^-$ were determined by measuring the time difference between the creation of photoelectrons at the cathode using the N$_2$ laser, and the arrival of ionization at the THGEM corresponding to the respective peaks. The 3.5 ns laser pulses generated what are essentially point-like ionization events in the longitudinal extent. The laser pulse also provided the trigger to the DAQ system and

gave us the initial time marker, T_0. We define the drift time as the time between the initial laser trigger and the arrival time of the pulse peak, T_p, rather than the leading edge of the ionization signal at the THGEM. The magnitude of the drift velocity, v_d, is then given by

$$v_d = \frac{L}{T_p - T_0},\qquad(7.5.1)$$

where, $L = 583\pm0.5$ mm, is the distance between the THGEM and the cathode. We measured the drift velocity over a range of electric field values $(86-1029\text{ V·cm}^{-1})$ and pressures (20, 30, 40 Torr). Following convention, we report the mobilities instead of drift velocities.

The mobility, μ, of a drifting ion at a specific gas density is related to the drift speed, v_d, and electric field, E, through the relation:

$$v_d = \mu \cdot E.\qquad(7.5.2)$$

A standardized quantity called the reduced mobility, μ_0, is derived from the measured mobility by the expression:

$$\mu_0 = \frac{v_d}{E}\frac{N}{N_0},\qquad(7.5.3)$$

where $N_0 = 2.687 \times 10^{19}$ cm^{-3} is the gas density at STP (0°C and 760 Torr) and N is the detector gas density at the time of measurement.

Our measured mobilities for CS$_2^-$, SF$_5^-$ and SF$_6^-$ are plotted in Figure 7.7 as a function of the reduced field, E/N, in units of the Townsend[4]. We find good agreement between our results for the reduced mobility of CS$_2^-$ in CS$_2$ and those reported by Ref. [140] in the low field regime (< 50 Td), where our data overlap. Our measurement of the reduced mobility of SF$_6^-$ in SF$_6$, extrapolated to zero field, is $\mu_0(\text{SF}_6^-) = 0.540\pm0.002$ cm^{2}V^{-1}s^{-1}, which agrees well with the result from Ref. [236]. There is also excellent agreement over the full range of reduced fields between our dataset for SF$_5^-$ and SF$_6^-$ mobilities in SF$_6$ with the mass-identified measurements reported in Ref. [236]. A comparison with other data-sets from Ref. [235] and [237],

---

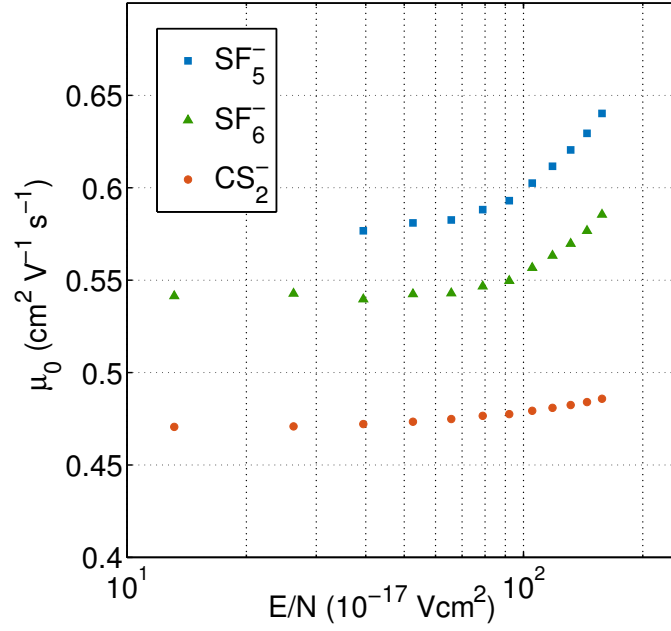[4]1 Td $= 10^{-17}$ V cm^2, 1 V cm^{-1} Torr^{-1} = 3.066 Td at $T = 296$ K.

Figure 7.7: *The reduced mobility as a function of reduced field for SF$_5^-$ and SF$_6^-$ in SF$_6$ and CS$_2^-$ in CS$_2$. The SF$_5^-$ mobilities only go down to about 40 Td below which its peak becomes difficult to identify. Our results for SF$_5^-$ and SF$_6^-$ are in excellent agreement with those found in Ref. [236] while the CS$_2^-$ results agree with those from Ref. [140]. The combined uncertainty due to instrumental precision is 1%.*

a majority of which do not have mass analysis, shows agreement over some ranges of reduced fields only.

The CS$_2^-$ mobility is about 13.1% lower than the SF$_6^-$ mobility at 13 Td, but this difference rises to about 17.0% at 158 Td which shows that SF$_6^-$ mobility increases more rapidly with reduced field than CS$_2^-$ mobility. This is unexpected, and goes against our assumptions in Section 7.4.3, because SF$_6$ is a much heavier molecule than CS$_2$ and the drift velocity for ions with mass, m, drifting in a gas with molecules of mass, M, is given by

$$v_d = \left(\frac{1}{m} + \frac{1}{M} \right)^{1/2} \left(\frac{1}{3kT} \right)^{1/2} \frac{eE}{N\sigma}, \tag{7.5.4}$$

where σ is the ion-gas molecule cross-section [247]. This implies that the cross-section for SF$_6^-$:SF$_6$ interaction is smaller than, and changes faster with increasing

field strength than that for the CS_2^-:CS_2 interaction. A similar comparison between SF_5^- and SF_6^- shows that the mobility of the former is 6.9% higher than the latter's at about 39 Td, and is 9.3% larger at 158 Td. Note also that transport processes are also energy dependent as can be seen with the rise in mobility with increasing reduced field for all of the negative ion mobilities shown in Figure 7.7. This has important implications for diffusion at the higher reduced fields, as shown in the next section.

7.6 Longitudinal diffusion

At low field strengths where the drifting charge cloud has thermal energy, the diffusion coefficient can be approximated by its zero reduced field limit, $D(0)$[5]. This is related to the mobility and gas temperature through the Nernst-Townsend-Einstein relation:

$$\frac{D(0)}{\mu(0)} = \frac{kT}{e}, \tag{7.6.1}$$

where e is the ion charge [248]. At higher field strengths, diffusion can enter the non-thermal regime where it is given approximately by the generalized Einstein relations:

$$\frac{D_L}{\mu} = \frac{kT_L}{e} \left[1 + K' + \Delta_L K' \right] \tag{7.6.2}$$

$$\frac{D_T}{\mu} = \frac{kT_T}{e} \left[1 + \frac{\Delta_T K'}{2 + K'} \right], \tag{7.6.3}$$

where K' is the field derivative of the mobility, defined as

$$K' = \frac{d \ln \mu_0}{d \ln(E/N)} = \frac{E/N}{\mu_0} \frac{d\mu_0}{d(E/N)} \tag{7.6.4}$$

and Δ_L and Δ_T are correction terms with magnitude ranging from 0 to 0.20 for the longitudinal and transverse diffusion coefficients D_L and D_T, respectively [249].

---

[5]In this regime the charge cloud diffuses isotropically, so the longitudinal and transverse components, D_L and D_T, are the same and equal to $D(0)$.

These predict that deviations from $D(0)$ will occur when the field derivative of the reduced mobility becomes non-zero, which, according to the data shown in Figure 7.7, is expected for $E/N \sim 60-70$ Td for SF$_6^-$. In the non-thermal regime, the deviations in longitudinal diffusion, D_L, are proportional to this derivative and larger than those in transverse diffusion, D_T. In this work we only measure longitudinal diffusion and, by comparing it with the predictions of Equation 7.6.1, look for deviations from the thermal limit.

From Equation 7.6.1, a starting point-like charge cloud drifting over a distance, L, has a longitudinal diffusion width, σ_z, given by

$$\sigma_z^2 = 2D_L t = \frac{4\epsilon L}{3eE} = \frac{2kTL}{eE}, \tag{7.6.5}$$

where $t = L/v_d$ and $\epsilon = 3/2kT$ [247]. As our measurements are of pulse widths, we relate the diffusion in the time domain, σ_t, to σ_z using the drift velocity:

$$\sigma_z = \sigma_t \cdot v_d. \tag{7.6.6}$$

Customarily, diffusion is expressed by normalizing the measured value relative to the drift length:

$$\sigma_0 = \frac{\sigma_z}{\sqrt{L}} = \sqrt{\frac{2kT}{eE}}, \tag{7.6.7}$$

where σ_0 is typically expressed in units of $\mu\text{m}/\sqrt{\text{cm}}$.

The pulses used to measure diffusion of SF$_5^-$ and SF$_6^-$ were obtained from waveforms generated using ionization produced at the cathode, a known $L = 58.3$ cm drift distance, with the N$_2$ laser as described in Section 7.3.2. One thousand of these waveforms were averaged together at each pressure and electric field to increase signal-to-noise, resulting in the averaged waveforms shown in Figures 7.2, 7.3 and 7.4. As the SF$_5^-$ or SF$_6^-$ pulses are not strictly Gaussian, some care was required in extracting their widths. The main contribution to their non-Gaussianity is from the positive ion tail on the right side, whose origin was explained in Section 7.4.2. To minimize its effect, only a fraction of the left hand side of the waveform above 10% of
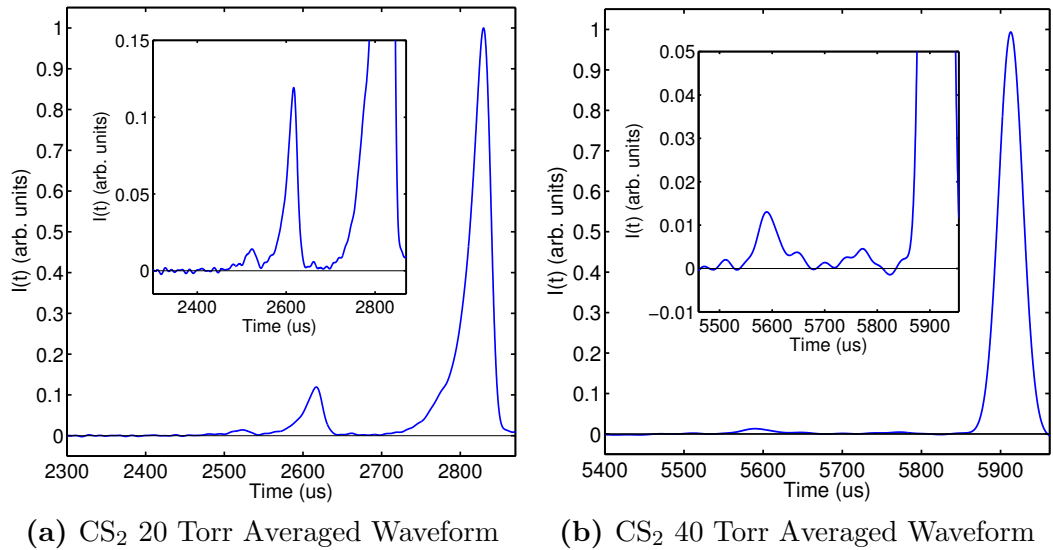
(a) CS$_2$ 20 Torr Averaged Waveform   **(b)** CS$_2$ 40 Torr Averaged Waveform

Figure 7.8: *(a) The averaged waveform for 20 Torr CS$_2$ at $E = 1029$ V·cm^{-1} showing the presence of a large secondary peak at ∼ 2600 μs and the possible appearance of two additional peaks at ∼ 2660 μs and ∼ 2520 μs (inset). In addition, the distortion in the waveform shape is clearly seen in both the primary and secondary peaks at this high reduced field. This behavior is not observed in the SF$_6$ waveforms at high reduced fields. (b) The average waveform for 40 Torr CS$_2$ at $E = 1029$ V·cm^{-1} which shows no clear secondary peaks or distortion in waveform shape.*

the peak was used to fit to a Gaussian curve. This fraction was determined iteratively by modeling the relative contributions of the collected charge signal and the positive ion induced signal to the pulse amplitude. Additionally, due to the broad structure from residual water vapor contamination at low reduced field (Section 7.4.2), only data with $E > 171$ V·cm^{-1} at 20 Torr and $E > 257$ V·cm^{-1} at 30 and 40 Torr were used.

Using this procedure we found σ_{fit}, which is mostly due to diffusion with small contributions from other effects. The latter are the smoothing time, σ_{smooth}, laser spot size, σ_{spot}, the spread in the electron-capture length, $\sigma_{\mathrm{capture}}$, and effects at the THGEM, σ_{THGEM}. We have no direct measurements of $\sigma_{\mathrm{capture}}$ or σ_{THGEM}, so we make no attempt to correct for them here. In our measurements, the laser spot size

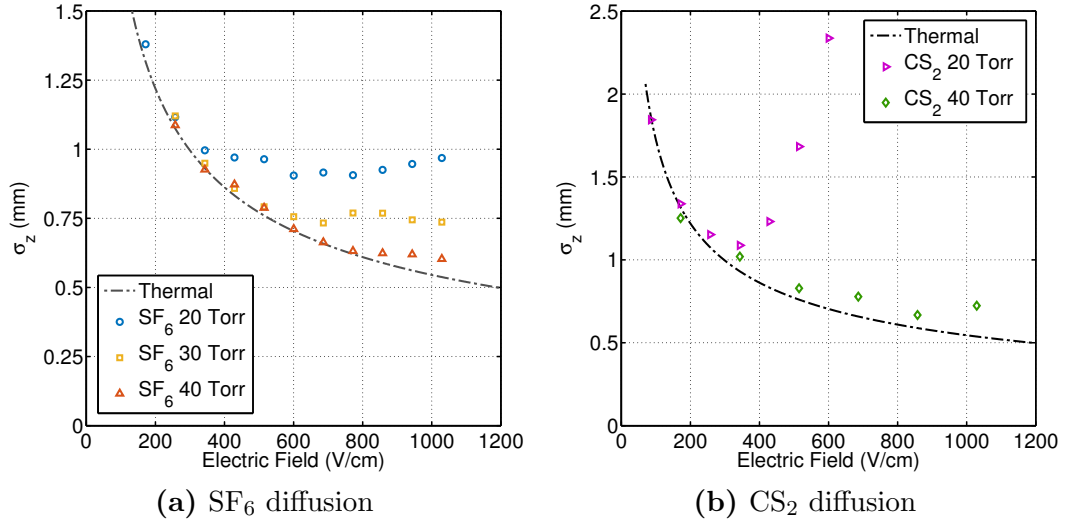**(a)** SF$_6$ diffusion   **(b)** CS$_2$ diffusion

Figure 7.9: *(a) The longitudinal diffusion, σ_z, for 20, 30, and 40 Torr SF$_6$ as a function of electric field for a drift length of 58.3 cm. The plotted quantity includes the broadening effects of the finite THGEM hole pitch as well as the capture process. The dot-dashed line shows the predicted width for thermal diffusion from Equation 7.6.5. For the 40 Torr data, the measured width begins to deviate away from the thermal prediction at ~ 800 V·cm^{-1}. Similarly for the 30 Torr and 20 Torr data, deviations from thermal diffusion occur at ~ 600 V·cm^{-1} and 400 V·cm^{-1}, respectively. (b) The fitted pulse width for 20 and 40 Torr CS$_2$. At 20 Torr the pulse width begins to deviate considerably from thermal at ~ 400 V·cm^{-1}. The corresponding distortion seen in the waveform in Figure 7.8a could, however, also be due to a longer electron capture mean-free-path at high E/p (refer to the text).*

contribution to the longitudinal width is negligible, so we set $\sigma_{\mathrm{spot}} \sim 0$. Thus, assuming no correlation, we subtract σ_{smooth} from σ_{fit} in quadrature to get the diffusion width in time:

$$\sigma_t = \sqrt{\sigma_{\mathrm{fit}}^2 - \sigma_{\mathrm{smooth}}^2}. \tag{7.6.8}$$

Using Equation 7.6.6, we finally get σ_z, the longitudinal spread of the charge distribution in space due to diffusion. The systematics on σ_z, mainly due to not accounting for $\sigma_{\mathrm{capture}}$ and σ_{THGEM}, are briefly discussed below.

The same fitting procedure was applied to our CS$_2$ data taken at 20 Torr (Figure 7.8a) and 40 Torr (Figure 7.8b). The 20 Torr, high reduced field waveform shown

in Figure 7.8a appears distorted on the left and has at least one additional secondary peak at ~ 2600 µs. These features are discussed in Section 7.6.4.

7.6.1 σ_z results

In Figure 7.9, the longitudinal diffusion, σ_z, is plotted as a function of electric field for 20, 30, and 40 Torr SF$_6$ and 20 and 40 Torr CS$_2$ data. Overlaid are curves for thermal diffusion calculated using Equation 7.6.5. In the 40 Torr SF$_6$ data, σ_z begins to deviate from the thermal prediction at around 800 V·cm^{-1}. Similarly, in the 30 Torr and 20 Torr SF$_6$ data, deviations from thermal diffusion occur at around 600 V·cm^{-1} and 400 V·cm^{-1}, respectively. In terms of the reduced field, the deviations all begin to occur at approximately $E/p = 20$ V·cm^{-1}·Torr or $E/N = 60$ Td. This is close to our estimate above of $E/N \sim 60 - 70$ Td based on the generalized Einstein relations.

The 40 Torr CS2 diffusion data shown in Figure 7.9 indicate a larger systematic than observed for SF$_6$. This is likely due to a longer mean free path for electron capture and is discussed further below in Section 7.6.2. Assuming that this systematic is field independent, the data appear to follow thermal diffusion out to $\sim$500 V·cm^{-1} (38 Td) and perhaps even to $\sim$800 V·cm^{-1} (61 Td). Precision measurements of σ_z [140] have confirmed thermal out to 23 Td and other measurements indicate that the low field approximation applies to CS$_2$ out to $\sim$42 Td.

At 20 Torr we observe a distortion in the waveform at high reduced fields and one or more smaller peaks begin to appear (Figure 7.8a), which also grow with E/p. The effect of the distortion on σ_z begins at $\sim$50 Td and is dramatic as seen in Figure 7.9. The origin of the distortion could be a deviation from thermal diffusion or a growing inefficiency in electron capture at high E/p, which naturally explains the observed tail on the fast side of the waveform. The fact that the reduced mobility has a weaker dependance on E/p than SF$_6^-$ (Figure 7.7) also points to electron capture. Measurements of the lateral diffusion should help determine which of these effects

dominates. The secondary features are discussed in Section 7.6.4.

7.6.2 Systematics on σ_z

Here we place bounds on the two primary sources of systematics to the measured diffusion width, the spread in the electron-capture mean-free-path and non-uniformity of the electric field near the THGEM. Given how well matched our σ_z values are to the diffusion limit at low reduced fields (Figure 7.9), any non-diffusion contributions cannot be large. At low reduced fields in 40 Torr CS$_2$, an upper bound on the spread in capture distance of 0.35 mm was estimated by Ref. [140]. Based on measurements of the attachment cross-section in SF$_6$, the mean free path for attachment in our experimental apparatus should be of order $\sim$1-10 µm and, hence, a negligible contribution to σ_z. The broadening effect due to the non-uniformity in the drift field close to the THGEM should depend on the THGEM pitch, and the fields in the holes and TPC drift region. This can be modeled but we can provide an upper bound estimate based on the low E/p region of the SF$_6$ data in Figure 7.9a, where we expect thermal diffusion. The σ_z data in this region are systematically slightly higher than the thermal prediction, thus, assigning the difference taken in quadrature to the THGEM, gives the upper bound of $\sigma_{\mathrm{THGEM}} < 0.2$ mm.

In 40 Torr CS$_2$, the systematic differences in the low E/p regime (Figure 7.9b) are larger than in SF$_6$, which is probably due to a longer electron capture distance as discussed above. Assuming that the contribution from the THGEM is the same for both gases, $\sigma_{\mathrm{THGEM}} \sim 0.2$ mm, we can assign the remaining difference to the spread in electron capture distance in CS$_2$. This gives $\sigma_{\mathrm{capture}} \sim 0.3$ mm, which is within the upper bound for CS$_2$ from Ref. [140] given above. In the 20 Torr CS$_2$ data we speculate that the large deviation in σ_z from thermal observed above 50 Td is due to inefficient electron capture, rather than diffusion. Measurements of lateral diffusion will help test this hypothesis. A more accurate estimate for the sum total of non-diffusion contributions, including σ_{THGEM} and $\sigma_{\mathrm{capture}}$, can also be determined

by measuring the waveform width as a function of drift distance. This is left for future work.

7.6.3 Implications for directional low-mass WIMP searches

For dark matter searches in the low, ~ 10 GeV/c^2, WIMP mass regime, the lowest possible energy thresholds are desired. For directional DM searches in low pressure TPCs, as discussed in some detail in Ref. [118], the ability to lower the pressure lengthens the tracks, which, in principle, will lower the *directional* energy threshold. With the assumption that the minimum track length for which directionality can be detected is an invariant, and using data at 100 Torr, Ref. [118] showed that pressures in the range $\sim 5-10$ Torr would be optimal for maximizing sensitivity for directional low mass WIMPs searches. This assumption requires that physical effects that could impact track reconstruction, such as diffusion, do not worsen at lower pressures.

In this regard, our measurements of diffusion at 20 Torr for both SF$_6$ and CS$_2$ provide an important data point to test this assumption. As discussed above and shown in Figure 7.9a, deviation from thermal diffusion in our SF$_6$ data occur at $\sim$70 Td at all pressures. At lower pressures, $\sim$70 Td corresponds to a lower drift field where thermal diffusion is higher, as can be seen in Figure 7.9a. Thus, in 20 Torr SF$_6$ the minimum longitudinal diffusion observed in our data is $\sigma_z \sim 0.9$ mm, quite a bit higher than the $\sigma_z \sim 0.63$ mm in 40 Torr. This means that the minimum track length with directionality is about 1.5 times longer at 20 Torr than at 40 Torr. If the trend we observe continues at lower, $10-15$ Torr pressures, it may impose a fundamental limit on the directional energy threshold imposed by diffusion.

For CS$_2$, the data at 20 Torr shown in Figures 7.8a and 7.9b are difficult to interpret from the diffusion perspective. As discussed above, the long tail on the fast side of the waveform is characteristic of electron capture mean free path, but this requires confirmation. This hypothesis is nevertheless supported by the mobility data of Figure 7.7, which suggests that diffusion in CS$_2$ is deviating less from thermal,

and at higher reduced fields, than SF$_6$.

It is clear that further detailed studies of diffusion for both CS$_2$ and SF$_6$ are needed to settle these questions. These should include measurements of the transverse component, and estimates of the systematics, which, together with the measurements in this work will provide better constraints on the possibility of directional low mass WIMP searches.

Nevertheless, the current data can be used to provide a reasonable estimation of the behavior of the tracking resolution with pressure. At low reduced fields, the tracking resolution defined as, $M \equiv \sigma(E)/R \propto \sigma(E) \cdot p$, is inversely proportional to the track range, R, and proportional to the pressure, p. Thus, M is defined as the minimum resolvable track range and reducing the pressure by a factor of two will improve the resolution by the same factor. However, at high reduced fields the scaling no longer holds because to stay within the thermal limit the electric field must also be reduced by the same factor to keep E/p constant and below the critical non-thermal reduced field. Because $\sigma \propto 1/\sqrt{E}$, lowering E raises the diffusion by the square root of the reduction factor. Hence, the best attainable resolution at a given pressure will improve by $\sqrt{f_p}$, where $f_p = p_1/p_2$ is the pressure reduction factor. Of course, this is only an approximate relation because from Figure 7.9a, the diffusion does, in fact, decrease slightly or remains constant for electric fields beyond the critical value where a deviation from thermal behavior is observed. Nevertheless, the approximate relation provides a reasonable estimation for the best attainable resolution at a given gas pressure. But even this approximate scaling will eventually break down at very low pressures as the electron capture length becomes a significant contribution to a diffusive-like spread in the track. The behavior of σ_z in 20 Torr CS$_2$ indicates this eventual outcome.

7.6.4 Secondary peak in CS$_2$

Finally, we return to the small, secondary peak observed in the 20 Torr CS$_2$ data shown in Figure 7.8a. This feature first appears at a drift field of $E = 343$ V·cm^{-1} at 20 Torr CS$_2$ and has a drift speed that is ∼6.2% faster than, and an amplitude only 0.4% that of the primary peak. When the drift field is increased to $E = 686$ V·cm^{-1}, the secondary peak's drift speed and amplitude increase to 6.8% and 4.6%, respectively, relative to that of the primary peak. Finally, at $E = 1029$ V·cm^{-1}, the secondary peak is about 7.5% faster than the primary while its amplitude continues to grow and reaches about 11.7% of the primary's peak value (Figure 7.8a). In the 40 Torr CS$_2$ data there is a hint of a secondary peak at the highest field, $E = 1029$ V·cm^{-1}, which is a factor of ∼10 lower in amplitude than the main secondary peak seen at 20 Torr.

Additional negative ion species have been observed in CS$_2$ gas mixtures when a small amount of O$_2$ is added [179]. In Ref. [179], at least three additional negative ion species (minority peaks) were reported, all with higher mobilities than CS$_2$, and peak amplitudes that grow, relative to the main CS$_2^-$ peak, with the O$_2$ fraction. The amplitude of the largest of these three peaks is approximately a factor 2× larger than the next highest, and this ratio is maintained independent of the O$_2$ fraction or drift field, up to $E = 580$ V·cm^{-1} [179, 111]. The only variable that affects the relative amplitudes appears to be the drift distance; increasing this lowers the amplitude of the middle peak. To date, the physical mechanism behind the minority peaks in the CS$_2$/O$_2$ mixture is unknown.

For a number of reasons, the secondary peak seen in our 20 Torr CS$_2$ data is unlikely to be one of the minority peaks due to O$_2$ contamination: we see only one peak whereas three should clearly be visible; our secondary peak's amplitude increases by an order of magnitude with E from 343 V·cm^{-1} to 686 V·cm^{-1}, but no significant variation in the minority peak amplitudes was observed over the range $E \sim 270 - 580$ V·cm^{-1} in Ref. [179]; a secondary peak is barely visible in our 40 Torr

data, which was acquired in similar conditions to the 20 Torr data.

We also note that although our acrylic TPC was a source of water vapor from out-gassing, as discussed in Section 7.4.3, the permeability coefficient of water vapor in acrylic is over three orders of magnitude larger than for O_2. Thus, the level of O_2 is probably too low to affect our data at the level seen in Figure 7.8a, which given all the other inconsistencies of this hypothesis, indicates a different origin for the small peak.

A more likely hypothesis is that the peak is due to S^- or CS^-, which are known products of the auto-dissociation of CS_2^{-*} [250, 251], similar to how SF_5^- is produced via Equation 7.4.4. The cross-sections for both S^- and CS^- production via this mechanism are non-zero at zero electron energy and peak at 0.5 eV and 1.2 eV, respectively. The S^- peak is narrower and larger by a factor $\sim$20 than that for CS^-. This suggests that our secondary peak is due to S^-, and also explains its rapid fractional increase with E described above since the S^- production cross-section increases with electron energy in the $0 - 0.5$ eV range.

7.7 Gas gain

Previous works have shown that gas gains greater than 1000 can be achieved in electronegative gases with proportional wires [252], GEMs [253], and bulk Micromegas (Micro Mesh Gaseous Structure) [254]. In contrast to electron gases where only moderate electric fields of order 100 V·cm^{-1}Torr^{-1} are needed to accelerate electrons to energies close to the ionization potential of the gas, electronegative gases require much higher electric fields to initiate avalanche even though the electron affinity is usually much lower than the ionization potential [255]. For CS_2, measurements show that the minimum reduced field, $(E/p)_{\mathrm{min}}$, needed to initiate avalanche is over one order of magnitude larger than for the electron drift gas P10 (10% methane in argon) [255]. A similar study can be done for SF_6, but in this section we omit a discussion

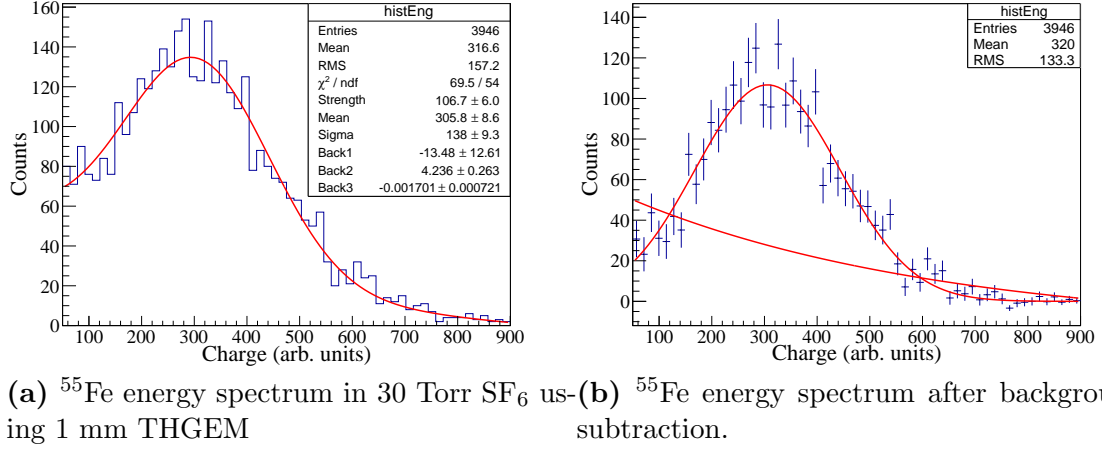of the detailed mechanism for avalanche and instead focus on the gas gains.

(a) ^{55}Fe energy spectrum in 30 Torr SF$_6$ us-**(b)** ^{55}Fe energy spectrum after background
ing 1 mm THGEM   subtraction.

Figure 7.10

(a) ^{55}Fe energy spectrum in 30 Torr SF$_6$ us-**(b)** ^{55}Fe energy spectrum after background
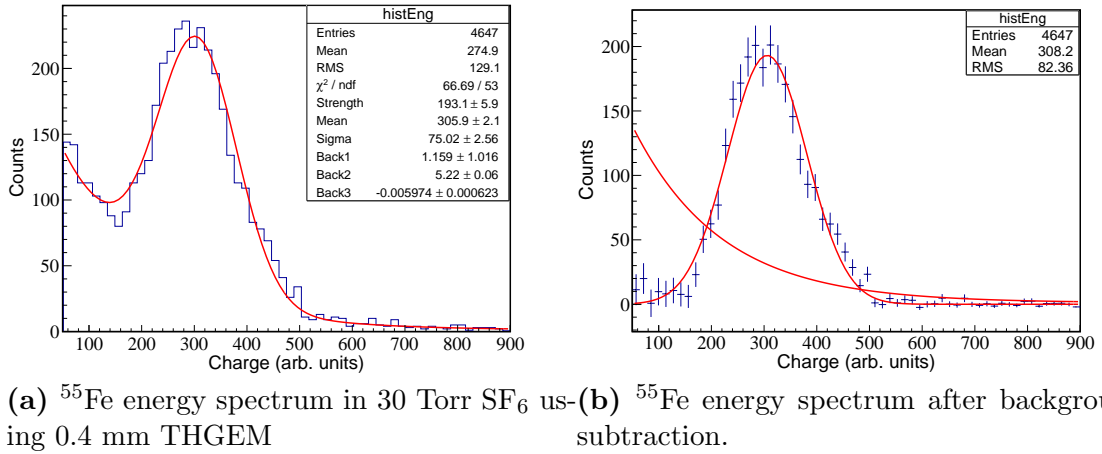ing 0.4 mm THGEM   subtraction.

Figure 7.11

Two THGEMs of thickness, 0.4 mm and 1 mm were used to achieve gas gain
in SF$_6$. Other than the thicknesses, the pitch and other THGEM parameters were
the same as those described in Section 7.3.1. To measure the gain an ^{55}Fe 5.89 keV
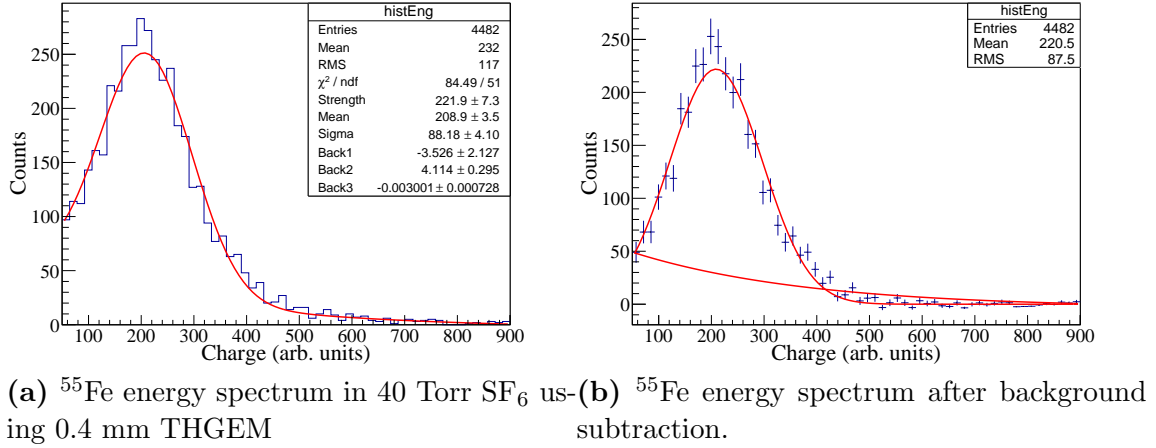
(a) ^{55}Fe energy spectrum in 40 Torr SF$_6$ using 0.4 mm THGEM

(b) ^{55}Fe energy spectrum after background subtraction.

Figure 7.12

X-ray source was employed. To convert the energy of the X-ray into the number of electrons produced during the initial conversion process, we used the W-factor, defined as the mean energy required to create a single electron-ion pair. For SF$_6$, this value has been measured using α particles [256] and a ^{60}Co γ source [257], giving W$_\alpha$ = 35.45 eV and W$_\gamma$ = 34.0 eV, respectively. The slight disagreement is actually consistent with other measurements of W-factors, which find that W$_\alpha$ exceeds W$_{\gamma,\beta}$ for molecular gases [258]. Because we used an X-ray source, we adopt the W-factor from Ref. [257], so the average number of primary electrons, N_p, created by an ^{55}Fe X-ray conversion in SF$_6$ is

$$N_p = \frac{E_{^{55}\text{Fe}}}{W_\gamma} = \frac{5.89 \text{ keV}}{34.0 \text{ eV}} \simeq 173. \tag{7.7.1}$$

The effective gas gain is then given by,

$$G_{\text{eff}} = \frac{N_{\text{tot}}}{N_p}, \tag{7.7.2}$$

where N_{tot} is the total number of charges read out with the preamplifier. In general, this is less than the total number of charges produced in the avalanche due to inefficient charge collection, hence, the measured gain is an effective and not an absolute

value. In our case, essentially all of the electrons produced in the avalanche were collected, but there was an additional contribution to the pulse from the positive ion induced signal. This systematic was not removed. To determine N_{tot} from the measured voltage pulse, $V(t)$, the standard calibration procedure of injecting a known charge into the preamplifier was used. For this we used an ORTEC 448 Research Pulser to inject charge into the 1 pF calibration capacitor inside the ORTEC 142 preamplifier.
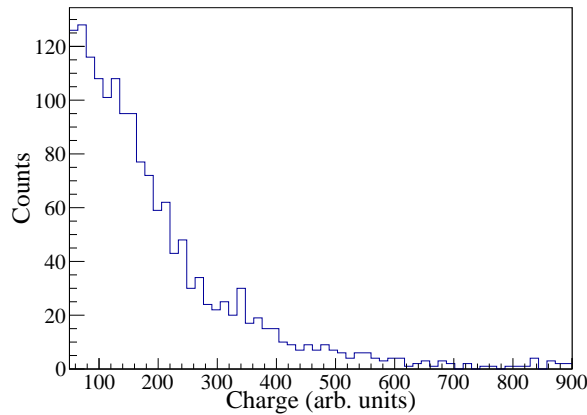

Figure 7.13: *An ^{55}Fe spectrum acquired in 60 Torr SF$_6$ using a 0.4 mm THGEMs. The peak is not observable due to a combination of low gain and large energy resolution. However, there is a clear rate difference between ^{55}Fe source on versus off, indicating there is indeed sufficient gas gain for detecting these low-energy events.*

For the gain measurement at each pressure, the THGEM voltage was raised until ^{55}Fe events were visible on the oscilloscope. The voltage ramp continued until energetic sparks were observed and/or until the rate of micro-sparks and background events approached that of the ^{55}Fe source. Figures 7.10a and 7.11a show the spectra acquired in 30 Torr SF$_6$ using a 1 mm and 0.4 mm THGEM, respectively. The spectrum taken with the 1 mm THGEM (Figure 7.10a) is much broader, indicating a worse energy resolution, than that taken with the 0.4 mm THGEM spectrum (Figure 7.11a). Figures 7.12a and 7.13 show the spectra acquired in 40 Torr and 60 Torr, respectively, both using the 0.4 mm THGEM. For the 60 Torr spectrum

the maximum stable gas gain was not sufficient to clearly resolve the peak above background. However, there was a clear rate difference above the trigger threshold when the ^{55}Fe source was switched on and off, indicating that the tail of the ^{55}Fe distribution is contained in the spectrum. At 20 and 100 Torr a similar rate difference was observed between source on and off using the 0.4 mm THGEM, but spectra were not acquired due to instability.

None of the spectra are Gaussians, but contain an extra exponential component due to micro-sparks and background events. To better identify the background and signal components and quantify their shapes, the spectra were fit with a Gaussian signal component, and an exponential plus constant for the background component. The fitted total spectrum and the separated signal and background components are shown in Figures 7.10a and 7.10b for the 30 Torr data acquired with the 1 mm THGEM. The reduced chi-square (χ^2/ndf) of the fit is 1.29. Similar fits are shown in Figures 7.11a and 7.11b for the 30 Torr data, and Figures 7.12a and 7.12b for the 40 Torr data, both acquired with the 0.4 mm THGEM. The reduced chi-squares for these fits are 1.26 and 1.66, respectively.

The mean of the Gaussian fit was used to derive the effective gas gain and the width gave the energy resolution, both of which are tabulated in Table 7.1 for each experimental configuration. Other important parameters that describe the operating conditions for the different gain measurements are also listed there to aid in interpreting our results. Of these, the reduced field inside the THGEM holes, E_h/p, will be most useful in understanding the differences in the energy resolution and gas gains shown in Table 7.1. The electric field, E_h, in the THGEM was approximated by $\Delta V/d$, where ΔV is the voltage across the THGEM and d is its thickness.

The spectra shown in Figures 7.10 - 7.13, with the corresponding gas gains and energy resolutions summarized in Table 7.1, can be understood with some knowledge of the physical processes governing the avalanche process in negative ion gases. These processes involve stripping the electron from the negative ion, which initi-

ates the avalanche, and the recapture of electrons by SF$_6$ in the avalanche, both of which can negatively impact gas gain and energy resolution. The stripping will occur at some depth, z, inside the THGEM hole that is determined by the electron detachment mean-free-path, λ_{detach}, a function of the reduced field. A large λ_{detach}, relative to the THGEM thickness, d, will lead to a larger average depth, z, where the avalanche begins, resulting in lower gas gains, larger gain fluctuations, and worse energy resolution.

In addition, the avalanche process in negative ion gases will suffer from a competition with recapture on the neutral molecule or its fragments produced in the THGEM holes (e.g., by auto-dissociation). In SF$_6$, although the cross-sections for attachment fall with electron energy, the higher electron energies in the THGEM will favor auto-dissociation to SF$_5^-$, SF$_4^-$, SF$_3^-$ and F$^-$[6], over collisional stabilization to SF$_6^-$, and these fragments have higher electron affinities than SF$_6^-$ (1.06 eV) [208]. Regardless of the details, if recapture occurs the avalanche is halted momentarily until the electron can be stripped again, which further suppresses the gain and worsens energy resolution. As the cross-sections for attachment, dissociation, and ionization of SF$_6$ and its fragments depend on the electron energy, the distinctive spectral shapes, energy resolutions, and gas gain must originate from the dependence on the reduced field in the THGEM.

With this overview, we can attempt to understand the spectra shown in Figures 7.10 - 7.13 (also refer to Table 7.1). A comparison of the 30 Torr spectra taken with the 0.4 mm and 1 mm THGEMs shows a factor $\sim$2 worse energy resolution in the 1 mm THGEM. This difference is clearly due to the 2$\times$ lower reduced field, E_h/p, in the 1 mm THGEM, which, as discussed above, will lead to a larger λ_{detach} and higher probability of recapture, both of which will lead to the large gain fluctuations that result in poor energy resolution. If the 1 mm THGEM could have sustained a

---

[6]The electron affinities of SF$_5$, SF$_4$, SF$_3$, and F are $2.7 - 3.7$ eV [239], 1.50 eV [260], 1.84 eV [260], and 3.4012 eV [259], respectively.

larger ΔV, leading to a higher E_h/p in the holes, a potentially much larger gas gain and better energy resolution could have resulted.

Next, we look at the differences between the 30 and 40 Torr spectra, both taken in the 0.4 mm THGEM. The energy resolution in 40 Torr is almost 2× worse, nearly as poor as for the 30 Torr data taken in the 1 mm THGEM. Here again, it is due to the lower reduced field in the 40 Torr case, $E_h/p = 550$ kV·cm^{-1}, relative to that for the 30 Torr case, $E_h/p = 683$ kV·cm^{-1}. The fact that the E_h/p lies closer to the 30 Torr, 0.4 mm case then to the 40 Torr, 1 mm case, indicates that either λ_{detach} or the attachment probability depend strongly on energy. Which of these variables dominates in the effects we see here is not known at this time. We note, however, that although the reduced fields differ, the electric fields are comparable for the two cases, $E_h \sim 20$ kV·cm^{-1}, which supports our claim that the relevant processes are governed by E_h/p.

The low gas gains at the higher $60 - 100$ Torr pressures were also due to low E_h/p, which we were unable to sustain at the levels achieved at low pressures. In the 60 Torr 0.4 mm THGEM data, we could only reach $E_h/p = 425$ kV·cm^{-1}, which was insufficient to raise all ^{55}Fe events above the trigger threshold. This along with the broadening of the peak at low avalanche reduced field cause the peak in the spectrum to fall below the range shown in Figure 7.13. Multiple THGEMs should work at higher pressures and other MPGD devices, such as thin GEMs and Micromegas, should be attempted as well. The latter two could also achieve much higher reduced fields, albeit over a shorter avalanche region, which could help with improving the energy resolution. These are interesting questions for future studies.

Table 7.1: *THGEM parameters and results*

d (mm)	p (Torr)	ΔV (V)	E_h (kV·cm^{-1})	E_h/p (V·cm^{-1}Torr^{-1})	G_{eff}	$\sigma/\mathcal{E}$ (%)
0.4	30	820	20.50	683	3000	25
1.0	30	1005	10.05	335	3000	45
0.4	40	880	22.00	550	2000	42
0.4	60	1020	25.50	425	-	-

7.8 Event fiducialization

7.8.1 ^{252}Cf data

We showed in Figure 7.2 of Section 7.4.2 that at high drift fields, the waveform of the charge arriving at the anode consists mainly of the two SF$_5^-$ and SF$_6^-$ peaks. Having two or more species of charge carriers with differing mobilities is critical for event fiducialization in gas-based TPCs employed in dark matter and other rare event searches. The ability to fiducialize in these experiments allows for the identification and removal of the most pernicious backgrounds, which originate at or near to the inner surfaces of the detector. While identifying the event location in the readout plane (X,Y) of a TPC is straightforward, locating the event along its drift direction (Z) is challenging. Unlike in accelerator-based experiments, the time of interaction (T$_0$) in a gas-based TPC used for rare searches is not available, so Z-fiducialization had proven difficult. The recent discovery of minority charge carriers in CS$_2$ + O$_2$ mixtures [179], has changed this by allowing the differences in their mobility to be used to derive the Z coordinate of the event. This has transformed the DRIFT dark matter experiment [111], which, until this discovery, had operated for close to a decade with backgrounds from radon progeny recoils at the TPC cathode that severely impacted the dark matter search [206, 261, 141, 163, 164].

The differences in the SF$_5^-$ and SF$_6^-$ mobilities in pure SF$_6$ can be used in a similar

manner to measure the Z coordinate of the event through the relation:

$$Z = \frac{v_s \cdot v_p}{v_s - v_p} \Delta T, \tag{7.8.1}$$

where v_p and v_s are the drift speeds of the negative ions in the primary (SF_6^-) and secondary (SF_5^-) peaks, respectively, and ΔT is the time separation of the peaks. Note that the anode (THGEM) is at $Z = 0$, and the cathode at $Z = 58.3$ cm.
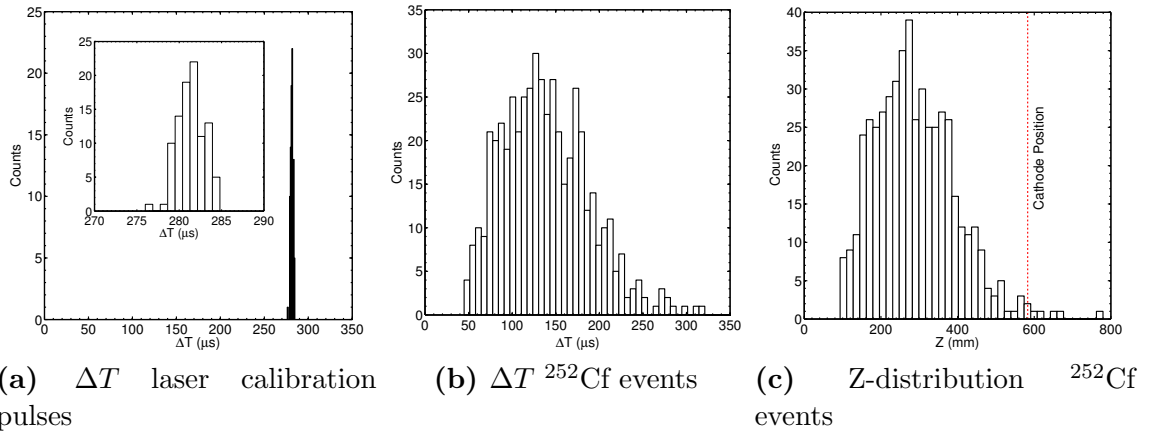

(a) ΔT laser calibration pulses   **(b)** ΔT ^{252}Cf events   **(c)** Z-distribution ^{252}Cf events

Figure 7.14: *(a) Distribution of the time difference between secondary, SF_5^-, and primary, SF_6^- peaks (ΔT) for the laser calibration pulses obtained in 30 Torr SF$_6$ and $E = 1029$ V·cm^{-1}. (b) The same distribution for triggered events that passed analysis cuts from the ^{252}Cf data shows a broad distribution of Z locations. (c) The distribution of the Z locations of events from the ^{252}Cf run after analysis cuts The vertical line shows the position of the cathode at $Z = 58.3$ cm. The events with Z locations greater than the cathode location are those that misidentified peaks. There are no events below 10 cm due to the fact that the two peaks are not separable for drift distances less than this.*

To test how well one can determine the location of events in SF$_6$ using this method, we used a ^{252}Cf source to generate ionization events at different locations in the detection volume. The ^{252}Cf source was placed near the outside surface of the vessel and about 20 cm from the cathode. The detector was operated at 30 Torr with $E = 1029$ V·cm^{-1} where the highest gas gains were achieved (Section 7.7). This was important for identifying the small SF$_5^-$ peak in low energy recoils, which produce less ionization than the nitrogen laser illuminating the cathode. Preceding the ^{252}Cf run,
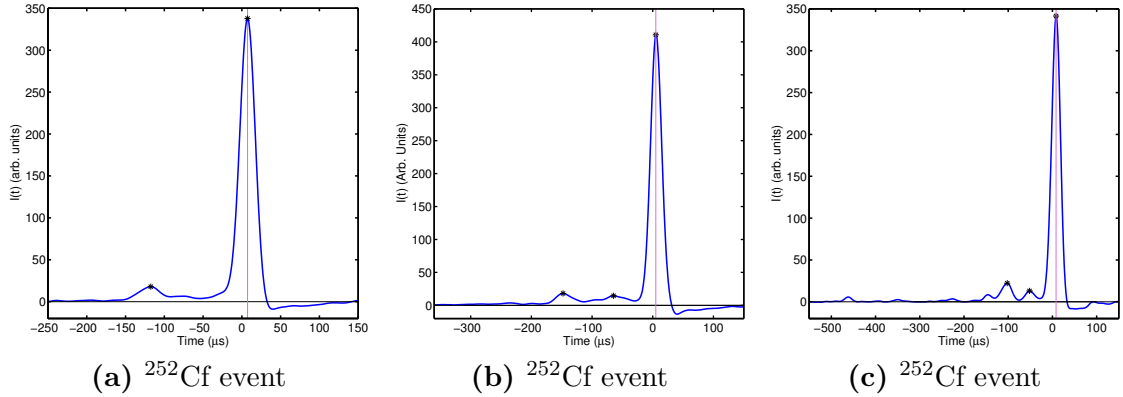
(a) ^{252}Cf event   **(b)** ^{252}Cf event   **(c)** ^{252}Cf event

Figure 7.15: *(a) An event from the ^{252}Cf run in 30 Torr SF$_6$ and $E = 1029$ V·cm^{-1} showing two distinct peaks. The black markers identify the locations of peaks detected by peak finding algorithm. The magenta vertical line passing through the black marker passes through the location of the primary, SF$_6^-$, peak. (b) An event from the same data run with three detected peaks. (c) An event with as many as five peaks; three are detected by the peak finding algorithm.*

an energy calibration was done with an internally mounted ^{55}Fe source. In addition, to calibrate ΔT we pulsed the laser onto the cathode to generate ionization from a known, fixed Z location.

The SF$_5^-$ and SF$_6^-$ peaks were found through an automated process using a derivative based peak finding algorithm. Although the algorithm performs efficiently for a large data-set, the derivative based approach tends to give false peak detections for noisy data. To reduce the chance of false peak detections affecting the accuracy of Z, we only accepted events that have two and only two identified peaks, one corresponding to SF$_5^-$ and the other to SF$_6^-$. This greatly reduced the efficiency of our analysis, but our aim here was only to demonstrate event fiducialization in SF$_6$, with work on increasing the efficiency left for future work. In addition, only events with energy > 60 keVee were accepted so that the SF$_5^-$ peaks were more easily identified, and also to better aid discrimination against electronic recoils due to the gamma-rays from the ^{252}Cf source.

The distribution of the time difference, ΔT, between the SF$_5^-$ and SF$_6^-$ peaks for

the laser calibration data is shown in Figure 7.14a. The distribution has a mean of 281.3 μs (583.5 mm) and FWHM of about 3.5 μs (7.3 mm), demonstrating the fundamental accuracy and precision of fiducialization in SF$_6$. The distribution of the same timing parameter from the ^{252}Cf run is shown in Figure 7.14b. The mean and shape of the distribution grossly agree with expectations based on the location of the source, which results in a larger solid angle intersecting the detector volume on the anode side. Note that there are no events seen with $Z < 10$ cm because the SF$_5^-$ and SF$_6^-$ peaks cannot be resolved individually at low Z by our simple peak finding algorithm.

A sample event from the ^{252}Cf exposure with a relatively well-defined SF$_5^-$ peak is shown in Figure 7.15a, demonstrating the feasibility of fiducialization on an event by event basis. Also note that the relative amplitude of the SF$_5^-$ and SF$_6^-$ peak in this event is 5.3%, higher than the laser generated ionization data from Section ref-sec:relativeratios at the same reduced field, and for some events in our dataset, the relative amplitude exceeded 8%. This could be explained by the fact that the energies of electrons created by a nuclear recoil could be significantly higher than those produced by laser illumination of the cathode, and higher than the energy gained from the drift field before capture.

Examples of events demonstrating this effect is shown in Figures 7.15b and 7.15c. These events possess more than two peaks, indicating that other negative ion species besides SF$_5^-$ and SF$_6^-$ are being produced due to the initial energies of liberated electrons. This adds a complication into the analysis to determine the event location, which requires further study. On the other hand, the sensitivity of the relative strength of the SF$_5^-$, SF$_6^-$, and other peaks to electron energies could open up possibilities beyond fiducialization. One potential application is for discriminating between electron and nuclear recoils. If the distribution of electron energies created by an electron recoil is characteristically distinct from the one created by a nuclear recoil, than the relative charge in the peaks could be used to identify the type of particle

that created the ionization.

7.8.2 Secondary peak enhancement

The efficiency with which one can fiducialize in SF$_6$ is largely dictated by how well the relatively small SF$_5^-$ peak is detected. Here we consider a few possible approaches that might enhance its relative abundance.
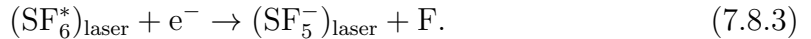
The first, motivated by the behavior of the minority peaks in CS$_2$ + O$_2$ gas mixtures [179], is to add a small amount (< 1 Torr to a few Torr) of O$_2$ into SF$_6$. We attempted this and, not surprisingly, saw no significant change in the relative abundance of SF$_5^-$. Another approach that is motivated by the energy dependence of the SF$_5^-$ and SF$_6^-$ production cross-sections, which favors a larger SF$_5^-$/SF$_6^-$ ratio at higher electron energies, is to operate at higher reduced drift fields. Depending on how high one needs to operate at, this could increase diffusion to unacceptable levels (Figure 7.9a).

Perhaps, the most straightforward path, however, is to increase the gas gain, thereby increasing the overall signal-to-noise for detecting the SF$_5^-$ peak. As the gains in our measurements with a single THGEM are already at or close to the maximum, two or more THGEMs as well as other MPGD amplification devices should be attempted. As discussed at length in Section 7.7, amplification devices with the highest possible reduced fields are desired to counteract the physical effects in a negative ion gas that compete with avalanche production. This is especially important for SF$_5^-$, which, due to its high electron affinity, would benefit from high E/p to efficiently strip the electron and initiate the avalanche.

There also exists an interesting alternative method to increase the production of SF$_5^-$ in SF$_6$. A study of the production cross-section for SF$_5^-$ by auto-dissociation has shown that the first peak at ~ 0.0 eV is very sensitive to temperature [262]. Over the temperature range 300 K to 880 K, the relative cross-section for the formation of SF$_5^-$ increases by about two orders of magnitude for electron energies ~ 0.0 eV,

while the cross-section hardly varies for energies near the second peak at 0.38 eV.

Since increasing the gas temperature effectively raises the vibrational and rotational excitation energy of the SF$_6$ molecules, this led Ref. [262] to consider the possibility of the photo-enhancement of SF$_5^-$ production via the processes:

$$n(hv)_{laser} + SF_6 \rightarrow (SF_6^*)_{laser} \tag{7.8.2}$$

$$(SF_6^*)_{laser} + e^- \rightarrow (SF_5^-)_{laser} + F. \tag{7.8.3}$$

Using a CO$_2$ laser $(9.4-10.6\,\mu m)$ to vibrationally excite SF$_6$ molecules, they observed an enhancement of SF$_5^-$ production that was radiation wavelength dependent and different for ^{32}S and ^{34}S isotopes. It should be noted that infrared excitation should not result in photodetachment of the SF$_6^-$ anion as measurements have shown that the threshold for this process is at 3.16 eV (392 nm) [263]. Nevertheless, implementing this idea or increasing the gas temperature for large TPCs presents practical challenges that must be weighed against any benefit. These are experimental questions that require further investigation.

7.9 Conclusion

We have shown that gas gain is achievable in a low pressure gas detector with SF$_6$ as the primary gas. Signals from low energy ^{55}Fe events were detected using 0.4 mm and 1.0 mm THGEMs with gains of between 2000-3000. The energy resolution appear to depend on the reduced field in the amplification region, implying that electron detachment and re-attachment in this high-field region could be responsible. Testing other GEM geometries and amplification devices in SF$_6$ to achieve even better gain and energy resolution could be the subject for future work.

The acrylic cylindrical detector design used in this work allowed for high reduced field operation and made possible the detection of unique features in SF$_6$ waveforms,

particularly the evolution of the waveform shape with reduced field and the identification of the SF$_5{}^-$ peak through its mobility. Using this secondary peak, we showed that fiducializing events in the drift direction is possible. Diffusion measurements showed thermal behavior for both SF$_6$ and CS$_2$, but only up to a critical reduced field. This has important implications for the optimization of tracking detectors utilizing these negative ion gases. There are features and behavior that remain unexplained, but these unanswered questions should provide ample motivation and opportunities for future studies on the use of SF$_6$ in TPCs.

Chapter 8

Novel High-Resolution Tracking Readout

8.1 Motivation

In a negative ion TPC (NITPC), the Z component of an ionization track can be measured by the length of time of the signal pulse because the drift velocity of the ions and electric field are known with sufficient precision. The X and Y components are usually measured with fine-pitched orthogonal wire grids, 2D strip readout boards, pixelated chips, or optical cameras. There are, however, several downsides to these methods. One is that the spatial resolution is limited by the pitch of the readout, which is typically ~ 1 mm for wires and down to ~ 400 µm for strips. Pixel boards can offer resolution on the order of ~ 10 µm but at the cost of an extremely large number of channels (N^2, where N is the number along each dimension) for large readout areas. The problem is exasperated if higher resolution is required. For example, to uniquely (no grouping or multi-plexing of channels) read out just the X dimension in a 4 cm region with a strip board at a pitch of 400 µm would require 10^2 channels. A coarser readout pitch would allow for a reduction in the number of channels but would negatively impact the ability to measure directionality in the lowest energy

nuclear recoils, something critical for a directional dark matter search.

Knowledge of the electric field and drift speed of the negative ions allows for the Z dimension of a track to be measured through a single timing signal from one channel. For example, the DRIFT dark matter NITPC measures recoil tracks in 2D using timing in Z and a second dimension, X, with an MWPC readout. The Z measurement gives superb resolution, corresponding to ~100 µm sampling of the recoil track, versus 2 mm with the MWPC wire plane. In this chapter, we discuss the possibility of measuring both the X and Y dimensions through timing signals. The essence of the concept is to keep the track reconstruction in the time domain which results not only in a resolution advantage but also a cost advantage since the complexity of the detector can be greatly reduced.

Consider a 3D detector with X and Y spatially measured by wire grids or a 2D strip board, this detector would require several hundred channels, but the same detector with X and Y measured through timing signals could conceivably require only three channels, one for each of the track dimension. Such a detector would require a negative ion drift, or a slow electron drift, and appropriate electronics in order to use timing to resolve tracks as is done in DRIFT. For the rest of this chapter, we assume a detector with negative ion drift to illustrate this new idea.

8.2   Working principle

8.2.1   Detector geometry

The fundamental question is what type of detector geometry would allow us to measure X and Y via timing? For now, to make the concept clearer, we only consider how to obtain one other dimension in addition to Z through timing and call this the X dimension. Z is defined to point upwards in the direction of the drifting negative ions while $+X$ will point to the right as is shown in Figure 8.1, which depicts a potential detector geometry for demonstrating the concept. The conversion, or drift,
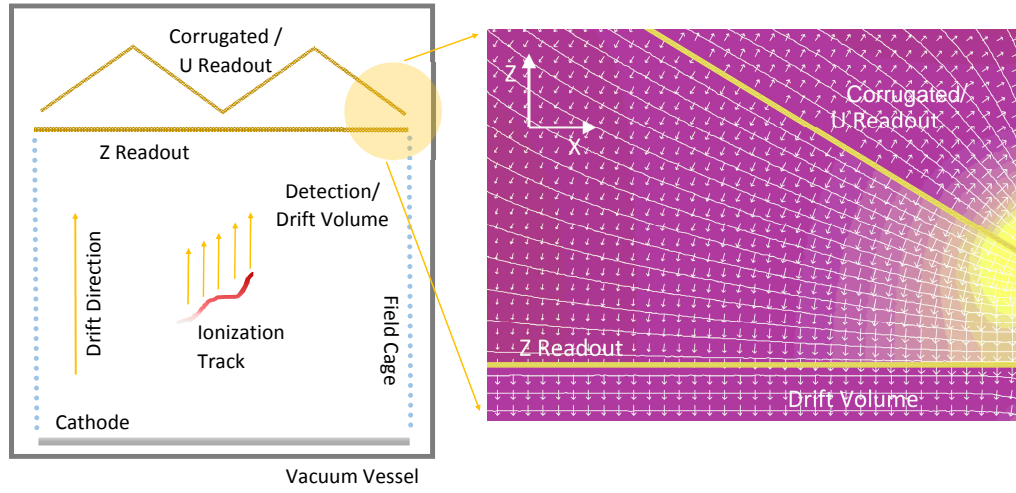
Figure 8.1: *(Left) The proposed geometry for a detector utilizing signal timing for track reconstruction. The principle of operation is similar to that of a low-pressure TPC where a uniform electric field is established between the cathode and readout plane. The distinguishing feature is the presence of a second readout (U) configured in a geometry different than the first readout (Z). (Right) A field simulation of the region between the Z-readout and the U-readout showing the equipotential lines and electric field map. Refer to the text for an explanation of the detector geometry.*

volume of the detector would be identical to that of a DRIFT-like detector. The amplification is provided by a single/double GEM structure lying along the $X - Y$ plane. But it is important to note that the amplification structure does not need to be comprised of GEMs. The requirements are that the amplification device must be fine-pitched to preserve track resolution, and semi-transparent to charge to allow for a secondary readout. Besides GEMs, there are potentially other gas amplification devices that possess those desired features. Nevertheless, for the remainder of this chapter we will consider GEMs as the readout of choice.

The horizontal GEM structure in Figure 8.1 will directly measure the Z component, via timing, of the ionization track. As such, we will call the horizontal GEMs the Z-GEM, or Z readout interchangeably. Sitting above the Z-GEM is what we call a corrugated/projection readout electrode with sides angled at $\alpha \sim 45°(135°)$ (Figure 8.2) and maintained at a single fixed potential which is different from that

of the Z-GEM surface facing it. This establishes an electric field inside the region between the two GEMs and allows charges to drift from the Z-GEM to the secondary readout, which we will refer to as the U-readout (Figure 8.1). In principle, the angled electrode does not need to be amplifying. However, in practice, amplification will be needed to resolve an issue that we will discuss in a later section. The length of each side from peak to trough could be on the order of a few centimeters with the region of unique readout being defined by one "rung" of corrugation (one left angled electrode and one right angled electrode), forming a inverted V shape. Depending on the application, the size of this region can be varied from a few centimeters to ten's of centimeters or larger. Finally, by considering the geometry in Figure 8.1, we see that in fact two channels, one for each of the left and right angled electrodes, will be needed to avoid track direction confusion. This will become clearer when we discuss the different track reconstruction cases in detail. However, this does not significantly increase the complexity of the readout electronics.
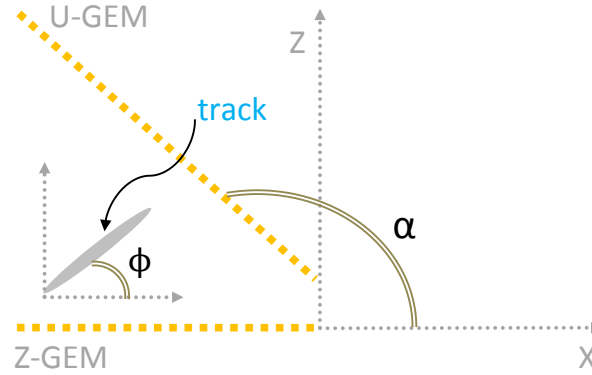
Figure 8.2: *The coordinate system relative to which the angles and directions are defined.*

To illustrate how the corrugated electrode can measure the X component of the track, we consider the case of a horizontal track (i.e. a track with no Z component and lying parallel to the Z-GEM) that is fully contained within the angled electrode on the right side (field simulation in Figure 8.1). As the track arrives at the Z-GEM

which lies in the $X - Y$ plane, a sharp, short duration pulse width is measured. In the idealized situation in which there is no diffusion, this pulse width would be essentially zero ($\Delta Z = 0$). During amplification, some of the electrons produced from the avalanche are collected on the Z-GEM surface to give the Z signal pulse. The remaining fraction of electrons are extracted from the GEM into the region between the Z-GEM surface and corrugated electrode; refer to the electric field simulation in Figure 8.1. This region is referred to as the transfer region. Once inside this region, the track will begin to drift towards the corrugated readout. The right side of the track will arrive much earlier than the left side due to the higher electric field and shorter drift path to the corrugated readout. As a consequence, the width of the pulse registered on the corrugated electrode is non-zero. This pulse width, however, does not directly give the X component of the track, hence the electrode is not referred as the the X readout. Nevertheless, it is the basis for determining the X component of the track.

The non-uniform electric field inside the region between the Z-GEM and the corrugated electrode are the key to reconstructing the X dimension of the track. Because the electric field is non-uniform and the separation between the two readouts is varying, the charge transfer time from the Z-GEM to corrugated electrode depends on where the charge is along the X axis; refer to Figure 8.2 for the defined coordinate system and the field map in Figure 8.1. Thus, a single charge arriving at large $|X|$ (where the GEM to corrugated electrode gap is large) will have a longer transit time from the GEM to the corrugated electrode. If, on the other hand, it arrives at small $|X|$ (where the GEM to corrugated electrode gap is small), the transit time is short. In summary, there is a one-to-one relationship, $X(\Delta T)$, between the X position of a piece of charge and its drift time from the Z to U GEM. Once this function $X(\Delta T)$ is measured, the X component, ΔX, of the track can be determined. Deriving the functional dependence of this timing difference on the drift time between the Z-GEM and U-readout on X can be done with careful calibration measurements.

Within each rung of corrugation, the timing difference between the arrival times at Z-GEM and the U-readout can be used to locate the X position of the leading edge of the track corresponding to those arrival times. The X position of the trailing edge can be measured in the same manner, and the length of the track along the X dimension is simply the difference between these two X positions. To reconstruct the Y dimension in a 3D detector that utilizes this reconstruction scheme, the geometry will be considerably more complicated and will not be discussed in this chapter. To illustrate the complexity of such a detector, we include a conception of what it would resemble in Figure 8.3,

Is a pixelized anode possible with three amplifier channels using variable time of flight delays?

GEM 1 and GEM 2 set at angle Θ experiences a variable time delay for receipt of event pulses dependent on location in **Y**

GEM 2 and GEM 3 set at angle Φ experiences a variable time delay for receipt of event pulses dependent on location in **X**
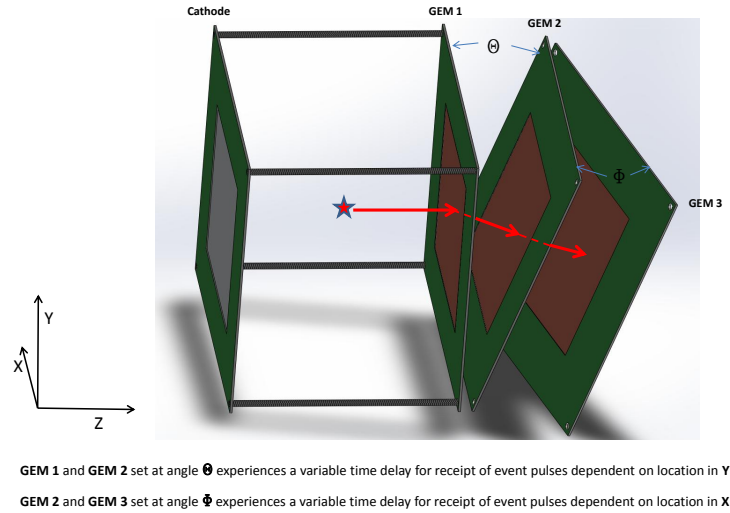
Figure 8.3: *A schematic of how a corrugated detector designed to measure all three dimensions of a track can be configured. This geometry is very complicated, but there are potentially other schemes that have simpler designs.*

8.2.2   Length determination

With the basic principle of operation discussed in the previous section, we now expound upon how the length components of a track are measured using the timing signals from the two readouts. Before we proceed, let us label, for brevity, the
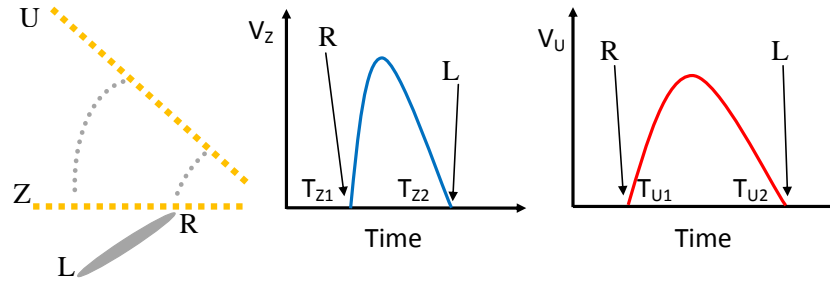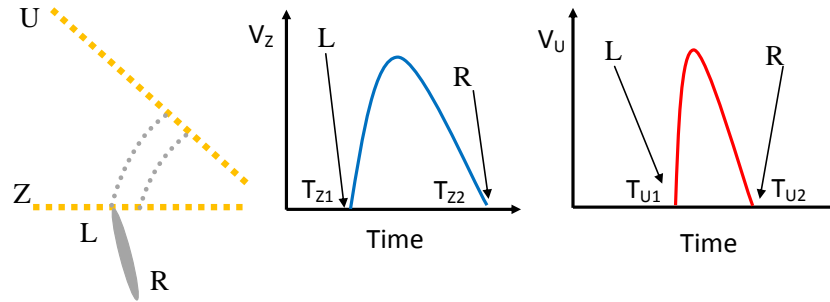
(a) U-Z Case I
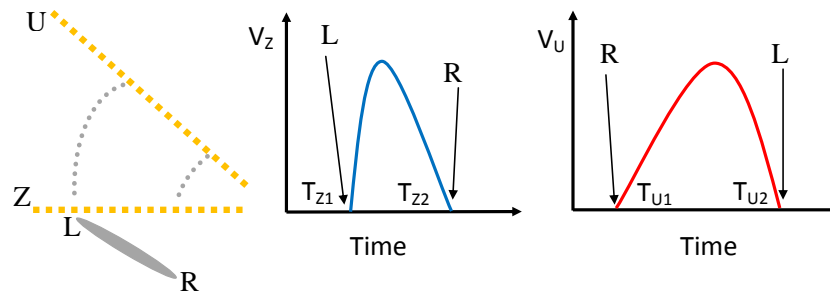
(b) U-Z Case II

(c) U-Z Case III

Figure 8.4: *The Z and U signals for the three possible track orientations: (a) The track is oriented at angle between 0° and 90°, (b) the track is oriented at angle between 90° and ϕ_{crit}, and (c) the track is oriented at angle between ϕ_{crit} and 180°. Case III is known as the inverted case because the ordering of left and right sides of pulse are reversed between the Z and U signals. This reverse ordering leads to an ambiguity in the X component of the track.*

GEM(s) lying in the $X - Y$ plane and used to measure the Z component of the track as the 'Z-GEM'. The corrugated(slanted) electrode is called the 'U-GEM' which measures some combination of the X and Z components. The relation to find the Z length, ΔZ, is straight forward and given by

$$\Delta Z = (T_{Z2} - T_{Z1}) \times v_d, \tag{8.2.1}$$

where v_d is the drift speed of the negative ions in the drift, or conversion, volume of the detector. Unlike the drift speed inside the transfer region, this quantity is a constant throughout the drift volume. In general, the X component of a track is determined by doing a series of simple calibration measurements of the time that it takes charge from the Z-GEM to drift to the U-GEM as a function of the distance along the X-axis. This can be accomplished by firing alpha particles from a collimated source at different X-positions along the GEM, thus, giving a functional relation between X, the position along the X-axis, and ΔT_{ZU}, the charge transfer time from the Z-GEM to the U-GEM at that position.

However, applying the functional relationship between ΔT_{ZU} and X is not always straight forward and depends on the orientation of the track, ϕ, and the angle of the corrugation, α. Shown in Figure 8.4 are three cases that we must consider and they are listed here as well:

- Case I: $0° \leq \phi \leq 90°$

$$X_1 = X(T_{U1} - T_{Z1})$$
$$X_2 = X(T_{U2} - T_{Z2})$$
$$\Delta X = X_2 - X_1 < 0$$

- Case II: $90° < \phi < \phi_{\text{crit}}$

$$X_1 = X(T_{U1} - T_{Z1})$$
$$X_2 = X(T_{U2} - T_{Z2})$$
$$\Delta X = X_2 - X_1 > 0$$

- Case III: $\phi_{\mathrm{crit}} \leq \phi < 180°$

$$X_1 = X(T_{U2} - T_{Z1})$$

$$X_2 = X(T_{U1} - T_{Z2})$$

$$\Delta X = X_2 - X_1 < 0$$

The first case, Figure 8.4a, is for track angles between $0°$ and $90°$ measured counterclockwise from the positive X-axis (Figure 8.2). The track in this case is described as 'right-handed' because the right side of the track arrives first at both the Z-GEM and U-GEM. To put it another way, T_{Z1} and T_{U1} are the times in which the right side (leading edge) of the track is detected at the Z-GEM and U-GEM, respectively. Similarly, T_{Z2} and T_{U2} are the times in which the left side (trailing edge) of the track arrives at the two respective readouts. The distinctive features of this case are that the ordering of the arrival times of each edge of the track between the Z-GEM and U-GEM is preserved and that the sign of $\Delta X \equiv X_2 - X_1$ is negative.

Case 2, Figure 8.4b, is the opposite of case 1 and is relevant for angles greater than $90°$ and less than the critical angle, ϕ_{crit}. The importance of the critical angle will be made clearer in the discussion of case 3, but it is approximately equal to the angle of corrugation ($\phi_{\mathrm{crit}} \simeq \alpha$). The two are exactly equal in the situation where the electric field is constant in the transfer region between the Z and U readouts. Unlike in case 1, here the left side of the track arrives first at both readouts and so the track is described as 'left-handed'. Although the ordering of arrival times is preserved, the sign of ΔX is now positive. At present, it may seem unclear why we are concerned with the sign of ΔX since we are only interested in measuring lengths which are definite positive quantities. The importance of the sign will be explained in case 3.

Case 3, Figure 8.4c, is neither 'left-handed' or 'right-handed but is rather inverted. This means that the left side (initial leading edge) of the track arrives at the Z-GEM first but its right side(initial trailing edge) is first to arrive at the U-GEM. Thus,

the ordering of arrival times at the two readouts is no longer preserved and will bring about an issue we called degeneracy. First of all, to see why the ordering is reversed, note that the electric field is higher on the right side of the track and also the gap distance between the Z and U readouts is shorter. For these reasons, if a track is perfectly horizontal ($0°(180°)$), it is clear that the right hand side of the track will arrive first on the U-GEM. However, if the track is angled at a shallower angle (e.g. $160°$), it is possible for the right side to arrive first at the U-GEM because the head-start of the left side of the track is compensated by a higher electric field and shorter path to the U-GEM afforded to the right side of the track. When the head start of the left side of the track is perfectly offset by the higher electric field and shorter travel distance, both sides of the track will arrive simultaneously on the U-GEM. The track angle at which this occurs is defined as the critical angle, ϕ_{crit}, and is dependent on the angle of corrugation, α, and the electric fields in the drift and transfer regions.

8.2.3 Degeneracy

The inversion of the track in case 3 causes a problem not only for $\phi_{\text{crit}} < \phi < 180°$ but also for $0° \leq \phi \leq 90°$ because we cannot determine in an unambiguous manner if the track is inverted simply by analyzing the waveforms from the two readouts as we did in cases 1 and 2. There is no confusion with case 2 because the sign of ΔX is positive so that tracks in this angular span can be distinguished from those in cases 1 and 3 where the sign of ΔX is negative. In principle, this degeneracy, or indistinguishability, between cases 1 and 3 can be removed if the sense of the track can be confidently determined. It is important to note that the context in which the word sense is being used is not necessarily to specify the true direction of the recoiling ion that generated the track as has been used in the previous chapters. A more appropriate description is left-handed vs. right-handed as we have used here.

In order to break the degeneracy, it is sufficient to be able to distinguish one end

of the waveform from the other end and detect the switch in the handedness of the track between the Z and the U signals. In principle, a false sense, or handedness, can be artificially imprinted into a track by an avalanche device with a variable gain along the X direction to allow for an easier distinguishing of track edges and break the degeneracy. This would, in effect, enhance the false sense already introduced by the variable charge extraction efficiency along the Z-GEM due to the field gradient (refer to the field simulation in Figure 8.1). The reason for such an approach is that true sense (head-tail) of a low energy nuclear recoil is extremely small and difficult to measure well on an event by event basis.

In an idealized situation where the sense/handedness of a track can be determined, there is no problem, but in practice the direction of a low energy nuclear recoil is extremely difficult to measure. We can adopt the position that all events in a which a sense/handedness cannot be determined should be thrown out and in which case the directional threshold will determine the discrimination threshold. However, such a position is quite unsatisfactory. Another approach is to adhere strictly to our criteria for how X should be related to U and Z for the normal, non-inverted, scenario, and so the 2D range will be correctly reconstructed for over half of the events (cases 1 and 2), assuming detected events are isotropically oriented. The situation is actually slightly better because some of the events that fall within $\phi_{\text{crit}} < \phi < 180°$ will have a detectable sense and be assigned the correct relation in determining ΔX. Nevertheless, it would be ideal to find a way to resolve the degeneracy.

One possible approach to break the degeneracy is to introduce an additional corrugated readout out of phase with the other one (U-readout), but this would add an addition layer of mechanical complexity and would require the first corrugated readout to be charge transparent, altogether degrading the simplicity of the initial detector concept. A partial solution could be to lower the angle of the corrugation, to say, $30°(150°)$, which would decrease the fraction of incorrectly reconstructed events. And perhaps there are yet to be identified detector geometries that are better suited
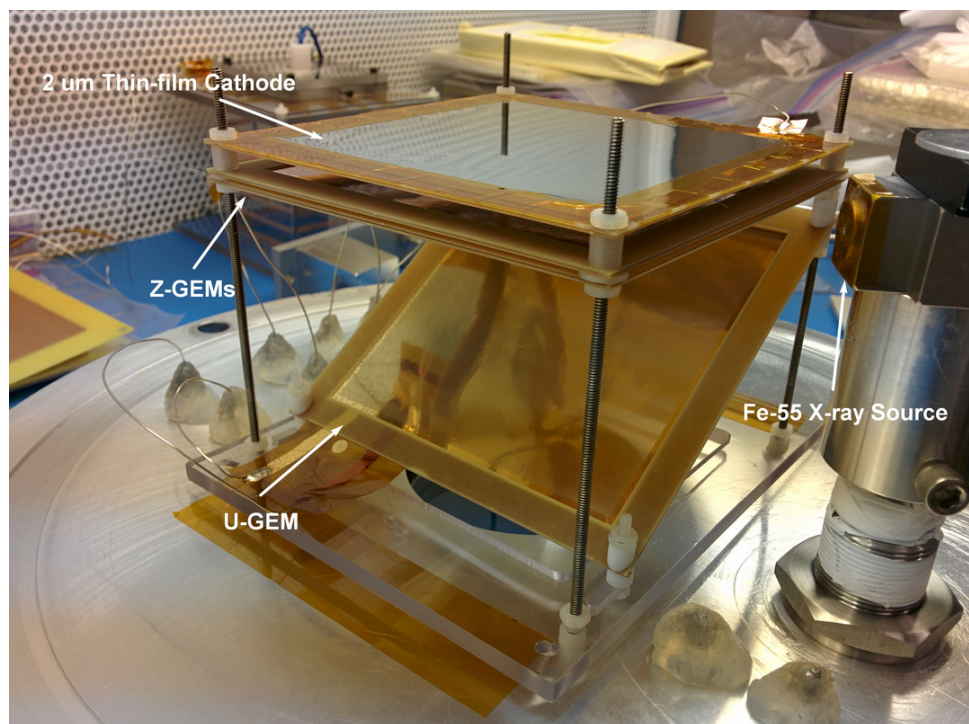
Figure 8.5: *A photo of the detector setup, showing the 2 µm thin-film cathode, Z-GEMs, and U-GEMs. The dimensions of the cathode and GEMs are 9.5 × 9.5 cm². An alpha source is positioned below the cathode (not shown) and an* ^{55}*Fe source is mounted on a rotary feed-through for calibration.*

for this concept. In Section 8.3.5, we will discuss a possible solution to the degeneracy problem without requiring any additional readouts or changes to the simple detector setup that has been discussed up until now.

8.3   Experimental setup

8.3.1   Detector

The detector used to demonstrate the concept discussed in this chapter utilized the same aluminum vacuum vessel that was used to make the measurements described in Chapters 4 and 6. But the internal components and arrangement were different.
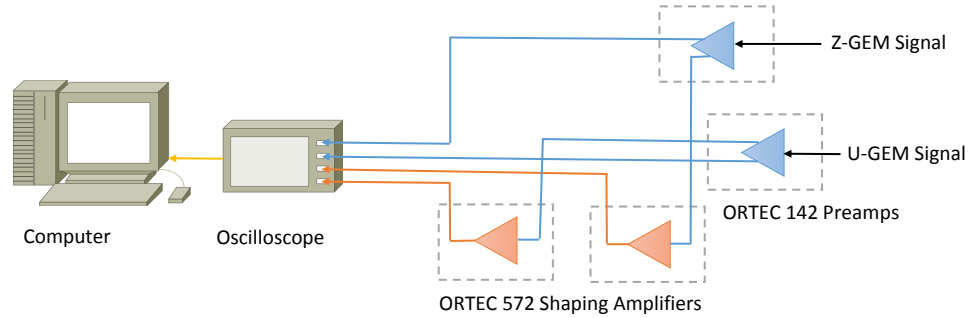
Figure 8.6: *A schematic showing the connections between the preamplifiers, amplifying shapers, and data acquisition system.*

The detector consisted of three standard copper GEMs [155] that were manufactured at CERN from 9.5×9.5 cm^2 sheets of kapton (50 µm thick) with copper cladding on both surfaces. The surface of each sheet was chemically etched with bi-conical holes of diameter of 50/70 µm (inner/outer) configured in a hexagonal pattern with 140 µm pitch. Two of the GEMs were mounted in the X-Y plane with 2 mm separation between them (Figure 8.5), and formed the Z-readout. More than one GEM was used for the Z-readout to provide good signal-to-noise for the Z signal. A cathode, fabricated from a 9.5×9.5 cm^2 sheet of 2 µm thick aluminized Mylar was mounted 8.3 mm below the Z-readout. This formed the drift volume. The third GEM (GEM3) was mounted on a 0.25 in acrylic frame that was angled at 32° from the Z-readout/X-Y plane and formed the U-readout. The pivot point of the U-readout, which is the edge closest to the Z-readout, was vertically offset by 1.6 cm to prevent sparking between the two readout surfaces. The detector was calibrated using ^{55}Fe (5.9 keV X-rays) and ^{210}Po (5.3 MeV alphas) sources, both mounted inside the vacuum vessel. Prior to operation, the vacuum vessel was pumped down to < 0.1 Torr and back-filled with a mixture of 100 Torr CF$_4$ and 51 Torr CS$_2$ gas.

8.3.2 Data acquisition

The top surface of GEM3 and the surface of the Z-readout GEM facing GEM3 were each connected to an ORTEC 142 charge sensitive preamplifier. Each preamplifier contained two identical outputs, labeled T and E, respectively. The T output was fed into an ORTEC 572 shaping amplifier. The amplifier outputs were then connected to a Tektronix TDS3054C digital oscilloscope. The non-amplified E outputs from the preamplifiers were directly connected to the two remaining inputs from the oscilloscope. The measurement waveforms were acquired with the oscilloscope and National Instruments data acquisition software where every triggered event is read out and saved to file for analysis. The trigger is set on the amplitude of the preamplifier signal from the Z-GEM. A schematic of the connections is shown in Figure 8.6. Each saved file contain the two raw voltage signals from the ORTEC charge sensitive preamplifiers as well as the two amplified signals from the shaping amplifiers. The raw voltage signals were converted to currents signals using the method described in Section 7.3.3. The two amplified signals were not used in the subsequent analysis of the data.

8.3.3 Voltages

The resistor chain and voltages of the GEMs 1, 2 (Z-GEM), and 3 (U-GEM) are shown in Figure 8.7. Each of the GEMs are powered by an independent high voltage power supply. This allowed for the GEM voltages to be changed independently, allowing maximum freedom in tuning the settings to find the most stable voltage configuration. Depending on the experimental setup and the particular GEMs used, the best voltage settings must be found through a methodical approach. Additionally, the cathode, not shown here, is powered with its own power supply and set to a fixed voltage of $-1000V$. This establishes a drift field of 482 V/cm in the 8.3 mm drift gap, and this value can be easily changed by setting the cathode voltage.
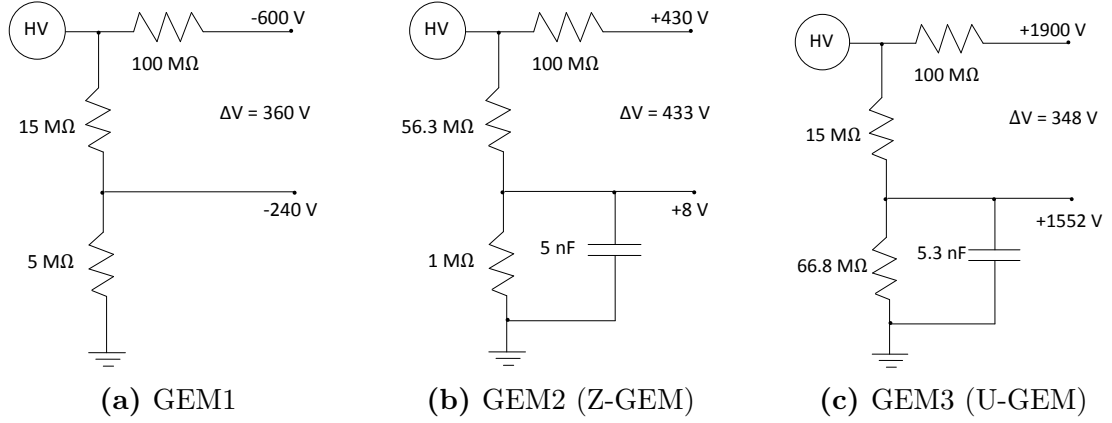
(a) GEM1   **(b)** GEM2 (Z-GEM)   **(c)** GEM3 (U-GEM)

Figure 8.7: *(a)-(c) Diagrams of the electrical connections and voltages for GEMs1 and 2 (Z-GEM) and GEM3 (U-GEM). The cathode voltage is set at a fixed value of -1000 V.*

8.3.4 Calibration

The critical piece of information needed to determine the X component of a track is the charge transit time between the Z-GEM and U-GEM as a function of the X position of the charge. In essence, we want to map this transit time into a unique X position, and doing this for each of the edges of a track gives us its length in the X dimension.

The calibration procedure used alphas from a highly collimated source which fired them perpendicular to the Z-GEM. The alpha source was mounted below the 2 µm thin film cathode (Figure 8.5). After penetrating the thin film, the alphas deposited charge inside the drift volume and then ranged out when they struck the surface of GEM1. By translating the collimated source for different known X positions and measuring the charge transit time, we mapped out the functional dependence of the transit time with X.

An apparatus was designed to collimate and translate the alpha source so that the X position of the source can be determined in-situ while making the transit time measurements. This apparatus is shown in Figure 8.8. It is composed of a source
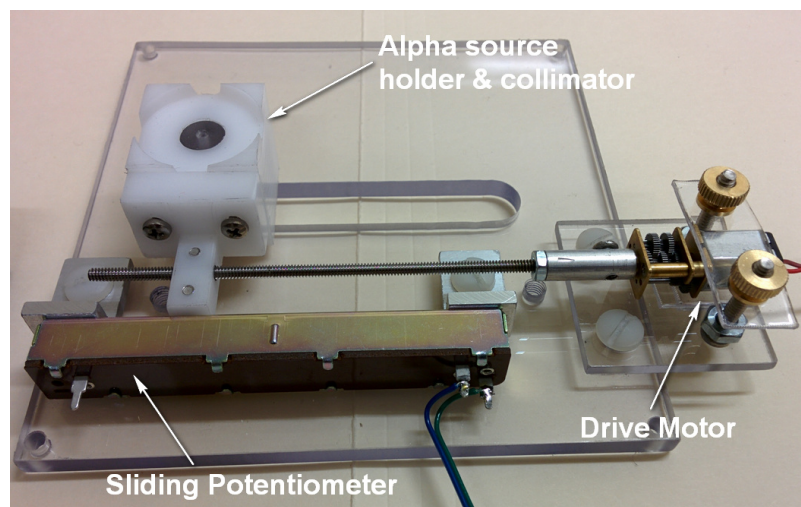
Figure 8.8: *A photograph of the position calibrating apparatus which includes the alpha source holder and collimator, the sliding potentiometer, and the drive motor. The entire setup is mounted on a 1/4 in. thick acrylic frame with the same dimensions as the GEMs used this experiment. The drive motor is battery powered while the potentiometer is connected to a multimeter to measure the resistance. (Designed by Eric. R Lee at the University of New Mexico)*

holder and collimator for a ^{210}Po alpha source, a sliding potentiometer, and a drive motor. The source holder is attached to a drive shaft and the potentiometer. The motor can drive the source in both directions, and when the source is moved, the resistance on the potentiometer changes. The X position of the source, as measured with a precision micrometer, and the corresponding resistance on the potentiometer, as measured with a Fluke multimeter, are tabulated. A plot of X as a function of the potentiometer resistance is shown in Figure 8.9.

Once the source position has been calibrated against the potentiometer resistance, the entire apparatus is mounted inside the vacuum vessel. Figure 8.10 shows the apparatus when it is mounted inside the vessel. The leads from the drive motor and potentiometer are connected through electrical feedthroughs. This allowed the motor to be powered by a battery and turned on or off with a switch. The potentiometer leads are connected to a multimeter to measure the resistance, from which the X
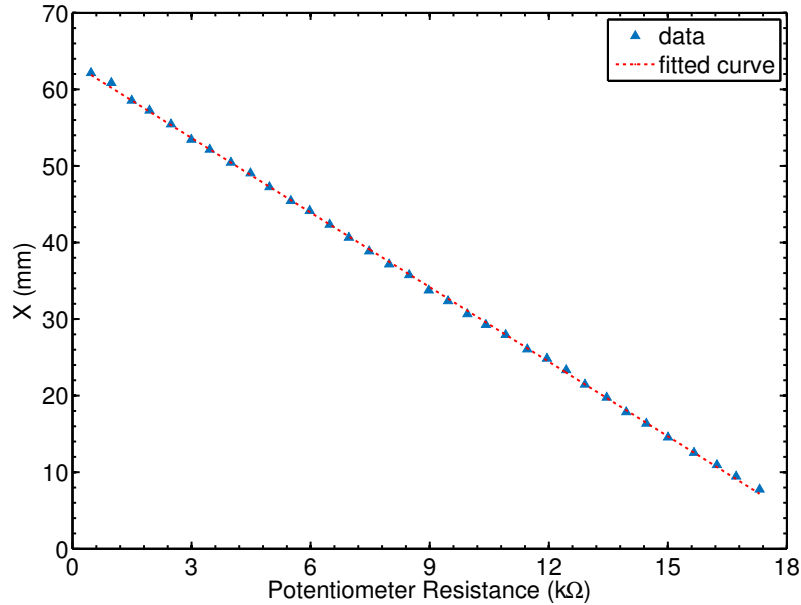
Figure 8.9: *The X position (mm) of the alpha source as a function of the potentiometer resistance. The position was measured using a precision micrometer and the resistance was read out from a Fluke multimeter. These measurements were taken before mounting the calibration apparatus inside the vacuum vessel.*

position can then be determined from the curve in Figure 8.9.

Measurements were taken for twelve different alpha source positions. The first position, X_1, is ~1 cm from the edge of the GEM because the electric fields in the drift volume are not uniform closer to the edges due to fringe effects. In Figure 8.11, we show the current waveforms for a sample event at X_1. The top figure contains the signals measured by the Z-GEM(Channel 1), while the bottom contains signals from the U-GEM(Channel 2). The signal in red is the primary Z-GEM signal. The width of this signal gives the Z component of the track and can also be used to measure the drift speed in the drift volume. The latter is possible because the Z extent of the drift volume is known precisely. The signal highlighted in blue is the primary U-GEM signal. Notice there is a small tail on the right side of the primary U-GEM signal. This is an induced signal caused by positive ions, produced from the avalanche at the U-GEM, drifting back towards the Z-GEM. The positive ion back-flow also induces
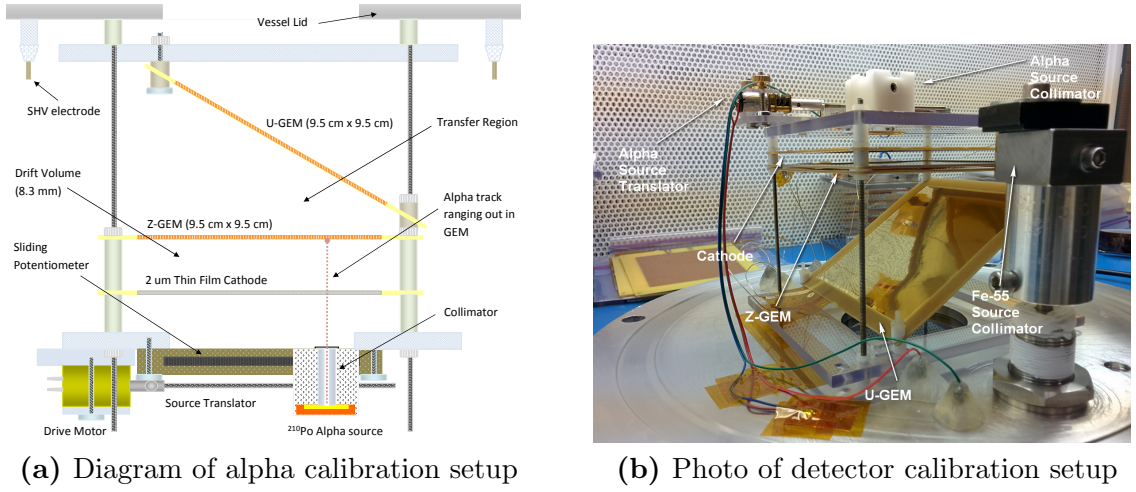
(a) Diagram of alpha calibration setup

(b) Photo of detector calibration setup

Figure 8.10: *(a) A diagram of the alpha calibration source and translator mounted in the detector. (b) A photograph of the calibration apparatus and the detector configuration.*

a signal on the Z-GEM, shown in orange. It has the opposite polarity to the induced signal on the U-GEM because the ions are drifting towards the Z-GEM and away from the U-GEM. Once the positive ions reach the Z-GEM, some fraction are collected on the bottom surface of GEM2(Z-GEM) and the remaining ions continue to follow the field lines towards the cathode, leading them away from GEM2(Z-GEM). As they drift away, they now induce a positive signal on the Z-GEM.

The induced signals can make identifying the edges of the track difficult. As such it is sometimes useful to look at a signal that is a product of the current times its first derivative. The derivative enhances the component of the signal due to the collected electrons produced in the avalanche, which is the part we want, and suppresses the induced positive ion part because of the differing mobilities of the two types of charges. This composite signal with the current signal overlaid on top is shown in Figure 8.12.

In Figure 8.13, the distribution of the primary Z signal pulse, ΔT_Z, and the distribution of the transit time from Z-GEM to U-GEM, ΔT_{ZU}, are shown. These distributions contain data for a single X position (X_1). The same distributions
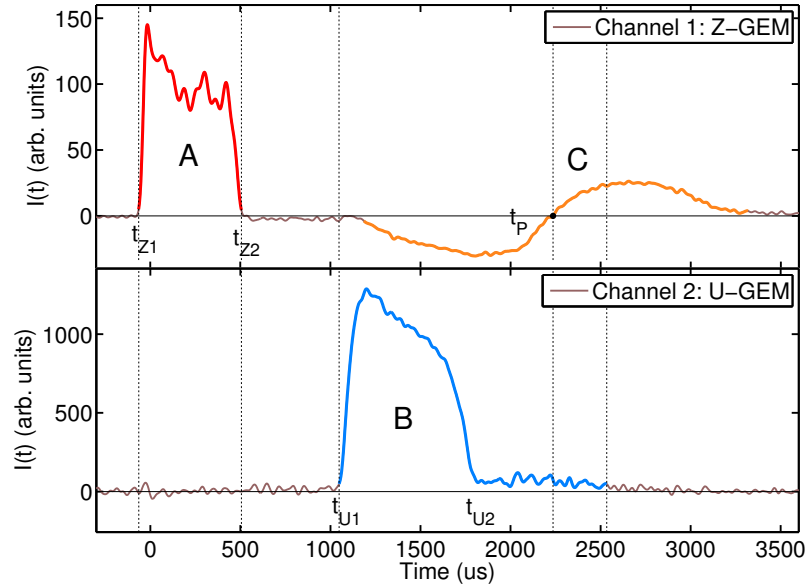
Figure 8.11: *The current vs. time waveform for a sample alpha calibration event. The alpha was directed vertically through a collimator, traversing the entire drift volume before ranging out in GEM1. The width of the primary signal, ΔT_Z, in the Z-GEM (red) can be used to measured the drift speed in the drift volume. The time difference, ΔT_{ZU}, in the arrival time of the leading edge in the Z-GEM and U-GEM is used to calibrated the X position. The signal highlighted in orange is the positive ion back-flow signal. Its importance will be discussed in Section 8.3.5.*

are also found for the other eleven X positions. The mean of the ΔT_{ZU} and its corresponding X is plotted in Figure 8.14. This is the principle calibration curve from which the results in Section 8.4 are derived.

8.3.5   Resolving the degeneracy

To resolve the degeneracy problem discussed in Section 8.2.2, which causes an ambiguity in the X component of the track length, requires an additional piece of information. This comes from the arrival time of the positive ion back-flow signal detected by the Z-GEM. Consider the current waveforms shown in Figure 8.11 for a calibration run event. The three signals from left to right are the primary Z signal (red) from the horizontal Z-GEM (A), the U signal from the slanted GEM (B)
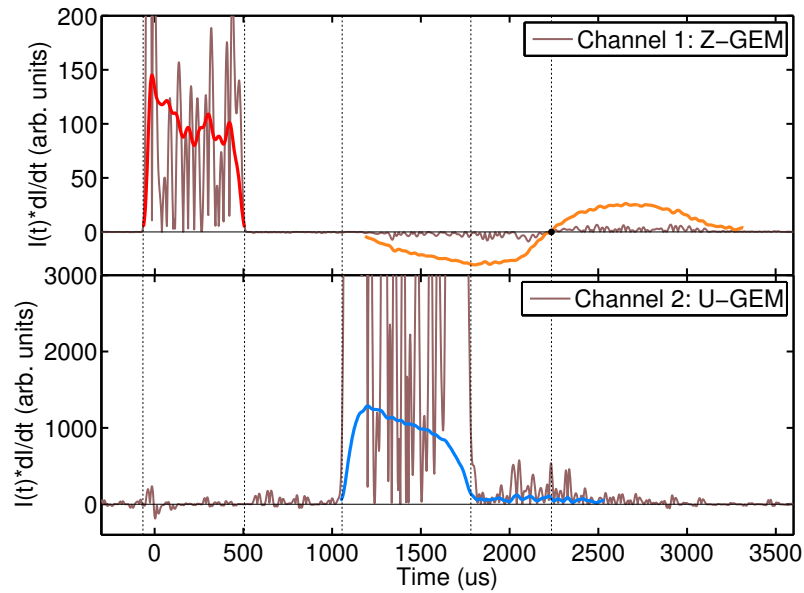
Figure 8.12: *Because the Z and U signals include combination of the signal of the electrons collected from the avalanche as well as induced signals of the drifting ions, it is helpful in some instances to look at the a quantity defined as the product of the current times its derivative. This tends to produce sharper signal edges and allows for better time measurements.*

(blue), and the signal from the ions created in the avalanche process at the U-GEM traveling back to and detected by the Z-GEM (C)(orange). Thus, the ion signal would explicitly require that the U electrode to be an avalanche device.

To understand how these signals can be used to resolve the problem, let's consider the front edge of signal U, and label it t_{U1}. This is the part of the track that arrives first at the U-GEM, but we do not know if this edge corresponds to the edge t_{Z1} or t_{Z2} in the Z-GEM signal and this is what brings about the degeneracy. Nevertheless, this front edge arrived at and was avalanched by the U-GEM first regardless which of the Z signal edges it corresponds to. The avalanche creates a large number of electrons as well as positive ions. The signal detected by the U-GEM is due to the avalanche electrons being collected on its top readout surface. Some of the positive ions created in the avalanche are collected on the bottom surface of the U-GEM, but
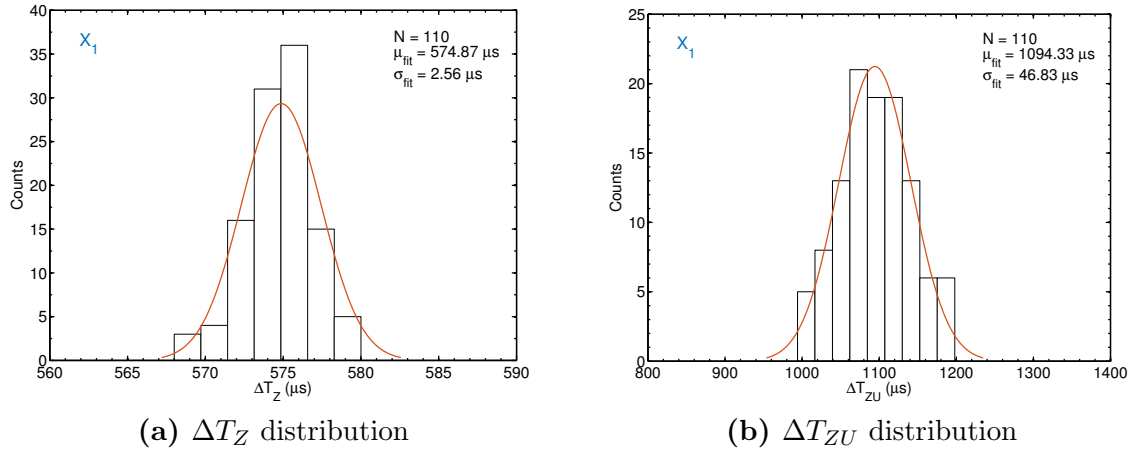
(a) ΔT_Z distribution

(b) ΔT_{ZU} distribution

Figure 8.13: *(a) A histogram of the width of the primary Z-signal (red), ΔT_Z, for one subset of the calibration data (position X_1). The drift speed is determined from this distribution because of the known extent of the drift volume. (b) A histogram of the time difference, ΔT_{ZU}, for the leading edge of the charge to arrive at the Z-GEM and U-GEM for one subset of the calibration data (position X_1). The X vs drift time curve in Figure 8.14 is measured by making these same measurements for other positions.*

a significant fraction of these travel back to the Z-GEM and is detected as signal shown in orange. The positive ions that arrive at the Z-GEM (at time t_P) correspond to the charge that arrived first at the U-GEM at t_{U1} in the degenerate cases (1 and 3). Recall that for case 2, ΔX is negative so there is no confusion with the two other cases. Thus, the time that it takes the positive ions which are created in the U-GEM to arrive at the Z-GEM, $\Delta t_{\text{ion}}^+ = t_P - t_{U1}$, uniquely determines the X-position of the leading edge of the track and resolves the degeneracy problem.

Another way to look at this is that the time difference, $t_P - t_{U1} \simeq t_{U1} - t_{Z1}$, in the normal case (case 1) where there is no inversion. But in the inverted case (case 3), $t_P - t_{U1} \simeq t_{U1} - t_{Z2}$ because the trailing edge at the Z-GEM (t_{Z2}) becomes the leading edge at the U-GEM (t_{U1}). The timing differences are not exact equalities because what is creating the Z and U signals are negative ions with some drift speed, v_1, whereas the positive ion back-flow signal is the result of positive ions which can be composed of sub-species of the molecular gas(e.g. CS_2^+, CS^+, ...) and so can have a
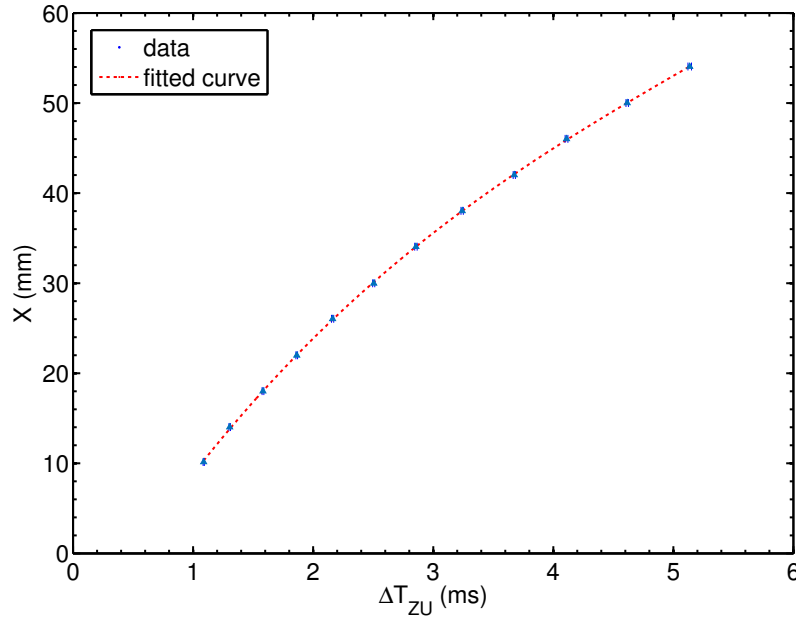
Figure 8.14: *The X position (mm) of the alpha source as a function of the time for charge to drift from the Z-GEM to the U-GEM, ΔT_{ZU}. A collimated alpha source produces alphas directed perpendicular to the Z-GEM. The position of the source was changed with the sliding potentiometer, and the resistance on the potentiometer allowed precise determination of the X position of the source while mounted inside the vacuum vessel.*

different mobility. We can measure the drift speed and timing of the positive ions as a function of its X-position in the same way we determine the curve in Figure 8.14.

8.4   Results

Data are presented for alpha tracks oriented at three different angles: 31°, 110°, and 149°. Each of the angles belong to one of three angular cases discussed in Section 8.2.2. For all of the angular cases, the calibration apparatus is removed and alpha particles are fired from a collimator with an opening angle of 6°. The angle of the collimator is adjusted manually as needed, and we estimate the accuracy of the set angle at 2°. Alphas escaping from the collimator penetrate the 2µm thin film cathode and range out on the GEM. As a result, the Z extent of the alpha track
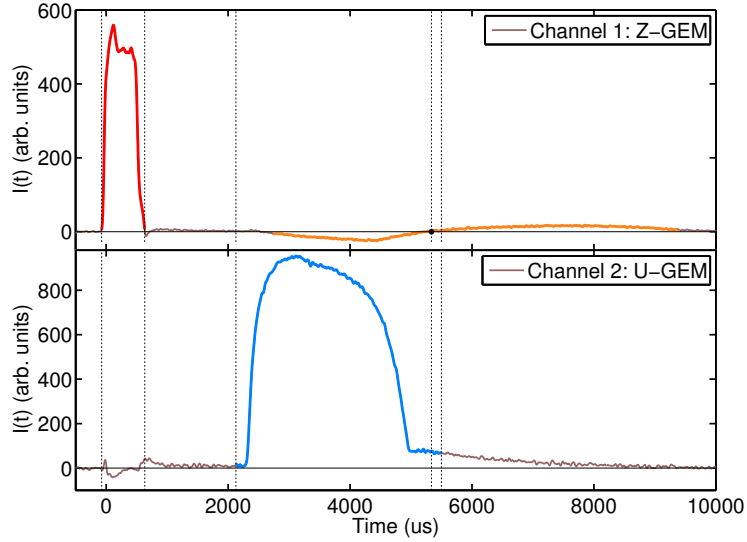
Figure 8.15: *Current waveforms for a sample alpha event angled at 31° relative to the Z-readout. The skew introduced into the U pulse (blue) is due to the higher electric field at the leading edge which results a higher extraction efficiency of charge from the Z-GEM into the transfer region and a higher drift speed towards the U-GEM than the trailing edge. The vertical lines show the detected edges of the track and the zero point of the positive ion induced signal (orange). Note how the right edge of the U pulse is not correctly detected due to the presence of an induced ion tail.*

detector by the Z-readout is always the set length of the drift volume (8.3 mm). So the ΔX extent of the track is solely determined by its angle. For the angular cases considered here, the expected, or true, ΔX extents are 13.8 mm (31°), 3.0 mm (110°), and 13.8 mm (149°). The results are in Figures 8.15-8.23.

- Case I: $\phi = 31°$

- Case II: $\phi = 110°$

- Case III: $\phi = 149°$
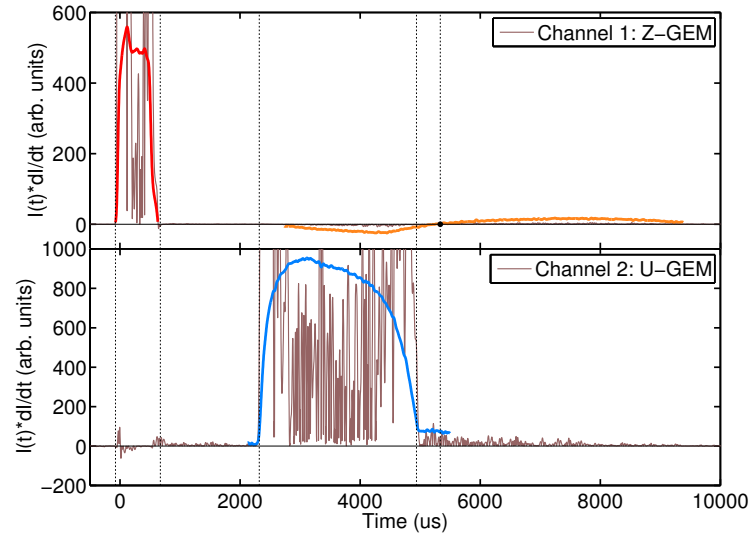
Figure 8.16: *The current waveforms weighted by their first derivative for the two readout channels for the 31° case. The edges of the signal are more easily identified in these waveforms. For visualization purposes, the current waveforms are overlaid on top. The right edge of the U pulse is now correctly detected and the start of the induced signal is more readily identified.*
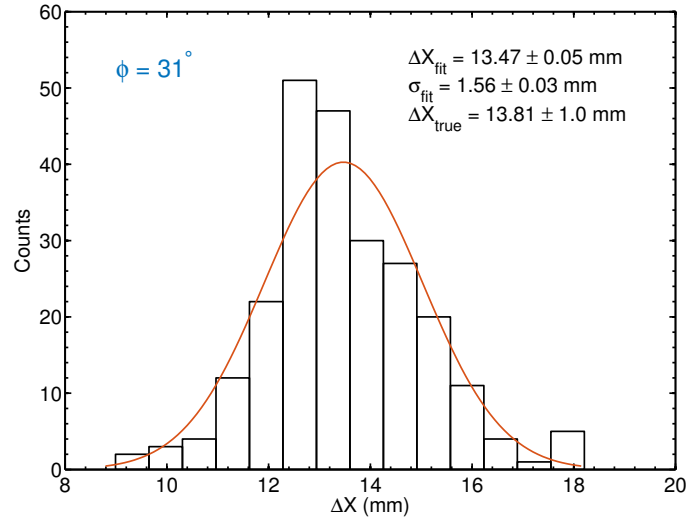

Figure 8.17: *The distribution of reconstructed ΔX lengths for the 31° case. The mean of the distribution of 13.47 mm is consistent with the expected value of 13.81 mm. The slight difference is likely the result of a small error in setting the angle of the collimator. The width of the distribution is primarily due to imperfect collimation which allows alpha particles to escape at angles as high as 6° from the mean direction.*
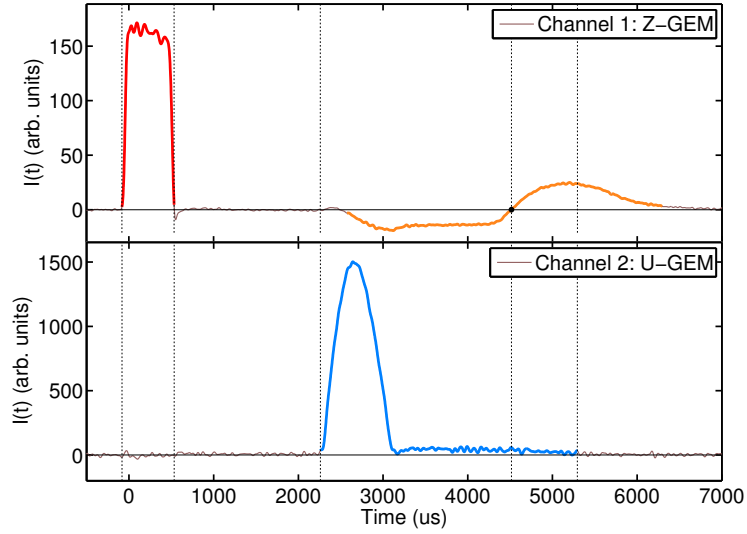
Figure 8.18: *Current waveforms for a sample alpha event angled at 110° relative to the Z-readout. Note how the U signal (blue) is much more compressed as compared to the same signal for the 31° case. Additionally, the positive ion back-flow signal (orange) is distinctly different than the other case. The length of the negative portion of the signal is comparable to the positive part, whereas in the 31° case, the positive portion is much longer.*
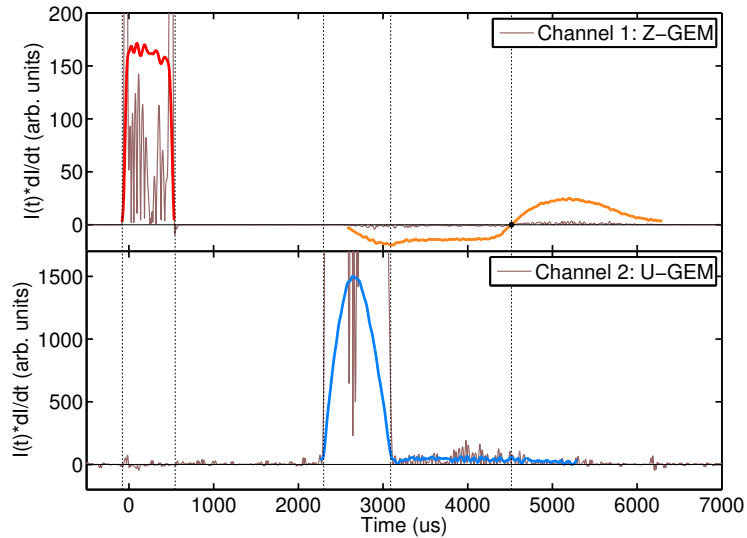

Figure 8.19: *The current waveforms weighted by their first derivative for the two readout channels for the 110° case. The edges of the signal are more easily identified in these waveforms. For visualization purposes, the current waveforms are overlaid on top.*
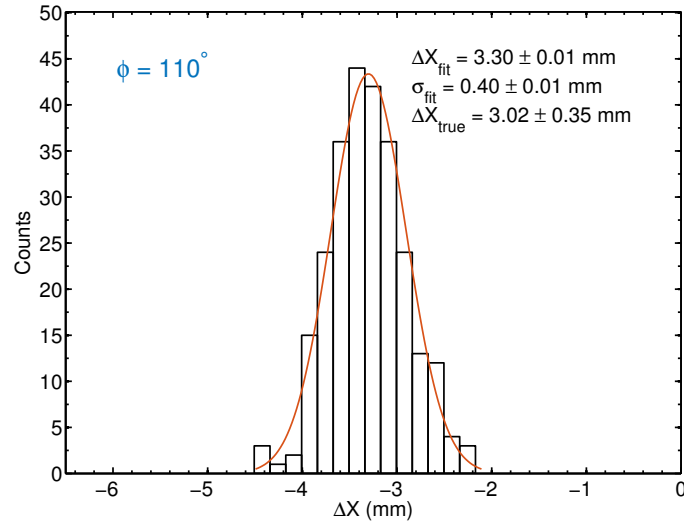
Figure 8.20: *The distribution of reconstructed ΔX lengths for the 110° case. The mean of the distribution of 3.3 mm is consistent with the expected value of 3.02 mm. The slight difference is likely the result of a small error in setting the angle of the collimator. The width of the distribution is primarily due to imperfect collimation which allows alpha particles to escape at angles as high as 6° from the mean direction.*
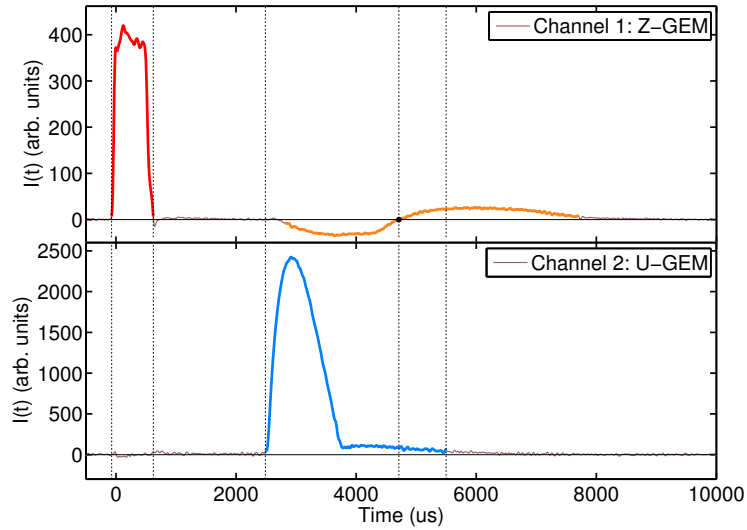

Figure 8.21: *Current waveforms for a sample alpha event angled at 149° relative to the Z-readout. Note how the width of the U pulse (blue) is much narrower than the mirror/inflected case of 31°. This is due to the competing effects of the higher electric fields at the trailing edge and the head start but lower field at the leading edge. Also, the U pulse displays an exaggerated skewness that is not present in the Z pulse (red).*
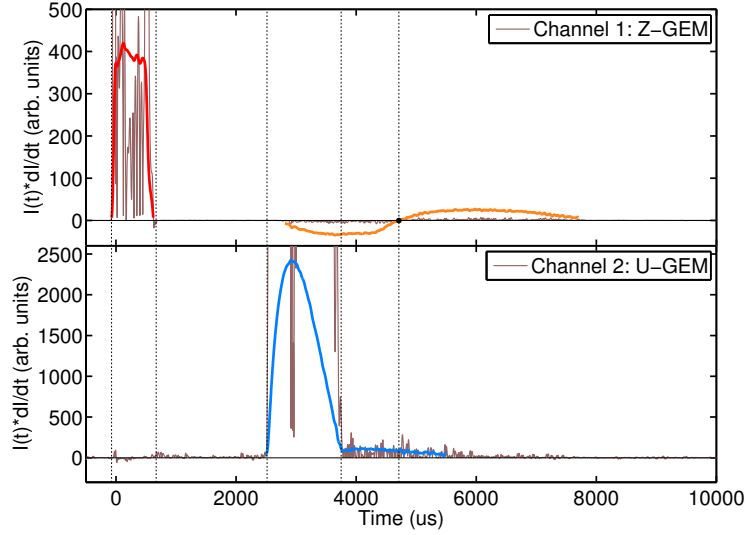
Figure 8.22: *The current waveforms weighted by their first derivative for the two readout channels for the 149° case. The edges of the signal are more easily identified in these waveforms. For visualization purposes, the current waveforms are overlaid on top.*
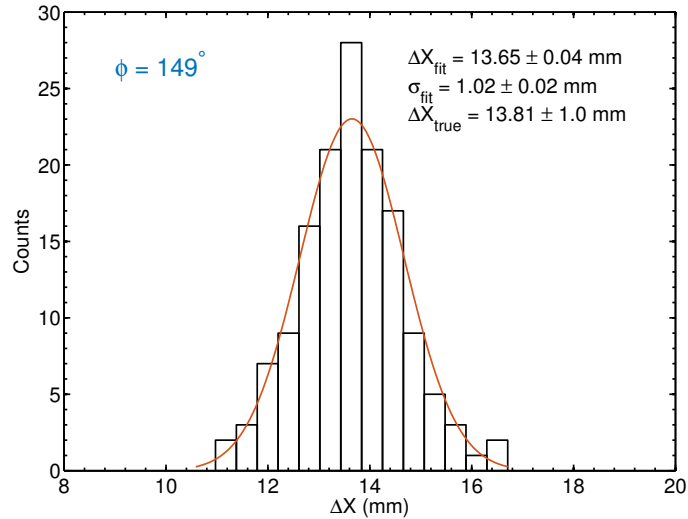

Figure 8.23: *The distribution of reconstructed ΔX lengths for the 149° case. The mean of the distribution of 13.65 mm is consistent with the expected value of 13.81 mm. The slight difference is likely the result of a small error in setting the angle of the collimator. The width of the distribution is primarily due to imperfect collimation which allows alpha particles to escape at angles as high as 6° from the mean direction.*

8.5 Conclusion

We have shown in this chapter that it is possible to reconstruct the 2D length of a track using timing signals from only two channels. The resolution of the reconstruction technique can be made much finer than any spatial track imaging device because the sampling frequency can be made as high as desired. The fundamental limitation to the resolution is gas diffusion and the pitch of the amplifying devices. The latter can be made as fine as needed without significant impact on the cost and complexity of the detector. The readout technology described here has the potential to greatly reduce the cost of high resolution detectors, enabling the scaling of directional dark matter detectors to reach ever higher sensitivities.

Chapter 9

Beyond Low-pressure Directional Detectors

9.1 Introduction

This thesis, thus far, has focused on how to increase the sensitivity of directional dark matter searches utilizing the low-pressure TPC technology. Although this technology is the most mature at the present time, it also has many shortcomings when applied to directional dark matter detection. Among these is the requirement for low-pressure operation to lengthen tracks which brings about a broad range of challenges. First of which is the issue of electrical stability at low pressures. Second is the low density of the detection medium which reduces the sensitivity per unit volume and necessitates very large detectors to compensate.

The other challenges are centered on the detection of the signal. Because the directional and discrimination information comes from measuring the spatial distribution of the ionization produced by a short-range recoil, a high-resolution readout is required. The high-resolution readout, in turn, is only useful if the ionization has not been diffused to an extent where its topological features have been wiped out. For this to occur, diffusion must be kept in check, but the side effect of this is that

scaling the detector becomes more difficult. As a consequence, all of these issues work to constrain the sensitivity of directional detectors while raising their costs and complexity. If a method could be devised for determining the direction of low-energy recoils without the need to image their ionization tracks, the constraints imposed by low-pressure operation could be circumvented and a new path towards increasing the sensitivity of directional detectors could be realized. Such a method could open up the possibility of a high-pressure directional detector.

9.2 Directional signature from primary ionization electron momentum distribution and multiple charge carriers

In the traditional low-pressure TPC, the direction of a recoil is determined from the ionization track and the asymmetry in the energy deposition, often called the head-tail effect. In effect, the direction of the recoil is derived from imaging the spatial distribution of the ionization. For most cases, however, diffusion, straggling, and the short range of the track (see Section 3.1) makes the direction reconstruction from the imaged ionization distribution challenging. But the observation of SF_5^- production in SF_6 and its dependence on the electron energies described in Chapter 7 could provide a new means of determining the recoil direction. This idea, in principle, could be applicable in other gases besides SF_6 (e.g. CS_2), but for concreteness, we will use SF_6 to help illustrate the concept in the following discussion.

Consider a nuclear recoil that is traveling downwards in the direction of the cathode and perpendicular to the readout plane, the electrons created in the ionization trail of the nuclear recoil have momenta that are preferably downward (Figure 9.1a) or highly anisotropic in some preferred direction. If this assumption is valid, then the concept is the following: Because the mean of the distribution of electron recoil di-
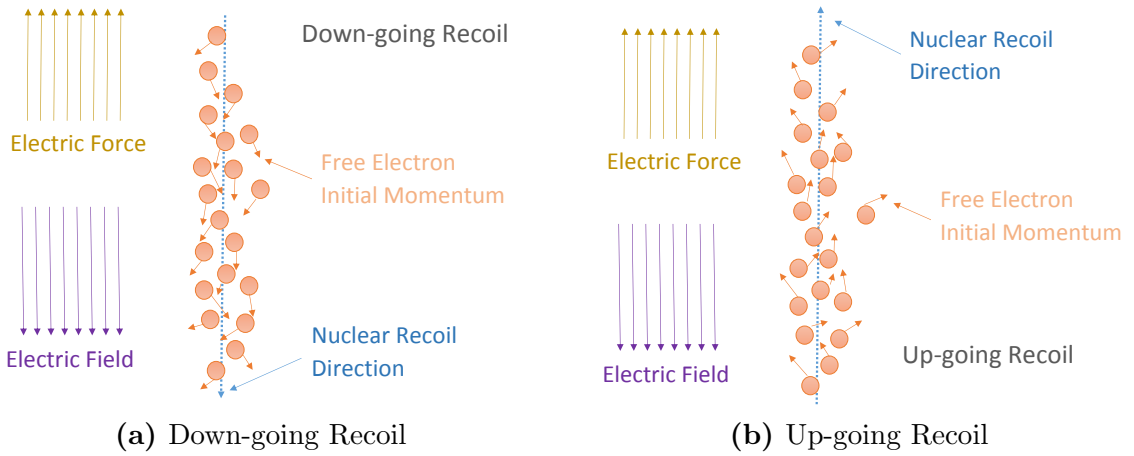
(a) Down-going Recoil **(b)** Up-going Recoil

Figure 9.1: *Two limiting cases where the recoil direction is anti-aligned (a) and aligned (b) with the electric force. The initial momentum vectors of the free electrons are shown, the average of which is in the direction of the recoil. The proposed method to measure the recoil direction described in the text rests on this critical assumption.*

rection is opposite to the force due to the electric field, the momenta of the electrons should be reduced (i.e. the electron energies are reduced). The electric field will act on the free electrons and lower their momenta until they are captured by neutral SF_6 molecules. The total work done by the electric field on the electron is determined by the field strength and the capture mean free path. The latter quantity is energy dependent, but in general, decreases with decreasing electron energy [208]. That is to say, low-energy electrons are captured more quickly than higher energy electrons. As a result of the action of the electric field, the ionization electrons are captured at lower energies than the energies at which they were produced. This should result in a lower probability for SF_5^- production because recall from Chapter 7 that the cross-section for attachment leading to the formation of SF_5^- increases with higher electron energies.

Conversely, if the nuclear recoil is traveling upwards towards the anode/THGEM (Figure 9.1b), the mean of the electron momentum distribution is in the upwards direction. In this case, the electron momenta are in the same direction as the electric

force, and so the momenta are boosted. Because the capture mean free path decreases with increasing electron energy, the electric field has an even longer path length to act on the electrons before they are captured. As a result, once the electrons are finally captured, they are captured with an energy that is higher than their original energies – the energies at which they were created with by the recoil ionization process. This should result in a higher SF_5^- fraction and a reduced SF_6^- fraction relative to the first case where the recoil's momentum is in the opposite direction of the electric force.

So at a given recoil energy, the fraction of the charge arriving at the readout as SF_5^- provides a measure of the direction of the recoil relative to the electric field (i.e. only the polar angle is measured). In some sense, this effect is of a similar flavor to D. Nygren's columnar recombination idea [121]. But unlike columnar recombination, the direction measured with this new method is a 1D *vector* measurement, whereas the columnar recombination method is a 1D *axial* measurement. Furthermore, this effect should also be sensitive for angles other than 0 degree or 180 degrees, i.e., it should not be sensitive just to recoils directed along only a narrow cone about 0 or 180 degrees. In terms of the dark matter discovery potential, a 1D directional experiment with vector sensitivity can provide a great improvement over an energy-only experiment and is only about a factor of three less efficient than a full 3D vector reconstruction experiment [149].

In contrast to the traditional method of imaging the spatial distribution of the primary ionization electrons to determine the direction of the recoil, this proposed method would rely on the electron momentum distribution's effect on the relative abundance of charge in multiple negative ion species. Considering that the major hindrance to accurately reconstructing the original spatial distribution of the ionization electrons once it finally arrives at the readout is due to a combination of diffusion and sampling resolution, the momentum distribution reconstruction does not suffer from these effects. Information about the latter is encoded in the relative charge abundance which should be invariant under diffusion and sampling resolution in the

lateral dimensions. Note that sampling resolution in the Z dimension is important in order to separate the different charge carriers. This, however, is relatively easy to achieve because the sampling is done in time rather than spatially. Such a distinction hearkens back to the advantage of time sampling over spatial sampling discussed in Chapter 8.

It may seem in the discussion thus far that a similar amount of information about a recoil event is derived from both the proposed method (momentum distribution) and more complex method (ionization imaging method). From a different point of view, the imaging method is merely providing more information about the recoil than is necessary for the application at hand. That is to say, it is providing details about the ionization track that are not necessary to the goals of directional dark matter detection. In these searches, only a few track parameters such as the energy, type of recoil, location of event, and direction are relevant. The traditional imaging method certainly provide all of those parameters and many others but at the expense of increased detector complexity. In a sense, the complexity arises from non-pertinent (to directional dark matter detection) track information entangling/mixing with the pertinent pieces, and this is what the momentum method might circumvent.

9.3   Promise and potential obstacles

If the effect described above exists, an advantage is its independence on diffusion/drift distance and relatively weak dependence on the pressure/track length at a given reduced field. Certain detector parameters, however, must be carefully tuned to maximize the effect. For example, the electric field, or more precisely, the reduced field (E/p), should be set such that the average energy gained by an electron before attachment is large enough to cause a significant change in the production of SF_5^-. In general, the energy dependent cross-sections for the production of SF_5^- and SF_6^- must be considered in choosing the optimal electric field strength and pressure. If a large
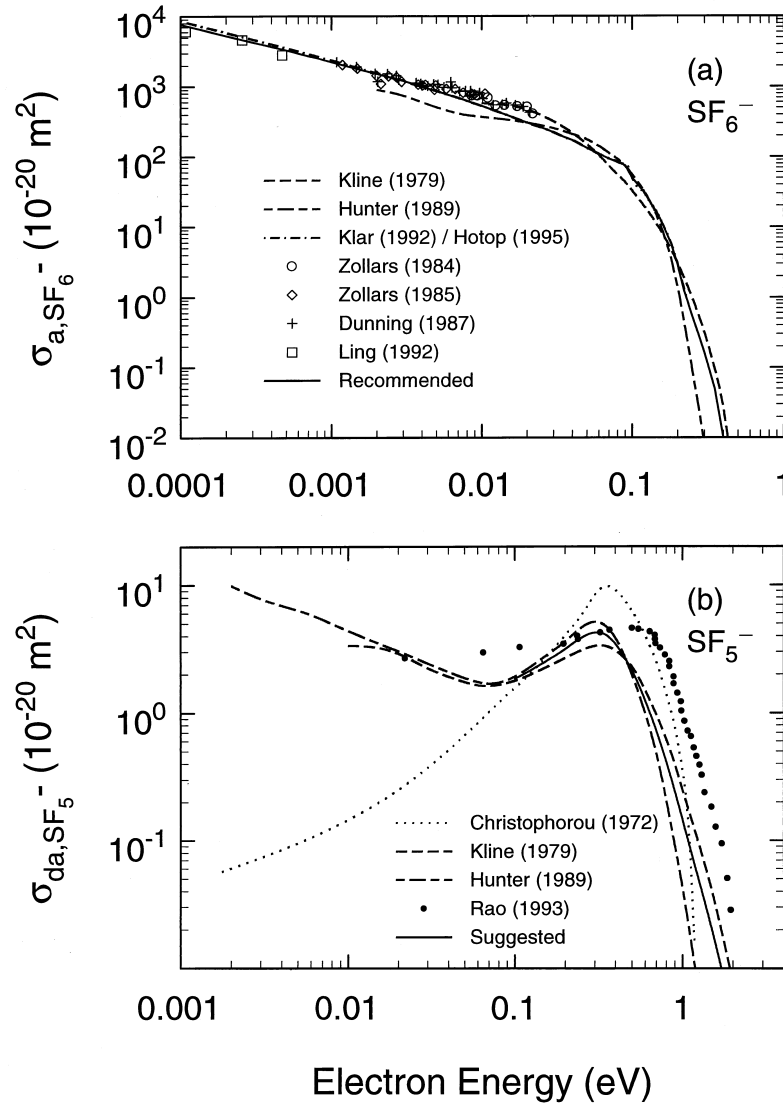
Figure 9.2: *Measurements of the electron attachment cross section for the production of SF_6^- from SF_6 as a function of the electron energy (top), and measurements of the dissociative electron attachment cross section for SF_5^- production from SF_6 as a function of the electron energy (bottom). Reproduced from Ref. [208] with permission of Elsevier.*

change in electron energy due to the electric field is required, there could be obstacles to ultra-high pressure operation at the many atmosphere level since extremely high voltages and fields would be required to provide the necessary reduced fields. But this obstacle appears to be practical rather than fundamental, and so could conceivably be

overcome. On the other hand, if the cross-sections are such that only a small change in electron energy is required to observe an effect, than there exists the possibility of a high-pressure directional detector.

To illustrate, consider the cross-section for electron attachment leading to the formation of SF_6^-, which falls precipitously at an electron energy of $\sim$0.1 eV (refer to Figure 9.2). Recall that the relative amplitude of the SF_5^- and SF_6^- peaks in the 1 kV/cm data at 20 Torr in Chapter 7 imply an electron energy of $\sim$0.1 eV. On the other hand, the cross-section for electron attachment leading to the formation of SF_5^- is relatively flat between $0.1 - 0.4$ eV. Thus, the results presented in Chapter 7 are obtained from a detector operating close to the threshold where the SF_5^- and SF_6^- charge ratio will significantly change with a small change in electron energy. This is somewhat analogous the effect exploited in transition edge sensors, where there is a strong temperature dependence on the resistance around the superconducting phase transition threshold. Since the effect would depend on the momenta of the liberated electrons which is in turn linked to the orbital momentum of those electrons in their atomic/molecular bound state, an additive gas mixed with SF_6 could provide a possible way to enhance the desired behavior.

Furthermore, recall that the time separation, ΔT, between peaks produced by two negative ion species with different mobilities is, $\Delta T \propto L * p$, where L and p are the drift length and pressure. Since diffusion scales as $\sqrt{L}$, the time separation of the peaks grows faster than their diffusive spread. This implies that if the two peaks are separated at some minimum drift length, $L_{\min}$, they will be separated for all longer drift lengths, $L > L_{\min}$. Consequently, a detector utilizing the ratio of charge carriers in time separated peaks to determine the recoil direction does not have the same constraint on its Z dimension as a detector utilizing the traditional track imaging method.

However, there are practical limitations to extending the detector drift length. One is that ultra-high voltages would be needed when the drift length is long to

provide the electric fields necessary to observe the effect. Secondly, diffusion increases with drift length and would reduce the amplitude of the smaller SF_5^- peak, possibly to a level where it becomes submerged in the electronic noise. But this can be counteracted with higher signal-to-noise.

On the other hand, the benefit is that the pressure can be raised higher than in many directional dark matter experiments because the consideration of the ratio of recoil track length to diffusion (usually, this quantity should be $\gtrsim 1$ to see a directional signature) is no longer necessary. But just as in the case of scaling the detector drift length, there are limitations to raising the pressure. When the pressure is raised, to maintain a given E/p requires that the electric field and cathode voltage be raised by the same factor. This could become difficult at high pressures (> 1 atmosphere). Also, at high pressures, gas gains could be difficult to achieve in an electronegative gas such as SF_6. But if the choice is made to operate in the low-pressure regime, a benefit is that it does not exclude the use of the traditional imaging technique for determining head-tail from charge asymmetry in the track profile. The imaging method and momentum distribution methods could conceivably be used in conjunction to obtain a better measure of the recoil direction.

9.4 Discrimination for high-pressure operation

If high-pressure operation is possible with this method, there is an important issue that remains to be addressed – discrimination between electron and nuclear recoils. In low-pressure TPCs, this is based on the difference in the stopping power, dE/dx, at a given energy. But with high pressure operation, the range can no longer be well-measured, and, hence, the stopping power is no longer a useful quantity for discrimination. Thus, to distinguish an electron recoil from a nuclear recoil, we must use a parameter that is not tied to the track topology. Speculatively, this parameter could again be derived from the energy distribution of the electrons freed during

the ionization process. But unlike our discussion of how to extract the direction of the recoil, here, we are not concern about the momenta of these electrons and their orientations relative to the electric field.

Assuming that the energy distribution of the electrons created by an electron recoil is significantly different than that created by a nuclear recoil, the relative amount of charge in the secondary peaks (not just SF_5^-) can provide a means for discrimination. Recall the waveforms of nuclear recoils from Chapter 7 showed multiple peaks which could not all be SF_5^-. Because these peaks were absent in the laser data, this implied that the electric field was not strong enough to produce these other peaks in addition to SF_5^- and SF_6^-. Much higher electron energies would be needed to produce them. The higher electron energy could have only come from the initial energy given to the freed electron during the ionization process. Given that the mass and charge of an electron recoil is very different than a nuclear recoil, the energy given to the electrons could be characteristically different. This, however, is an experimental question and must be determined from measurements.

The measurements can be done by utilizing radiation sources to produce nuclear and electron recoils over a broad range of energies. For these measurements, there are relatively few, if any, constraints on the pressure and electric field of the detector because we are only interested in the initial energy distribution of the ionization electrons. As such, pressure and electric field combinations that give low reduced fields are probably more preferred so as not to drastically alter the initial electron energies. At a given ionization energy, the fraction of charge in the secondary peaks between the electron and nuclear recoils can be compared. To accomplish this will require sufficient gas gains so that the secondary peaks are not buried within the electronic noise. Conceptually, the way discrimination is derived from this approach is very similar to discrimination in noble liquid detectors, where the prompt and delayed scintillation signals are compared. In our case, the prompt signal is from charges in the secondary peaks (SF_5^-, SF_4^-, SF_3^-, F^-, etc.) which arrive much earlier

than the delayed signal. The latter is due to charges in the primary SF_6^- peak.

Having said that, it would seem that the approach to discrimination and the effect that would make it possible would be inseparable from the directional effect. A careful consideration suggests that the strength of the electric field in the drift volume will usually not be high enough to considerably boost the electron energy before capture (no peaks other than SF_5^- in the laser data of Chapter 7). This means that the directional effect is mostly imprinted in the SF_5^- and SF_6^- peaks. Charge in the peaks that arrive at the readout at earlier times than SF_5^- are mostly due to electrons with initially high energies rather than the energy gained from the electric field. Of course, the alignment of the initial electron momentum with the electric field can influence the abundance of charges in these other peaks. But the formation of these peaks and their abundance relative to SF_5^- and SF_6^- are greatly suppressed by the cross-sections for attachment leading to their production. Therefore, we posit that the directional effect comes from the relative abundance of charge in the SF_5^- and SF_6^- peaks, while the discrimination effect derives from the relative abundance of charge in all secondary peaks.

9.5 Conclusion

Admittedly, the discussion in this chapter has been speculative in nature. The ultimate test on whether the ideas presented here are valid rest with measurements. But before devoting time to construct an experimental setup to make these, simulation studies may be a necessary first step to gauge the feasibility of measuring the effects described here. But the challenges for directional detection with low-pressure TPCs presented throughout this thesis show that novel approaches and speculative ideas need to be considered if the hope of directional detection of dark matter and the subsequent era of WIMP astronomy are ever to be realized.

References

[1] F. Zwicky, Helvetica Physica Acta, 6, 110, (1933). 1, 10

[2] S. Weinberg, *Cosmology*, Oxford University Press, (2008). 1, 25

[3] PLANCK Collaboration, A&A 594, A13 (2016). 5, 7, 8, 9, 12

[4] G. Byrd, A. D. Chernin, P. Teerikorpi, M. Valtonen, *Paths to Dark Energy: Theory and Observation*, Walter de Gruyter, (2012). 7, 13

[5] PLANCK Collaboration, A&A 594, A1 (2016). 8

[6] T.-P. Cheng, *Relativity, Gravitation and Cosmology : A Basic Introduction*, Oxford University Press, (2010). 8

[7] T. Padmanabhan, *An Invitation to Astrophysics*, World Scientific Publishing, (2006). 11

[8] S. Tremaine and H. M. Lee, *Dark Matter In The Universe*, "Dark Matter in Galaxies and Galaxy Systems", World Scientific Publishing, Ch. 6, 72-75, (2004). 12

[9] A. Cavaliere and R. Fusco-Femiano, Astron. and Astrophys. 49, 137-144 (1976). 14

[10] A. Cavaliere and R. Fusco-Femiano, Astron. and Astrophys. 70, 677-684 (1978). 14

[11] A. D. Lewis, E. Ellingson, S. L. Morris, and R. G. Carlberg, Astrophys. J. 517, 587-608 (1999). 14

[12] V. C. Rubin and W. K. Ford Jr., Astrophys. J. 159, 379-403 (1970). 15

[13] R. N. Whitehurst and M. S. Roberts, Astrophys. J. 175, 347-352 (1972). 15

[14] R. N. Whitehurst and M. S. Roberts, Astrophys. J. 201, 327-346 (1975). 15

References

[15] J. Einasto, E. Saar, A. Kaasik, and P. Traat, Astronomicheskii Tsirkulyar 811, 3-4 (1974). 15

[16] J. P. Ostriker, P. J. E. Peebles, and A. Yahil, Astrophys. J. 193, L1-L4 (1974). 16

[17] J. F. Navarro, C. S. Frenk, and S. D. M. White, Astrophys. J. 264, 563-575 (1996). 16

[18] F. Nesti and P. Salucci, J. Cosmos. Astropart. Phys. 7, 16 (2013). 16

[19] F. Iocco, M. Pato, G. Bertone, and P. Jetzer, JCAP 11, 29 (2011). 16, 30

[20] D. S. Gorbunov and V. A. Rubakov, Introduction to the Theory of the Early Universe: Hot Big Bang Theory (2011). 16

[21] B. J. Carr and M. Sakellariadou, Astrophys. J. 516, 195 (1999).

[22] B. Paczynski, Astrophys. J. 304, 1 (1986). 18

[23] L. Wyrzykowski et al., MNRAS 397, 1228 (2009). 18

[24] P. Tisserand et al., A&A 469, 387 (2007). 18

[25] G. C. Lacey and J. P. Ostriker, Astrophys. J. 299, 633 (1985). 18

[26] A. De Rjula, P. Jetzer, and E. Massa, A&A 254, 99 (1992). 18

[27] J. Chaname, A. Gould, Astrophys. J. 601, 289 (2004). 18

[28] D. P. Quinn, M. I. Wilkinson, M. J. Irwin, J. Marshall, A. Koch, and V. Belokurov, MNRAS 396, L11, (2009). 18, 19

[29] M. A. Monroy-Rodrguez and C. Allen, Astrophys. J. 790, 159 (2014). 18

[30] P. W. Graham, I. G. Irastorza, S. K. Lamoreaux, A. Lindner, and K. A. van Bibber, Annu. Rev. Nucl. Part. Sci. 65, 485514 (2015). 20, 21

[31] C. Baker et al., Phys. Rev. Lett. 97, 131801 (2006). 20

[32] R. D. Peccei and H. R. Quinn, Phys. Rev. Lett. 38, 1440 (1977). 20

[33] R. D. Peccei and H. R. Quinn, Phys. Rev. D 16, 1791 (1977). 20

[34] S. Weinberg, Phys. Rev. Lett. 40, 223 (1978). 20

[35] F. Wilczek, Phys. Rev. Lett. 40, 279 (1978). 20

References

[36] H. Y. Cheng, Phys. Rep. 158, 1 (1988). 20

[37] M. S. Turner, Phys. Rep. 197, 67 (1990). 20

[38] G. G. Raffelt, Phys. Rep. 198, 1 (1990). 20

[39] H. Primakoff, Phys. Rev. 81, 899 (1951). 21

[40] G. G. Raffelt, Annu. Rev. Nucl. Part. Sci. 49, 163 (1999). 21

[41] K. van Bibber, P. M. McIntyre, D. E. Morris, and G. G. Raffelt, Phys. Rev. D 39, 2089 (1989). 21

[42] E. Arik et al. (CAST Collab.), J. Cosmol. Astropart. Phys. 0902, 008 (2009). 21

[43] S. Aune et al. (CAST Collab.), Phys. Rev. Lett. 107, 261302 (2011). 21

[44] I. G. Irastorza et al., J. Cosmol. Astropart. Phys. 1106, 013 (2011). 21

[45] R. Bradley et al. Rev. Mod. Phys. 75, 777 (2003). 21

[46] S. J. Asztalos et al. (ADMX Collab.), Phys. Rev. Lett. 104, 041301 (2010). 22

[47] S. J. Asztalos, L. J. Rosenberg, K. van Bibber, P. Sikivie, K. Zioutas, Annu. Rev. Nucl. Part. Sci. 56, 293326 (2006). 22

[48] K. Ehret et al., Phys. Lett. B 689, 149 (2010). 22

[49] R. Bähre et al., arXiv:1302.5647 [physics.ins-det], (2013). 22

[50] A. Boyarsky, O. Ruchayskiy, and M. Shaposhnikov, Annu. Rev. Nucl. Part. Sci. 59, 191214 (2009). 23, 24

[51] P. B. Pal and L. Wolfenstein, Phys. Rev. D 25, 766 (1982). 23

[52] A. D. Dolgov and S. H. Hansen, Astropart. Phys. 16, 339 (2002). 23

[53] K. Abazajian, G. M. Fuller, W. H. Tucker, Astrophys. J. 562, 593 (2001). 23

[54] K. N. Abazajian, M. Markevitch, S. M. Koushiappas, R. C. Hickox, Phys. Rev. D 75, 063511 (2007). 23

[55] S. Riemer-Srensen, S. H. Hansen, K. Pedersen, Astropart. Phys. 644, L33 (2006). 23

[56] A. Boyarsky, O. Ruchayskiy, M. Markevitch, Astropart. Phys. 673, 752 (2008). 23

References

[57] C. R. Watson, J. F. Beacom, H. Yuksel, T. P. Walker, Phys. Rev. D 74, 033009 (2006). 23

[58] A. Boyarsky, J. W. den Herder, A. Neronov, O. Ruchayskiy, Astropart. Phys. 28, 303 (2007). 23

[59] H. Yuksel, J. F. Beacom, C. R. Watson, Phys. Rev. Lett. 101, 121301 (2008). 23

[60] A. Boyarsky, D. Malyshev, A. Neronov, O. Ruchayskiy, MNRAS 387, 1345 (2008). 23

[61] M. Loewenstein, A. Kusenko, P. L. Biermann, arXiv:0812.2710. 23

[62] J. L. Feng, Annu. Rev. Astron. Astrophys. 48, 495545 (2010). 22, 26, 27

[63] K. Griest and M. Kamionkowski, Phys. Rep. 333-334, 167-182 (2000). 29

[64] G. Jungman, M. Kamionkowski, and K. Griest, Phys. Rep. 267, 195-373 (1996). 29

[65] M. W. Goodman and E. Witten, Phys. Rev. D 31, 3059 (1985). 29

[66] J. D. Lewin and P. F. Smith, Astropart. Phys., 6, 87-112 (1996). 30, 32, 38, 39, 45, 118

[67] M. S. Alenazi and P. Gondolo, Phys. Rev. D 77, 043532 (2008). 32, 34, 35, 47, 50

[68] R. H. Helm, Phys. Rev. 104, 466 (1956). 33

[69] J. Engel, S. Pittel, and P. Vogel, Int. J. Mod. Phys., E1 (1992) 1. 33, 37

[70] J. R. Ellis and R. A. Flores, Phys. Lett. B, 263, 259266 (1991). 37, 148

[71] J. Engel and P. Vogel, Phys. Rev. D 40, 31323135 (1989). 37

[72] P. C. Divari, T. S. Kosmas, J. D. Vergados, and L. D. Skouras, Phys. Rev. C 61, 054612 (2000). 37

[73] M. T. Ressell et al., Phys. Rev. D 48, 55195535 (1993). 37

[74] J. Engel, S. Pittel, E. Ormand, and P. Vogel, Phys. Lett. B 275, 119123 (1992). 33, 37

[75] M. T. Ressell and D. J. Dean, Phys. Rev. C 56, 535546 (1997). 37

References

[76] D. S. Akerib et al., Phys. Rev. Lett. 116, 161301 (2016). 41, 44, 50, 121

[77] C. Amole et al. (PICO Collaboration), Phys. Rev. D 93, 061101 (2016). 43, 50, 51, 122

[78] C. Amole et al. (PICO Collaboration), Phys. Rev. D 93, 052014 (2016). 43, 50, 51, 52, 122

[79] H. Baer, C. Balazs, A. Belyaev, and J. OFarrill, JCAP 0309, 007 (2003). 43

[80] G. Angloher et al., Eur. Phys. J. C 74, 3184 (2014). 43

[81] M. Kuzniak, M. Boulay and T. Pollmann, Astropart. Phys. 36, 77 (2012). 43

[82] J. H. Davis, C. McCabe and C. Boehm, JCAP 1408, 014 (2014). 43

[83] J. H. Davis, Int. J. Mod. Phys. A, 30, 1530038 (2015). 43

[84] A. K. Drukier, K. Freese, and D. N. Spergel, Phys. Rev. D, Vol. 33, No. 12, (1986). 44

[85] D. N. Spergel, Phys. Rev. D 37, 1353 (1988). 44, 46, 47, 118

[86] N. Bozorgnia, G. B. Gelminia, and P. Gondolo, JCAP 06, 03 (2012). 46

[87] K. Blum, arXiv:1110.0857. 44

[88] J. P. Ralston, arXiv:1006.5255. 44

[89] D. DAngelo (Borexino Collaboration), arXiv:1109.3901. 44

[90] E. Fernandez-Martinez and R. Mahbubani, J. Cosmol. Astropart. Phys. 07, 029 (2012). 44

[91] J. H. Davis, Phys. Rev. Lett. 113, 081302 (2014). 44

[92] R. Bernabei et al., Eur. Phys. J. C 56, 333 (2008). 44

[93] R. Bernabei, P. Belli, F. Cappella, V. Caracciolo, S. Castellano et al., Eur. Phys. J. C 73, 2648 (2013). 44

[94] G. Angloher et al., Eur. Phys. J. C 72, 1971 (2012). 44

[95] C. E. Aalseth et al., Phys. Rev. D 88, 012002 (2013). 44

[96] R. Agnese et al., Phys. Rev. Lett. 111, 251301 (2013). 44

[97] E. Aprile et al., Phys. Rev. Lett. 109, 181301 (2012). 44, 52

References

[98] R. Agnese et al., Phys. Rev. Lett. 112, 241302 (2014). 44

[99] D. P. Snowden-Ifft, C. J. Martoff, and J. M. Burwell, Phys. Rev. D 61, 101301 (2000). 47

[100] G. J. Alner et al., Nucl. Instr. Meth. Phys. Res. A 535, 644655 (2004). 47

[101] K. Miuchi et al., Phys. Lett. B 654, 58 (2007). 47

[102] D. Santos et al., J. Phys. Conf. Ser. 65, 012012 (2007). 47

[103] D. Dujmic et al., Nucl. Instr. Meth. A 584, 327 (2008). 47, 53

[104] S. E. Vahsen et al., The Directional Dark Matter Detector (D3), EAS Publications Series, 53, pp 43-50, (2012). 47

[105] P. Gondolo, Phys. Rev. D 66, 103513 (2002). 48

[106] E. Behnke et al., Phys. Rev. D 86, 052001 (2012). 51, 52

[107] S. Archambault et al., Phys. Lett. B 711, 153 (2012). 51

[108] M. Felizardo et al., Phys. Rev. D 89, 072013 (2014). 51

[109] S. Ahlen et al., Phys. Lett. B 695, 124 (2011). 51

[110] K. Nakamura et al., Prog. Theor. Exp. Phys., 043F01 (2015). 51

[111] J. B. R. Battat et al., Phys. Dark Univ. 9-10, 1-7 (2015). 50, 51, 54, 98, 148, 149, 177, 185

[112] D. S. Akerib et al., Phys. Rev. Lett. 112, 091303 (2014). 52

[113] P. Agnes et al., arXiv:1510.00702v1. 52

[114] R. Agnese et al., Phys. Rev. D 92, 072003 (2015). 52

[115] P. Grothaus, M. Fairbairn, and J. Monroe, Phys. Rev. D 90, 055018 (2014). 51

[116] F. Ruppin, J. Billard, E. Figueroa-Feliciano, and L. Strigari, Phys. Rev. D 90, 083510 (2014). 51

[117] C. A.J. OHare, A. M. Green, J. Billard, E. Figueroa-Feliciano, and L. E. Strigari, Phys. Rev. D 92, 063518 (2015). 51

[118] F. Mayet et al., Physics Reports 627, 149 (2016). 47, 51, 175

[119] T. Naka et al., Nucl. Instr. Meth. A 718, 51952 (2013). 47, 53

References

[120] N. DAmbrosio et al., JINST 9, C01043 (2014). 47, 53

[121] D. R. Nygren, J. Phys.: Conf. Ser. 460, 012006 (2013). 47, 53, 223

[122] V. M. Gehman et al., JINST 8, C10001 (2013). 47, 53

[123] F. Cappella et al., Eur. Phys. J. C 73, 2276 (2013). 47, 53

[124] S. Ahlen et al., Int. J. Mod. Phys. A 25, 1-51 (2010). 47

[125] S. Burgos et al., Astropart. Phys. 31, 261266 (2009). 53, 54, 59, 105

[126] D. Nygren, PEP-198-1975. 53

[127] S. Burgos et al., Nucl. Instr. Meth. A 600, 417-423 (2009). 54, 105

[128] J. F. Ziegler, J. P. Biersack, and U. Littmark, "The Stopping and Range of Ions in Solids" (Pergamon Press, New York, 1985), http://www.srim.org. 54, 55, 75, 95

[129] L. G. Christophorou, J. K. Olthoff, and M. V. V. S. Rao, J. Phys. Chem Ref. Data 25, 1341 (1996). 57, 58, 74

[130] M. G. Curtis, I. C. Walker, and K. J. Mathieson, J. Phys. D 21, 1271 (1988). 57, 58

[131] M. S. Naidu and A. N. Prasad, J. Phys. D 5, 983 (1972). 57, 58

[132] C. S. Lakshminarasimha, J. Lucas, and D. A. Price, Proc. IEE 120, 1044 (1973). 57, 58

[133] L. G. Christophorou and J. K. Olthoff, J. Phys. Chem Ref. Data 28, 967 (1999). 57, 74

[134] Y. Hayashi and Y. Nakamura, Proceedings of the International Conference on Atomic and Molecular Data and their Applications, NIST Special Publication 926 , edited by W. L. Wiese and P. J. Mohr (U.S. Department of Commerce , Gaithersburg, MD, 1998); p.248. 57

[135] C. J. Martoff et al., Nucl. Instr. Meth. A 440, 355-359 (2000). 57, 148

[136] T. Ohnuki, D. P. Snowden-Ifft, and C. J. Martoff, Nucl. Instr. Meth. A 463, 142148 (2001). 57

[137] C. J. Martoff et al., Nucl. Instr. Meth. A 555, 5558 (2005). 57

References

[138] K. Pushkin and D. P. Snowden-Ifft, Nucl. Instr. Meth. A 606, 569577 (2009). 57

[139] M. P. Dion, S. Son, S. D. Hunter, and G. A. de Nolfo, Nucl. Instr. Meth. A 648, 186191 (2011). 57

[140] D. P. Snowden-Ifft and J.-L. Gauvreau, Rev. Sci. Instr. 84, 053304 (2013). 57, 58, 167, 168, 173, 174

[141] J. B. R. Battat et al., JINST 9 P11004 (2014). 58, 185

[142] C. K. Shalem, R. Chechik, A. Breskin, K. Michaeli, Nucl. Instr. Meth. A 558, 475489 (2006). 58, 89, 124, 130

[143] C. K. Shalem, R. Chechik, A. Breskin, K. Michaeli, N. Ben-Haim, Nucl. Instr. Meth. A 558, 468474 (2006). 58, 89, 124, 130

[144] A. Hitachi, J. Phys.: Conf. Ser. 65, 012013 (2007). 59

[145] B. Morgan and A. M. Green, Phys. Rev. D 72, 123501 (2005). 59, 97, 117

[146] B. Morgan, A. M. Green, and N. J. C. Spooner, Phys. Rev. D 71, 103507 (2005). 59, 97, 110, 117, 119

[147] C. J. Copi, L. M. Krauss, D. Simmons-Duffin, and S. R. Stroiney, Phys. Rev. D 75, 023514 (2007). 59, 97

[148] A. M. Green and B. Morgan, Astropart. Phys., 27, 142149 (2007). 59, 60

[149] J. Billard, Phys. Rev. D 91, 023513 (2015). 59, 97, 223

[150] F. A. F. Fraga et al., Nucl. Instr. Meth. Phys. Res. A 471, 125130 (2001). 129

[151] F. A. F. Fraga et al., Nucl. Instr. Meth. Phys. Res. A 478, 357361 (2002). 129

[152] F. A. F. Fraga et al., Nucl. Instr. Meth. Phys. Res. A 513, 379387 (2003). 129

[153] F. Sauli and A. Sharma, Annu. Rev. Nucl. Part. Sci. 49, 34188 (1999). 67

[154] RD51 Collaboration, http://rd51-public.web.cern.ch/RD51-Public/. 67

[155] F. Sauli, Nucl. Instr. Meth. Phys. Res. A 386, p. 531 (2010). 68, 129, 204

[156] A. F. Buzulutskov, Instr. Exp. Tech. 50, 3, 287 (2010). 68, 132

[157] A. Morozov, M. M. F. R. Fraga, L. Pereira, L. M. S. Margato, S. T. G. Fetal, B. Guerard, G. Manzin, F. A. F. Fraga, Nucl. Instr. Meth. Phys. Res. B 268, 14561459 (2010). 69

References

[158] A. Kaboth et al., Nucl. Instr. Meth. A 592, 63 (2008). 69, 92

[159] G. F. Reinking, L. G. Christophorou, and S. R. Hunter, J. Appl. Phys. 60, 499 (1986). 70, 134

[160] A. Bondar et al., Nucl. Instr. Meth. A 535, 299-302 (2004). 70

[161] J. R. Janesick, "Scientific Charge-coupled Devices" (Society of Photo Optical Press, 2001). 71

[162] S. F. Biagi, Nucl. Instr. Meth. A 421, 234-240 (1999). 74

[163] J. B. R. Battat et al., Nucl. Instr. Meth. Phys. Res. A 794, 3346 (2015). 80, 82, 185

[164] J. Brack et al., Physics Procedia 61, 130137 (2015). 80, 82, 185

[165] Q. Riffard et al., arXiv:1504.05865v1. 83, 98

[166] A. Hitachi, Rad. Phys. Chem. 77, 13111317 (2008) . 84, 87, 104

[167] O. Guillaudin, J. Billard, G. Bosson, et al., EAS Publ. Ser. 53, 119 (2012), arXiv:1110.2042. 87

[168] K. N. Buckland, M. J. Lehner, G. E. Masek, and M. Mojaver, Phys. Rev. Lett. 73, 1067 (1994). 89

[169] K. N. Buckland, M. J. Lehner, G. E. Masek, IEEE Transactions on 44.1, 6-13 (1997). 89

[170] A. Pansky, A. Breskin, A. Buzulutskov, R. Chechik, V. Elkind, J. Vavra, Nucl. Instr. Meth. Phys. Res. A 354, 262-269 (1995). 92

[171] M. M. Fraga, F. A. F. Fraga, S. T. G. Fetal, L. M. S. Margato, R. Ferreira Marques, A. J. P. L. Policarpo, Presented at the Beaune 2002 Conference on New Development in Photodetection, Nucl. Instr. and Meth. A 504, 88 (2003). 92

[172] A. Kozlov, I. Ravinovich, L. Shekhtman, Z. Fraenkel, M. Inuzuka, I. Tserruya, Nucl. Instr. Meth. Phys. Res. A 523, 345354 (2004) . 92

[173] P. Magain, F. Courbin, and S. Sohy, Astrophys. Journ., 494, 472-477 (1998). 93

[174] H. Demers et al., Scanning 33, (3), 135146 (2011). 95

[175] J. Billard, F. Mayet, and D. Santos, JCAP 07, 020 (2012). 96

References

[176] D. Santos et al., J. Phys.: Conf. Ser. 460, 012007 (2013). 98

[177] S. E. Vahsen, M. T. Hedges, I. Jaegle, S. J. Ross, I. S. Seong, T. N. Thorpe, J. Yamaoka, J. A. Kadyk, M. Garcia-Sciveres, arXiv:1407.7013. 98

[178] J. B. R. Battat, Journal of Physics: Conference Series 469, 012001 (2013).

[179] D. P. Snowden-Ifft, Rev. Sci. Instr. 85, 013303 (2014). 98, 148, 149, 177, 185, 189

[180] N. S. Phan et al., arXiv:1609.05249. 98

[181] K. V. Mardia and P. Jupp, Directional Statistics (Wiley, New York, 2002). 102, 119

[182] N. I. Fisher, T. Lewis, and B. J. J. Embleton, Statistical Analysis of Spherical Data (Cambridge University Press, Cambridge, England, 1987). 102

[183] K. V. Mardia, Statistics of Directional Data (Academic Press, New York, 1972). 102

[184] G. J. G. Upton and B. Fingleton, Spatial Data Analysis by Example Vol. 2: Categorical and Directional Data, (John Wiley & Sons, New York, 1989). 102

[185] P. Berens, CircStat: A Matlab Toolbox for Circular Statistics, Journal of Statistical Software, Volume 31, Issue 10, (2009). 109

[186] J. H. Zar, *Biostatistical Analysis*, Pearson, (2010). 110

[187] B. R. Moore, Biometrika, Vol. 67, No. 1, pp. 175-180 (Apr., 1980). 112

[188] C. Bingham, The Annals of Statistics 2, 1201 (1974). 119

[189] E. M. Giné, The Annals of Statistics 3, 1243 (1975). 119

[190] M. S. Briggs, Astrophys. J. 407, 126 (1993). 119

[191] J. Tatarowicz and C.J. Martoff, Astropart. Phys. 35, 235241 (2011). 124

[192] R. W. Crompton and G. N. Haddad, Aust. J. Phys. 36, 15-25 (1983). 147, 154

[193] D. Smith, N. G. Adams and E. Alge, J. Phys. B: At. Mol. Phys. 17, 461 (1984). 147, 154

[194] Z. L. Petrovic and R. W. Crompton, J. Phys. B 17, 2777-2791 (1985). 147, 154

References

[195] T. M. Miller, A. E. Stevens Miller, J. F. Paulson, and Xifan Liu, J. Chem. Phys. 100, 8841 (1994). 147, 154, 166

[196] P. G. Datskos, L. G. Christophorou,and J. G. Carter, J. Chem. Phys. 99, 8607 (1993). 147, 154

[197] P. Spanel, S. Matejcik and D. Smith, J. Phys. B: At. Mol. Opt. Phys. 28, 2941 (1995). 147, 154

[198] M. Braun, C. Barsotti, S. Marienfeld, E. Leber, M.-W. Ruf, and H. Hotop, Eur. Phys. J. D 35, 177 (2005). 147, 154

[199] A. A. Viggiano, T. M. Miller, J. F. Friedman, and J. Troe, J. Chem. Phys. 127, 244305 (2007). 147, 154

[200] R. L. Merlino and S.-H. Kim, J. Chem. Phys. 129, 224310 (2008). 147, 154

[201] L. G. Christophorou, J. K. Olthoff, and D. S. Green, NIST Technical Note 1425 (1997). 147

[202] L. G. Christophorou and J. K. Olthoff, J. Phys. Chem. Ref. Data, Vol. 29, No. 3 (2000). 147, 154, 155, 156

[203] P. Camarri et al., Nucl. Instr. and Meth A 414, 317 (1998). 147

[204] G. Aielli et al., Nucl. Instr. and Meth A 493, 137 (2002). 147

[205] D. R. Nygren, Journal of Physics: Conference Series 65, 012003 (2007). 147

[206] S. Burgos et al., Astropart. Phys., 28, 409421 (2007). 148, 185

[207] S. J. Cavanagh, S. T. Gibson, and B. R. Lewis, J. Chem. Phys. 137, 144304 (2012). 148

[208] L. G. Christophorou and J. K. Olthoff, Int. J. Mass Spectr. 205, 27 (2001). 148, 183, 222, 225

[209] E. P. Grimsrud, S. Chowdhury, P. Kebarle, J. Chem. Phys. 83, 1059 (1985). 148

[210] E. C. M. Chen, J.R. Wiley, C.F. Batten, W.E. Wentworth, J. Phys. Chem. 98, 88 (1994). 148

[211] NIST Standard Reference Database 69: NIST Chemistry WebBook. 149

[212] L. G. Christophorou, "Insulating Gases," Nuclear Instruments and Methods in Physics Research, Vol. A268, pp. 424-433, (1988). 149

References

[213] L. G. Christophorou and S. R. Hunter, "From Basic Research to Applications", in Electron-Molecule Interactions and Their Applications, L. G. Christophorou (Ed.), Academic Press, NY, Vol. 2, Chap. 5, (1982). 149

[214] Th. Aschwanden, "Swarm Parameters in SF6 and SFe/N2 Mixtures Determined from a Time Resolved Discharge Study", in Gaseous Dielectrics IV, L. G. Christophorou and M. 0. Pace (Eds.), Pergamon Press, NY, pp. 24-32, (1984). 149

[215] W. P. Wood, J. Heicklen, J. Phys. Chem. 75, 7, 861-866 (1971). 150

[216] D. R. Nygren, 7th Symposium on large TPCs for low-energy rare event detection, Paris (2014). 150

[217] D. Edelson, J. E. Griffiths, and K. B. McAfee, Jr., J. Chem. Phys. 37, 917 (1962). 155

[218] R. N. Compton, L. G. Christophorou, G. S. Hurst, and P. W. Reinhardt, J. Chem. Phys. 45, 4634 (1966). 155

[219] P. W. Harland and J. C. J. Thynne, J. Phys. Chem. 75, 3517 (1971). 155

[220] L. G. Christophorou, *Atomic and Molecular Radiation Physics* (Wiley, New York, 1971), Ch. 6. 155

[221] L. G. Christophorou, Adv. Electron, Electron Phys. 46, 55 (1978). 155

[222] L. G. Christophorou, D. L. McCorkle, and A. A. Christodoulides, Electron-Molecule Interactions and Their Applications, edited by L. G. Christophorou (Academic, New York, 1984), Vol. 1, Chap. 6. 155

[223] J. M. S. Henis and C. A. Mabie, J. Chem. Phys. 53, 2999 (1970). 155

[224] R. W. Odom, D. L. Smith, and J. H. Futrell, J. Phys. B 8, 1349 (1975). 155

[225] M. S. Foster and J. L. Beauchamp, Chem. Phys. Lett. 31, 482 (1975). 155

[226] E. W. McDaniel, E. A. Mason, The Mobility and Diffusion of Ions in Gases, John Wiley & Sons, USA, 1973. 155

[227] B. Lehmann, Z. Naturforsch. 25A, 1755 (1970). 156

[228] M. V. V. S. Rao, S. K. Srivastava, in: T. Andersen, B. Fastrup, F. Folkmann, H. Knudsen (Eds.), Proceedings of the 18th International Conference on the Physics of Electronic and Atomic Collisions, Aarhus, Denmark, July 21-27, 1993, Abstracts of contributed papers, p. 345. 156

References

[229] L. E. Kline, D. K. Davies, C. L. Chen, P. J. Chantry, J. Appl. Phys. 50, 6789 (1979). 156

[230] L. G. Christophorou and J. K. Olthoff, Int. J. Mass Spectrom. 205, 27-41 (2001). 156

[231] H. Hotop, D. Klar, J. Kreil, M.-W. Ruf, A. Schramm, J. M. Weber, in: L. J. Dube, J. B. A. Mitchell, J. W. McConkey, C. E. Brion (Eds.), The Physics of Electronic and Atomic Collisions, AIP Conference Proceedings, vol. 360, AIP Press, Woodbury, New York, 1995, p. 267. 156

[232] D. Klar, M.-W. Ruf, H. Hotop, Aust. J. Phys. 45, 263 (1992). 156

[233] X. Ling, B. G. Lindsay, K. A. Smith, F. B. Dunning, Phys. Rev. A 45, 242 (1992). 156

[234] S. R. Hunter, J. G. Carter, L. G. Christophorou, J. Chem. Phys. 90, 4879 (1989). 156

[235] P. L. Patterson, J. Chem. Phys. 53, 696 (1970). 156, 167

[236] J. de Urquijo-Carmona, I. Alvarez, H. Martinez, and C. Cisneros, J. Phys. D 24, 664 (1991). 156, 167, 168

[237] I. A. Fleming and J. A. Rees, J. Phys. B: At. Mol. Phys. 2, 777-9 (1969). 156, 167

[238] Y. Wang, R. L. Champion, L. D. Doverspike, J. K. Olthoff, and R. J. van Brunt, J. Chem. Phys. 91, 2254 (1989). 157

[239] A. A. Christodoulides, D. L. McCorkle, and L. G. Christophorou, in *Electron-Molecule Interactions and Their Applications*, edited by L. G. Christophorou (Academic, New York, 1984), Vol. 2, Chap. 6. 157, 183

[240] J. K. Olthoff, R. J. van Brunt, Y. Wang, R. L. Champion, and L. D. Doverspike, J. Chem. Phys. 91, 2261 (1989). 157

[241] R. L. Champion, in *Gaseous Dielectrics VI*, edited by L. G. Christophorou and I. Sauers, (Plenum, New York, 1991), p. 1. 157

[242] H. Haberland, H. Langosch, H.-G. Schindler, and D. R. Worsnop, J. Phys. Chem. 88, 3903-3904 (1984). 162

[243] H. Haberland, C. Ludewigt, H.-G. Schindler, and D. R. Worsnop, J. Chem. Phys. 81, (8) (1984). 162

References

[244] W. B. Knighton, D.R. Zook, E. P. Grimsrud, J. Am. Soc. Mass Spectrom. 1, 372-81 (1990). 162

[245] L. W. Sieck, J. Phys. Chem. 90, 6684-6687 (1986). 162

[246] S. T. Arnold and A. A. Viggiano, J. Phys. Chem. A 105, 3527-3531 (2001). 162, 163

[247] W. Blum and L. Rolandi, "Particle Detection with Drift Chambers", New York: Springer-Verlag (1994). 168, 170

[248] E. A. Mason and E. W. McDaniel, *Transport Properties of Ions in Gases* (Wiley, New York, 1988). 169

[249] L. A. Viehland and E. A. Mason, Atomic Data and Nuclear Data Tables 60, 37-95 (1995). 169

[250] E. Krishnakumar and K. Nagesha, J. Phys. B: At. Mol. Opt. Phys. 25, 1645 (1992). 178

[251] S. A. Rangwala, S. V. K. Kumar, and E. Krishnakumar, Phys. Rev. A 64, 012707 (2001). 178

[252] D. P. Snowden-Ifft et al., Neutron recoils in the DRIFT detector, Nucl. Instr. Meth. A 498, 155-164 (2003). 178

[253] J. Miyamoto et al., GEM operation in negative ion drift gas mixtures, Nucl. Instr. Meth. A 526, 409-412 (2004). 178

[254] I. Giomataris, R. De Oliveira, S. Andriamonje, S. Aune, G. Charpak, P. Colas, G. Fanourakis, E. Ferrer, A. Giganon, Ph. Rebourgeard, P. Salin, Micromegas in a bulk, Nucl. Instr. Meth. A 560, 405-408 (2006). 178

[255] M. P. Dion, C. J. Martoff, and M. Hosack, Astropart. Phys. 33, 216-220 (2010) . 178

[256] Y. H. Hilal and L. G. Christophorou, J. Phys. D: Appl. Phys. 20 (1987). 180

[257] I. Lopes, H. Hilmert, and W. F. Schmidt, J. Phys. D: Appl. Phys. 19 (1986). 180

[258] L. G. Christophorou, "Atomic and Molecular Radiation Physics", New York: Wiley-Interscience (1971). 180

[259] C. Blondel, P. Cacciani, C. Delsart, R. Trainham, Phys. Rev. A 40, 3698 (1989). 183

References

[260] A. E. Stevens Miller, T. M. Miller, A. A. Viggiano, R. A. Morris, J. M. Van Doren, S. T. Arnold, and J. F. Paulson, J. Chem. Phys., 102(22), 8865 (1995). 183

[261] J. Brack et al., JINST 9, P07021 (2014). 185

[262] C. L. Chen and P. J. Chantry, J. Chem. Phys. 71, 3897 (1979). 189, 190

[263] P. G. Datskos, J. G. Carter, and L. G. Christophorou, Chem. Phys. Lett. 239, 38 (1995). 190